FINAL REPORT

Development of a 1 kW Modular Direct Carbon Fuel Cell Demonstration Plant (RDE493-23)

Professor Scott Donne

University of Newcastle

July 2021

Submitted to Coal Innovation NSW

Project Commence Date: July, 2017

Project Cessation Date: June 2019

Project Duration: 2 years

Funding Allocated: $1,643,001

Phone: (02) 4921 5477

Fax: (02) 4921 5472

Email: Scott.Donne@newcastle.edu.au

Address: Discipline of Chemistry, University of Newcastle, Callaghan NSW 2308

ACKNOWLEDGEMENTS AND DISCLAIMER

EXECUTIVE SUMMARY

The direct carbon fuel cell (DCFC) is a future energy technology that is an efficient process for electrical energy generation from carbon-based sources. This technology has an extremely high theoretical efficiency due to favourable thermodynamics of the electro-oxidation reactions in the process. However, several technical challenges exist which must be addressed before the technology can be commercialized. This project will bridge a crucial gap between research and commercialization of DCFC technology where many fundamental challenges of operation of a pilot scale cell are addressed, and the findings translated to a fully functioning modular demonstration unit capable of generating 1 kW. Initially the project scope was for a 10 kW system; however, during the design stage of the project it was identified that such a large scale system would involve substantial duplication of key components, involve added complexity above and beyond the present system, as well as be physically unable to be accommodated in the research space available. Under these circumstances, a revised 1 kW system was targeted, that would nevertheless use many of the components of a larger system. Broadly, the project has two discrete streams: (i) fundamental research and developmental work, and (ii) design and build a 1 kW demonstration module.

In the first stage, fundamental research and developmental work on the following aspects have been the main focus: mass and energy balance, materials corrosion, anode formulation and processing, and cathode optimization. A steady state model has been built which allows assessment of the final system efficiency and sensitivity of the values to several variables including the achievable electrochemical efficiency of the system and the extent of parasitic gasification of the fuel (reverse Boudouard reaction). Corrosion studies were performed on stainless steels (316L and 253MA) for fuel cell tank and other metals (silver, nickel, copper, iron and titanium) for anode current collector applications in the corrosive carbonate media at high temperatures. A series of full-cell experiments were conducted for anode formulation and processing and cathode optimization. The effects of coal particle size, impurities/catalysts (SnO_2, CeO_2, Fe_2O_3, and Mn_2O_3) in the slurry (coal + carbonates), sweep gas in the anode compartment, and anode current collector area were studied. Optimization of the cathode materials (Lanthanum Strontium Magnetite (LSM) and silver paste) preparation and application, and current collector (silver wire/mesh) configuration were done for enhanced cell performance. The fuel gasification in the slurry and the flowability of the slurry at high temperatures were also examined.

The second stream of this project involves system design, unit construction and commissioning, unit testing and operation, commercial module development, and life cycle analysis. It was decided to first build and test a 1 kW unit which will allow trial of several key elements of the 10 kW design on a smaller scale before investing in larger versions. The concept design, construction and testing of a 1 kW unit is complete and included cell design (cell dimensions, arrangement of YSZ tubes, and placement of silver current collectors), construction and preliminary testing. An electrical heating system was chosen for heating the slurry in the fuel cell tank and pre-heating air that passes through the YSZ tubes. The critical gland design has been developed.

Preliminary testing of the DCFC is complete. This included a thorough safety evaluation, as well as testing system heating and operation. The system operated with an areal power output of ~138 mW/cm^2, leading to an overall power output of 945 W.

LAY SUMMARY

The supply of energy is a critical element of contemporary society. In the Australian context, this has been met primarily with fossil fuels such as coal, oil and gas. While these fossil fuels have provided the energy for economic growth for centuries, their continued use in the future will be limited by environmental concerns related to emissions, as well as more practical concerns such as their finite availability. While more renewable and sustainable energy sources gain traction in the marketplace, strategies need to be implemented to ensure that the more immediate use of fossil fuels is associated with higher efficiency processes and lower emissions.

This project has involved the continued development of the direct carbon fuel cell (DCFC). The DCFC is a hybrid fuel cell system that makes use of coal as a fuel to generate electrical energy directly in a process that is considerably more efficient than a conventional coal-fired power station (CFPS). A CFPS makes use of many energy transformation steps to generate electrical energy, the efficiencies of each when combined lead to a system with an overall efficiency of 35-40%. The DCFC employs only one energy transformation step – chemical energy in coal to electrical energy – meaning that its efficiency is much higher – 100% theoretically, but ~80% practically.

This project has taken previous more fundamental outcomes and combined them to develop a 1 kW DCFC demonstration plant. The intent was to scale-up laboratory based outcomes, and this has been completed successfully at the University of Newcastle.

TABLE OF CONTENTS

Figure 22: (a) DTA response for different kaolin loadings heated at 10°C/min, and (b) activation energy versus extent of conversion for different loadings of kaolin.

Figure 23: Schematic of the 1kW DCFC unit showing the ancillary components and layout of the YSZ tubes.

Figure 24: Isometric diagram of the fuel cell tank.

Figure 25: Two different designs for the gland to hold YSZ tubes in position in the cell.

Figure 26: (a) Small cell setup showing cathode current collector arrangement; Anode current collector configurations: (b) spiral silver wire, and (c) silver mesh; performances of direct carbon fuel cell with: (d) silver wire, and (e) silver mesh.

Figure 27: Photographs of the small cell showing slurry leak-out through: (a) both the glands, (b) the gap between the gland and YSZ tube.

Figure 28: Gland design showing positions of the seal ring, ceramic rope and YSZ tube. (Solid red lines indicate the gap between YSZ tube and seal ring/reducing bush).

Figure 29: An engineering drawing of the furnace design for the fuel cell.

Figure 30. Gland design and the slurry leak path (red dashed line).

Figure 31. (a) Gland assembly design, (b) Kao-tex ceramic rope, and (c) nickel lubricant.

Figure 32. Photographs of the lab-scale cell after two different testing periods: (a) no leaking of the slurry after 4 h testing, and (b) severe leaking of the slurry after 16h testing.

Figure 33. A sealant (Deacon 8875) was applied and cured at 200°C for 2h.

Figure 34. Revised gland design with tapered seal ring and washer.

Figure 35. High density ceramic braid (Kao-tex 2000)

Figure 36. A photo of the gland after testing (Method 5) showing severe slurry leak and corrosion of the gland.

Figure 37. Photograph of the gland after testing (method 6).

Figure 38. Isometric section view of the YSZ tube and a ceramic tube for passing air.

Figure 39. Schematic of the charging vessel and the cell tank.

Figure 40. Arrangement of the YSZ tubes ($7 \times 4 = 28$ tubes) in the tank cell.

Figure 41. Anode mesh current collector placement in the cell tank.

Figure 42: Model of the DCFC unit: (a) elevation, (b) plan view and (c) isometric view.

Figure 43: Isometric views of the cell, including two plenums and charging vessel.

Figure 44: General arrangement of the furnace for fuel cell tank and pre-heating gases.

Figure 45: Internal block diagram of the digital control system.

Figure 46. Metal plates and machined parts of the cell unit.

Figure 47. A photograph of the base metal structure of the furnace unit being built.

Figure 48: Process and instrumentation diagram for the 1 kW unit.

Figure 49: Photograph of a modular programmable load device.

Figure 50: Circuit diagram showing the DCFC connected in series to an output load (display feature).

Figure 51. OCV for the DCFC at 600°C.

Figure 52. Performance output of the DCFC.

Figure 53. Measured current as a function of time.

Figure 54. Schematic of the direct carbon fuel cell.

Figure 55. Block diagram of the alternative energy generation systems.

Tables

LIST OF ABBREVIATIONS

235MA – stainless steel grade

316L – stainless steel grade

CFPS – coal fired power station

D50 – particle size distribution where 50% of the sizes are less than this value

DTA – differential thermal analysis

DCFC – direct carbon fuel cell

η -- electrochemical efficiency

ERS – electrochemical reaction site

EDS – energy dispersive spectrometry

ΔH, H – (change in) enthalpy (J)

keV – kiloelectron volts (accelerating voltage in SEM)

ΔS, S – (change in) entropy (J/K/mol)

FE-SEM – field emission scanning electron microscope

ΔG, G – (change in) Gibbs free energy (J)

HAZOP – hazardous operations (safety)

HDCFC – hybrid direct carbon fuel cell

LSM – lanthanum strontium manganate

LCA – life cycle analysis

LSV – linear sweep voltammetry

MCFC – molten carbonate fuel cell

OCP – open circuit potential

OCV – open circuit voltage

P&ID – process and instrumentation diagram

TPB – three phase boundary

t, Mt – tonnes, megatonnes (mass)

tCO_2-e – tonnes CO_2 equivalent

SEM – scanning electron microscopy/microscope

SSZ – Scandia stabilized zirconia

SOFC – solid oxide fuel cell

TGA – thermogravimetric analysis

mW, W, kW – milliwatts, watts, kilowatts (power)

YSZ – yttria stabilized zirconia

kWh, MWh – kilowatt hours, megawatt hours (energy)

INTRODUCTION

The direct carbon fuel cell (DCFC) is an innovative low carbon technology option that has the potential to cause a paradigm shift in the way we generate electrical energy from coal resources. Traditional methods of generating power from coal involve combustion, where chemical energy is converted into electrical energy through a series of energy transformations. Even using state-of-the-art techniques in coal fired power stations, overall efficiencies of less than 40% are generally accepted as best practice. Due to the nature of the combustion process, a large flue stream is also generated which contains particulates, NO_x, SO_x as well as diluted carbon dioxide, meaning further treatment of the flue gas is required to generate a clean, sequestration-ready carbon dioxide stream. This separation and clean-up process (post combustion and capture) is energy intensive and uses parasitic energy from the process, reducing efficiency even further.

The direct carbon fuel cell (DCFC) is a fuel cell technology employing the direct electrochemical oxidation of coal (carbon) to produce electrical energy. In the DCFC there is only one energy transformation process employed; namely the electrochemical conversion of the chemical energy in coal to electrical energy, and as such the DCFC is often referred to as being an efficient means of direct energy production. The overall reaction involved in the DCFC is the same as in a CFPS; i.e.,

$$C + O_2 \rightarrow CO_2$$

except in the case of the DCFC this is broken down into two electrochemical half reactions; i.e.,

$$C + 2O^{2-} \rightarrow CO_2 + 4e^- \text{ (anodic process)}$$

$$O_2 + 4e^- \rightarrow 2O^{2-} \text{ (cathodic process)}$$

where the oxide anion (O^{2-}) is the ionic charge carrier. Each of these half reactions is carried out in separate compartments of the fuel cell, as shown schematically below. Separating the compartments is an ionically conducting medium, or electrolyte. In the below schematic this is a combination of a solid oxide ion conductor; e.g., yttria stabilized zirconia (YSZ), and a molten mixture of Li_2CO_3, Na_2CO_3 and K_2CO_3. The solid YSZ physically separates the two compartments, while still allowing for ionic transport, while the molten carbonate media essentially acts as a carrier for oxide anions to facilitate their ready access to the carbon surface.
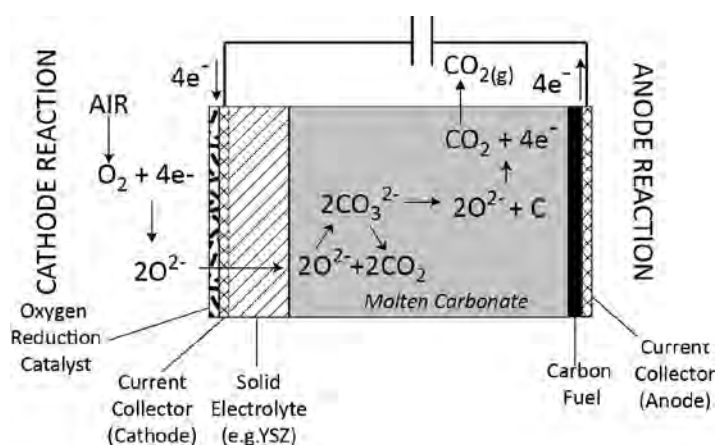
Thermodynamically and kinetically the efficiency of a DCFC is much higher than that of a coal fired power station; i.e., thermodynamic efficiency is 100%, while practical (kinetic) efficiencies are ~80% (cf. <40% in a state-of-the-art coal-fired power station). Since the reaction is the direct electrochemical generation of carbon dioxide in an inert gas atmosphere, the flue gas has the potential to be pure, sequestration ready carbon dioxide with zero particulates with little to no flue gas treatment

required. Since particulates and other pollutants potentially harmful to human health are not significant, the equipment can be located in residential or high population areas, removing inefficiencies and expenses incurred by centralized energy generation systems related to poles and wires. The system could be designed in a manner which is self-continued in a modular unit, using minimal operator intervention.

The DCFC is not a new concept. The idea of electrochemical conversion of carbon fuels was originally proposed as early as the 1800s. However, initial attempts did not have access to the advanced materials developed in recent years. DCFC technology has seen renewed research interest in the last decade due to developments in solid oxide fuel cell technology, including development of non-precious metal oxygen reduction catalysts, and advanced ionically conductive high temperature membranes. Assessment of several possible cell arrangements has occurred in recent years with varying degrees of success. High performing cells have been reported, although only on a laboratory scale. Best arrangements on the small scale utilize a combination of both solid oxide fuel cell (SOFC) technology as well as that of molten carbonate fuel cells (MCFC) in a hybrid arrangement. This ideal combination allows physical separation of fuel and oxidant through a solid oxide membrane while still allowing uninhibited transport of the oxide ion to the carbon fuel through the molten carbonate medium. Including previous studies conducted by our research group, great advances in this area have been made, with increased understanding of kinetics, catalysis and different reaction sensitivities, together with fuel type and pre-treatment being better understood. Despite many advances in this area however, several technical challenges still exist which must be addressed before the technology can be meaningfully commercialized.

This project will bridge a crucial gap between research and commercialization of DCFC technology where many fundamental challenges of operation of a pilot scale cell are addressed and findings translated to a fully functioning modular demonstration unit capable of generating 1 kW on a continuous basis. The purpose of the demonstration plant will be to firstly prove the technology on a larger scale, and then evaluate its performance capabilities and emissions.

The project has been organized in two discrete streams. The first stream includes fundamental/pilot scale work predominately, which builds on successful work conducted at the University of Newcastle to date. The second stream is heavily involved in commercialization activities and the final build of a demonstration module.

The overarching aim of this project is the development of a 1 kW DCFC demonstration plant. To accomplish this we have fundamental research and developmental objectives.

Fundamentally, we focus on the following areas:
(i)   Mass and energy balance
(ii)   Materials corrosion
(iii)   Anode formulation and processing
(iv)   Cathode optimization
(v)   Molten carbonate recycling and Recovery

From a developmental perspective, our ultimate object will be to combine the fundamental outcomes above into a functioning system. The steps involved with this are:

(vi)   System design
(vii)   1 kW unit construction and commissioning
(viii) Unit testing and operation
(ix)   Commercial module development
(x)   Life cycle analysis

PROJECT AIM, OBJECTIVES, MILESTONES AND PERFORMANCE MEASURES

The overarching aim of this project is the development of a 1 kW DCFC demonstration plant. To accomplish this we have fundamental research and developmental objectives. Fundamentally, we will focus on the following areas:

(i) Mass and energy balance – to examine conversion efficiencies (85% sustained over 10 days), and emissions 20% of an equivalent coal fired power station)

(ii) Materials corrosion – to ensure material stability in the DCFC environment (10+ years stability)

(iii) Anode formulation and processing – to ensure efficient fuel utilization (>150 mW/cm^2)

(iv) Cathode optimization – to ensure efficient overall cell operation (ensure balanced cell operation)

(v) Molten carbonate recycling and recovery – to minimize system emissions (approaching 100% recovery of molten carbonate, as well as process development for the recovery of contaminant metals)

From a developmental perspective, our ultimate object will be to combine the fundamental outcomes above into a functioning system. The steps involved with this are:

(i) System design – develop an optimized stacked system design for construction and evaluation building on fundamental outcomes and previous experience

(ii) 1 kW unit construction and commissioning – transferring the design into a functioning system, including fuel pre-processing, DCFC system, and thermal management (minimize waste heat)

(iii) Unit testing and operation – evaluation of performance characteristics such as intrinsic performance (>150 mW/cm^2 anode power output), extended use (10+ days), overall emissions reduction of 80% over conventional coal-fired generation (t CO_2-e), efficiency (85% thermal efficiency), fuel introduction including pre-processing, and heat management

(iv) Commercial module development – optimize the modular, stand-alone nature of the system for commercialization

(v) Life cycle analysis – this will incorporate the findings from the mass and energy balance to develop a more sophisticated life cycle analysis for the system to highlight the anticipated reduced emissions 20% emissions of a coal fired power station)

The milestones for the current project are listed in Table 1.

Table 1. Project milestones summary table.

ID	Milestone	Status	Relevance to Project	Achievements
1	Mass and energy balance	Complete	This milestone will use the existing pilot cell design and will involve building on operational hours, collecting operational information including performance, extended time trials, off-gas sampling and analysis, and optimization studies to give an overall mass and energy balance of the process for the pilot cell.	A steady state model has been built which allows assessment of the final system efficiency and sensitivity of this value to several variables including the achievable electrochemical efficiency of the system, and the extent of parasitic gasification of the fuel (reverse Boudouard reaction). A detailed scientific paper (see Appendix 1) on the mass and energy balance has been prepared for submission to a journal.
2	Corrosion and material investigation	Complete	Extensive studies on corrosion properties of molten carbonates in a DCFC operating environment will be carried out to firstly understand and secondly modify materials of interest for application to the DCFC system.	Both electrochemical and immersion corrosion tests were carried out to determine the stability of critical aspects of the DCFC, in particular the electrode current collectors and DCFC cell walls. It was demonstrated that nickel and silver were suitably stable, with silver chosen because of its added benefit as a catalytic substrate. Various steel substrates were examined for their stability in the molten carbonate eutectic for use as the cell walls. They were shown to be stable in the medium term (<2-3 years) but for longer term operation it was recommended to coat the steel with a ceramic lining.
3	Anode formulation and processing	Complete	The use of a solid carbon fuel is unique to the DCFC and early designs for adaption of this technology to enable a continuous process have been developed. This concept is very new, however, and will require optimization studies to	The cell performance with different alkali metal carbonate mixtures, i.e., ternary eutectic (Li_2CO_3/ Na_2CO_3/K_2CO_3) and binary eutectics Li_2CO_3/K_2CO_3 and Li_2CO_3/Na_2CO_3, showed that Li_2CO_3/K_2CO_3 (47/53) exhibited the highest

				occur over the project life including both electrochemical and engineering investigations to fine-tune the design of this key component.	performance over the temperature range between 600-800°C, whereas at 860°C Li_2CO_3/Na_2CO_3 (52/48) was superior. It was also found that Fe_2O_3 and SnO_2 as additives (5 wt%) to the fuel mixture increased the power output of the cell. Coal particle size did not significantly affect the cell performance. Higher coal loadings improved performance but limited flowability within the system.
4	Cathode optimisation	Complete		Limited work to date has been carried out in order to optimize the solid oxide interface with the molten carbonate for the DCFC. This requires further investigations on the bench scale to examine the membrane interface and assess its effect on overall electrochemical performance.	Commercial mixture of LSM-YSZ as the cathode material performed better than lab-prepared mixture. The homogeneous nature of the commercial LSM-YSZ mixture compared to the lab-prepared mixture has improved the performance. Increase in the thickness of the YSZ tube (0.87 mm to 1.57 mm) did not significantly affect the performance of the cell. For cathode current collector, silver wire was superior to nickel wire, and the increase in the surface area of silver wire improved the performance significantly. Silver paste and wire/mesh combination on the cathode side showed the best performance.
5	Molten carbonate properties	Complete		Molten carbonates are a key component of the pilot cell design, yet surprisingly little information is available regarding their thermal properties under various conditions including gas environment, presence of impurities and the possible catalytic effect of these salts on various major and side reactions which occur with the DCFC. For extended DCFC operation carbonate stability and fouling will be an important	Half-cell study showed that kaolinite addition (up to 15 wt%) to the fuel mixture (coal + carbonate) exhibited catalytic effect, i.e., enhanced electro-oxidation of carbon. The flowability of the coal-carbonate mixture (5 and 10 wt.% coal) at 800°C was high, whereas for 30wt.% coal it was satisfactory, and became very poor for 50wt.% coal mixture. Thermal analysis results showed that the mass loss of the slurry

			concern and the change in physical properties needs to be understood The possible recycle and recovery of different materials from the carbonate environment will also be considered.	samples increased as the carbon content of the slurry increased. Thus, it can be said that fuel (carbon) gasification is the main factor in slurry mass loss at elevated temperatures above 700°C.
6	Initial design (1 kW unit)	Complete	Initial design will consist of both process and component design. Process design will cover process flow and instrumentation design (P&ID development), hazard and operability (HAZOP) studies to ensure safe operation of module, and detailed design of the integration of the balance of plant (including pumps, heat exchangers, instrumentation and control, and coal pre-treatment). Finalization of the DCFC modular design will be completed including consideration of large scale cathode and solid electrolyte membrane manufacture.	The performance of a small cell (similar to 1 kW cell design) with two different cathode configurations (silver wire and silver mesh) was tested at 800°C in 20 wt% coal slurry. The cell with silver wire as the anode exhibited a power density of 79 mW/cm^2, whereas the silver mesh anode increased the power density to 138 mW/cm^2, close to our target of 150 mW/cm^2. The concept design of 1 kW unit is complete. Electrical heating system has been chosen for heating the slurry in the fuel cell tank and pre-heat air passing through the YSZ tubes. The critical gland design has been tested in our lab for leak-proof sealing. In a horizontal configuration where the electrolyte slurry is pressing on the seal this leads to substantial leakage. However, redesign with a vertical arrangement and no liquid pressure applied to the seal was found optimal.
7	Unit build	Complete	Using external contractors and suppliers as well as the University of Newcastle workshop, the design finalized and agreed on in the initial design phase will be built. The module will also be initially commissioned and all separate parts tested for operation.	The 1 kW DCFC system was constructed according to the design using a combination of in-house and external contractors. All aspects of the overall system were constructed in a timely manner, except for the digital control system, which took an extended time to be completed.
8	Unit testing	Complete	Once assembled, the module will be operated and performance evaluated. Testing will be	Testing of the 1 kW DCFC systems was carried out to firstly establish safe operation. Stability

			extensive including component optimization and troubleshooting, extended operation hours, reduction of operator input requirements and automation design, as well as evaluation of final energy output and efficiency. Gas analysis will be carried out to ensure compliance with environmental requirements.	was established through monitoring of the open circuit potential over time. Testing of the overall system was conducted to establish i-V data, and the voltage of peak power. Extended operation of the DCFC system at the peak power voltage was carried out until fuel supply became limiting. Emissions from the system were examined and found to contain no CO, SO_x or NO_x, confirming expectations.
9	Commercial module development	Complete	Using learnings from 1 kW module developed, further refinement and design work will be carried out in order to prepare an overall technology licence package ready for deployment.	Recommendations for the next stages of DCFC development have been made. This includes a focus on the heating system to minimize the need for void space heating as well as on excessive component heating, the electrode arrangement to optimize system power output, and fuel input to be more automated to sustain ongoing operation.
10	Final report including life cycle analysis and techno-economic modelling	Complete	Life cycle analysis for cradle to grave analysis of emissions.	LCA has been carried out with input from DCFC development and performance. Techno-economic modelling of the current system was very primitive because of its prototype nature.

METHODOLOGY

Fundamental Approach

In support of the fundamental aspects of this project, thermogravimetric, microstructural and electrochemical analyses were performed.

Thermogravimetric Analysis

For thermogravimetric analysis, ~10 mg of sample (carbonates/coal/coal-carbonates) was loaded in a 20 μL alumina crucible and placed in a TGA instrument (Netzsch STA 2500 Regulus). The sample was heated to 220°C at 10°/min and held isothermally for 10 min to remove both the physically and chemically bound water. The data was normalized at 220°C; i.e., when the sample was dry. The temperature was then ramped to 700°C at 10°C/min before holding isothermally for 10 min, after which the temperature was ramped further to 800°C at the same heating rate and held for 10 min. The final heating ramp was to 860°C at 10°C/min. Either CO_2 or N_2 was passed over the sample at 40 mL/min during the experiment.

Microstructure Analysis

A Carl Zeiss Sigma Field Emission–Scanning Electron Microscope (FE–SEM) coupled with an Energy Dispersive Spectroscopy (EDS) system equipped with a Bruker light element silicon drift detector was used to identify the mode of corrosion and corrosion products of the anode current collector (nickel, silver) and stainless steel (cell body). The SEM was operated at 15 keV accelerating voltage.

Electrochemical Analysis

Fuel: The fuel was made up of a thermal coal char mixed with a ternary alkali metal carbonate eutectic; i.e., Li_2CO_3, Na_2CO_3 and K_2CO_3 (43.5: 31.5: 25 mol%, respectively). Preparation of the coal char involved pyrolysing a thermal coal by heating to 800°C at 5°C/min, then holding isothermally for 2 h under N_2 gas in a tube furnace. The eutectic was prepared from dry reagents of the individual carbonates, which were thermally fused at 600°C for 2 h before being ball milled.

Button Cathode: A commercially available cathode disk (Fuel Cell Materials) was used as both the solid oxide electrolyte and the oxygen reduction catalyst. The solid oxide electrolyte component was scandia-stabalized zirconia (SSZ) and the oxygen reduction catalyst was comprised of two layers; i.e., one inside layer of lanthanum strontium manganite - gallium doped ceria (LSM-GDC) and a second outside layer of LSM material. The cathode disk was sintered to an alumina tube (Solid Oxide Fabricators) using glass sealing tape (Kerafol), and held isothermally at 860°C for 1 h to form a strong adhesion.

Tubular Cathode: Yittria stabilized zirconia (8YSZ, containing 8 wt.% yittria) tubes were purchased from Lianyungang Highborn Technology Co (China) with the following dimensions: inner diameter = 9.5 mm, outer diameter = 12.5 mm (thickness = 1.5 mm) and length = 100 mm. The cathode paste was modified from a stock mixture containing LSM powder in a terpinol based ink vehicle (Fuel cell Materials), for which the solids loading was ~65 wt%. 8YSZ powder was added to the stock mixture to make up a 50/50 mol% ration of 8YSZ/LSM, and an ink vehicle was added to maintain the consistency. A hand mortar was used to ensure that a homogenous mixture was produced.

The modified mixture was coated onto 8YSZ tubes using a foam brush, and care was taken to ensure that the coating was both even and thin. The electrodes were then sintered to 1300°C at a rate of 1°C/min and held isothermally for 1 h before being cooled to ambient temperature. Silver wire (outer

diameter = 0.35 mm, Goodfellow) was then wrapped around the tubes and adhered in place using silver paste, which was cured in a drying oven at 100°C for 1 h. The silver wire on the outside of the tubes was used as a cathode current collector. Care was taken to ensure that the electrode fabrication process was consistent between the individual tubes.

Cell Arrangement: The tubular electrode was positioned in the centre of an alumina crucible (outer diameter = 84 mm, height = 60 mm), and held in place using a base plate with a hole (diameter = 17 mm) purposely positioned to accommodate the electrode. An air gas line was fed into the cathode chamber through another hole in the base plate, and second gas line was positioned atop the electrode feeding directly into the anode compartment. CO_2 was passed through the anode gas line depending on the individual experiment, and the flow rate for all gasses was held at 40 mL/min. Electrical connections to the potentiostat (Solartron SI 1287 Electrochemical Interface) were made outside the rear of furnace, and a two-electrode setup was employed, as shown in Figure 1.
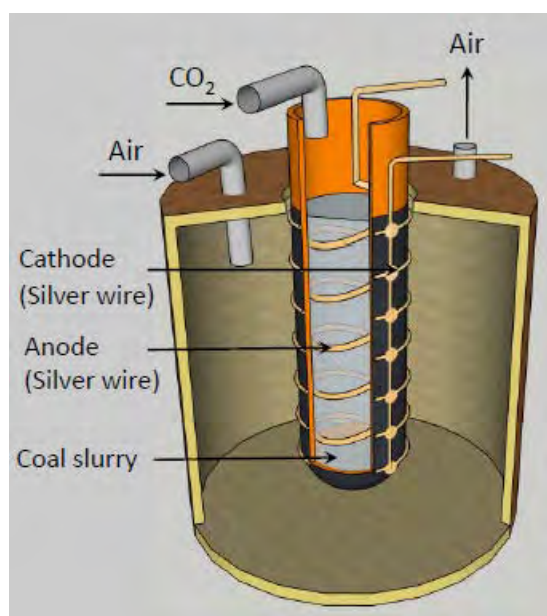
Figure 1. Schematic of the test cell.

Electrochemical Testing: Firstly, the open circuit potential (OCP) was measured as the cell was heated from ambient temperature to the desired operational temperature (600-860°C) at ~3°C/min. Once the operation temperature was reached, the potential was swept from OCP (0.8-1.1 V) to the short circuit (~0 V) at 5 mV/sec. Chronologically, the linear sweep voltammograms (LSVs) were measured in ascending temperature order, i.e., 600°C, 700°C, 800°C and 860°C. A ten-minute isothermal period was allowed at each temperature prior to measuring a voltammogram to allow the sample to reach a relatively stable OCP.

RESULTS AND DISCUSSION

Milestone 1: Mass and Energy Balance

A detailed mass and enthalpy balance of a direct carbon fuel cell system has been carried out in order to understand achievable system efficiency of a 10 kW system. Using reasonable literature input data, a steady state model has been built which allows assessment of the final system efficiency and sensitivity of this value to several variables including the achievable electrochemical efficiency of the system, and the extent of parasitic gasification of the fuel (reverse Boudouard reaction). It was shown that for a hybrid DCFC system, which utilizes both primary (solid oxide membrane) and secondary (molten carbonate) electrolytes, a slurry based feed of coal and carbonate could provide enough waste heat from electrochemical inefficiency to both retain the molten feed temperature, as well as provide pre-heating for inlet air streams to achieve an overall system efficiency of over 70%. Higher system efficiencies may be possible, however will depend heavily on the cell design, in particular external heating necessary for the DCFC, as well as on increasing the electrochemical efficiency at the expense of waste heat generated. Additional parasitic power input is required in these cases. A base case of assumptions has been evaluated with sensitivity of the system efficiency compared for the carbon slurry loading, the carbon and oxygen conversion per pass of the fuel cell (fuel utilisation), equipment heat losses, amount of coal char ash present and the extent of carbon corrosion within the cell. Under the base case investigated, life cycle emissions of the technology have been estimated at 647 kg CO_2/MWh at 70% system efficiency, with no carbon storage, while emissions of 93 kg CO_2/MWh at 66% system efficiency are achievable if carbon dioxide is able to be effectively sequestered. A detailed scientific paper (see Appendix 1) on the mass and energy balance has been published. Further information in this regard has also been included in the life cycle analysis for the process, updated with inputs from system testing.

Milestone 2: Corrosion and Material Investigation

Electrochemical Testing

The electrochemical corrosion behavior of silver, nickel, copper, iron and titanium in ternary carbonate eutectic at 650°C was evaluated using a potentiostat and a three-electrode system consisting of the test metal as the working electrode and graphite rods as counter and reference electrodes. Potentiodynamic polarization experiments were performed to calculate the corrosion current using Tafel plots. The test metal was polarized in the cathodic and anodic directions with respect to the open circuit potential to obtain the Tafel slopes. Figure 2 shows the corrosion potentials and corrosion currents of the metals, and the corresponding corrosion rates are presented in Table 2. The corrosion potentials of silver and copper are towards the noble direction in comparison with that of titanium, nickel and iron. However, silver and nickel exhibited lower corrosion currents as compared with titanium, copper and iron. Accordingly, the corrosion rates of silver and nickel were lower than that of titanium, copper and iron.

(a)

(b)
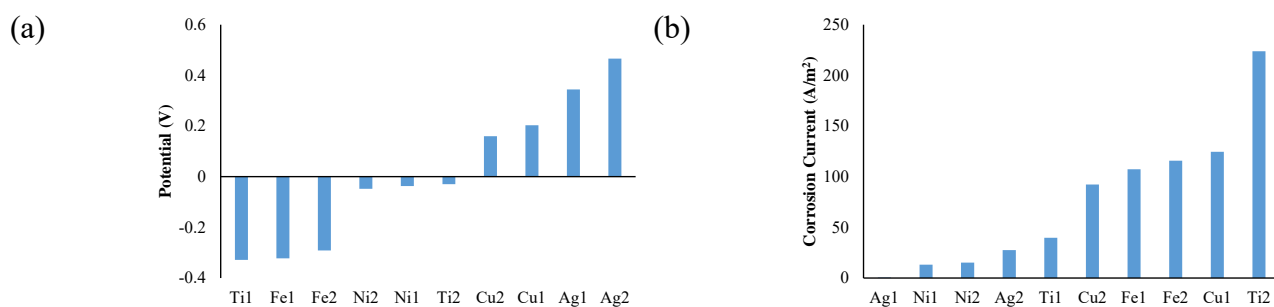
Figure 2. (a) Corrosion potentials and (b) corrosion currents of various metals in the ternary carbonate eutectic at 650°C. Note: 1 and 2 are sample numbers.

Table 2. Corrosion rates of various metals in ternary carbonate eutectic at 650 °C.

Metal	Corrosion Rate (m/y)
Silver	0.0245 ± 0.0022
Nickel	0.0142 ± 0.0014
Titanium	0.0688 ± 0.0160
Iron	0.1217 ± 0.0037
Copper	0.1257 ± 0.0187
Mean $\pm$ SD; n = 2	

<u>Current Collector</u>

Nickel mesh was tested as a current collector at the first attempt of full-cell testing. This material was chosen because of its high corrosion resistance to the alkali metal carbonate media. However, at the end of the linear seep voltammetry (LSV) experiment the mesh was found to be corroded leaving behind a black embrittled material. Scanning electron microscopy (SEM) and energy dispersive spectroscopy (EDS) analysis were employed to elucidate the chemical nature of the corrosion product. Three different sample conditions were analyzed; i.e., relatively unaffected, pre-acid washed and post-acid washed.
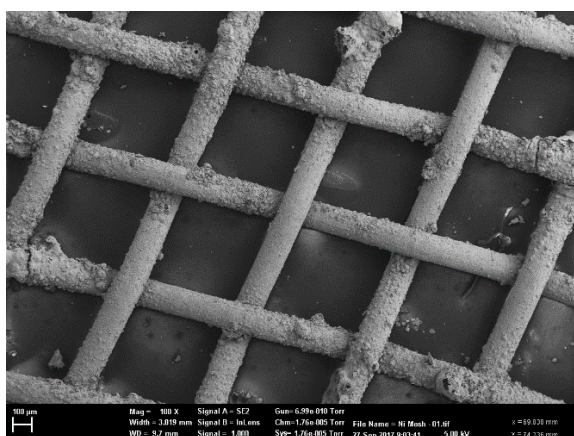
(a)   (b)
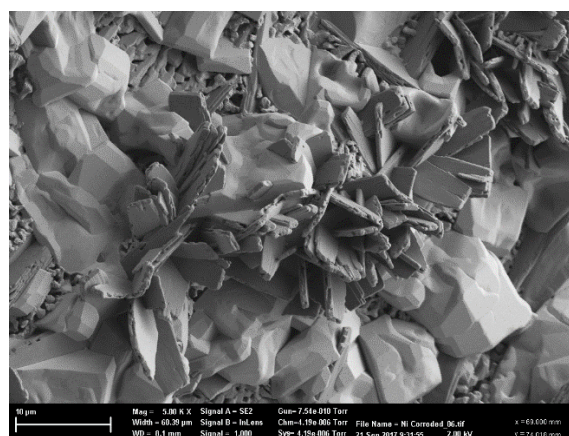
Figure 3. SEM images of corroded nickel mesh: (a) not physically in contact with the slurry, (b) completely immersed in the slurry.

Interestingly, the mesh which was not physically in contact with the slurry (Fig. 3a) showed evidence of corrosion which can be attributed to the gas-phase reaction. However, the mesh completely immersed in the slurry exhibited high corrosion. Energy dispersive spectroscopy (EDS) showed a high abundance of both carbonate and oxide crystals. Here, corrosion occurs via a carburization mechanism, which involves carbon diffusing into nickel across an activity gradient forming nickel carbide, which is characteristically a black brittle material. At the same time the reverse Boudouard gasification occurs, where CO_2 reacts with particulate carbon in the slurry at 700°C to produce CO

(Eqn 1):

$$C + CO_2 \leftrightarrow 2CO \qquad \qquad \dots(1)$$

Both the alkali metal carbonate media and the nickel metal are catalysts for the reverse Boudouard gasification, hence this reaction may be quite facile under these conditions. The CO then goes on to react with nickel carbide [2], which forms nickel oxide (Eqn 2); i.e.,

$$NiC_3 + CO \rightarrow NiO + C \qquad \qquad \dots(2)$$

On the other hand, the silver (Ag) anode current collector showed minimal corrosion even after a number of experiments. Hence, we decided to use Ag wire/mesh as the anode current collector. Due to its high corrosion resistance and good electrical conductivity at high temperatures, Ag was also used as a cathode current collector.

Fuel Cell Tank Material Corrosion

Stainless steels are known for their high corrosion resistance and excellent mechanical properties. Hence, we decided to test two types of stainless steels; i.e. 316L, (16 wt.% Cr and 11wt. % Ni) and 235MA (21 wt.% Cr and 11 wt.% Ni) for fuel cell tank body. 235MA is reported to have better corrosion resistance at high temperatures, but are more expensive than 316L. The corrosion behavior of 316L and 235MA in a slurry containing 20 wt% coal and 80 wt% ternary-eutectic (43.5 mol% Li_2CO_3, 31.5 mol% Na_2CO_3 and 25.0 mol% K_2CO_3) with nitrogen as a sweep gas at 800⁰C was examined for a four-week period. The samples were first surface finished by grinding with SiC paper and then ultrasonically cleaned in acetone. After cleaning and drying, the samples were weighed before the corrosion test. The samples were ultrasonically cleaned after the corrosion test with water to remove the slurry residue sticking to the sample surface and then the samples were dried and weighed again. The results indicated that the weight gain (due to corrosion product buildup) for both the stainless steels was marginal after 7 day exposure, i.e., 0.4% and 0.5% for 316L and 253MA, respectively. After 30 days exposure, the weight gain increased to 0.98% for 316L, whereas for 253MA the weight gain remained at ~ 0.5% (Fig. 4a). Visual observations of the samples revealed marginal corrosion on both the samples (Fig. 4 b).

Interestingly, in the small cell test (Fig. 4c), we noticed that the 316L stainless steel gland (exposed to air) corroded severely due to the slurry leak through the gland. However, the corrosion of the inside cell wall was minimal, where CO_2 was the sweep gas. In order to understand if oxygen in air affects the corrosion behavior of the two stainless steels, an experiment was conducted with air as the sweep gas (20 ml/min) for 4 days at 800°C. The weight gain was 4.6×10^{-3} g/cm^2/day and 6.0×10^{-3} g/cm^2/day for 253MA and 316L, respectively. Comparing these results to the ones with the nitrogen sweep gas (253MA: 3.4×10^{-3} g/cm^2/day; 316L: 2.5×10^{-3} g/cm^2/day), it is can be said that oxygen increases the corrosion of 316L more severely than that of 253MA. Since the corrosion rate of 316L and 253MA stainless steels in the cell environment is > 1 mm/year, a high-temperature resistant ceramic coating on the inside wall of the stainless steel tank is recommended, especially for long-term (~10 year) service.
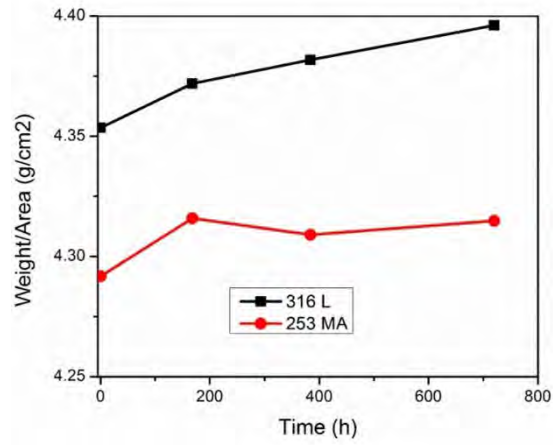
(b)
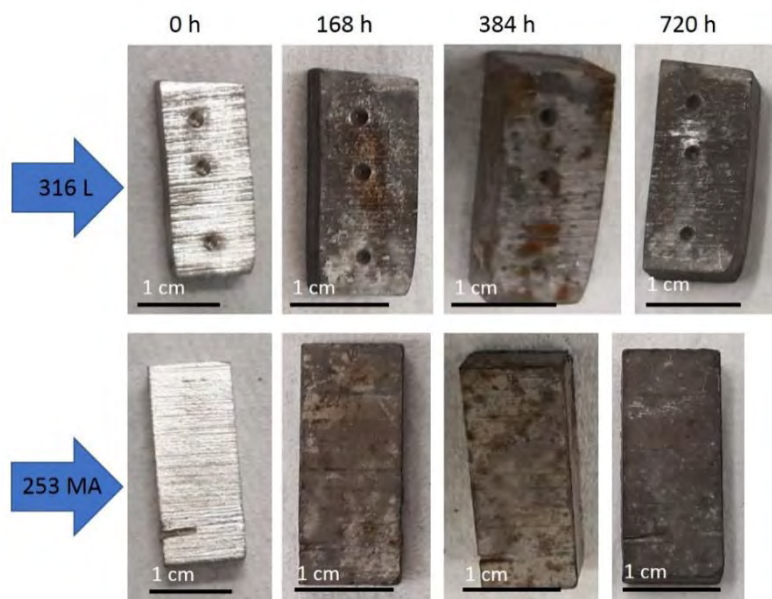
(c)

Figure 4. (a) Corrosion data of 316L and 253MA exposed to a slurry (coal + carbonates), (b) post-corrosion photographs, and (c) photograph of the small cell after testing (gland severely corroded).

Milestone 3: Anode Formulation and Processing

Cell Configuration

Button Cell

A schematic and photographs of the button cell setup are shown in Figure 5. A commercially available disk-cathode (Hionic Support-Cathode) was used as solid oxide electrolyte and cathode in the full cell set-up . Hionic Support is scandia doped zirconia-based substrate and the cathode layer is composed of two layers, one inside layer of lanthanum strontium manganate gallium doped ceria (LSMGDC) and a second outside layer of LSM material. The solid oxide electrolyte membrane together with molten carbonate (a ternary mixture of lithium (43.5 mol%), sodium (31.5 mol%), and potassium (21.0 mol%) carbonates [1]) forms a hybrid redox medium in the cell. Initially, graphite powder was used as fuel (carbon source) and mixed in a ratio of 4:1 with ternary carbonate eutectic. Anode compartment of the cell was packed with this mixture. Air and CO_2 streams were provided to cathode and anode, respectively; air as a source for oxygen in the cathode and CO_2 to prevent carbonate decomposition and loss from the anode. Air was on from the beginning of experiment but CO_2 was turned on just after melting point of eutectic (~400°C). Potential scan was carried out after all cell compartments were equilibrated at 700°C.

(a)

(b)
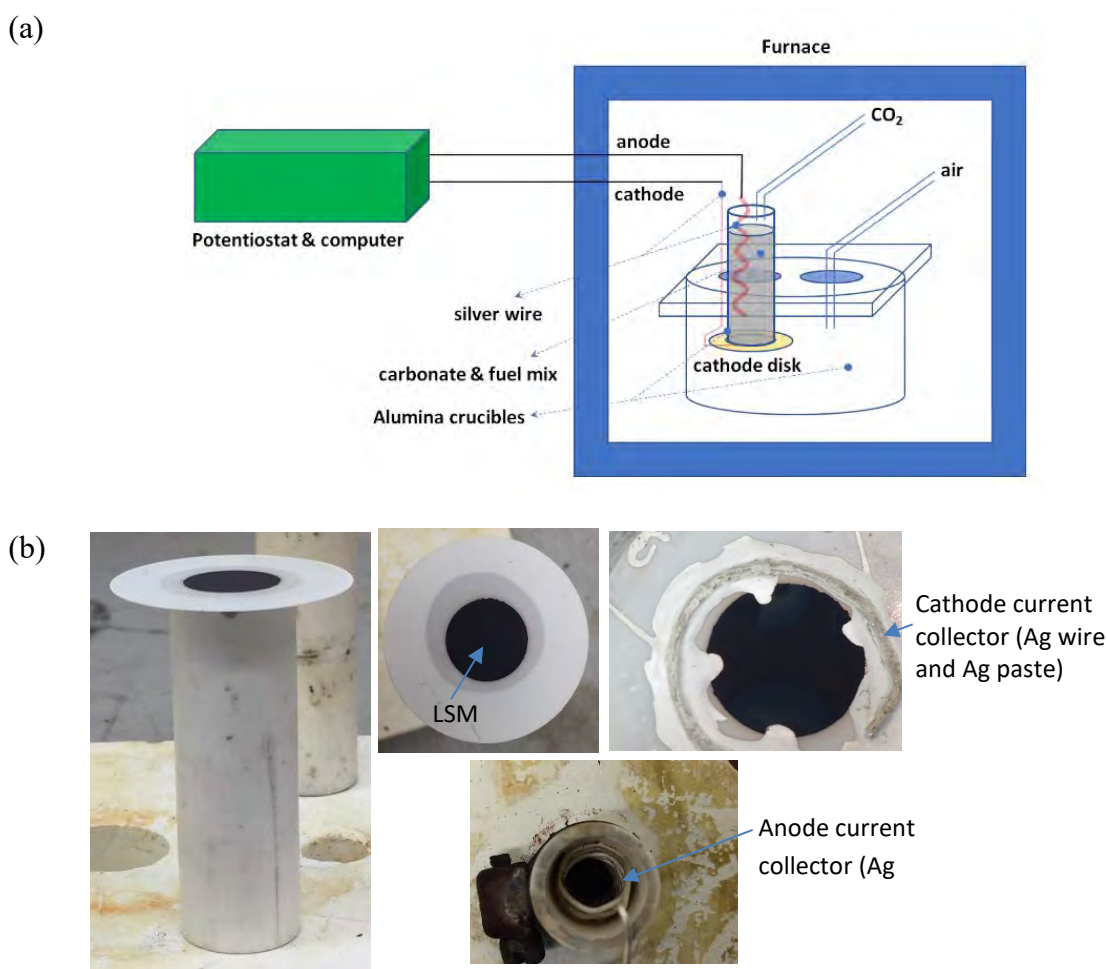
Figure 5. (a) Schematic of the button cell setup, and (b) photographs of the button cell.

The open circuit potential (OCP) of the cell was increased from ~0.3 V to 0.9 V over the temperature range 400-700°C. After the maximum temperature (700°C) was reached, the system was held at OCP for 20 min, where the potential remained relatively stable at 0.9 V. Following this, a linear sweep voltammetry (LSV) was carried out where potential was swept from 0.9 V (OCP) to 0.05 V at 5

mV/sec. Cell performance in terms of current and power density outputs was not high (Fig.6), i.e. maximum current density of 15 mA/cm^2 and maximum power density of 3.2 mW/cm^2.
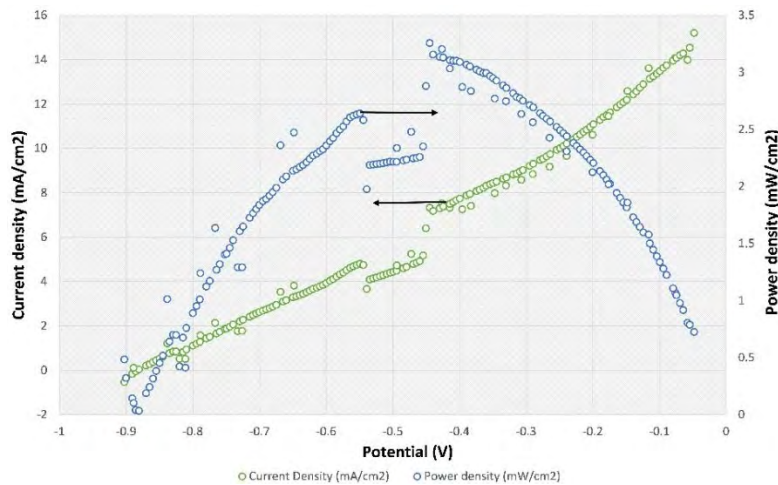
Figure 6: LSV curve generated from the button cell experiment at 700°C.

There are several factors that can be attributed to such a poor performance of the cell:

- Fuel leak: Different materials, i.e., Resbond (ceramic paste), Kerafol (glass sealing tape) and Ag paint, were used to glue the disk-cathode and alumina tube. However, as shown in Fig. 7 leaking of the carbonate from the anode compartment through the interface between the alumina tube and disk-cathode was observed.
- Eutectic loss: There were signs of formation of a thin layer of carbonate in the cathode compartment. Carbonate vapor could be carried out of the anode compartment by CO_2 stream that is used mainly to prevent carbonate decomposition [2]. There is relatively higher chance for the carbonate eutectic loss to happen if high flow rate of CO_2 is used. In addition, there is another way of carbonate vapor affecting the performance of the full cell by poisoning the cathode through precipitation on its surface and blocking oxygen pathway. Traces of carbonate on the cathode surface was evident which could have been another factor for the poor performance of the cell.
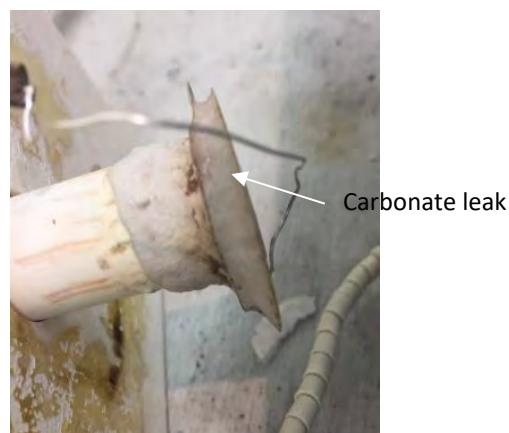
Figure 7. Photograph of the button cell after testing.

Tubular Cell

The laboratory-scale cell design was changed from a button cell to a closed end tubular cell. This modification was an important step towards the final 1 kW prototype which will utilize an array of electrode tubes. The transition to a tubular design resulted in a three-fold improvement in power output; i.e., 19 mW/cm^2 versus 5 mW/cm^2 (normalized with respect to surface area of silver wire current collector in the anode compartment) for the closed end tubular cell and the button cell respectively, both using 10 wt% coal char and operating at 700°C.

The closed end tubular cell is a blend of 8 mol% yttria + 92 mol% zirconia (8YSZ) (Highborn Technology Co), which is a different solid oxide electrolyte compared to what was used in the button cells; i.e., scandium stabilized zirconia. YSZ is a commonly utilised solid oxide electrolyte material due to a combination of factors including mechanical stability, facile oxide conductivity and well matched thermal expansion coefficient with the oxygen reduction catalyst; i.e., lanthanum strontium manganate (LSM) [3].

Changes were also made to the air and CO_2 flow rates. Air was passed over the cathode for the oxygen reduction reaction, as follows:

$$O_2 + 4e^- \rightarrow 2O^{2-} \qquad \qquad …(3)$$

The flow rate of air was doubled from 20 mL/min to 40 mL/min. This was done to ensure that the availability of oxygen would not limit the rate of the overall electrochemical process. The CO_2 flow was also modified, where previously the flowrate was set to 20 mL/min after the cell reached 400°C. This was so that the powdered carbonate and coal char mixture would not blow off prior to forming a molten slurry at 400°C. More recently, however the rate was set to 20 mL/min from ambient to 400°C, then increased to 40 mL/min between 400-700°C. Maintaining a CO_2 atmosphere is critical for mitigating carbonate decomposition (Eqn 4).

$$CO_3^{2-} \rightarrow CO_2 + O^{2-} \qquad \qquad …(4)$$

Current Collector

Since silver was found to be the most corrosion resistant material among the materials tested in carbonate electrolyte, it has been used as the anode current collector. In the anode, electrochemical oxidation of solid fuel happens on the surface of current collector. Therefore, performance of the full cell can be impacted if anode current collector's surface area is a limiting factor. In fact, the current collector is a component in three-phase boundary formation with the other two being fuel and electrolyte. Increase in the surface area (as shown in Fig.8), increased the peak current, which suggests that replacing silver wire with silver mesh can help in increasing the surface area and thus improve the cell performance.
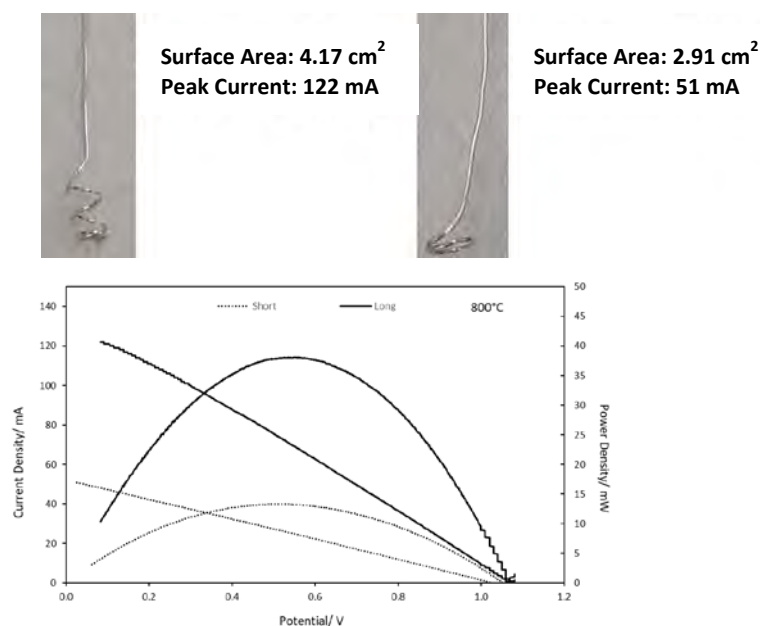
Figure 8: Effect of anode current collector (Ag wire) surface area (20 wt.% coal at 800°C) on the cell performance.

Electrolyte

When selecting a secondary electrolyte for DCFC the Li_2CO_3/K_2CO_3 binary eutectic followed by the ternary eutectic are the two most commonly used mixtures [4, 5]. The factors to consider when choosing a secondary electrolyte include melting point, performance, cost and corrosivity. We examined the performance of a selection of different alkali metal carbonate mixtures in a full cell arrangement. The purpose was to identify the highest performing mixture. Four mixtures were chosen, i.e., ternary eutectic ($Li_2CO_3/$ Na_2CO_3/K_2CO_3 and binary eutectics Li_2CO_3/K_2CO_3 and Li_2CO_3/Na_2CO_3. The Na_2CO_3/K_2CO_3 eutectic was not examined since it has a higher melting point and has also been reported to exhibit poor performance. An 8YSZ tube was used as the primary electrolyte and silver was employed for both the cathode and anode current collectors. A slurry arrangement was used for the anode where the loading was 20 wt% coal char, and the rest was made up with the carbonate electrolyte. The coal char was prepared by thermal coal pyrolysis up to 600°C, and the coal char particles were sized between 63-106 μm. The results from the electrochemical tests are shown in Fig.9. The results suggest that Li_2CO_3/K_2CO_3 (47/53 mol%) performed better than the other mixtures over the temperature range of 600-800°C. However, at 860°C the Li_2CO_3/Na_2CO_3 (52/48) binary eutectic exhibited the highest performance. Considering the followability and cost of these electrolytes, we have decided to use ternary eutectic in the fuel cell.

Fuel and Anode Compartment Gas Flow

Although in our preliminary experiments we used graphite as a fuel, in our later experiments we used coal char ((C 65.5 wt% (db) and 29 ash wt % (db)) and this will the fuel in the 1 kW module [6]. Coal char is amorphous which means that the electro-oxidative activity is expected to be higher as compared to graphite [6, 7], which is a uniform crystalline material. For half-cell configurations the OCP of coal char was ~ 0.2 V more anodic than the graphite [7], which translates to both higher power and operating efficiency. Coal ash is soluble in the molten carbonate [8] which likely improves the fuel wettability and flow properties [9].

The gas flow over the anode compartment was alternated from CO_2 to N_2 and the cell performance was monitored. The performance of the cell decreased significantly across the full temperature window examined (700-900°C) when N_2 was passed over the anode compartment as compared to

CO_2 i.e., at 800°C the power density was 4.69 mW/cm^2 versus 11.70 mW/cm^2 for N_2 and CO_2, respectively. The reverse Boudouard reaction (Eqn (5)) under CO_2 potentially agitates the system and thus facilitating transport of the carbon particulates to the anode current collector.
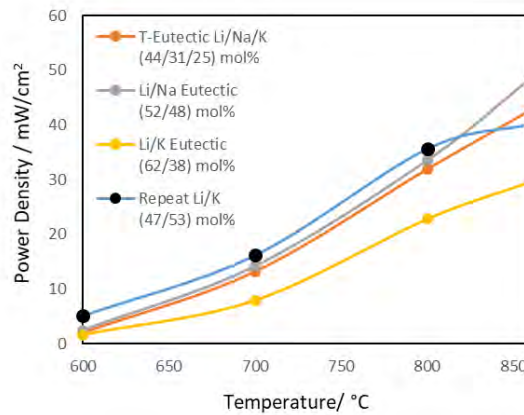
Figure 9. Cell performance results comparing four different carbonate compositions as the secondary electrolyte.

$$C + 2CO_2 \rightarrow 2CO \qquad \qquad \ldots(5)$$

This result suggests that the system may be mass transport limited on the anode side, meaning that further improvement in the performance could be achieved by agitating the slurry in the cell.

In order to discern whether mass transport of the particulate fuel to the current collector is limiting anode performance, full-cell experiments were conducted with particulate carbon (in ternary carbonate eutectic) and compared with that of a solid graphite rod. Interestingly, the power density achieved with the solid graphite rod was lower compared to that with the slurry system, which suggests that mass transport is not a limiting factor at high temperatures (>800°C). To further understand the mechanism, we compared the performance of the graphite rod under CO_2 vs N_2 in the anodic compartment. Similar to the slurry system, the performance of the cell under CO_2 was higher compared to that under N_2 (Fig. 10a). In the slurry system, under CO_2 the reverse Boudouard reaction (CO gas formation) agitated the slurry and thus facilitated transport of the carbon particulates to the anode current collector; however, such a mechanism seems unlikely with the graphite rod system.

The performance of the graphite slurry was tested and compared with coal slurry. The graphite slurry performed better than coal slurry at 700 and 800°C, but they performed similarly at 860°C (Fig. 10b).
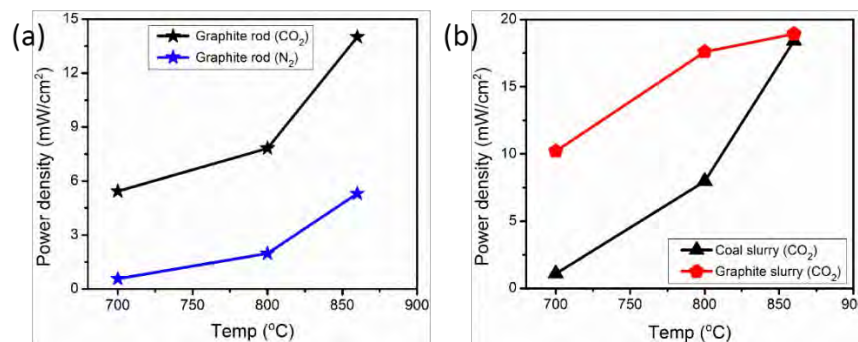
Figure 10. Comparing the discharge performance data of the fuel cell: (a) graphite rod under CO_2 vs N_2 anode compartment atmosphere, and (b) coal slurry vs graphite slurry under CO_2 anode compartment atmosphere.

The effect of coal particle size on the performance was examined for small (8-38 µm), intermediate (63-105 µm) and large (212-835 µm) particles at 800°C. For these experiments, a silver cathode was implemented and CO_2 was used as the anode sweep gas (40 mL/min). The particle sizes and distribution were measured using dynamic light scattering, and the results are shown in Fig. 11a. The D50 values were 24.5 µm, 110 µm and 428 µm for the small, intermediate and large particles, respectively. A short silver wire anode was used instead of the metal in the form of coil to purposefuly impair the performance of the anode, thus ensuring that the cell was kinetically limited by the anode. Linear sweep voltammetry (LSV) was used to calculate the peak power desity of each sample and the results are shown in Fig. 11a. Fig. 11b shows that the larger particles displayed the highest performance, and there is no significant difference between the small particles compared to the intermediate particle size. When using a short anode, most of the fuel is not physically contacting the current collector, and the fuel is gasified to produce CO, which is evolved out of the cell. Smaller coal particles are gasified at a faster rate compared to larger particles, thus increasing the probability of the larger parcticles physically contacting with the current collector and undergo electro-oxidation. These results indicate that there is no advantage in using fine particles size of coal in the DCFC, which means energy saved otherwise would be spent on performing a size reduction of the feed.
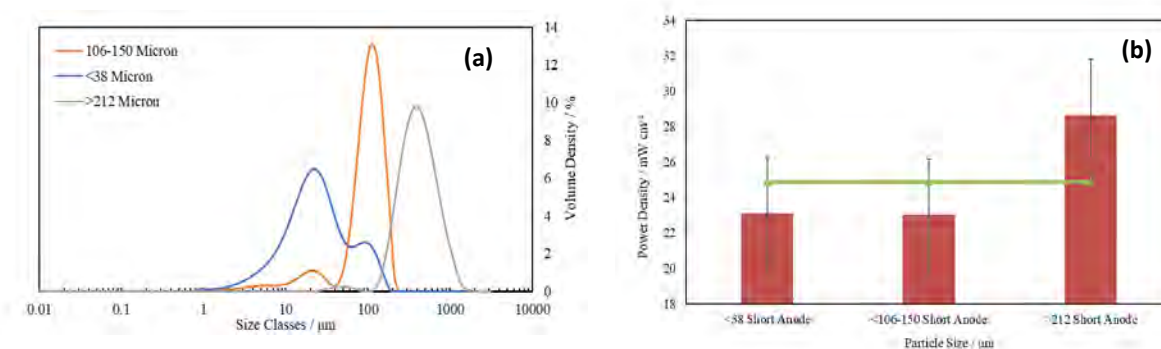
Figure 11: (a) Coal partice size and distrubution curves measured from three distinctly different particle size ranges, and (b) the corresponding power density obtained from the full cell experiments.

Slurry

The effect of coal loading (10, 20, 50 to 80 wt%) in the slurry on the cell performance was studied. Fig. 12 shows that in terms of peak power density the loadings can be rated as follows 50 wt% (7.0 mW/cm^2) >20 wt% (5.5 mW/cm^2) > 80 wt% (5.4 mW/cm^2) > 10 wt% (4.5 mW/cm^2), thus an intermediate loading of 50 wt% gave rise to optimal performance. This was expected because both fuel and carbonate electrolyte are required for four-electron oxidation from C^0 to C^{4+} to take place, and a limited availability of either is expected to cause a deviation from optimal reaction kinetics.

$$C + 2CO_3^{2-} \rightarrow 3CO_2 + 4e^- \qquad \qquad \dots(6)$$

The flowability of the slurry should be considered before proposing high amount of coal in the system. Hence, a qualitative flow test was conducted using different mixtures of coal (5, 10, 30 and 50 wt%) and carbonates at 800°C. It was found that the flowability of the mixture (5 and 10 wt% coal) was high, i.e., water-like flow. For 30 wt% coal mixture, the flowability was satisfactory, i.e., slurry flows down when the crucible was tilted by ~45° angle. However, for 50 wt% coal mixture, the flowability was very poor, i.e., the mixture was clumsy and sticking to the crucible. Hence, in the 1 kW test unit we have considered using 20-30% coal slurry for their better flowability.
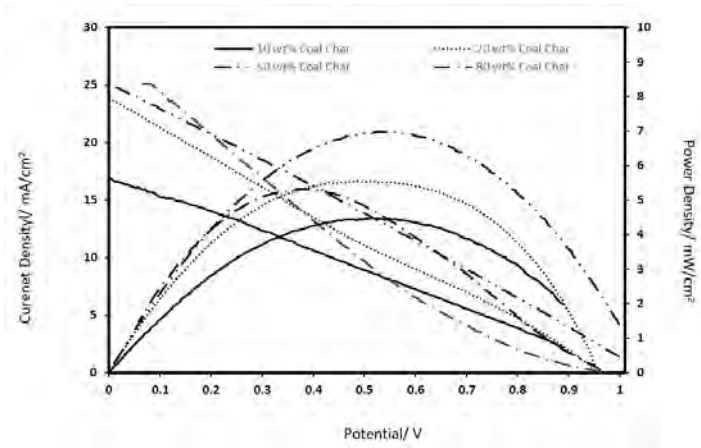
Figure 12: Current density and power density versus potential for various coal char loadings of 10, 20, 50 to 80 wt%.

Catalyst

A major challenge in all types of DCFCs is to bring either the oxygen or carbon together in an effective way for the cell reaction. In the molten carbonate fuel cells (MCFC) and hybrid direct carbon fuel cells (HDCFC), oxidation of solid carbon fuel takes place at the extended three-phase boundary (TPB), or so-called electrochemical reaction site (ERS), as molten carbonate electrolyte enhances the reaction interface in the anode compartment of the cell and facilitates diffusion of the reactants [10]. It also acts as an electrochemical mediator in oxidising carbon or carbon monoxide to carbon dioxide.

We tested various metal oxides such as SnO_2, CeO_2, Fe_2O_3, and Mn_2O_3 as additives (5 wt%) to the fuel mixture. LSV results showed that Fe_2O_3 and SnO_2 increases the power output of the cell (Fig. 13a), which could be attributed to a single step chemical oxidation of carbon to carbon monoxide and subsequent electrochemical oxidation to carbon dioxide at ERS. It was also noted that the cell performance increased with increasing the operating temperature - a maximum power density of 96 mW/cm^2 was achieved with 5 wt% of Fe_2O_3 at 850°C (Fig. 13b).
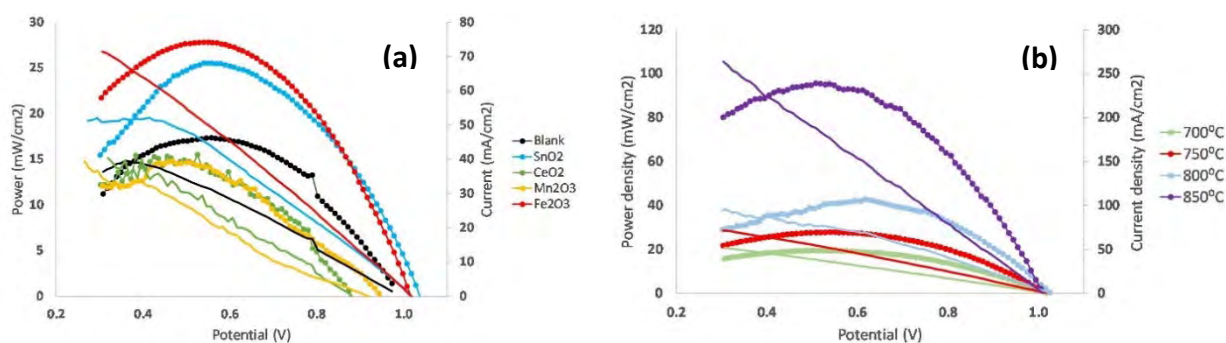
Figure 13: Comparison of cell performance: (a) different metal oxides as additives to anode compartment at 750 °C, and (b) temperature effect on the performance of cell with 5 wt% of Fe_2O_3.

Milestone 4: Cathode Optimization

Silver – Cathode Material/Current Collector

Silver has been widely used as a current collector in DCFC/SOFC due to its good electrical conductivity and corrosion resistance at high temperatures. Silver is also an oxygen reduction catalyst [11], hence it acts as a cathode material as well. We conducted experiments to examine the surface

area effects of silver to further understand its role as a cathode material.
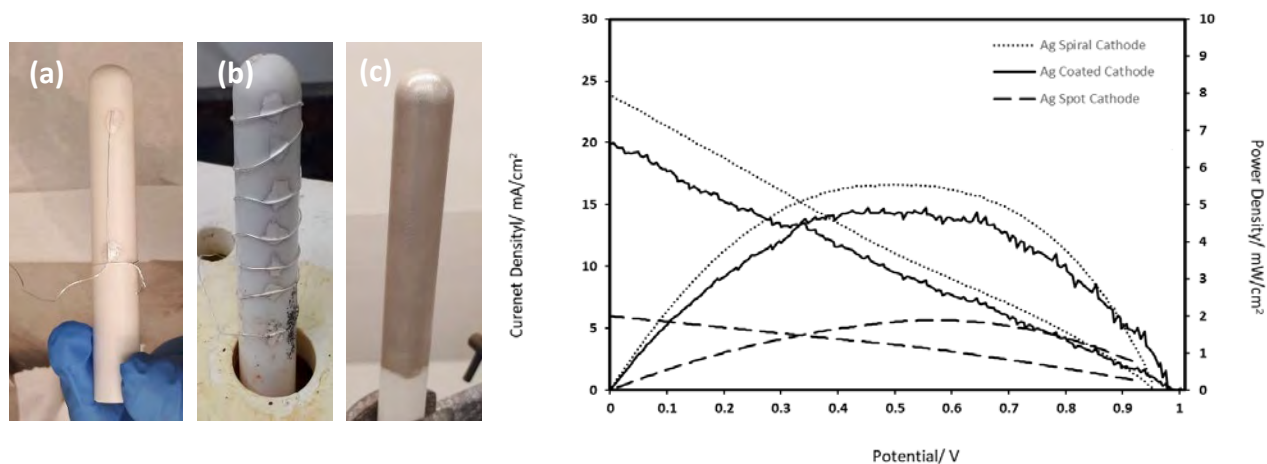
Figure 14: Current density and power density versus potential for various current collector surface areas; i.e., spot (lowest), spiral (intermediate) and coated (maximum). 20 wt% coal char was used with a scan rate of 5 mV/sec from 1-0 V at 700°C; Photographs of the cell with: (a) silver spot, (b) silver spiral wire and (c) coated with silver paste.

Fig. 14 shows that the electrode with the intermediate cathode surface area demonstrated the highest power density (5.5 mW/cm^2) compared to both the lowest (1.9 mW/cm^2) and the maximum surface area (4.9 mW/cm^2). An increased cathode surface area enables a higher turnover rate for the oxygen reduction reaction, thus also increasing specific power. This is evident when comparing the peak power of the spot (lowest) to the spiral (intermediate) current collector (Fig. 14a). The spot was fabricated from a single strand of silver wire attached at two points to the YSZ tube using silver ink, whereas the spiral was wound around the tube from a much longer (2-3 fold) piece of silver wire which was attached at several points using silver ink (Fig. 14b). In both the aforementioned cases there was still a considerable amount of bare YSZ exposed air. The coated (maximum) electrode was completely covered in silver ink (Fig.14c), so that the YSZ was not directly exposed to the air. The performance of the coated electrode was lower than the spiral electrode despite having a larger cathode surface area, which was due to the lack of contact between the air and the YSZ. Despite being able to act as an oxygen reduction catalyst, silver metal is not able to transport oxide anions, which is why some exposed YSZ is required at the triple phase boundary. The coated electrode still performed better than the single spot, indicating that there may have been small areas exposed in the coating, or perhaps silver oxide can act as an oxide conductor. Silver oxide is an oxidation product of silver metal; however, it is expected to form a passivation layer on the outside contacting the air which is not ideal. For optimal results, the oxide anion conductor should not physically occlude the oxygen reduction catalyst from accessing O$_2$. To better understand the role of silver as a cathode material, systematic changes were made to the cathode configuration and the performance of the cell was examined.

Silver Paste

Silver paste was coated onto the YSZ tube in a crisscross pattern, to allow ample space in-between the lines where bare YSZ was exposed. Loop of silver wire at the top of the tube connected the cathode to the current collector, however the length of this wire was very short. The power density of the silver paste electrode improved at 860°C i.e., 18.41 mW/cm^2 versus 20.37 mW/cm^2 for the silver wire + silver paste connector, and silver paste dots, respectively. The performance improvement was due to the ability of the silver paste to act as an oxygen reduction catalyst in direct contact with the YSZ tube.

Another cathode was fabricated where the silver paste was coated onto the YSZ tube in a crisscross fashion, as before, however this time silver wire was wrapped around the tube as well. What made this electrode unique is that it had both a high surface area of silver paste and silver wire. The electrode which had a high surface area of both wire and paste produced the highest performance of 50.33 mW/cm^2 at 860°C. This result showed that the superior electrical conductivity of the silver wire coupled with the oxygen reduction capabilities of the silver paste generated the best overall performance.

Silver Paste Surface Area:

Given that the silver paste used in the cathode influences the performance of the cell, a systematic study was conducted to further understand its contribution to the cell performance. Firstly, the effect of surface area of the silver paste was examined in two sets of experiment: In set 1 and set 2 experiments, silver ink surface area was 1.83 cm^2 and 3.29 cm^2, respectively. The anode slurry was composed of coal char, ternary eutectic, and an inert filler (SiC) with a ratio of 20:75:5 wt% and electrochemical discharge tests were conducted at 700, 750, 800, 850°C. Figure 15 shows the performance of the cells which were normalised using the cathode surface area. It can be concluded that the full cell performance is limited by the anode performance at 700°C and 750°C since by increasing the cathode area there was a reduction in the normalised power output of the cell. Interestingly, the normalised performance of the full cell for set 1 and set 2 experiments were similar at higher temperatures (800°C and 850°C). This indicates that the full cell performance is limited by the cathode performance at higher temperatures.
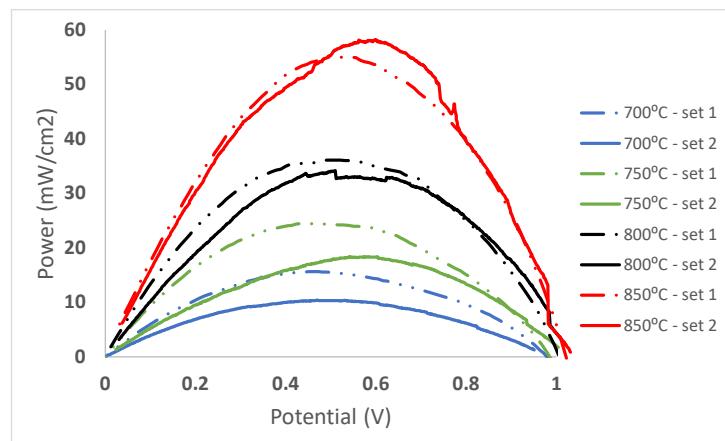
Figure 15: Power density of cell with two different cathode surface area (1.83 cm^2 and 3.29 cm^2 for set 1 and set 2, respectively) at different temperature.

Current Collector Material

The current collector material was changed from silver to nickel to see the impact this would have on the performance, given that nickel is commonly used in the literature [10, 12, 13]. In these experiments, the LSM cathode was absent, meaning that oxygen reduction was occurring from the silver paste used to adhere the nickel wire to the YSZ tube. The results showed that the performance was significantly lower at 800°C; i.e., 1.31 mW/cm^2 versus 11.23 mW/cm^2 for nickel and silver, respectively. Further, the performance of nickel decreased with temperature. The decrease in the performance when using nickel as the current collector can be attributed to the poor electrical conductivity of nickel at high temperature due to the formation of a nickel oxide layer (Eqn (7)).

$$2Ni + O_2 \rightarrow 2NiO \qquad \qquad \dots(7)$$
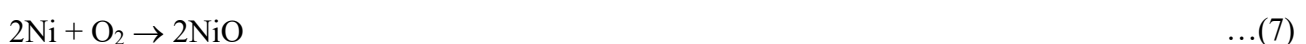
Lanthanum Strontium Manganite (LSM)

The performance of LSM as an oxygen reduction catalyst was compared to silver paste in separate experiments. To fabricate the electrodes, LSM was carefully coated onto the YSZ tubes using a brush before being heated in the furnace at 2°C/min to 850°C and held isothermally for 2 h. After being removed from the furnace, the terpinol-based solvent (Fuel Cell Materials) was completely removed and the LSM powder flaked off the tubes. In order to overcome this, 10 wt% silver ink was mixed in with the LSM paste to improve the adhesion [14], and the curing protocol was modified; i.e., a heating rate of 1°C/min to 1100°C. These modifications prevented the LSM powder from flaking off; however, the performance of the LSM coated cathode was inferior to the control which only utilised small spots of silver ink to physically adhere to the silver wire current collector; i.e., (4.7 mW/cm^2 versus 5.5 mW/cm^2, respectively (see Figure 16).

There are a number of possible reasons why the control performed better than the LSM coated cathode. The oxide anion conductivity of LSM is reportedly very poor below 800°C [10], which is below the operation temperature used in these experiments (700°C). LSM work best when a thin monolayer is applied to the solid oxide electrolyte substrate, due to the poor electrical and oxide anion conductivity of the material. Ideally an intergrowth layer should form resulting from the sintering process, where both LSM and YSZ domains overlap, thus allowing for oxide to pass directly to the YSZ which is a superior conductor. What is critical here is the triple phase boundary between the oxygen reduction catalyst, the oxide anion conductor and fresh O$_2$ [10].

In order to achieve this intergrowth layer and maximise the surface area of the triple phase boundary an appropriate sintering protocol was employed. We used YSZ powder mixed with LSM cathode paste in 50/50 mole ratio to improve the adhesion. The coating produced from the mixture was highly adherent to the YSZ tube. The performance of the LSM-YSZ mixture cathode was compared to a silver cathode, and it was found that the peak power of the silver cathode was 43 % higher at 800°C. However, at ~830°C the power density of the LSM-YSZ cathode was 16% higher than silver cathode; i.e., 15.83 mW/cm^2 versus 18.41 mW/cm^2 for the silver and LSM-YSZ cathodes, respectively. This could be due to higher oxide conductivity of LSM above 800°C, as reported in the literature [10]. We also tested the commercial mixture of LSM-YSZ as the cathode material and found that the performance increased substantially, i.e., more than 2-fold (Fig.17). It is possible that the homogeneous nature of the commercial LSM-YSZ mixture compared to the lab-prepared mixture has improved the performance.
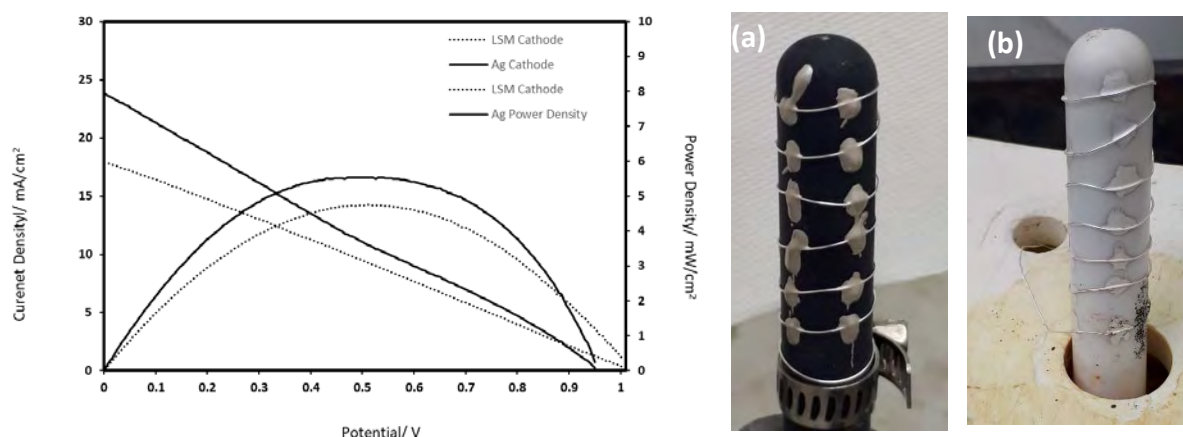
Figure 16: Current density and power density versus potential for LSM coated cathode versus a control that did not contain LSM, both using 20 wt% coal char at 700°C scanned from 1-0 V at 5 mV/sec; Photographs of the cell with coiled silver wire: (a) LSM coated, and (b) without LSM.
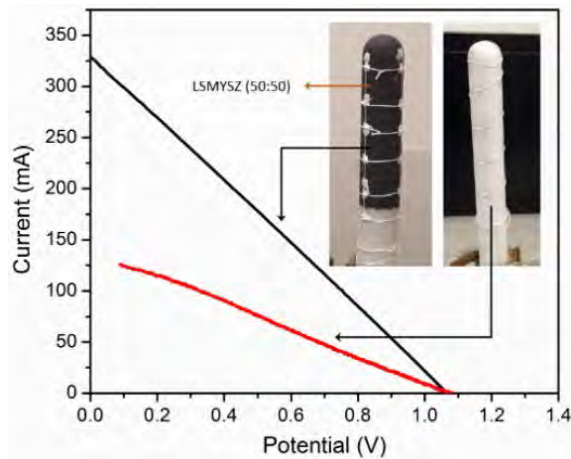
Figure 17: Photographs of YSZ tube with silver wire/paste cathode and YSZ tube with LSM-YSZ paste and silver wire/paste cathode and their discharge performance data at 800°C.

Air Flow in Cathode Compartment

A long-term (5 h) chronoamperometry experiment was conducted to assess the effect of air flow rate on the cathode performance where the air flow rate was adjusted between (40-1500 mL/min). Fig. 18 shows that there is no clear correlation between air flow rate and cell performance. Initially, as the air flow rate increased, the performance of the cell decreased significantly. This decrease could be due to two reasons: (i) decay of current with time as the carbon is consumed, and (ii) decrease in cathode compartment temperature due to increase in air flow rate, since a cool stream of compressed air was entering the furnace. The kinetics of the cathode are heavily dependent upon temperature [15], hence operating the cell at lower temperature would undoubtedly be deleterious to the performance.
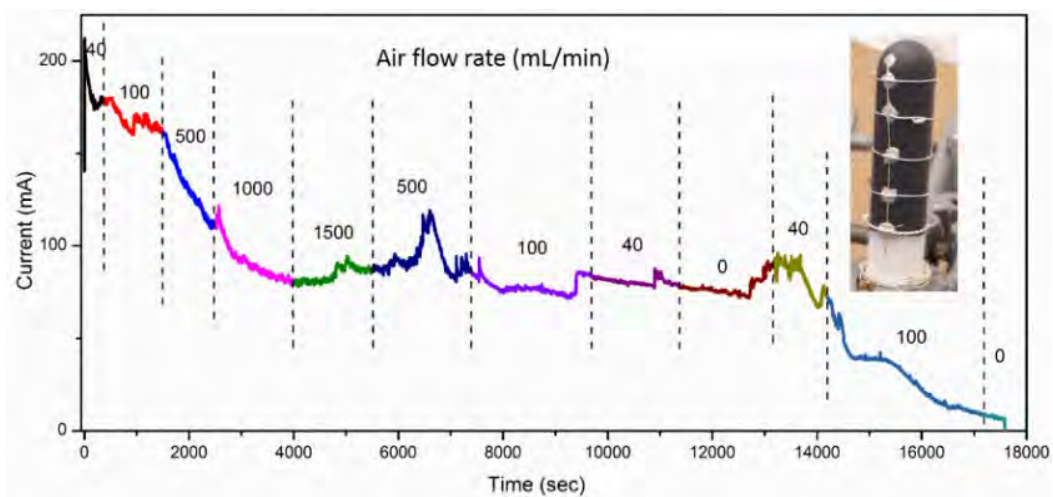
Figure 18: Discharge performance data of the fuel cell at different air flow rate.

YSZ Thickness

Mechanical stability of the YSZ tubes is an important factor that must be considered in the fuel cell design. Increase in the wall thickness of YSZ tube will improve the mechanical integrity, but the performance of the cell may be affected [3]. In order to study the thickness effect on the performance, YSZ tubes with two different wall thickness; i.e., 0.87 mm and 1.57 mm, were tested. Fig. 19 shows that the performance difference between the two tubes is not significantly different. Therefore, it is worth increasing the YSZ tube thickness to improve the mechanical integrity of the YSZ tubes

because the performance is not significantly affected.
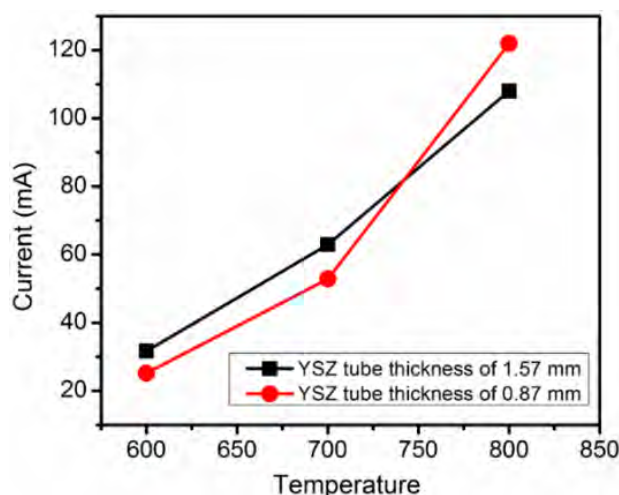
Figure 19: Comparing the discharge performance data of the fuel cell with different YSZ tube wall thickness.

Milestone 5: Molten Carbonate Physical Properties and Recycle/Recovery

Impurities

Mineral impurities are present in coal and can leach into the molten carbonate, which may influence the thermal properties of the carbonate eutectic and hence the cell performance. It has been reported that some minerals display a catalytic effect on the electrochemical oxidation of carbon [16], while others decrease the power output [17]. In this work, the influence of impurities on the melting point of the ternary alkali metal carbonate eutectic (398°C [1]); i.e., Li_2CO_2 (43.5 mol%), Na_2CO_3 (31.5 mol%) and K_2CO_3 (25.0 mol%), was examined. Impurities added to the eutectic carbonate mixture are kaolin, SiO_2, Fe_2O_3, FeS, TiO_2, $CaCO_3$ and $CaSO_4$ at the 5% wt% concentration level. Analysis was carried out using a Perkin−Elmer Diamond TGA/DTA instrument at different heating rates (2, 5, 10 and 20°C/min). Table 3 shows the changes in melting point of the eutectic carbonate mixture when adding the impurities at the 5 wt% concentration level. It was found that kaolin and $CaCO_3$ significantly decreased the melting temperature of the eutectic carbonate mixture, while SiO_2 increases the melting temperature by approximately 3°C, due to the formation of alkali metal silicates [18] and the subsequent destabilisation of the liquid phase by increasing the chemical potential (μ). Impurities such as Fe_2O_3, FeS, $CaSO_4$ and TiO_2 also decreased the melting temperature of the carbonate eutectic, however to a much lesser extent.

A decrease in melting temperature demonstrates that the melting point depression phenomenon is in effect, which is a colligative property that only takes place when dissolution occurs [19]. Therefore, all of the minerals examined dissolve in the molten carbonate. This is also true for SiO_2 which displays more complex behaviour, as SiO_2 is converted to alkali metal silicates (Eqn 8) which dissolve at a higher temperature (449°C).

$$M_2CO_3 + SiO_2 \rightarrow M_2SiO_3 + CO_2 \quad\quad\quad …(8)$$

Table 3: Influence of coal impurities on the melting point of eutectic carbonate mixture (heating rate 5°C/min).

Added Impurities (5 wt%)	Melting point (°C)
None (Pure eutectic carbonate)	387
$CaCO_3$	376
Kaolin	374
Fe_2O_3	387
TiO_2	383
SiO_2 (peak1)	401
SiO_2 (peak2) M_2SiO_3 dissolution	449
$CaSO_4$	381
FeS	383

In Eqn (8) M represents an alkali ion metal either Li^+, Na^+ or K^+. The degree to which the melting point is depressed can be correlated with the amount of each mineral dissolved. It is expected that there will be a solubility limit for each individual mineral species, at which point the excess material will precipitate. This could present a challenge for DCFC operation because certain minerals have an inhibitory effect on electro-oxidation [17], such as SiO_2 which typically accounts for 70-90 wt% of the mineral content of anthracitic coal [6]. In addition, mineral precipitates will absorb heat, thereby imposing an energy penalty on the system and may also interrupt the flow properties of the slurry.

Gasification

Slurry samples composed of coal char + ternary eutectic were analyzed by both thermal gravimetric analysis (TGA) and differential thermal analysis (DTA) to investigate the chemical processes that take place in the DCFC under open circuit conditions. The coal char loading in the slurry was systematically varied between 10-80 wt%; in addition, controls were made up of unmodified coal char and eutectic which were analyzed in separate experiments.

The TGA results showed that the mass loss is considerably higher for the coal sample under a CO_2 atmosphere (18 wt%) compared with N_2 (7 wt%) when heated to 860°C at 10°C/min. Under CO_2 mass loss is due to the reverse Boudouard gasification (Eqn (9)), while the mass loss under N_2 is due to continued devolatilization of the char.

$$C + CO_2 \rightarrow 2CO \qquad \qquad \qquad \qquad \text{...(9)}$$

There was no significant difference in mass loss when the unmodified eutectic was heated to 700°C under CO_2 (4%) or N_2 (6%), which is similar to what was reported by Olivares et al. [2] who examined the thermal stability of a ternary carbonate mixture under CO_2, air and Ar. For slurry mixtures there was a correlation between mass loss and char loading in the slurry under both N_2 (4-74 wt% mass loss) and CO_2 (6-56 wt% mass loss). A similar trend in mass loss was observed when holding isothermally at 700°C for 1000 min. Based on these results, it can be concluded that gasification

accounts for considerable mass loss under open circuit conditions at elevated temperature (≥700°C), hence measures must be taken to minimise gasification during the operation of DCFC for higher efficiency.

Electrochemical Analysis - Kaolin Doped Half Cell

One of the common minerals present in thermal coal is kaolinite [6], which has been found to impact the activity of carbon electro-oxidation in the DCFC anode chamber [17]. To investigate this further, kaolinite was added to the electrolyte; i.e., a ternary carbonate eutectic, in various loadings (5-20 wt%) and the electrochemical performance was monitored.

Open circuit potential (OCP) measurements and linear sweep voltammetry (LSV) experiments were conducted for electrochemical characterization using a half-cell set up (as show in Fig. 21) consisting of graphite pellet as working electrode, and graphite rods as reference and counter electrode.
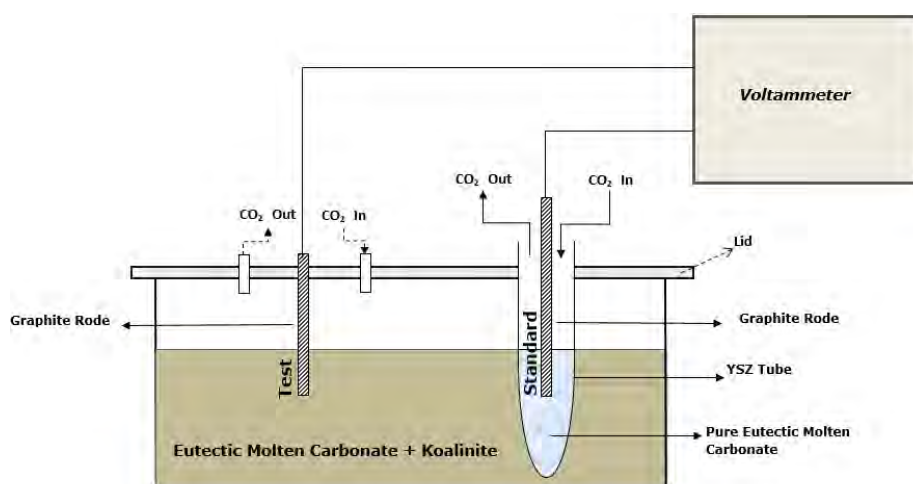
Figure 20: Schematic of the half-cell setup used for electrochemical analysis.

The voltammetry experiments were performed at 600°C under a CO_2 environment, and the potential was scanned from OCP to 0.5 V at 5 mV/sec (Fig.21). Kaolinite increased the OCP of the cell; i.e., from -0.25 V for the unmodified electrolyte to +0.05 V for the 15 wt% kaolinite containing electrolyte. The LSV results (Fig. 21) show the catalytic effect of kaolinite on the electro-oxidation of carbon. Interestingly, it was observed that the performance of the cell decreased when increasing the kaolinite content above its saturation limit (20 wt%).

Differential Thermal Analysis of Kaolin Doped Eutectic

The thermal behaviour of the mixtures was investigated using differential thermal analysis (DTA). From DTA results (Fig.22) it is evident that kaolinite has depressed the melting point of the mixture (373°C), which reduced the amount of heat energy required to melt the mixture, thus increasing the cell operating efficiency. Increasing the kaolinite content in the electrolyte up to 15 wt% decreased the activation energy of the melting process, which was calculated using the Friedman method [8,20]. Above 15 wt%, the excess kaolin precipitates out, because the saturation limit for kaolin in the ternary eutectic has been exceeded.
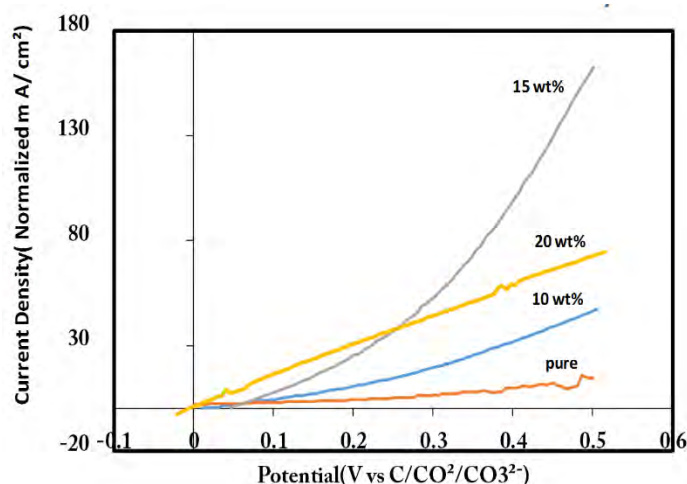
Figure 21: LSVs showing the effect of kaolinite concentration in the ternary carbonate eutectic on the electro-oxidation of graphite.
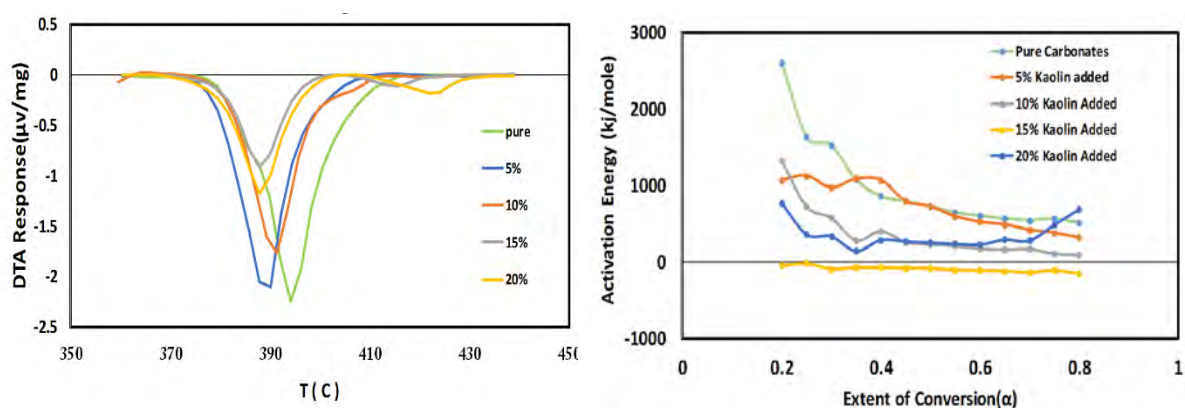
Figure 22: (a) DTA response for different kaolin loadings heated at 10°C/min, and (b) activation energy versus extent of conversion for different loadings of kaolin.

Further outcomes in this area of the project are published in journal articles contained within the Appendix.

Milestone 6: Initial Demonstration Unit (1 kW) Design

Throughout the course of this project, the design of the DCFC evolved as more insight was gained. What follows is the evolution of DCFC design broken down into quarterly stages.

Stage 1

While the initial objective was to build a 10 kW DCFC demonstration plant, it was realized quite early that this would involve considerable repetition of a smaller scale module, and so the decision was made to focus on the smaller 1 kW system because it was believed to be able to demonstrate all relevant aspects of the system design. This allowed for the trial of several key elements on a smaller scale before investing in larger versions. In some cases, however, the commissioning elements; i.e., instrumentation will be the same for 10 kW unit, even though they will be operated on the 1 kW unit first. This lead to a more cost-effective approach to achieve objectives of the project with realistic timelines. For the 1 kW unit design and construction, we engaged with external contractors. The

design work was divided into three phases:

Phase 1: Concept design: This phase converted the diagrammatic representations, process requirements and project needs into a workable machine-solution suitable for more detailed development in the next phase. This phase also included facilitation of one HAZOP session to identify and evaluate potential process problems and identify risks to equipment and personnel.

Phase 2: Component engineering design and detailing: This phase involved engineering analysis (i.e., mechanical, structural, thermal, etc.) of the components and their assemblies. The primary system elements such as molten carbonate and coal mixing tank, fuel cell tank reactor, dump tank, and reservoir holding tank were designed.

Phase 3: Integration and commissioning: In this phase the necessary designs and drawings to permit integration of the main unit and auxiliary equipment, and also interfacing arrangements were considered.

A schematic of the conceptual design of 1 kW DCFC module is shown in Fig. 23. Alkali metal carbonates and pre-processed coal char were to be fed into the mixing tank, where the temperature was planned to be ~500⁰C. The slurry in the mixing tank was to be then gravity fed to the fuel cell tank where it was to be heated to desired operation temperature (~800⁰C). Pre-heated air was to be passed through the YSZ tubes to complete the electrochemical reaction in the cathode. After electrochemical discharge of carbon energy, the coal-lean carbonate is transferred to the dump tank.
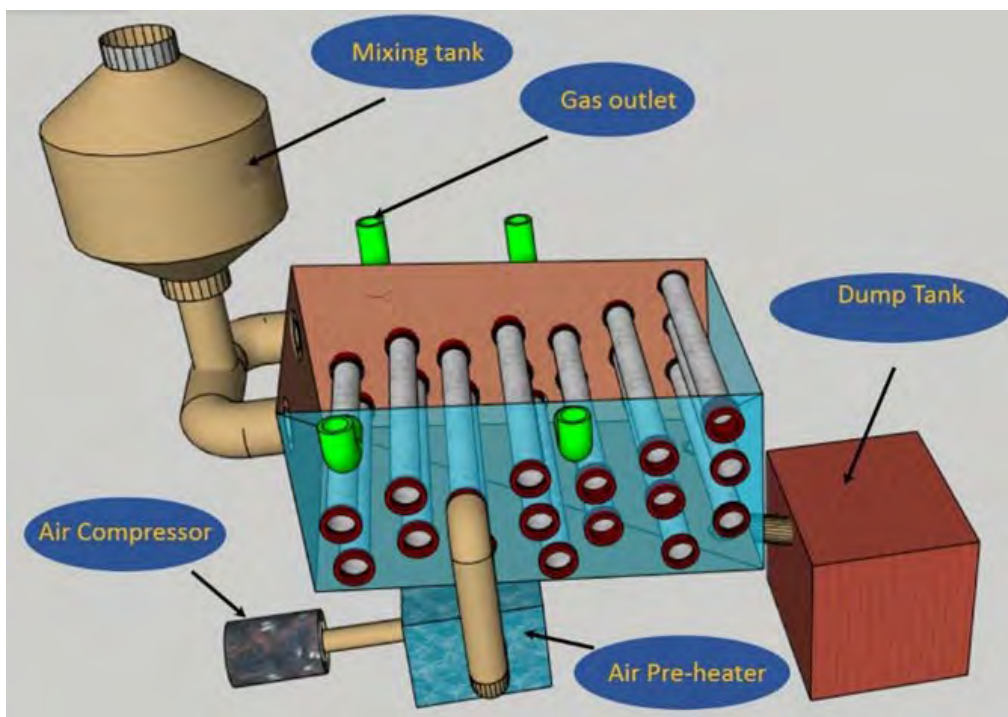
Figure 23: Schematic of the 1kW DCFC unit showing the ancillary components and layout of the YSZ tubes.

Cell Design

The cell design, as shown in Fig. 24, was developed after a number of iterations of cell tank size, slope of the tank, number and of placement of the YSZ tubes, plenum size and location, etc. The fuel cell was to contain the following main components:

• Fuel cell tank

- YSZ tubes (27) placed horizontally in a staggered fashion for better flow behaviour of the slurry
- Two plenums at opposite sides of the fuel cell tank for air flow (in and out) through the YSZ tubes
- Silver mesh wrapped around the YSZ tubes, acts as anode current collector
- Silver wire/mesh placed inside the YSZ tubes, acts as cathode current collector
- Level sensors and thermocouples
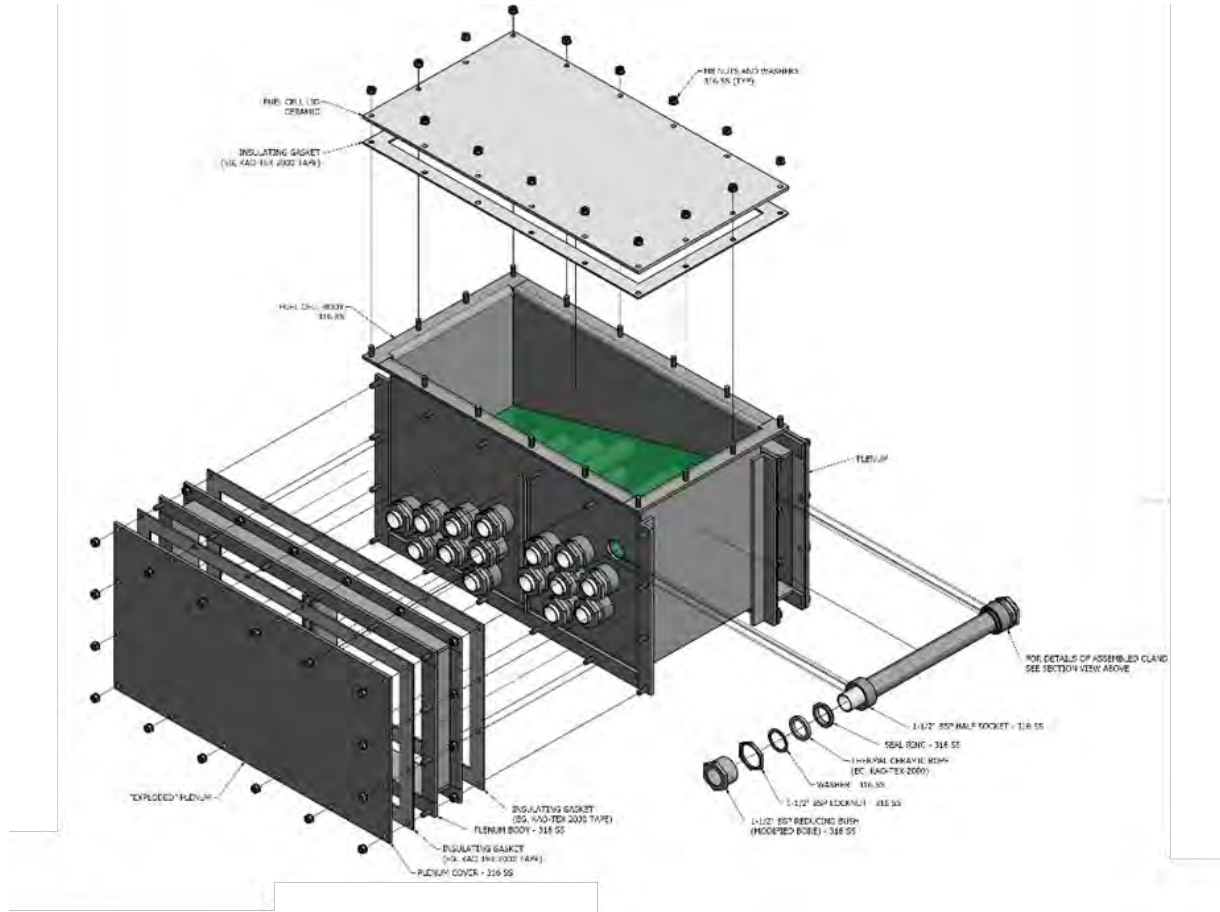
Figure 24: Isometric diagram of the fuel cell tank.

Gland Design

A critical part of the fuel cell design was the gland design; i.e., attachment of the YSZ tubes to the fuel cell tank walls, in a way that it provides a leak-proof sealing when it is in contact with the molten carbonate at high temperatures. The gland design was intended to accommodate differences in the thermal expansion of YSZ tube and stainless steel body of the cell. Two different gland designs, as shown in Fig. 25, were considered. However, the design with reducing bush (design 1) was chosen since this design could provide uniform pressure on the ceramic rope resulting in a good sealing.

To test the gland, a small cell which accommodates one YSZ tube (15 cm length) was constructed. The suitability of the gland in providing leak-proof sealing for molten carbonate, as well as the performance of the cell were tested. The short-term experiments (<12 hours) were successful; i.e., no leaking was observed. Fig. 26 shows the two different arrangements of the anode and cathode current collectors (silver wire or silver mesh) and their corresponding cell performances. These performances are from testing the cell at 800°C using slurry with carbonate to coal being 4:1 (mass ratio). The cell with silver wire as anode current collector exhibited a maximum power density of 79 mW/cm^2, whereas the power density of the cell with silver mesh as the current collector was increased to 138 mW/cm^2.
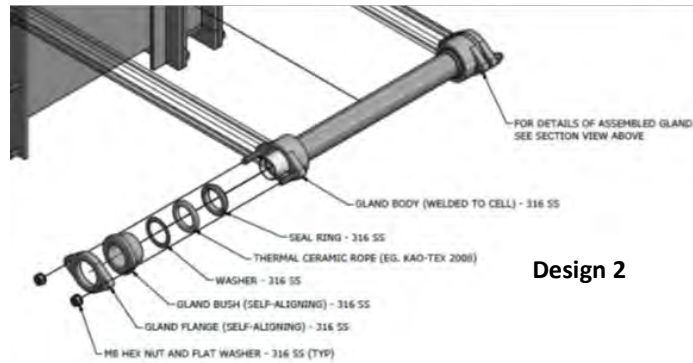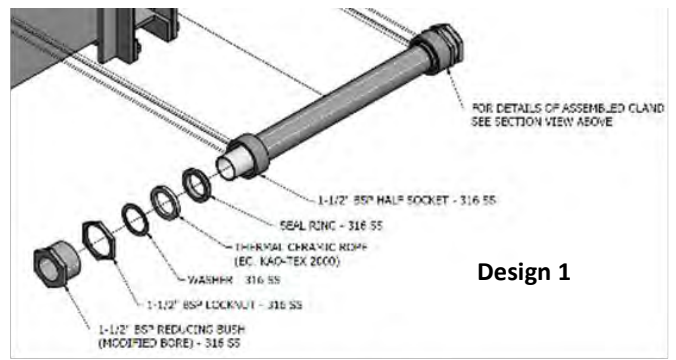
Figure 25: Two different designs for the gland to hold YSZ tubes in position in the cell.
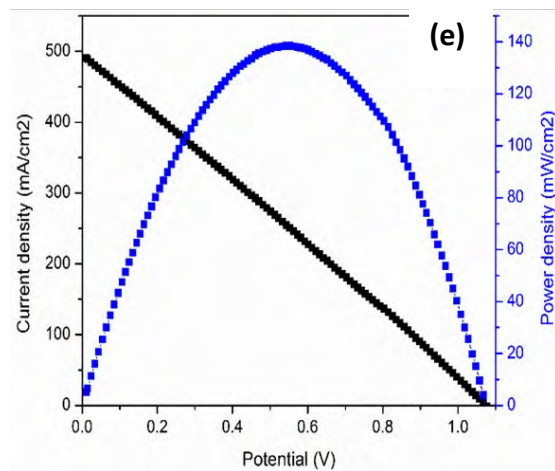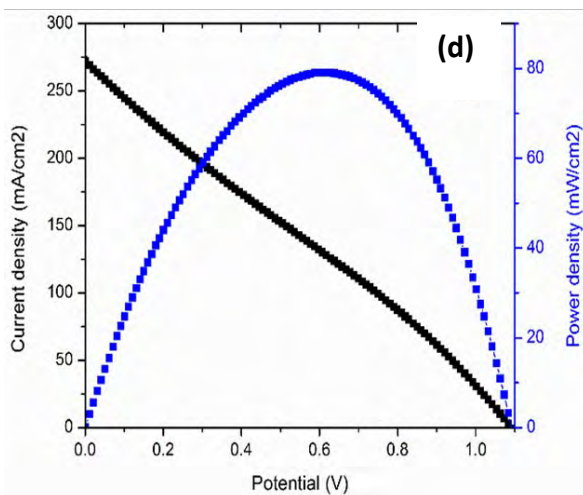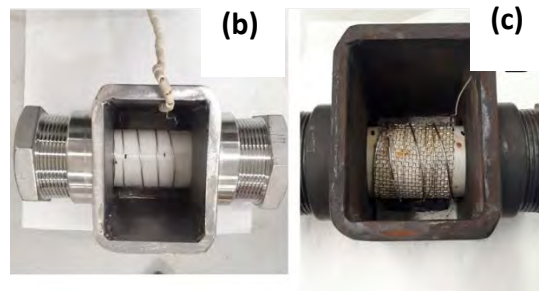
Figure 26: (a) Small cell setup showing cathode current collector arrangement; Anode current collector configurations: (b) spiral silver wire, and (c) silver mesh; performances of direct carbon fuel cell with: (d) silver wire, and (e) silver mesh.

Unfortunately, in the long-term test (~24 h) the slurry leaked out of the small cell through the gap between the YSZ tube and the gland. It was evident from Fig. 27 that the slurry severely corroded the stainless steel glands. Interestingly, the cell inside wall exhibited minimal corrosion, where CO_2 was the sweep gas. To understand if oxygen in air affects the corrosion behavior of the stainless steel, an immersion experiment was conducted for two stainless steel samples (253MA and 316L) with air as the sweep gas (20 ml/min) for 4 days at 800°C. The weight gain was 4.6×10^{-3} g/cm^2/day and 6.0×10^{-3} g/cm^2/day for 253MA and 316L, respectively. Comparing these results to the those with the nitrogen sweep gas (253MA: 3.4×10^{-3} g/cm^2/day; 316L: 2.5×10^{-3} g/cm^2/day), it is can be concluded that oxygen increases the corrosion of 316L more significantly than 253MA.
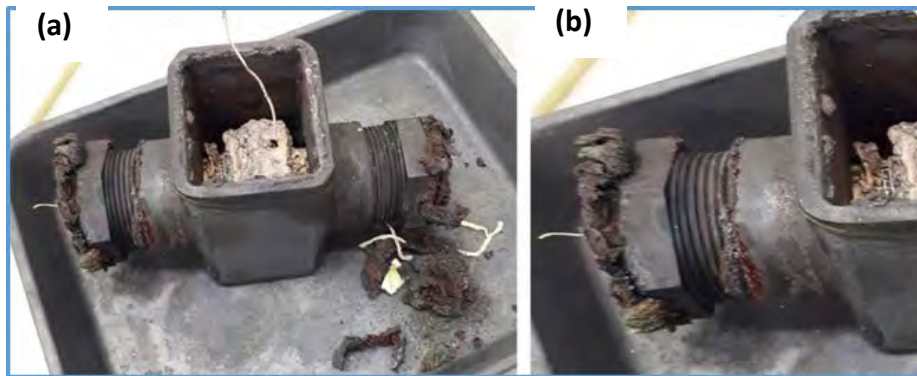
Figure 27: Photographs of the small cell showing slurry leak-out through: (a) both the glands, (b) the gap between the gland and YSZ tube.

In order to combat the leaking of the slurry, two different methods were tested: (i) increasing the packing of the ceramic rope, and (ii) soaking the ceramic rope in sodium silicate which is known to swell and seal at high temperature. In both the tests, leaking of the slurry through the small gap between the YSZ tube and the gland was noticed (Fig. 28) and so redesigning of the gland with tapering in the seal ring and washer for close contact between the ceramic rope and the YSZ tubes was undertaken. A high temperature sealant was also been identified to fill the gap between the YSZ tube and seal ring/ceramic rope.
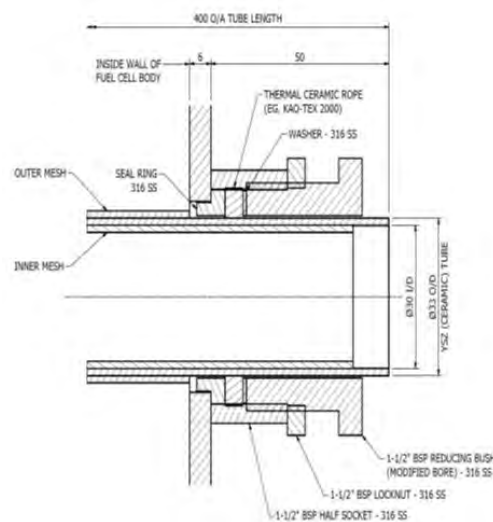
Figure 28: Gland design showing positions of the seal ring, ceramic rope and YSZ tube.

Furnace Design

Early in the project it was recognised that an elegant solution to heat all DCFC components was to use a furnace. Calculations were used to ascertain the design requirements for a natural gas fired furnace. Easy access to the cell and component connections were mainly considered in designing the furnace. Later, we discovered that an electrically heated furnace could be a more economical system for this purpose. A furnace company was engaged to develop an electrically heated furnace to be built for the 1 kW demonstration unit. The design of the furnace including connections to the mixing and dump tanks is shown in Fig. 29.
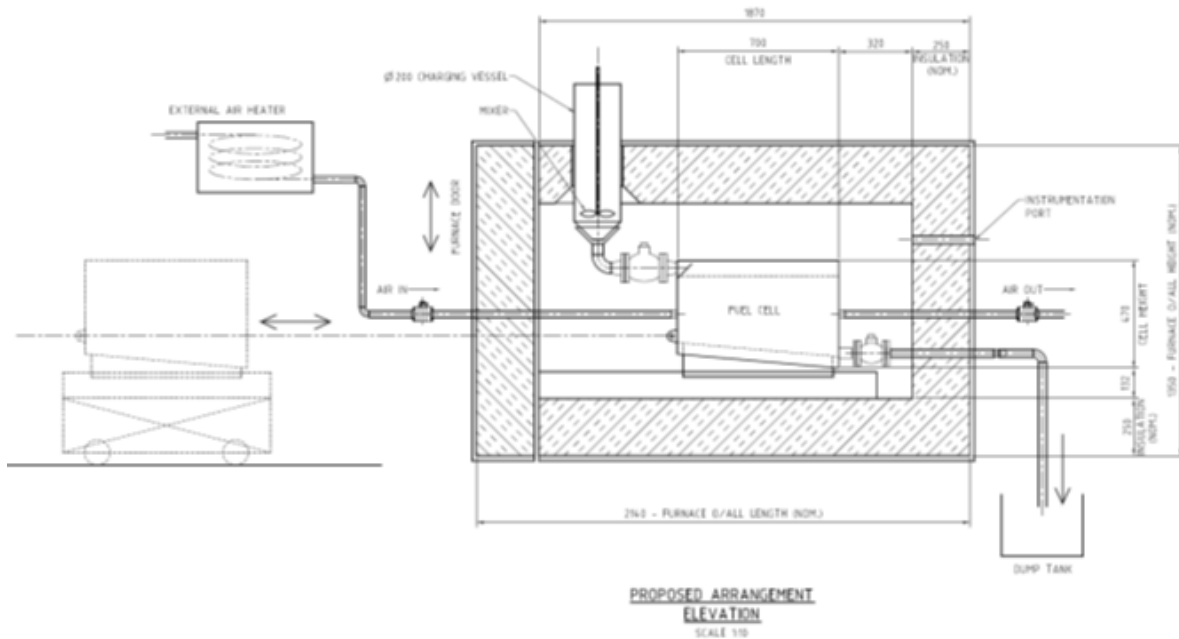
Figure 29: An engineering drawing of the furnace design for the fuel cell.

Stage 2

After the further refinements (Figure 30) to the gland design proposed above, unfortunately under long-term tests (>48h) the slurry leaked out of the cell through the tube/gland gap. In fact, the slurry severely corroded the stainless steel gland. In order to stop the slurry leak, different methods were tested.
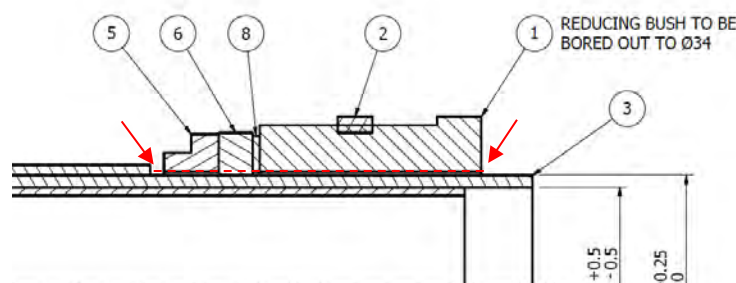
Figure 30. Gland design and the slurry leak path (red dashed line).

Method 1: Ceramic rope packing

A ceramic rope (two layers; Kao-tex, 6 mm diameter) was packed tightly between the seal ring and the washer (Fig. 31). To avoid metal-metal joining at high temperature, a nickel lubricant was also applied on the threads of the gland. The cell was examined after 4 h testing, where no sign of leaking were noticed (Fig. 32a). However, after 16 h testing extensive slurry leak was observed (Fig. 32b)
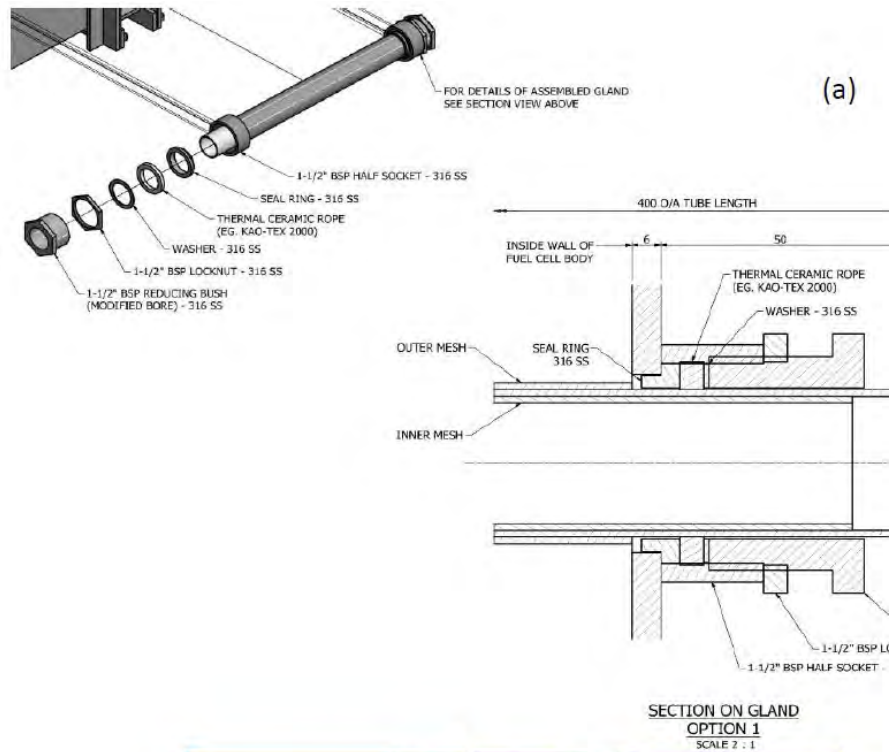
Figure 31. (a) Gland assembly design, (b) Kao-tex ceramic rope, and (c) nickel lubricant.
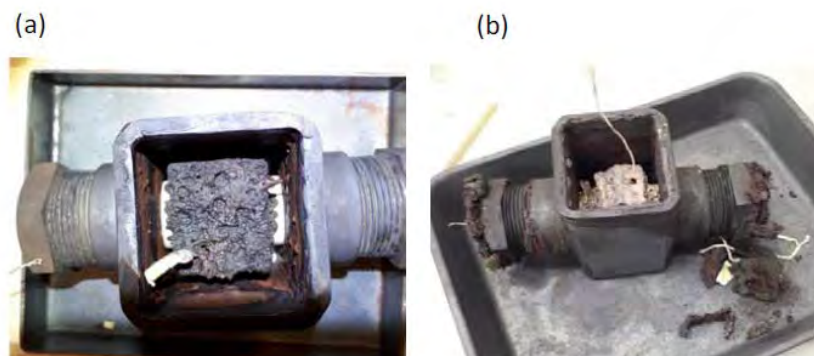
Figure 32. Photographs of the lab-scale cell after two different testing periods: (a) no leaking of the slurry after 4 h testing, and (b) severe leaking of the slurry after 16h testing.

Method 2: Sealant

A high temperature sealant (Deacon 8875, clay-based compound) (Fig. 33) was used to first fill the gap between the ceramic tube and the seal ring. The sealant was generously applied and cured at 200°C for 2 h. Following that, ceramic rope packing (Method 1) was done to provide additional protection. However, the slurry leaked out after 24 h testing. The sealant appeared very brittle after the curing process.

Figure 33. A sealant (Deacon 8875) was applied and cured at 200°C for 2h.

Method 3: Design – tapered seal ring and washer

In order to exert more pressure on the ceramic rope (for tight packing) while tightening the gland, a tapered seal ring and washer arrangement were used (Fig. 34). As followed in Method 2, the sealant was cured before placing the ceramic rope. The slurry leak did not stop completely with this method, but it had largely reduced.

9	2	1-1/2" BSP HALF SOCKET
8	1	KAO-TEX 2000, 6mm SQUARE SECTION (OR EQUIV.)
7	1	SILVER MESH, 0.35 DIA WIRE, 110 WIDE x 288 LG (TO SUIT TUBE O/D)
6	1	SILVER MESH, 0.35 DIA WIRE, 105 WIDE x 380 LG (TO SUIT TUBE I/D)
5	1	TAPER WASHER, 44 O/D x 34 I/D x 2.5 THK
4	1	SEAL RING, 44 O/D x 34 I/D x 8 THK
3	1	CERAMIC (YSZ) TUBE, 33 O/D x 29.5 I/D x 400 LG
2	1	1-1/2" BSP HEX LOCKNUT
1	1	1-1/2" BSP REDUCING BUSH (MODIFIED)
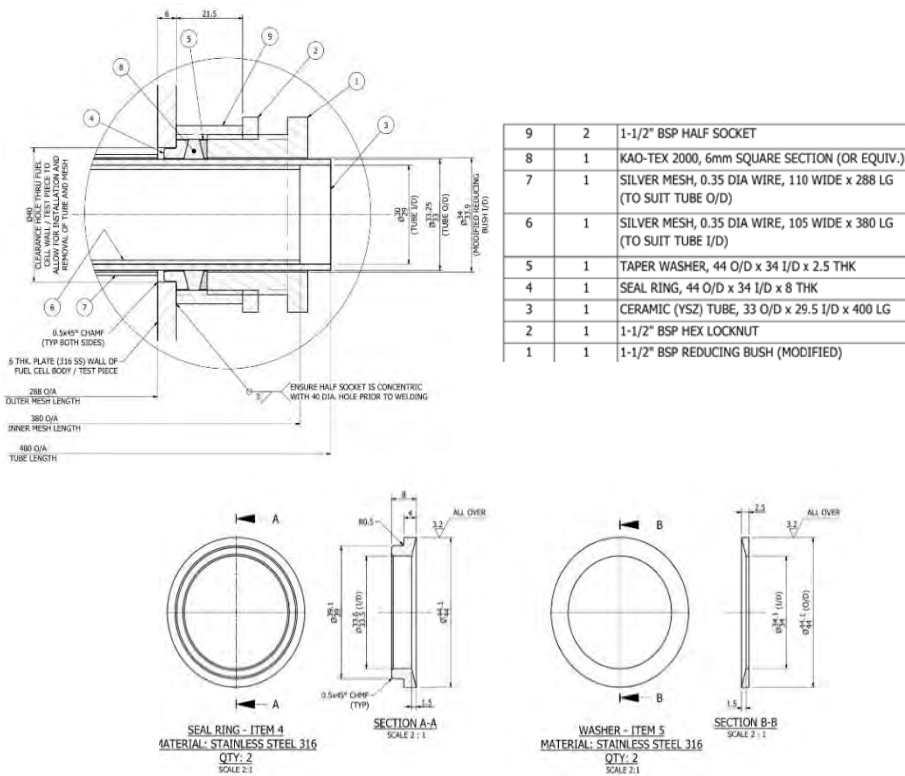
Figure 34. Revised gland design with tapered seal ring and washer.

Method 4: High density ceramic braid

A high density ceramic square braid (Kao-tex 2000) was used in place of the normal ceramic braid (Fig. 35). Method 2 steps, i.e., filling the gap with a sealant before placing the ceramic braid, were followed. The slurry leak was minimal, but did not stop completely in the 24 h testing.

Figure 35. High density ceramic braid (Kao-tex 2000)

Method 5: High density ceramic braid + sodium slicate

Sodium silicate is known to swell at high temperatures. Hence, in this method the high density square braid was soaked in sodium silicate for 1 h and then placed between the seal ring and washer. To fill the small gaps, sodium silicate solution was added on top of the ceramic braid before tightening the gland. The cell was then taken to 100°C for 3 h to remove the solvent. Unfortunately, the leaking was very severe in this case. The expansion of sodium silicate has created through-pores, which led to slurry leak. The gland was also severely corroded.

Figure 36. A photo of the gland after testing (Method 5) showing severe slurry leak and corrosion of the gland.

Method 6: Ceramic paste (Resbond)

In this method, the ceramic square braid was soaked in a ceramic paste (Resbond) for 1 h and then placed between the seal ring and washer. For effective sealing, Resbond was applied on the ceramic square braid and then the gland was tightened. The cell was taken to 100°C for 3 h to remove the solvent. Testing at high temperature caused fine cracks in the Resbond and thus failed to stop the leaking of the slurry.
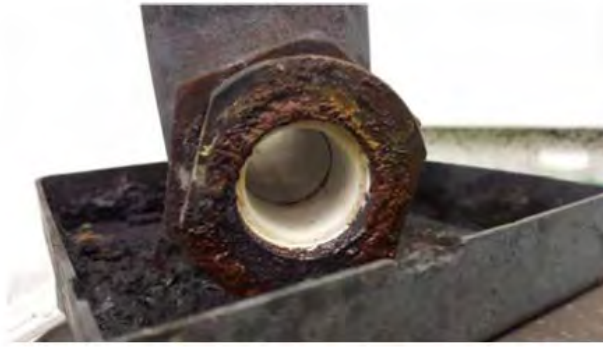
Figure 37. Photograph of the gland after testing (method 6).

Stopping the slurry leak through the gland/tube gap was a larger challenge than expected. The thermal expansion difference between the metal and ceramic parts in the gland has made it difficult to find a suitable material for this purpose. Considering the time we have to move forward to the next stage, we decided to make changes to the cell design where the slurry leak can be completed avoided.

New Cell Design

The new cell design of the DCFC was done primarily to overcome the slurry leaking issues. The new design had the same anode and cathode materials, but the YSZ tubes were closed-end (Fig. 38) and placed vertically in the cell tank.
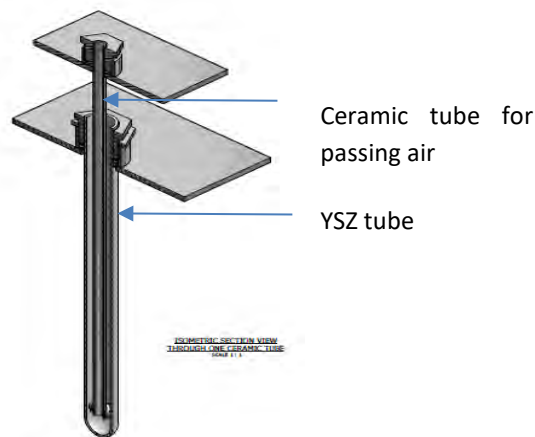
Figure 38. Isometric section view of the YSZ tube and a ceramic tube for passing air.

A schematic of the cell tank and charging vessel is shown in Fig. 39. The cathode side consists of (i) YSZ tubes, (ii) alumina tubes (for passing air for cathodic reaction), (iii) plenum 1 and (iv) plenum 2. As shown in Fig. 40, in this cell design there are 28 YSZ tubes held in place with a sealed gland, each with an alumina tube. Air is fed to the cathode through an inlet socket where it enters plenum 2, which is a large section where the air flows into the cell. From here it moves down the hollow alumina tubes. The alumina tubes are placed inside of the YSZ tubes with sealed base, which directs the flow of air. The air flows through the alumina tubes and flow back up the inside of the YSZ tube allowing for oxygen reduction reaction. The oxygen depleted air enters plenum 1 and leaves through the air outlet socket.
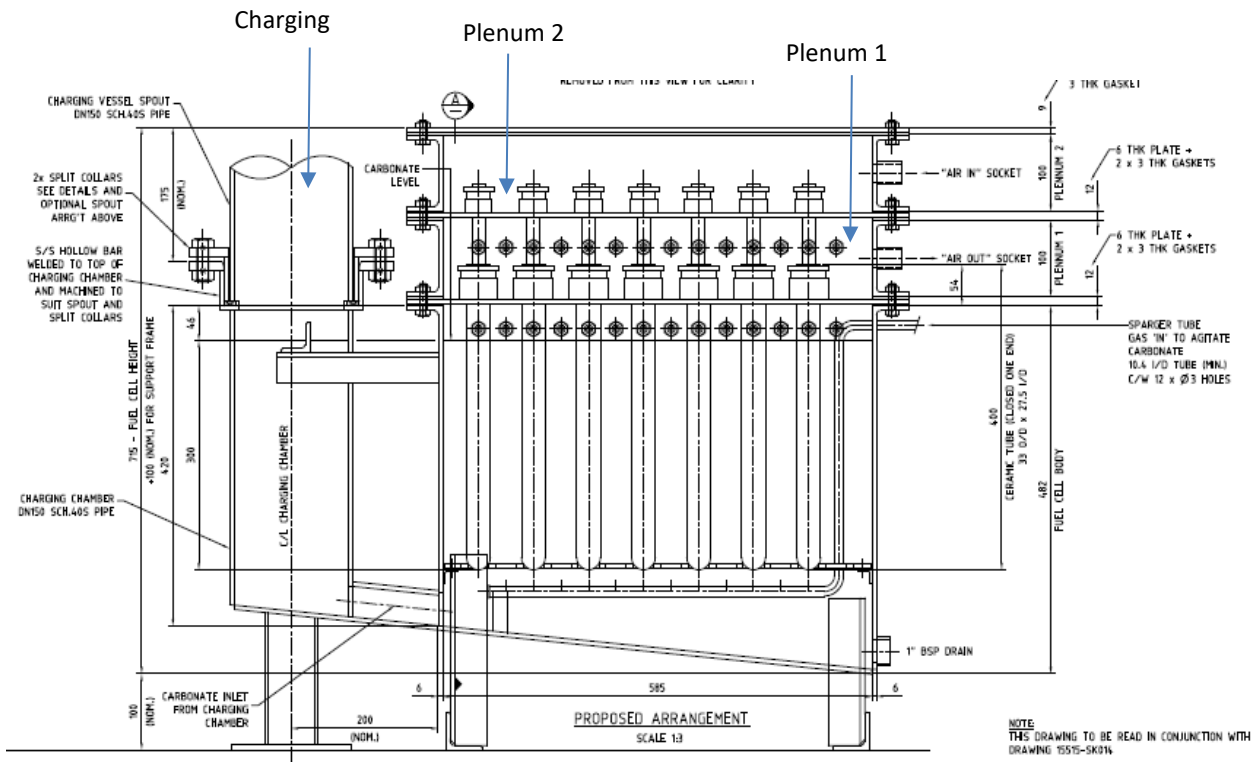
Figure 39. Schematic of the charging vessel and the cell tank.
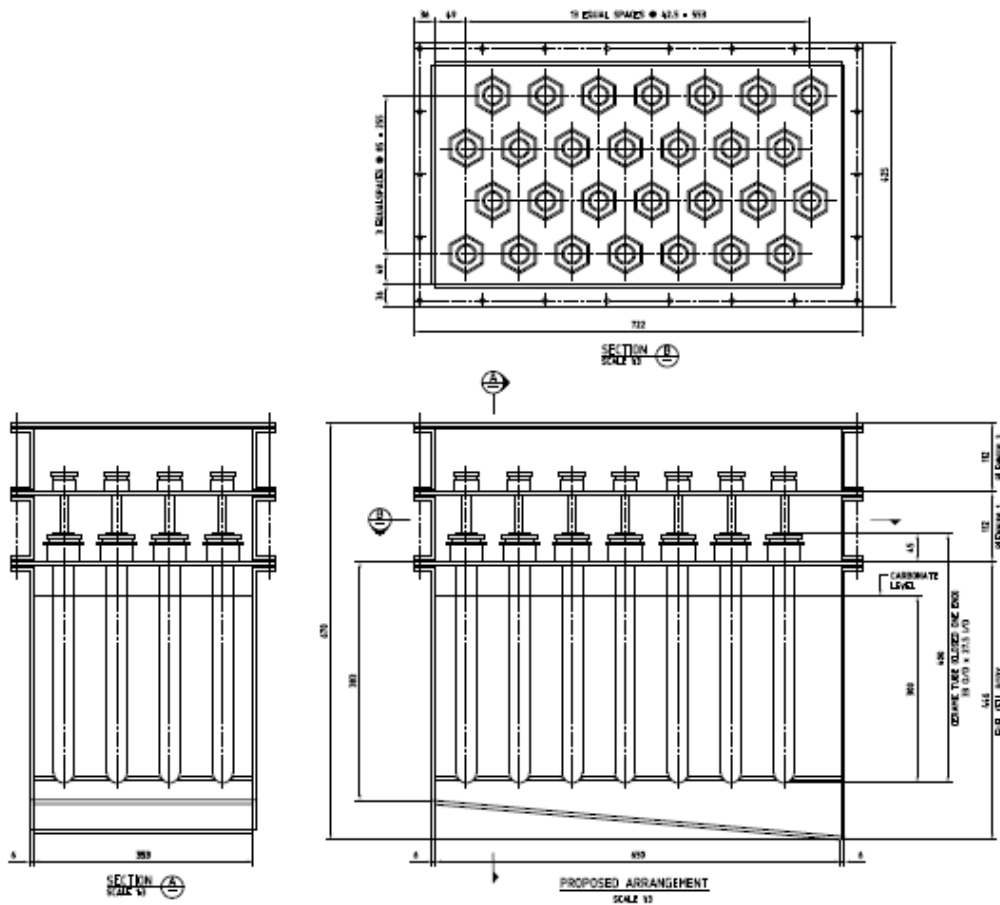
Figure 40. Arrangement of the YSZ tubes (7×4 = 28 tubes) in the tank cell.

Inside each of the YSZ tubes, silver mesh was pressed against the walls and silver paste was applied to function as the cathode current collector. The current was carried out of the cell using wires to a programmable load. Each of the silver current carrying wires was insulated, stopping any electrical connection with the cell walls or other current collectors. The cathode chamber was sealed to be gas tight to stop any oxygen escaping or entering the anode chamber. The seal on the YSZ tube gland was achieved using a ceramic insulation material.

The anode chamber consisted of two sections: (i) charging chamber, and (ii) anode chamber (Fig. 39). This was where fresh slurry was added to the cell to maintain continuous operation. In this cell, the slurry was a mixture of coal and ternary eutectic. The slurry was 20 wt% coal and 80 wt% eutectic. This allowed for sufficient flow in the cell for continuous operation. The slurry was compressed into pellets through a pelletiser to allow for easy handling and loading into the cell. The charging chamber was accessed from above through a knife gate valve that allowed for safe introduction of the fuel from the loading chamber above. Once the slurry pellets were placed inside the loading chamber, the chamber was sealed and nitrogen used to remove any oxygen present. Once the chamber was purged, the knife gate valve was opened and the pellets fall into the charging chamber.

The pellets were melted in the charging chamber, flowing through to the anode chamber. In the anode chamber, the 28 YSZ tubes were submerged in the slurry. A stainless steel mesh sits beneath the YSZ tubes to offer structural support. The 28 tubes were evenly spaced into 7 rows of 4 tubes. Between the 7 rows of YSZ tubes, 14 sections of silver mesh were placed upon 7 frames which offer structural support to the mesh (Fig. 41). These 14 sections of silver mesh acted as the anode current collector. From each of these sections of mesh, a wire carries the current out of the cell to the programmable load.
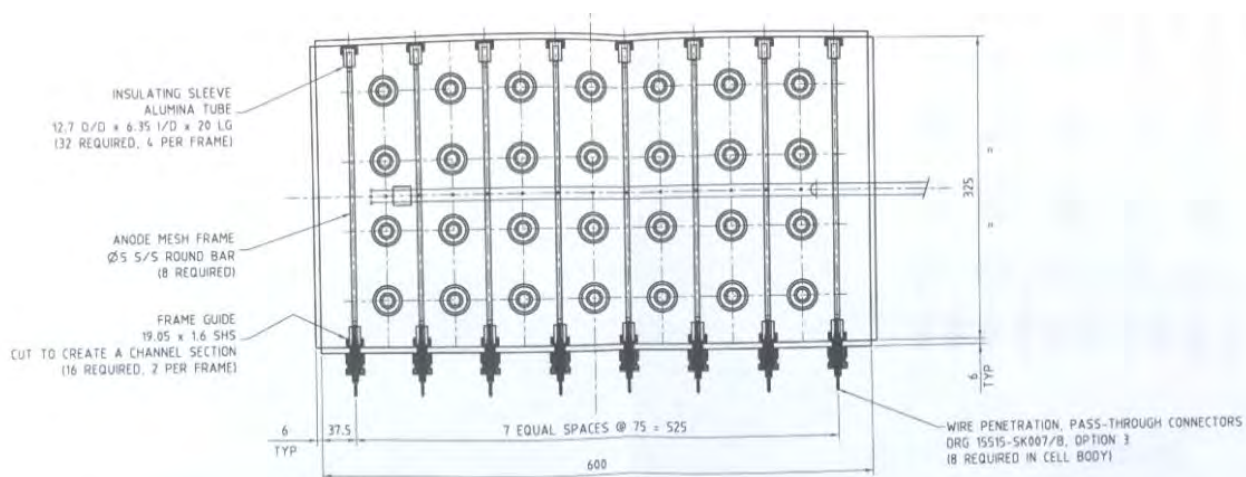
Figure 41. Anode mesh current collector placement in the cell tank.

Underneath the YSZ tubes rests a sparger. The sparger is supplied with CO_2 allowing for agitation of the slurry in the anode chamber to improve reaction kinetics. The sparger gas was preheated to 800°C through the use of a heater prior to entering the cell. To allow for a continuous operation, a drain valve was located at the bottom of the cell on the opposite wall to the feed from the charging chamber. This allowed for carbonate and mineral matter to be removed from the cell, while fresh slurry is added. Through the operation of the cell CO_2 was produced, as well as the gases added by the sparger. These gases exited the anode chamber through an outlet socket above the carbonate level to ensure no carbonate enters the outlet. The anode off gases pass through a cooler and are then collected for analysis.

Various sensors were in the anode chamber of the cell. Multiple thermocouples were used to monitor the temperature inside the cell at various points in the slurry. Silver wires were used to create custom

level sensors that can withstand the extreme environment of the cell. This allowed for monitoring of the flows in and out of the furnace and indicate any problems encountered during a run of the cell.

Upon shutdown of the cell, the furnace temperature was maintained to ensure the carbonate does not solidify. The drainage valve can then be opened until the cell was drained. The cell was then cooled to room temperature. Water can then be flushed through the system to remove any excess carbonate that remains in the cell. When the carbonate leave the cell, it goes through a custom valve, which directs the flow to a dump tank that cools and stores the carbonate.

Stage 3

Fig. 42 shows the different views of the DCFC model unit consisting of cell tank, feed tank and dump tank.
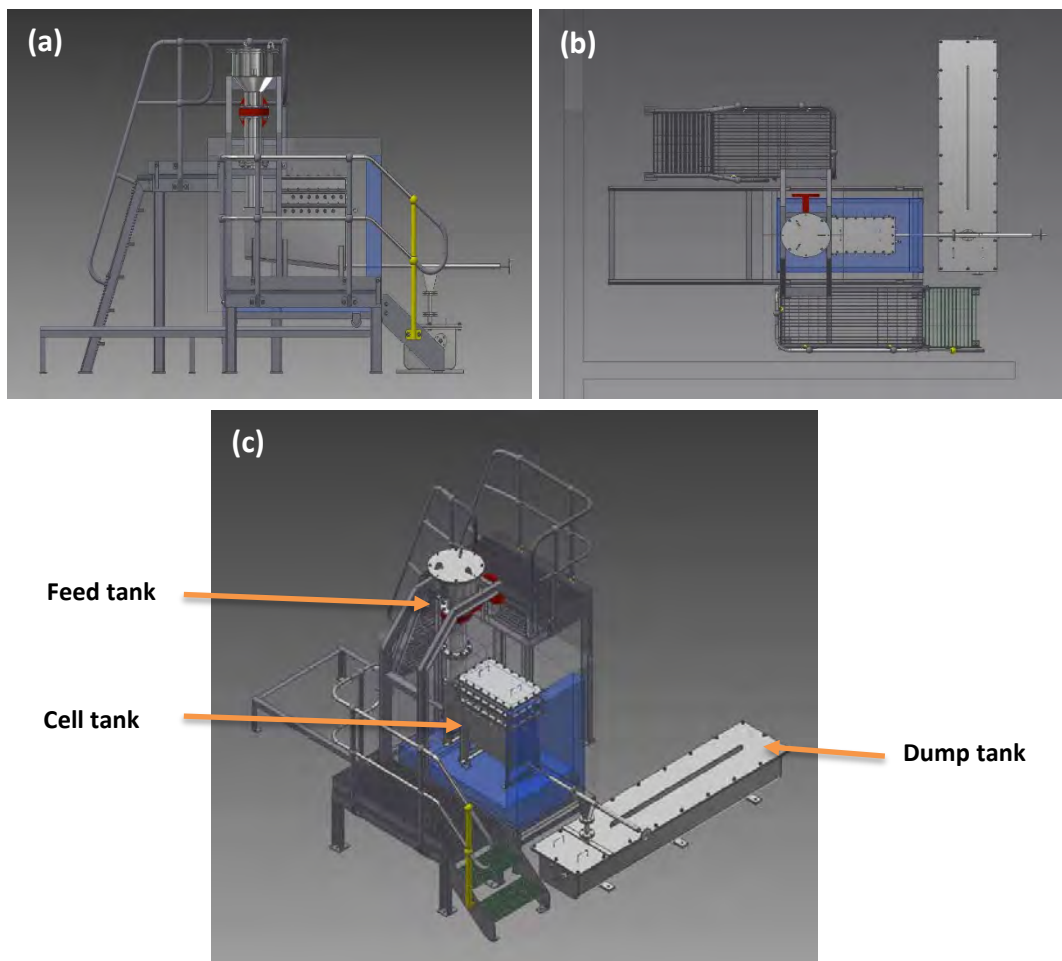
Figure 42: Model of the DCFC unit: (a) elevation, (b) plan view and (c) isometric view.

Cell Design

Fig. 43 shows the isometric views of the cell tank. In this cell, there were 28 YSZ tubes held in place with sealed glands, each with an alumina tube. Air was fed to the cathode through an inlet socket where it enters the upper plenum (D), which is a large section where the air flows into the cell through hollow alumina tubes. The alumina tubes were placed inside of the YSZ tubes with sealed base, which directs the flow of air. The air flows through the inner alumina tubes and then back up the inside of the YSZ tube allowing for the oxygen reduction reaction. The oxygen depleted air enters plenum (C), leaving the system through the air outlet socket. Inside each of the YSZ tubes, silver mesh was pressed

against the inner walls, and held in place with silver paste. This silver mesh acts as the cathode current collector. The current was carried out of the cell using copper bus-bars to a programmable load. A sparger (placed below the YSZ tubes) was supplied with CO_2 allowing for agitation of the slurry in the anode chamber to improve reaction kinetics. The sparger gas was preheated to 800°C through the use of a heater prior to entering the cell.

c	24	M10 HEX. NUT & FLAT WASHER
b	22	M10 x 30 LG HEX. HD. SET SCREW c/w HEX. NUT & 2 x FLAT WASHERS
a	20	M10 x 40 LG HEX. HD. BOLT c/w HEX. NUT & 2 x FLAT WASHERS
M	3	GASKET
L	14	ANODE BUSBAR
K	14	CATHODE BUSBAR
J	28	VERTICAL CERAMIC TUBES
H	1	SPARGER TUBE
G	2	BUSBAR SUPPORT RAIL
F	1	TUBE SUPPORT MESH
E	1	COVER PLATE
D	1	PLENNUM 2
C	1	PLENNUM 1
B	1	FUEL CELL
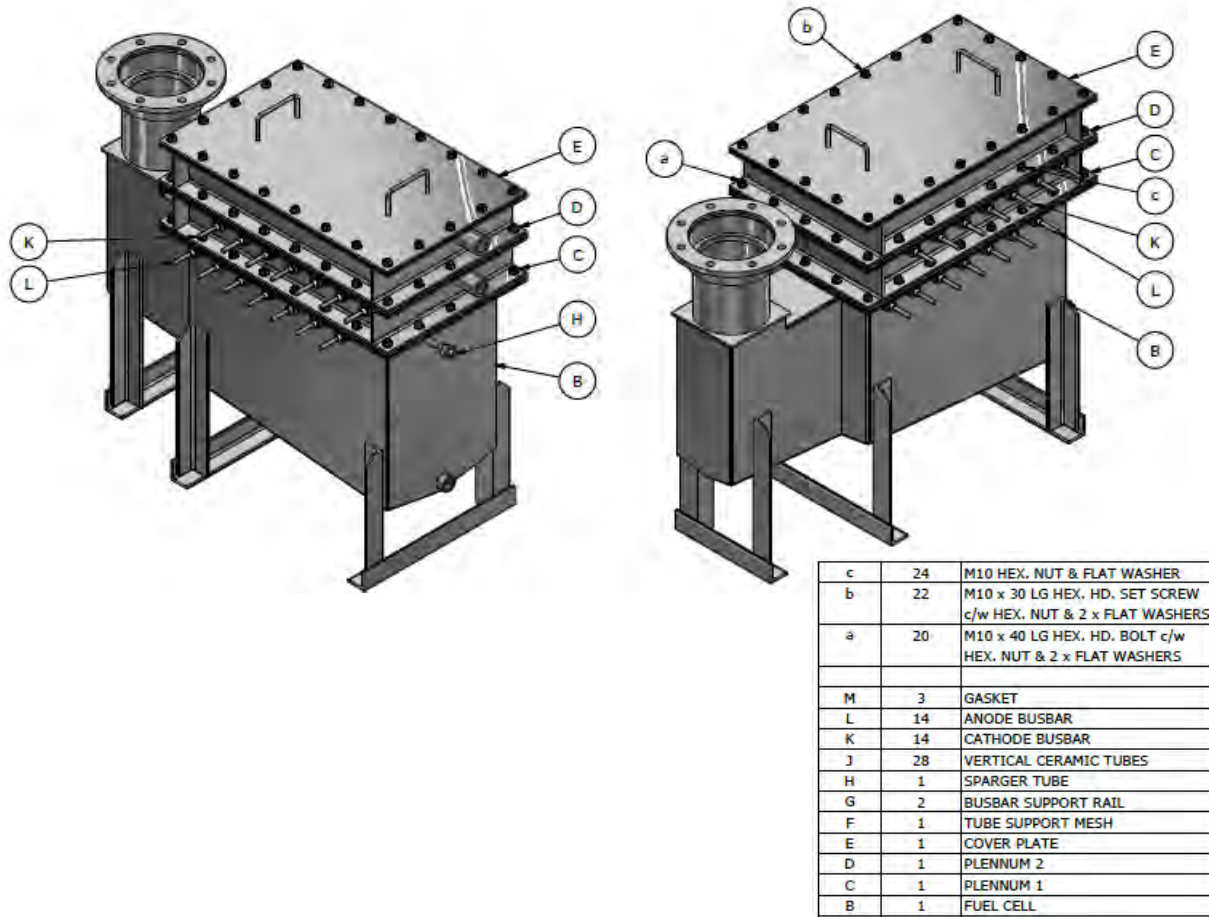
Figure 43: Isometric views of the cell, including two plenums and charging vessel.

The completed detailed cell design work includes:

- Fuel cell body and YSZ tubes arrangement

- Glands for securing the YSZ tubes to the plenum lids

- Plenums for hot air entry and exit

- Frames to secure the anode current collectors (silver mesh)

- Bus-bars for anode and cathode current collection and support structures for busbars

- Level sensors (silver wire) to monitor the slurry level in the cell tank

- Feed tank and knife gate valve separating the cell tank

- Sparger tube for mixing the slurry using nitrogen gas

- Dump tank for coal-lean carbonate and provision for cooling using air flow

The HAZOP/Risk Assessment of the final design and safe operating procedures has been completed.

Furnace Design

The general arrangement of the furnace system for the fuel cell tank and pre-heating gases is shown in Fig. 44. The major components in the furnace system include:

- Main body furnace (Internal size: 1350mm (W) x 1020mm (H) x 850mm (D); External size: 2000mm (W) x 1600mm (H) x 1200mm (D)) - bogie body concept, on wheel and rail system with a labyrinth seal; kanthal spiral wound elements for heating; over temperature control circuit; lifting lugs attached to body.

- Hot air/gas heating furnaces - two long ceramic tube furnaces (Ø52mm x 700mm) with embedded elements and dedicated control system to heat up to 850°C.

- Outlet Hot Valve System Dump tank heating- will house the Ø52mm x 700mm long ceramic tube furnace with embedded elements and dedicated control system to heat up to 500°C.

- Temperature Controllers with digital display and set values and auto tune function of PID parameters will be mounted inside the control box.

- Junction box - is fitted to the stationary wall of the furnace, this box houses the switch gear and controllers for the three tube furnaces, and has a flexible power cable.
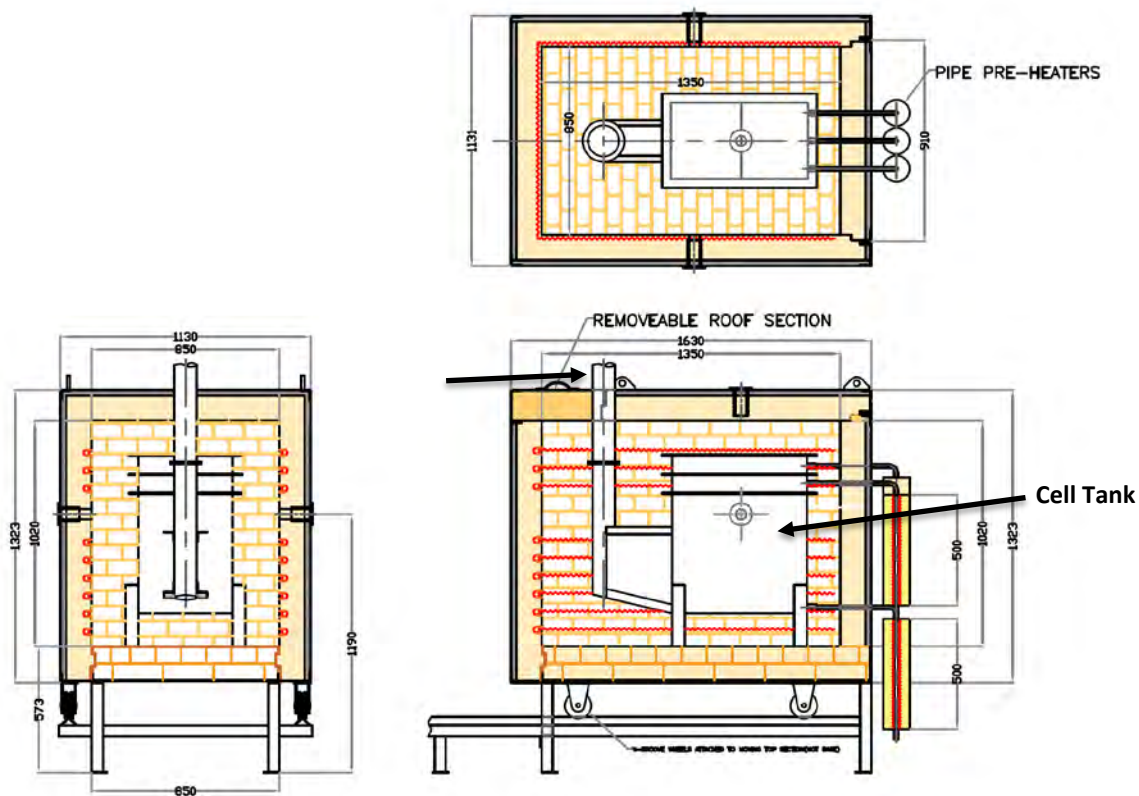
Figure 44: General arrangement of the furnace for fuel cell tank and pre-heating gases.

Instrumentation Design

The process and instrumentation diagram (P&ID) was also completed. The required valves, pressure gauges, flow meters and level sensors were implemented. The design and construction of the digital control system was based on the internal block diagram shown in Fig. 45. The main tasks included:

- Detailed system descriptions - product breakdown structure, cable connectivity diagrams and

interface requirements specification

- Configuration data – embedded computers, acquisition devices, display, network switch and display computer
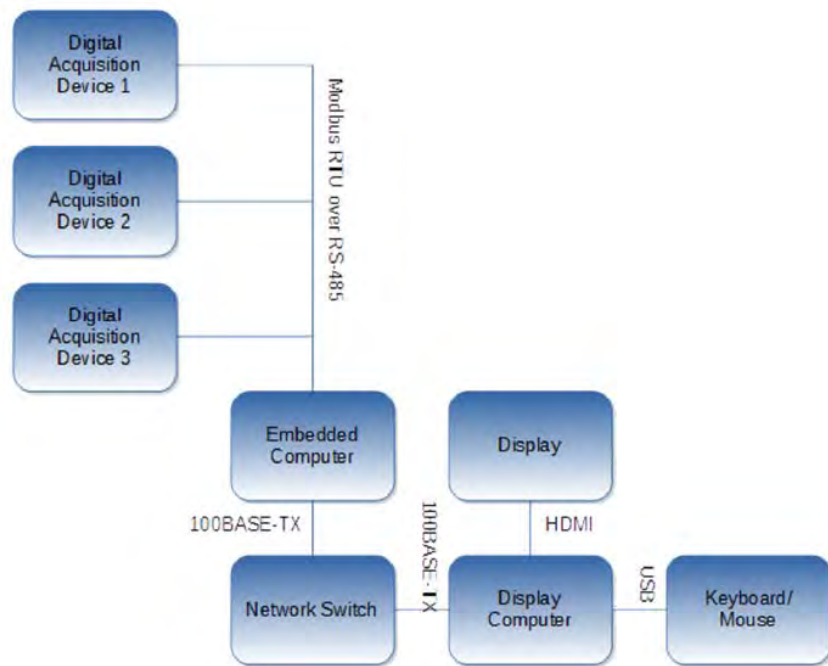
Figure 45: Internal block diagram of the digital control system.

Milestone 7: Unit Build

The fabrication of the 1 kW unit was completed on the 31 May, 2019.

Cell Fabrication:

A number of manufacturing companies for the fabrication of the cell, including the cell tank, feed tank and dump tank, were contacted. Based on quotation and lead time, MCM Manufacturing Pty Ltd was chosen for fabrication of the unit. The cell fabrication process was completed, with an indication of the required metal plates and machined parts shown in Fig. 46.

Figure 46. Metal plates and machined parts of the cell unit.

Furnace Fabrication:

Tetlow Kiln & Furnaces was contracted to design and build the furnaces. As detailed in the previous section, there will be one large furnace for heating the cell and three small furnaces for pre-heating the gases and pipe/valve leading to the dump tank. Fig. 47 shows the base metal structure of the furnace being built.

Figure 47. A photograph of the base metal structure of the furnace unit being built.

Commissioning:

Novecome Pty Ltd. provided instrumentation support including integration, installation and commissioning of the control system. For piping and installation of the unit, we used Thermaline Mechanical Services.

The process and instrumentation diagram (P&ID) was finalized (Fig. 48). Placement of the valves, pressure gauges, flow meters and level sensor were finalized. Piping and instrumentation were done by specialist contractors, who worked closely with our team on product specifications and purchasing of the ancillary components.
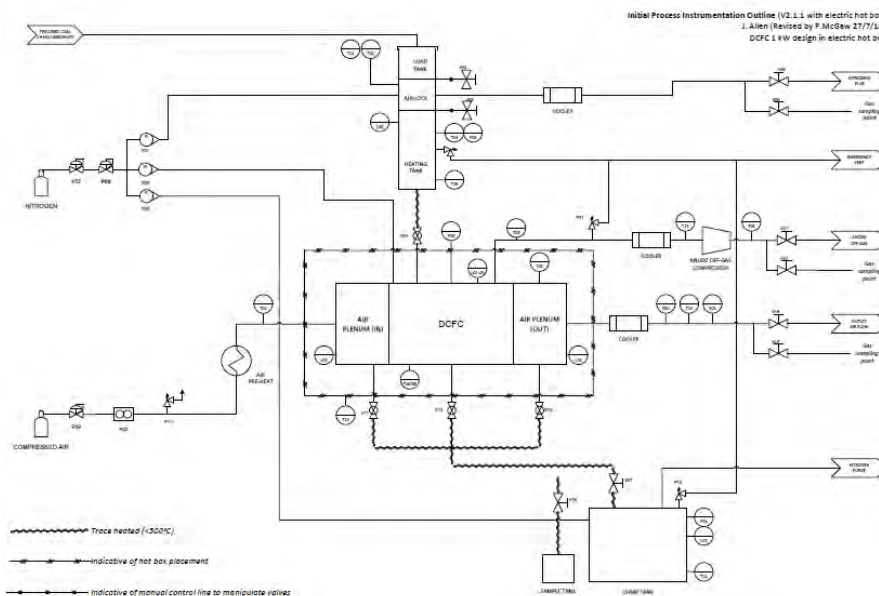
Figure 48: Process and instrumentation diagram for the 1 kW unit.

For electrical interfacing and monitoring of the system during operation, external contractors with expertise in electrical and software engineering were used. Specifically, they sourced testing equipment, developed monitoring software and designed a display feature powered by the 1 kW module. The test equipment consists of a programmable load with appropriate number of channels (27 nos.) to monitor the output of each electrode and has the capacity to handle high current operation (2000 A) (Fig. 49).

Figure 49: Photograph of a modular programmable load device.

The monitoring software compiled the readings from each of the transducers; e.g., thermocouples, mass flow controllers, rotameters and pressure sensors, into a single display screen with pre-programmed warning signals to prevent any emergency. Fig. 50 is a circuit diagram showing the connection of individual cells are connected in series to the converter, which was in turn connected to the output load (display feature).
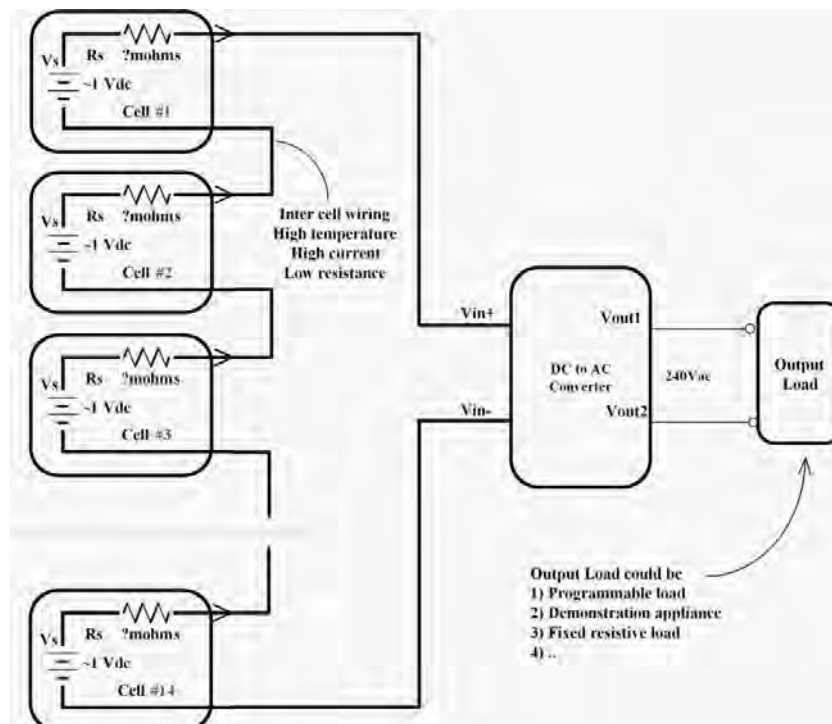
Figure 50: Circuit diagram showing the DCFC connected in series to an output load (display feature).

A sort video showing the time-lapse construction of the DCFC at the University of Newcastle is contained in Appendix 9.

Milestone 8: Unit Testing and Operation

Following construction, the 1 kW DCFC system was subjected to preliminary testing over the course of 2-3 months to examine various aspects of its performance. The following aspects of system behaviour were examined:

Safety

Prior to operation of any aspect of the DCFC a thorough safety analysis was conducted to minimize any risks associated with system operation. This included the system itself, as well as the room in which the DCFC was located.

The most serious features of the system that required special attention were:

(i)   Gas generation – In this case substantial ventilation was included with construction to ensure any build-up of gases such as CO_2 could be avoided.

(ii)   High temperatures – This is of course most relevant to the furnace in which the DCFC is located, in which case external insulation is sufficient to minimize risks associated with contacting the furnace during operation. Nevertheless, sufficient barriers are in place to prevent inadvertent contact with the external furnace surfaces.

(iii)   High currents – Electrical outputs from the DCFC include large currents. Great lengths were taken to ensure that all cables were shielded and cooled to prevent electrical hazards.

The objective of this testing was to firstly ensure safe operation of the system. Following this, each of the individual components within the system were evaluated to determine their function. This included the feed tank, furnace and thermal stability, cell leakage and emptying of the DCFC while at temperature. Procedures were developed for the safe operation of these components before commencement of electrochemical testing. Certainly, considerable electrochemical testing on individual cells had been conducted previously, so the majority of the initial system testing was focused on ancillary components.

Electrochemical testing on the 1 kW system began with measuring the stability of the open circuit voltage. A stable open circuit voltage has many implications, most of which revolve around the establishment of good contacts within the cell. This includes electrical and ionic contact between the current collector, catalyst, molten carbonate electrolyte and active materials. It also indicates stability of other ancillary components within the system because their instability (e.g., corrosion) would cause changes in the measured values. Following establishment of a stable open circuit voltage a load was connected to the system to draw power. The load used was essentially a large resistance that enabled us to fix the output voltage of the DCFC and dissipate the power generated as resistive heating. The first experiment reported in this regard varied the applied cell voltage to measure the resultant current, and thus generate output system power. This enabled identification of the peak output power and its corresponding voltage. The next stage of testing involved setting the system at peak power and observe system stability. Testing under these conditions will enable assessment of system stability and long-term operation.

Temperature Stability

One of the first trials conducted with the DCFC system was temperature stability, which was conducted initially with an empty DCFC system; i.e., no electrolytes or fuel present in the system, and no gas flow. The purpose of this analysis was to highlight any thermal gradients within the DCFC, since the internal cavity of the furnace is quite large with a significant void space. Experiments in this regard were carried out over the course of 24 h, which included 3-4 h of warm up time.

In its empty state, it was noted that there was a reasonable thermal gradient (~50°C) between the expected temperature set-point and the centre of the furnace, as measured using an IR gun. This gradient was consistent irrespective of the set-point temperature (500°-800°C). This was initially a cause for concern; however, with open gas lines into and out of the furnace some degree of ventilation was apparent.

This temperature measurement experiment was repeated with pre-heated gases flowing into the cell, in which case the temperature gradient was diminished (~20°C). It was also repeated with a load of molten carbonate eutectic in the DCFC, and in this case, the thermal gradient was minimal. Clearly, the heat capacity of the pre-heated gases, as well as the electrolyte serve to minimize any thermal gradients.

Dump Tank

Operation of the dump tank for draining the DCFC was important to examine since without its reliable operation the prototype DCFC we have developed would be prohibitively difficult to maintain. The dump tank was designed such that when molten, the electrolyte and fuel can be drained out of the DCFC under an inert atmosphere into a container where it can cool and solidify for later recycling. The inert atmosphere is important here because of the need to prevent the high temperature fuel and electrolyte composite coming into contact with air, in which case the fuel would burn. For the times we have used the dump tank this procedure worked well enabling safe removal of the molten electrolyte.

For the limited number of times this procedure was used it was noted that the knife valve on the bottom of the DCFC above the dump tank was getting more difficult to open which was not surprising given the corrosive nature of the high temperature molten carbonate. This has been identified as an area for future development.

Open Circuit Voltage

The first electrochemical experiment conducted on the DCFC was the measurement of open circuit voltage (OCV) over time. For this a ternary carbonate eutectic was used, together with our bulk coal sample that had been pre-pyrolyzed at 600°C. The cathodes for cell operation were prepared as described previously; i.e., Ag mesh lining the inner surface of the closed-end 8YSZ tubes. In this case, only four of the possible 28 tubes were used in the DCFC. Experiment temperature was also 600°C. Figure 51 shows the system OCV as a function of time over the course of ~24 h.
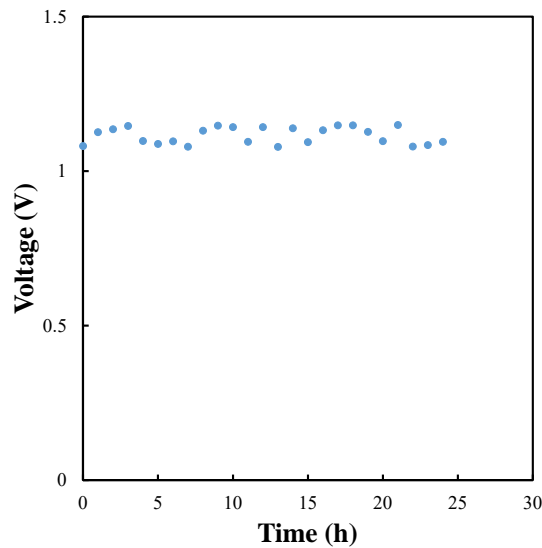
Figure 51. OCV for the DCFC at 600°C.

This result is indicative of a mean DCFC OCV of 1.11 V that is stable over the course of the experiment. The slight fluctuation in OCV is believed to be due to the movement of coal particles within the molten carbon electrolyte. It is also indicative of reliable electrical connections within the cell.

Performance

Using the same electrode design and experimental conditions as above, including the use of only four electrodes, an electrochemical performance experiment was conducted using the programmable electronic loads. The intent here is to demonstrate the performance of the DCFC with an artificial load attached rather than to use the system to provide power for something at the University of Newcastle. As such, the electronic load just dissipates the electrochemical response as heat. The protocol used here was that after the system reached operating temperature (600°C), the voltage of the DCFC was controlled in a step-wise fashion from the open circuit voltage (1.1 V) down to 0.1 V with a 3 hour residence time at each voltage to establish stability. The output of this experiment is shown in Figure 52. In terms of specific performance metrics this corresponds to a power density of ~130 mW/cm^2, comparable to the power density achievable in laboratory based experiments. Furthermore, extrapolating this to full cell operation equates to ~970 W. Both of these measurements indicate success in this project.
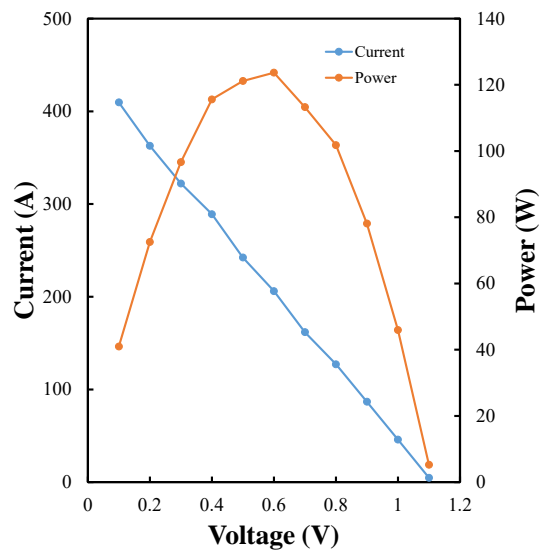
Figure 52. Performance output of the DCFC.

This same experiment was repeated with the intention now of having the DCFC operate at peak power (0.5 V) for an extended period of time. Thus, after draining the DCFC and recharging, the experiment was repeated with 0.5 V applied through the electronic load. This was maintained for three days, with the results shown in Figure 53. This corresponds to a system power output of 118 W. Furthermore, there is no evidence of current decay with time indicating a stable output with gas formation in the anode suspension enabling sufficient mixing, and that coal loading within the cell is not yet limiting.
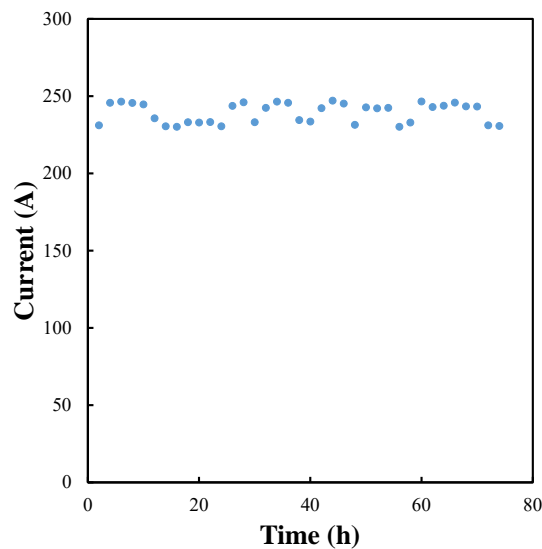
Figure 53. Measured current as a function of time.

As a final experiment, this DCFC composition was examined in a full cell configuration. That is, a full complement of 28 closed 8YSZ tubes at 600°C with 25% coal loading in the anode. This system was run for slightly longer than two days with the behaviour as expected based on Figure 53. In this case, the output current was 1890 A equating to an output power at 0.5 V of 945 W. The rate of consumption of fuel in this experiment was substantial leading to some concentration polarization within the cell. Unfortunately, the gravity fed fuel supply used in this prototype was not optimal, and is a point of future development with the system. Electrically and electrochemically the system

performed as expected without any restrictions. Fuel supply was the issue preventing ongoing longer term testing, together with the need to evaluate a range of other system aspects.

Samples of the flue gas from the system were taken and analyzed using GC-MS to determine if any CO was present as a result of Boudouard gasification. No trace of CO was found in the flue gas.

<u>Final Comments</u>

The testing regime employed here represents the initial round of testing to demonstrate the function of the 1 kW DCFC demonstration plant. Operation of individual components was carried out initially to ensure their function. Testing was then conducted to examine the stability of the system at rest, with no load applied. This led to examination of temperature stability within the system, as well as open circuit potential stability, both of which were achieved. Both of these characteristics were measured over the course of a day and found to be stable. Operation of the 1 kW DCFC was then carried out over the course of 3 days during which time the system functioned as planned.

Initially, the plan was to conduct longer term testing over the course of 10 days or more; however, this did not eventuate due to time limitations. Nevertheless, the stability of the testing conducted did suggest that system operation could be continued without appreciable variation. Certainly, future testing and development of this system will involve such longer terms tests, as well as increasing the power output.

Milestone 9: Commercial Module Development

The DCFC system as developed, constructed and presented represents the largest operating system in the world. Nevertheless, it is still a prototype system, with inherent flexibility for modifications. After the experience of going through the design, construction and operation of the system there are a number of aspects of the overall system that need attention before commercialization. Much was developed concerning the operation of this large-scale prototype unit. At present, this is the first such system in the world, developed primarily from in-house research. Prototype systems are an essential intermediate stage in further development and commercialization because they provide a platform for further system refinements, particularly in terms of overall system efficiency and componentry. The next stage of development is to build on the findings, performance and efficiency of the prototype to develop ultimately a commercialization-ready system. This will involve considerable effort towards modularization of the DCFC technology, concurrent with the further refinement to improve performance and efficiency. This can only be accomplished through further research and development focused on these aspects of the system. Specifically, this will involve a focus on:

(i) Mass and energy balance – this is the key tool in determining system efficiency;

(ii) Modularization of the DCFC system;

(iii) Anode performance and fuel delivery – this is the key energy providing material within the DCFC and so the nature of the fuel used, together with its introduction will be an ongoing critical component;

(iii) Material requirements for long term operation – understanding how the DCFC operates over even longer timeframes is key to commercialization;

(iv) System maintenance, recycling and recovery – essentially the best practice for using the DCFC under real conditions.

Other system components requiring optimization include:

<u>Heating System</u>

For the DCFC to function it requires an elevated temperature so as to maintain a molten alkali metal carbonate eutectic electrolyte, drive fast transport properties, and enable facile electrochemical kinetics. In the present prototype system, this is achieved via a large volume furnace in which the DCFC system is positioned. This choice was deliberate so that modifications could be made and not restrict system testing. However, what this does mean is that considerable excess heat is required to maintain operating temperature, including the void space in the furnace.

In a commercial system, one that is optimized in terms of construction and operation, void space within the system will be minimized, and together with improved insulation, the energy required to maintain system temperature will be minimized.

Electrode Arrangement

In the present DCFC system the arrangement of electrodes is such that there is effectively one cell under consideration with all current being derived from that cell. While this has been successful in demonstrating the operation of the DCFC system, further development can be carried out in this regard to optimize power output. The focus in this case will be on the series and parallel arrangement of individual cells to optimize voltage and current output, all the while maintaining suitable fuel flow to individual cells.

Fuel Input

The DCFC developed in this work uses a hopper system in which the fuel is gravity fed into the DCFC. This aspect of the system worked perfectly well for the experiments conducted but for ongoing longer life testing a continuous automated fuel introduction system will be necessary.

Milestone 10: Life Cycle Analysis and Techno-Economic Assessment

A thorough theoretical mass and energy balance of DCFC operation was conducted as part of Milestone 1. With further refinements to the operation of the DCFC this can be continued to be optimized. Part of that involved consideration of the life cycle analysis, which has been updated based on the outputs of the present study.

For any energy generation system it is necessary to conduct a life cycle analysis of the complete process to effectively account for all inputs and outputs. Of course, the focus is largely on the quantity of emissions per unit of energy produced; however, a detailed life cycle analysis can also be used as a tool to measure system efficiency and highlight aspect of the overall process that require attention.

The traditional approach to energy generation is through a coal-fired power station (CFPS). In the CFPS the chemical energy stored in coal undergoes a number of energy transformations, leading ultimately to electrical energy leaving the plant. Each of these energy transformations has an associated inefficiency, and so a CFPS typically produces electrical energy with 35-40% efficiency. While this represents a very inefficient way to produce energy, the abundance of coal in Australia and around the world has meant that this has been the preferred approach to energy generation since the Industrial Revolution in the early 1800's.

As a source of energy, coal is a limited resource. The majority of global coal reserves were deposited during the Carboniferous geological period (359-299 million years ago; 60 million years duration). Global consumption of coal by humans began in earnest during the Industrial Revolution, and at this stage, estimates are that all this coal will be consumed within ~500 years. This rate of consumption, with a rate of coal generation compared to rate of coal usage of ~1.2×10^5 times, guarantees that coal is a limited resource.

At present rates of coal consumption it is estimated that there is somewhere between 100-150 years of coal remaining. During this time, it is expected that other forms of energy production will be developed and implemented on the global scale. In the interim, the efficiency of coal utilization needs to be improved, as does a reduction in emissions from the use of coal. A possible approach is to improve the efficiency of CFPSs; however, these will always be limited by thermodynamic efficiencies, which are intrinsically low. Another alternative, which is the focus of this research, is the direct carbon fuel cell.

The direct carbon fuel cell (DCFC) is a fuel cell technology employing the direct electrochemical oxidation of coal (carbon) to produce electrical energy. In the DCFC there is only one energy transformation process employed; namely the electrochemical conversion of the chemical energy in coal to electrical energy, and as such the DCFC is often referred to as being an efficient means of direct energy production. The overall reaction involved in the DCFC is the same as in a CFPS; i.e.,

$$C + O_2 \rightarrow CO_2$$

except in the case of the DCFC this is broken down into two electrochemical half reactions; i.e.,

$$C + 2O^{2-} \rightarrow CO_2 + 4e^- \text{ (anodic process)}$$

$$O_2 + 4e^- \rightarrow 2O^{2-} \text{ (cathodic process)}$$

where the oxide anion (O^{2-}) is the ionic charge carrier. Each of these half reactions is carried out in separate compartments of the fuel cell, as shown schematically in Fig. 54. Separating the compartments is an ionically conducting medium, or electrolyte. In Fig.54 this is a combination of a solid oxide ion conductor; e.g., yttria stabilized zirconia (YSZ), and a molten mixture of Li_2CO_3, Na_2CO_3 and K_2CO_3. The solid YSZ physically separates the two compartments, while still allowing for ionic transport, while the molten carbonate media essentially acts as a carrier for oxide anions to facilitate their ready access to the carbon surface.
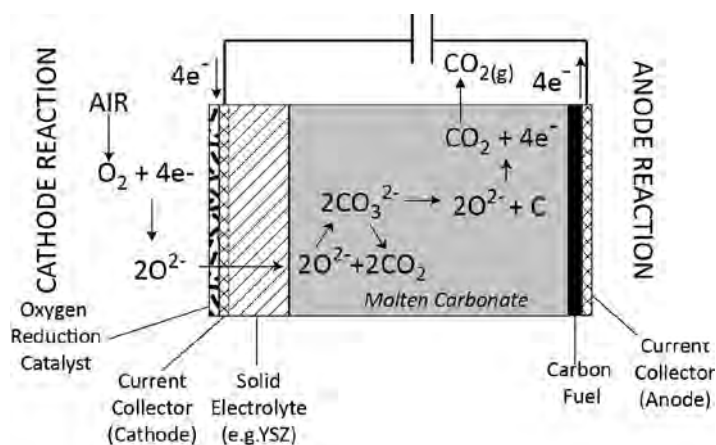
Figure 54. Schematic of the direct carbon fuel cell.

The efficiency of a fuel cell system such as the DCFC is assessed electrochemically, and revolves around how much of the chemical energy in the fuel is converted into electrical energy. Therefore, for the overall reaction we can define a reaction enthalpy ($\Delta_r H$) corresponding to the amount of chemical energy present in the fuel (carbon). Likewise, for the electrochemical oxidation of carbon we can define a reaction Gibbs energy ($\Delta_r G$) which in ideal terms corresponds to the maximum amount of electrical work the reaction can do, or in practical terms the amount of electrical work actually done by the system. The efficiency (η) is then defined as

$$\eta = \frac{\Delta_r G}{\Delta_r H} = \frac{\Delta_r H - T\Delta_r S}{\Delta_r H} = 1 - \frac{T\Delta_r S}{\Delta_r H}$$

where $\Delta_r S$ is the entropy change on reaction. For the oxidation of carbon the reaction entropy is always close to zero, and as such the theoretical efficiency of the DCFC will be close to unity. For example, the standard entropy of formation for graphite (carbon source), oxygen and carbon dioxide (at 298.15 K and 1 atm pressure) are 6,205 and 214 J/K/mol, respectively. Therefore, $\Delta_r S$ for Eqn (1) is 3 J/K/mol. Under the same conditions, the enthalpies of formation are 0, 0 and -394 kJ/mol for graphite, oxygen and carbon dioxide, respectively, leading to an overall reaction enthalpy of -394 kJ/mol. Substitution leads to a theoretical efficiency of 1.002, or just over 100% efficient. Of course, this can vary depending on the heat content of coal compared to graphite, as well as in terms of the entropy of formation of coal relative to graphite. Nevertheless, the calculation shows that high efficiencies are expected, much greater than a CFPS. In practice the amount of electrical work extracted from the DCFC is limited by overpotentials associated with the individual redox half reactions. Literature has reported efficiencies in the range of 80%, and we have also reported similar efficiencies.

Comparative Life Cycle Analysis

For the purposes of the life cycle analysis we will be carrying out a comparative analysis between the DCFC and a CFPS. This is considered to be the most straightforward approach, essentially allowing for a direct comparison between the technologies. Furthermore, it also makes sense to use such an approach since many features of both technologies are common, as highlighted in the block diagram in Fig. 55.
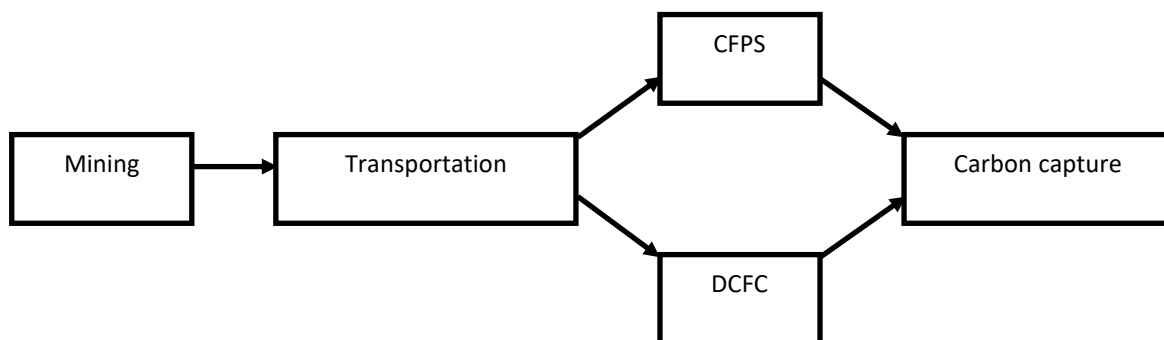
Figure 55. Block diagram of the alternative energy generation systems.

As can be seen, common aspects of energy generation include mining, transportation and ultimately sequestration.

Coal Mining

Of course, coal mining is essential for operation of both a CFPS and the DCFC. For a CFPS thermal coal is used, while for the DCFC there is no particular differentiation in place presently to assign a specific coal type for DCFC usage. In fact, most of the experimental work conducted thus far with the DCFC has been with the use of a thermal coal, with only selected experiments conducted with a metallurgical coal. As such, at this time we will assume that the process for mining coal will be the same irrespective of the end use application of the coal; i.e., a CFPS or DCFC.

Transportation

Transportation of the coal from the mine to its end application is also a critical aspect of the LCA. Thermal coal usage for a CFPS will involve transportation of the coal primarily from the mine to either a port for exportation or directly to the CFPS. Certainly, export coal (via ship) will require additional energy inputs to travel the longer distances. Transportation costs and energy consumption to use coal in the DCFC has the potential to be very similar to the CFPS particularly if the DCFC system used is a large centralized energy generation facility, like a CFPS. However, if the DCFC system used is much smaller, perhaps on the community scale, then there will be a need for additional transportation infrastructure to distribute the coal more broadly to the smaller scale systems.

Carbon dioxide Capture

For a CFPS, post-combustion capture of carbon dioxide emissions is a viable alternative for emissions reduction. The flue gas coming from a CFPS is composed primarily of nitrogen, and carbon dioxide resulting from coal combustion. However, there are other gaseous (SO_x and NO_x gases) and particulate species present that must be removed first before separation of the carbon dioxide from nitrogen can occur. These two separation processes incur a significant energy penalty. For the DCFC the situation is quite different. In the absence of a combustion process where air is required, there will only be carbon dioxide produced, with no NO_x gases generated, and minimal SO_x gases. Furthermore, there will be no particulates produced, instead these will be contained within the molten carbonate electrolyte used in the DCFC.

LCA Points for Consideration

Throughout this LCA we will endeavour to make as fair a comparison as possible between the emissions and energy outputs coming from both CFPS and DCFC systems. It is important to specify what will be considered in the analysis. Here we will try and focus on as many aspects of the systems as possible, but one aspect that will not be examined is the energy consumption and emissions coming from the construction of both the CFPS and DCFC systems. At least for the DCFC system this is a very large unknown, particularly on the large scale, and so we have chosen to ignore it at this stage. Similarly, the energy consumption and emissions resulting from the construction of mining equipment and transportation infrastructure used in the operation of the CFPS or DCFC systems will not be considered.

Base Case – Coal Fired Power Station (CFPS)

The base case for LCA comparison is the CFPS, the energy inputs and emissions from which can be summarized in Table 4. This data was sourced from a Worley Parsons publication, and relates to the energy inputs and outputs, materials usage and emissions arising from the extraction and processing of 10 Mt of black coal per year.

Table 4. Base case energy and material inputs and emissions arising from the mining, transportation and use of 10 Mt per annum black coal.

Base Case	Energy and Material Input		GHG Outputs	
10 Mt pa Production	**Sources**	**Quantities**	**Source**	**tCO₂-E pa**
Coal Mining	Diesel use	42,600 kL (1.7 PJ)	Diesel	115,000
	Use of grid power	174,800 MWh (0.63 PJ)	Grid power	180,000
			Explosives	2,500
	Explosives	14,700 t	Fugitives	375,200
			Slow combustion	18,500
	Other materials	n/a	Slow oxidation	1,800
Transportation	Diesel use	7600 kL (0.3 PJ)	Diesel	20,500
Energy Generation	Coal use	270 PJ	Combustion	23,880,000
Total Energy Consumption		**272.63 PJ**	**Total Emissions**	**24,593,500**

Based on the data in Table 4 we are now in the position of being able to calculate the total emissions resulting from the production of electrical energy. So for a total of 270×10^{15} J of input energy from coal, and assuming a CFPS efficiency of 35%, the total electrical energy output is therefore 94.5×10^{15} J, or 26.25×10^{6} MWh. With total emissions arising from this energy production amounting to 24,593,500 tCO₂-e per year, the emissions efficiency equates to <u>0.9369 tCO₂-e/MWh</u>.

DCFC Specific Features

To assess the emissions efficiency of the DCFC we have to examine the features of the system that are specific to the DCFC. To do that we will begin with a naïve interpretation of the DCFC system, and work from there incorporating more of the complexities of the DCFC system, essentially outcomes from the fundamental studies we have conducted.

Naïve Interpretation

As a first assessment of the emissions efficiency of the DCFC we can take the total energy input from the coal (270×10^{15} J), with the theoretical efficiency of DCFC operation (100%), with the same emissions, and determine an emissions efficiency of <u>0.3279 tCO₂-e/MWh</u>. This is best considered as the optimum emissions efficiency, representing ~35% of the emissions from a CFPS.

Increased Transportation Network

A point made previously was that the transportation network for the DCFC may need to be larger depending on the size of the DCFC system. Certainly, if a single DCFC system was sufficiently large enough to cope with the 10 Mt per annum of coal used in the base case in Table 4, then the

transportation network would be the same in both cases. However, if the operational DCFC systems were smaller and more distributed in nature, then a greater transportation network would be needed. Concomitant with that are greater emissions from transportation. For the purposes of this LCA we will presume that the diesel consumption will double to accommodate this need for an increased distribution network; i.e., 15,200 kL, amounting to emissions of 41,000 tCO_2-e per annum. This brings the total emissions to 24,614,000 tCO_2-e per annum, and again assuming a 100% efficiency for DCFC operation, the emissions efficiency increases slightly to <u>0.3282 tCO_2-e/MWh</u>.

DCFC Efficiency

Previously it was naively assumed that the DCFC operates at its optimum efficiency. In practice this is not the case, with reported experimental efficiencies being closer to 80%. This is consistent with the efficiencies determined as part of this project. Under these circumstances the total input energy from the coal (270×10^{15} J) transforms into 216×10^{15} J of electrical energy, or 60×10^6 MWh. Assuming again the emissions from the expanded transportation network, the emissions efficiency becomes <u>0.4102 tCO_2-e/MWh</u>, which is still only 43.8% of the emissions from a comparable CFPS.

Coal Pre-Pyrolysis

As an outcome of the fundamental studies we have conducted it was determined to be necessary to pre-pyrolyze the coal prior to use to remove volatiles that would otherwise adversely affect the operation of the DCFC. To examine the energy requirements necessary to do this we have assumed that the coal will be heated from ambient temperature (25°C) to 700°C, a temperature difference of 675 K. We have also assumed a heat capacity for coal of 1.38 kJ/K/kg. So, for the total amount of coal used on an annual basis (10×10^6 t), the energy input required is 9.315×10^{12} kJ, with a thermal efficiency of 100%. More realistically with a heating efficiency of say 80%, the required energy input is 11.64×10^{12} kJ. This energy input equates to 3.234×10^6 MWh, which when comes from a CFPS with an efficiency of 35%, equates to an additional 3.030×10^6 tCO_2-e per annum, bringing the total emissions to 27,644,000 tCO_2-e per annum. Combining the reduced efficiency of the DCFC (80%) and expanded transportation network leads to an emissions efficiency of <u>0.4607 tCO_2-e/MWh</u>, which is 49.2% of the emissions from a comparable CFPS.

The volatile species arising from the pre-pyrolysis of the coal can also be used as a source of energy rather than just being considered as emissions. The volatiles given off are essentially mid-range chain length hydrocarbons, which can be combusted directly to produce heat and steam for a mini-turbine. In the absence of knowing the thermal content of these volatiles, which will be specific to the type of coal used in the DCFC, it is not possible to calculate with any certainty the energy available here. As an estimate, if we assume that 2% of the coal is lost as volatiles, then the quantity lost is ~0.2 Mt per annum. Again, now assuming an average alkane chain length of C10, the energy available from these volatiles is ~9×10^{15} J, which is available for recovery.

Heating of the DCFC

The DCFC is a high temperature fuel cell and so energy has to be added to maintain operating temperature. For the sake of this LCA analysis we will assume that the operating temperature of the DCFC is 700°C, in line with the pre-pyrolysis temperature of the coal. This is not a random temperature. Fundamental experimentation we have conducted has shown that 700°C is sufficiently high a temperature to ensure fast anodic and cathodic kinetics, but not too high a temperature to facilitate Boudouard gasification of the coal; i.e., chemical corrosion of coal.

Under these conditions, the main component that requires heat to remain at this temperature is the molten carbonate electrolyte. We have assumed here that the coal entering the DCFC still remains at

the pre-pyrolysis temperature, and thus does not require additional heating. At this time, it is unknown with any certainty how much of the electrolyte will be required to operate the DCFC under such large scale conditions. It is a component of the DCFC that is not consumed, and so what we have assumed for the LCA is that the amount of molten carbonate electrolyte required is 20% of the total amount of coal used; i.e., 10 Mt of coal are used annually, suggesting the use of 2 Mt of the molten carbonate electrolyte. The heat capacity of the molten carbonate electrolyte is quoted in the literature (Trans. Faraday Soc., 1963, 59, 841-845) as being 168.9 J/K/mol or 1.687 kJ/K/kg. Therefore, for 2×10^9 kg of electrolyte the heat input required is 2.277×10^{12} kJ. At 80% thermal efficiency this is an energy input of 2.847×10^{12} kJ. This energy input equates to 0.791×10^6 MWh. When this energy comes from a 35% efficient CFPS, it adds a further 0.741×10^6 tCO_2-e per annum, leading to total emissions of 28,384,900 tCO_2-e per annum. This leads to an emissions efficiency of <u>0.4731 tCO_2-e/MWh</u>, which is 50.5% of the emissions from a comparable CFPS.

DCFC Inefficiency

As discussed previously the DCFC is a high efficiency process. With a working efficiency of 80% the power output from coal is far superior to that coming from a CFPS. While this working efficiency is high, the inefficiency can also contribute to the operation of the DCFC. For an input energy of 270×10^{15} J, and with an 80% electrochemical efficiency, this leads to an output of 216×10^{15} J, or 60×10^6 MWh. The inefficiencies in the process (54×10^{15} J) are associated with electrochemical overpotentials for the anodic and cathodic processes and resistances in the DCFC. This energy is not lost from the DCFC, but is instead evident as heat contributions to the DCFC, in effect contributing to the ongoing heating of the DCFC. If this is indeed the case, then the thermal energy arising from the inefficiencies in the DCFC are considerably larger than that required to heat the molten carbonate electrolyte in the cell; i.e., 2.847×10^{15} J, or only 5.3% of the energy lost due to inefficiencies in coal utilization. Therefore, even assuming poor thermal insulation within the DCFC, the emissions arising from heating the DCFC can be negated, and potentially even those arising from pre-pyrolysis of the coal.

Waste Gas Stream

The carbon dioxide emissions arising from the DCFC also carry a considerable amount of energy tied up with the heat capacity of the gas. This can also be used as a means of energy recovery before release. If we consider the base case in terms of carbon dioxide emissions (24,593,500 tCO_2-e per year), then with a heat capacity of 37 J/K/mol, the amount of energy available for capture associated with the carbon dioxide stream is (assuming a temperature drop from 700°C to 25°C) 13.96×10^{15} J. This energy can be used for heating the DCFC, or even direct energy generation. Whatever the application, the use of the heat associated with this waste carbon dioxide stream will diminish the external energy requirements even further.

Carbon dioxide Capture

Capture of the carbon dioxide waste stream is expected to be more energy efficient for the DCFC compared to a CFPS. The main reason for this is that no post combustion separation of the carbon dioxide is required for the DCFC. If we assume the energy penalty for carbon capture is 13% for a CFPS, based on the energy output, this adds an additional energy requirement of 12.29×10^{15} J and emissions of 3,197,155 tCO_2-e per annum. This ultimately leads to total emissions of 27,790,655 tCO_2-e per annum, and an emissions efficiency of <u>1.0587 tCO_2-e/MWh</u>.

For the DCFC where no post-combustion separation is necessary, much less energy is required to capture and compress the essentially pure carbon dioxide stream coming from DCFC usage. To assess

the energy requirement for compression, we have assumed an energy penalty of 2% based on the total output energy. This requires an input energy of 4.32×10^{15} J, which corresponds to emissions of 567,698 tCO_2-e per annum. This brings the total emissions from the DCFC to 28,952,598 t-CO_2-e per annum, and registers an emissions efficiency of 0.4825 tCO_2-e/MWh, which is 45.6% of the CFPS with a similar sequestration requirement.

Summary

As a result of this life cycle analysis we have shown that the DCFC is a lower emissions energy generation technology. Table 5 is a summary of the energy generated, emissions and emissions efficiency for the DCFC compared to the CFPS.

Table 5. Summary of the DCFC emissions performance.

Situation	Energy (J pa)		Emissions	
	Input	Output	tCO₂-e pa	tCO₂-e/MWh
CFPS				
Base case	270×10^{15}	94.5×10^{15}	24,593,500	0.9369
+ Carbon capture	282.3×10^{15}	94.5×10^{15}	27,790,655	1.0587
DCFC				
Naive analysis	270×10^{15}	270×10^{15}	24,593,500	0.3279
+ Increased transportation network	270.6×10^{15}	270×10^{15}	24,614,000	0.3282
+ Lower efficiency	270.6×10^{15}	216×10^{15}	24,614,000	0.4102
+ Coal pre-pyrolysis	282.2×10^{15}	216×10^{15}	27,644,000	0.4607
+ DCFC heating	285.0×10^{15}	216×10^{15}	28,384,900	0.4731
+ Carbon capture	289.3×10^{15}	216×10^{15}	28,952,598	0.4825
DCFC inefficiency	↓	216×10^{15}	↓	↓
Waste gas stream	↓	216×10^{15}	↓	↓

Techno-Economic Assessment

A techno-economic assessment of the present DCFC prototype has been conducted but is very primitive given the prototype nature of the present system. Key points in the present assessment include:

(i)   DCFC unit cost was $150000. This takes into account all costs, including materials, contract labour and initial consumables to charge the system.

(ii)   Power output was 945 W. Using a time scale of 1 year, this equates to an energy output of $8.278×10^3$ kWh or $2.980×10^{10}$ J.

Under these conditions, the cost of energy output from the DCFC is $\underline{\$18.12 \text{ per kWh}}$.

(iii)   Consumable material inputs into the DCFC operation include coal and the ternary carbonate eutectic. The cost of raw coal is estimated to be $144 per tonne with a calorific output of $24×10^6$ J/kg. Given the energy output of the DCFC ($2.980×10^{10}$ J) for one year of operation, together with the efficiency of operation of the DCFC (80%), the required input energy from coal is $3.725×10^{10}$ J, or 1552 kg of coal. The cost of coal is therefore $223.50 for one year of DCFC operation. The cost of the coal will increase because of the need for pre-pyrolysis, which we have estimated will increase the cost by 50% to $335.

(iv)   The ternary carbonate eutectic is a relatively expensive, costing $255 per kg. The question then becomes how much of the eutectic is consumed by the DCFC. While the carbonate electrolyte is not consumed by the DCFC, some is added with the coal as a feed and some is drained off to remove impurities. Estimating 10% of the mass of coal is added as electrolyte, together with its removal, this equates to an extra 155.2 kg of ternary carbonate eutectic being added, at a cost of $39627.

The added cost to the energy output equates to $\underline{\$22.95 \text{ per kWh}}$.

(v)   Additional DCFC operational costs will include system maintenance, mainly predicted to be associated with the electrodes, specifically the YSZ solid electrolyte. Their main cause of failure is due to thermal expansion and contraction. However, the use of 5% YSZ solid electrolytes, which have a greater structural integrity, as well as the ongoing nature of the DCFC operation under these circumstances, means that their replacement will be relatively infrequent. Estimating their replacement to be twice annually, for 28 electrodes in the DCFC to be fully replaced twice annually, this equals 56 new tubes. At a cost of $25 each, this leads to an added expense of $1400.

This increases the cost of energy to $\underline{\$23.11 \text{ per kWh}}$.

The costs of DCFC operation described above represent the main consumables and maintenance costs. Of course, there will be added labour costs, and processing costs associated with CO_2 capture, as well as electrolyte recycling. Estimating these is impractical at this stage.

What this assessment has indicated is that the key areas for future cost reduction are associated with longer term operation, as well as reducing the cost of the initial build.

GENERAL DISCUSSION

The direct carbon fuel cell (DCFC) presents an innovative, high efficiency low emission approach to the generation of energy from a fossil fuel such as coal. Unlike a coal-fired power station (CFPS) that involves many inefficient energy transformation steps, the DCFC involves only one; i.e., the direct transformation of the chemical energy stored in coal to electrical energy via electrochemical conversion. Electrochemical processes, such as those that occur in all fuel cell systems, are known to be highly efficient, and the DCFC is no exception, with a demonstrated ability to generate electrical energy at ~80% efficiency. Furthermore, in the absence of combustion processes, common emissions from a CFPS such as particulates and SO_x and NO_x gases are considerably reduced, if not eliminated. With these promising characteristics having been demonstrated in the research laboratory, this project set about further exploring the development of a larger scale DCFC system for evaluation. The project was broken into parallel fundamental and developmental streams, with the fundamental stream informing the choices of materials and configurations for use in the developmental stream.

Fundamental Stream

As mentioned, the fundamental stream for this project was intended to provide guidance for the development of a large prototype DCFC system. Each component of the fundamental stream was intended to address key aspects of DCFC operation.

1. Mass and Energy Balance

Central to the development of any energy supply system is an examination of process efficiency, balancing inputs and outputs to determine the overall suitability of the process. In this project we have carried out a thorough theoretical mass and energy balance for a 10 kW DCFC, itself informed by the fundamental experiments described previously.

The integrated process approach used in this modelling has allowed insight into the effect process variables have on the energy balance, including electrochemical efficiency and Boudouard corrosion, while also demonstrating insight into the heat generated internally in the process, as well as the need for external energy inputs. Electrochemical efficiency is the most important variable in determining overall system efficiency. The balance point determined, where no additional heating was needed, was seen to be 70% electrochemical efficiency, which allows generation of enough waste heat within the system to allow almost complete self-heating. This has been demonstrated on the bench scale, through careful consideration of activation, ohmic and concentration polarisation losses. Other major areas of optimisation include ensuring high cathodic oxygen conversion to avoid excessive heating in this stream, as well as limiting carbon corrosion through reverse Boudouard reaction.

2. Corrosion and Materials Investigation

For system longevity, it is important to know that all material components within the DCFC will last without a decrease in performance. In this project component, aspects of the electrode current collectors and DCFC body were examined for their corrosion resistance in the high temperature molten carbonate medium. Experimental techniques for evaluating the corrosion rates included electrochemical testing, as well as immersion testing. It could be argued the carbon corrosion is an important aspect of DCFC operation; however, this has been considered elsewhere in the project because of its direct relevance to electrochemical carbon oxidation performance.

Electrochemical experimentation was used to determine the corrosion rate of various metallic substrates to be used as anodic current collectors in the molten carbonate medium, with the requirement that the substrate be stable, as well as active towards carbon oxidation. Electrochemical

experimentation was used because of the need to examine the corrosion rates of potential substrates at various potentials within the molten carbonate medium. Furthermore, this type of testing can be considered as very aggressive, providing a maximum expected corrosion rate in the electrolyte environment. In this case, silver and nickel were identified as being the most corrosion resistance, with corrosion rates of 0.0245 and 0.0142 m/y per year. Silver has also been identified as being sufficiently catalytically active for use as the anode substrate. Thus, it was adopted for use.

In terms of the body of the DCFC, the focus was on identifying a corrosion resistant steel. Two steel materials were chosen for examination; namely, 235MA which was reported to have better corrosion resistance at high temperatures, compared to 316L which is a lower cost option. To evaluate the corrosion resistance of these steel samples, immersion tests were carried out rather than electrochemical testing because the steel of the DCFC body was not going to be polarized at any stage of DCFC operation, and so its straightforward reactivity to the molten carbonate medium is of most importance. While the corrosion rate of these steel samples over the course of a 30 day test was minimal, it was recommended to coat the inside of the DCFC system with a ceramic such as zirconia to ensure long term integrity of the system.

3. Anode Formulation and Processing

The anode composition in the DCFC is a key aspect of system performance, playing a substantial role in determining the operation of the DCFC. The first stage in this section of the fundamental stream was the design of a suitable test cell. Previous designs based on a button cell (Figure 7) were prone to leakage, with a relatively low success rate in terms of generating data. As such, as closed tubular cell was developed that removed the need for sealing interfaces in the molten carbonate medium. This design proved to be very effective, enabling examination of anode variables such as the choice of current collector, molten carbonate electrolyte, gas atmosphere, coal slurry loading, and catalyst. Examination of all of these variables was focused on improving the anodic power density.

4. Cathode Optimization

While carbon oxidation in the anode is the most innovative aspect of the DCFC, oxygen reduction in the cathode is also a critical aspect of operation. Quite advantageously, oxygen reduction is the cathodic reaction in most, if not all, fuel cell systems meaning that considerable literature is available for guidance in the development of this component of the DCFC. The focus of the activities in this component of the fundamental stream was on understanding the nature of the oxygen reduction zone at the three-phase boundary between the current collector, oxygen gas and ionic conductor (YSZ).

As mentioned above, silver and nickel were identified as possible materials because of their low corrosion rates, and so each was investigated as a candidate for current collector. Ultimately, silver was identified as the most catalytically active material. In many other high temperature fuel cell systems, such as the solid oxide fuel cell system, lanthanum strontium manganate (LSM) is used as an oxygen reduction catalyst. It too was examined here, but because of the lower temperature of DCFC operation, it did not perform as well as expected.

Other variables considered in this component included air flow rate, as well as the composition and thickness of the YSZ oxide ion conductor. In the latter case, choices were available in terms of the yttria content, which had an impact on the kinetics of oxide ion transport and the mechanical integrity of the tube. While 8% yttria has been identified as the YSZ composition with the best kinetics of oxide ion conduction, it was not as mechanically sound as desired. Therefore, the choice was made to use 5% yttria in YSZ as a compromise between oxide ion conductivity and mechanical integrity.

5. Molten Carbonate Physical Properties, Recycling and Recovery

In this component considerable experimentation was conducted to examine the impact of common coal impurities on the properties of the molten carbonate electrolyte. Thermal testing methods were developed the explore the dissolution of impurities and their impact on the colligative properties of the electrolyte, in particular freezing point depression, which has an impact on the energy required to keep the electrolyte molten. The effect of these impurities was also examined in terms of their ability to gasify the carbon in a molten carbonate medium, which of course will have an impact on overall DCFC efficiency. The role of these impurities in terms of their catalytic activity towards carbon oxidation was also explored. This was carried out with kaolin (clay), alumina and silica as additives. Recovery of these impurities by electrodeposition was also carried out and found to be a viable alternative, leading to deposits rich in the impurity elements, as well as very interesting carbon deposits suitable for other applications.

Applied Stream

6. Initial Demonstration Unit Design

The first stage in the development of a large scale operational DCFC involved the development of a suitable design. This in itself involved three phases; namely, concept design, component engineering design and detailing and integration and commissioning.

The first concept for the DCFC design involved a horizontal electrode configuration passing a suspension of coal in the molten carbonate eutectic. The intent with this design was to ensure as large a possible interface between the cathode and anode, with the capacity for the oxidant (oxygen in air) to flow through the system, as well as enable ease of fuel (coal) addition to the tank. While enabling each of these aspects of the DCFC system, it did place high demands on the seal (gland) between the coal in molten carbonate suspension and the air access manifold. Considerable testing was carried out in this regard, with a range of sealants and gland designs, and while the electrochemical performance of this configuration was excellent, it was however determined that irrespective of the configuration, the reliability of the seal was not satisfactory to ensure effective long term operation. Leaking of this seal does lead to extensive corrosion, particularly when the molten carbonate electrolyte accesses the oxygen-rich environment outside of the DCFC tank. The main reasons for the leaking were the differences in thermal expansion between the YSZ and the components within the gland.

Under these circumstances, a new design was developed based on a vertically aligned electrode. In this case, leaking within the seal would only allow minor amounts of gases to intermix, thus avoiding the dependence of the seal on preventing liquid electrolyte leakage. Thus, the electrode configuration was re-designed to enable vertical gas manifolds, rather than horizontal. A significant development in this regard was the development and use of cylindrical YSZ tubes sealed at one end as the solid electrolyte. This was not a trivial development since the moulding and sintering of such a YSZ tube was not straightforward. Thus, the inner surface of the sealed YSZ tubes was designed to be used as the cathode, which was subsequently immersed in a suspension of coal in molten carbonate eutectic as the anode. This configuration could have been reversed, and indeed it was used in some fundamental testing; however, continuous coal and eutectic addition to such a small cylinder would have been difficult.

With the design of an individual cell satisfied, remaining design activities focused on various ancillary aspects of DCFC design. This included design of the DCFC tank, the furnace for heating, gas inlet and output ports, fuel introduction, electrical connections, digital control systems, as well as ample safety considerations.

Throughout the design process, consideration was always given to ease of access to all components of the DCFC system so as to ensure that maintenance, modifications and repairs could be made easily

and conveniently. While this does not represent the design of the end product for ultimate commercial use, it does represent the characteristics of a prototype with in-built flexibility.

7. Unit Build

With finalization of the DCFC system design, construction and acquisition of components was carried out using a combination of in-house and contract manufacturing. All design components were completed in a timely manner, except for the digital control system, which took much longer than expected and promised. Indeed, the development and installation of the digital control system was the main factor causing delays in system testing and evaluation.

8. Unit Testing and Operation

After construction completion the DCFC was subjected to a thorough safety review before being evaluated for its performance. The focus of the safety testing was on gas generation, high temperature system safety, and electrical safety. After passing this examination, a variety of component operations were carried out to understand their operation, including charging the cell, fuel feeding to the cell during operation, pre-heated gas flow to the cell and exhaust gas handling, temperature stability, and dump tank operation for draining the DCFC tank.

With successful completion of these activities, electrical measurements were conducted on the DCFC system, starting with the open circuit potential. This was conducted as an indicator of system stability in terms of electrical contacts fuel and oxidant access to catalyst and current collector surfaces, as well as general stability of the system. The output system voltage of 1.11 V was as expected based on our fundamental testing.

Energy generation from the DCFC was then carried out through the use of an electronic load. This is effectively a resistance through which the current from the DCFC was passed to simulate energy generation. It was also used as a means of controlling the output cell voltage to explore current generation and enable identification of peak power. This analysis was conducted successfully to identify the voltage of peak power generation, which was 0.5 V. This voltage was then applied to the full prototype to examine operational stability, which was demonstrated successfully over the course of three days. After this time system performance decreased due to fuel depletion, which is a function of both availability and mixing within the suspension. As mentioned previously, ongoing fuel supply is an aspect of future system development.

9. Commercial Module Development

After the experience of conceiving and developing a large scale DCFC, certain critical aspects of the system have been identified as requiring further development before system commercialization. This includes:

(i) The heating system, which has the capacity to be optimized so as to minimize void volume and excessive volumes of coal in electrolyte suspension;

(ii) The electrode arrangements to optimize the overall system output voltage and current, to thus maximize output power; and,

(iii) Fuel input, which has to be automated to maintain ongoing system operation.

We consider these to be the main components of the overall system needing further development.

SUMMARY AND CONCLUSIONS

Mass and Energy Balance

A steady state model has been built which allows assessment of the final system efficiency and sensitivity of this value to several variables including the achievable electrochemical efficiency of the system, and the extent of parasitic gasification of the fuel (reverse Boudouard reaction). A detailed scientific paper (see Appendix 1) on the mass and energy balance has been prepared for submission to a journal.

Corrosion and Materials Investigation

316L or 253MA stainless steel can be used as a material for fabricating the fuel cell tank, however for a short-term service (<1 year). 253MA is superior to 316L in air + carbonate environment, but it is expensive (2x) than 316L. For long-term service (~10 years) of the fuel cell tank, the stainless steel (316L or 253MA) should be coated with a high temperature resistance ceramic material. For the application of current collectors, silver metal was found to be superior to other metallic materials such as nickel, copper, iron and titanium.

Anode Formulation and Processing

The cell performance with different alkali metal carbonate mixtures, i.e., ternary eutectic (Li_2CO_3/ Na_2CO_3/K_2CO_3) and binary eutectics Li_2CO_3/K_2CO_3 and Li_2CO_3/Na_2CO_3, showed that Li_2CO_3/K_2CO_3 (47/53) exhibited the highest performance over the temperature range between 600-800°C, whereas at 860°C Li_2CO_3/Na_2CO_3 (52/48) was superior. It was also found that Fe_2O_3 and SnO_2 as additives (5 wt%) to the fuel mixture increased the power output of the cell. Coal particle size did not significantly affect the cell performance.

Cathode Optimization

Commercial mixture of LSM-YSZ as the cathode material performed better than lab-prepared mixture. The homogeneous nature of the commercial LSM-YSZ mixture compared to the lab-prepared mixture has improved the performance. Increase in the thickness of the YSZ tube (0.87 mm to 1.57 mm) did not significantly affect the performance of the cell. For cathode current collector, silver wire was superior to nickel wire, and the increase in the surface area of silver wire improved the performance significantly. Silver paste and wire/mesh combination on the cathode side showed the best performance.

Molten Carbonate Properties

Half-cell study showed that kaolinite addition (up to 15wt.%) to the fuel mixture (coal+ carbonate) exhibited catalytic effect, i.e., enhanced electro-oxidation of carbon. The flowability of the coal-carbonate mixture (5 and 10 wt.% coal) at 800°C was high, whereas for 30wt.% coal it was satisfactory, and became very poor for 50wt.% coal mixture. TGA results showed that the mass loss of the slurry samples increased as the carbon content of the slurry increased. Thus, it can be said that fuel (carbon) gasification is the main factor in slurry mass loss at elevated temperatures.

System Design

The performance of the small cell (similar to 1 kW cell design) with two different cathode configurations (silver wire and silver mesh) was tested at 800°C in 20 wt.% coal slurry. The cell with

silver wire as the anode exhibited a power density of 79 mW/cm^2, whereas the silver mesh anode increased the power density to 138 mW/cm^2, which is close to our target of 150 mW/cm^2. The concept design of 1 kW unit is complete. Electrical heating system has been chosen for heating the slurry in the fuel cell tank and pre-heat air passing through the YSZ tubes. The critical gland design has been tested in our lab for leak-proof sealing. In a horizontal configuration where the electrolyte slurry is pressing on the seal this leads to substantial leakage. However, redesign with a vertical arrangement and no liquid pressure applied to the seal was found optimal.

Construction and Testing

The DCFC system was constructed as designed and subjected to initial testing. Outputs indicate a successful conversion of laboratory based testing into the larger scale. The system was evaluated for longer term testing (days) as well as power output. The maximum power output achieved was 945 W.

RECOMMENDATIONS

This project was successful in improving the fundamental understanding associated with many aspects associated with DCFC operations. These were then successfully implemented into the design, construction and testing of a 1 kW demonstration scale DCFC. Additionally, much was developed concerning the operation of this large-scale prototype unit. At present, this is the first such system in the world, developed primarily from in-house research. Prototype systems are an essential intermediate stage in further development and commercialization because they provide a platform for further system refinements, particularly in terms of overall system efficiency and componentry. The next stage pf development is to build on the findings, performance and efficiency of the prototype to develop ultimately a commercialization-ready system. This will involve considerable effort towards modularization of the DCFC technology, concurrent with the further refinement to improve performance and efficiency. This can only be accomplished through further research and development focused on these aspects of the system. Specifically, this will involve a focus on:

(i) Mass and energy balance – this is the key tool in determining system efficiency;

(ii) Modularization of the DCFC system;

(iii) Anode performance and fuel delivery – this is the key energy providing material within the DCFC and so the nature of the fuel used, together with its introduction will be an ongoing critical component;

(iii) Material requirements for long term operation – understanding how the DCFC operates over even longer timeframes is key to commercialization;

(iv) System maintenance, recycling and recovery – essentially the best practice for using the DCFC under real conditions.

Each of these key aspects will be supported by a fundamental research stream, the outcomes from which will allow us to continue the more applied development.

An important point is that ongoing development of the DCFC will focus on combining fundamental and developmental research to assemble a commercialization-ready modular DCFC system. Development of a large-scale prototype DCFC system is essential for bridging the gap between fundamental outcomes and a commercial ready unit. This was the feedback we received after a number of early discussions with potential commercial partners, who were reluctant to invest in the early stage development of this technology. This is a non-trivial exercise since it is the first of its kind, at this scale, across the globe.

REFERENCES

1.   Janz, G.J. and M.R. Lorenz, *Solid-Liquid Phase Equilibria for Mixtures of Lithium, Sodium, and Potassium Carbonates.* Journal of Chemical & Engineering Data, 1961. **6**(3): p. 321-323.

2.   Olivares, R.I., C.L. Chen, and S. Wright, *The Thermal Stability of Molten Lithium-Sodium-Potassium Carbonate and the Influence of Additives on the Melting Point.* Journal of Solar Energy Engineering-Transactions of the Asme, 2012. **134**(4).

3.   Badwal, S. and F. Ciacchi, *Oxygen-ion conducting electrolyte materials for solid oxide fuel cells.* Ionics, 2000. **6**(1-2): p. 1-21.

4.   Allen, J., et al., *Molten Carbonate Composition Effects on Carbon Electro-Oxidation at a Solid Anode Interface.* Journal of The Electrochemical Society, 2015. **162**(1): p. F76-F83.

5.   Cantero-Tubilla, B., et al., *Investigation of anode configurations and fuel mixtures on the performance of direct carbon fuel cells (DCFCs).* Journal of Power Sources, 2013. **238**: p. 227-235.

6.   Allen, J.A., et al., *An investigation of mineral distribution in coking and thermal coal chars as fuels for the direct carbon fuel cell.* Fuel, 2018. **217**: p. 11-20.

7.   Allen, J., M. Glenn, and S. Donne, *The effect of coal type and pyrolysis temperature on the electrochemical activity of coal at a solid carbon anode in molten carbonate media.* Journal of Power Sources, 2015. **279**: p. 384-393.

8.   Glenn, M.J., J.A. Allen, and S.W. Donne, *Thermal Investigation of a Doped Alkali Metal Carbonate Ternary Eutectic for Direct Carbon Fuel Cell Applications.* Energy & Fuels, 2015.

9.   Chen, C.C., et al., *Wetting Behavior of Carbon in Molten Carbonate.* Journal of the Electrochemical Society, 2012. **159**(10): p. D597-D604.

10.   Rady, A.C., et al., *Review of fuels for direct carbon fuel cells.* Energy & Fuels, 2012. **26**(3): p. 1471-1488.

11.   Wang, B., *Recent development of non-platinum catalysts for oxygen reduction reaction.* Journal of Power Sources, 2005. **152**: p. 1-15.

12.   Jiang, C., et al., *Challenges in developing direct carbon fuel cells.* Chemical Society Reviews, 2017. **46**(10): p. 2889-2912.

13.   Giddey, S., et al., *A comprehensive review of direct carbon fuel cell technology.* Progress in Energy and Combustion Science, 2012. **38**(3): p. 360-399.

14.   Sakito, Y., et al., *Silver infiltrated La 0.6 Sr 0.4 Co 0.2 Fe 0.8 O 3 cathodes for intermediate temperature solid oxide fuel cells.* Journal of Power Sources, 2008. **182**(2): p. 476-481.

15.   Jørgensen, M.J., et al., *Effect of sintering temperature on microstructure and performance of LSM–YSZ composite cathodes.* Solid state ionics, 2001. **139**(1-2): p. 1-11.

16.   Wang, C.Q., et al., *Significant improvement of electrooxidation performance of carbon in molten carbonates by the introduction of transition metal oxides.* Journal of Power Sources, 2013. **233**: p. 244-251.

17.   Tulloch, J., et al., *Influence of selected coal contaminants on graphitic carbon electro-oxidation for application to the direct carbon fuel cell.* Journal of Power Sources, 2014. **260**: p. 140-149.

18.   Kim, J.-W., Y.-D. Lee, and H.-G. Lee, *Decomposition of Na2CO3 by Interaction with SiO2 in Mold Flux of Steel Continuous Casting.* ISIJ international, 2001. **41**(2): p. 116-123.

19.   Atkins, P. and J. De Paula, *Atkins' physical chemistry.* 2014: Oxford University Press.

20.   Botas, J., et al., *Kinetic modelling of the first step of Mn2O3/MnO thermochemical cycle for solar hydrogen production.* International Journal of Hydrogen Energy, 2012. **37**(24): p. 18661-18671.

APPENDICES

Appendix 1: Staff associated with this project:

Supported by the University of Newcastle

 Professor Scott Donne

 Dr. Jessica Allen

Supported by Coal Innovation NSW

 Dr. Bobby Mathan

 Dr. Yaser Beyad

 Dr. Md Monirul Islam

 Dr. Michael Glenn

 Ms. Simin Moradmand (study towards a PhD)

 Mr. Ciaran Moloney (research assistant)

 Ms. Chelsee Green (research assistant)

 Mr. Miguel Rivera (research assistant)

Appendix 2

JA Allen, M Glenn, SW Donne; "Analysis of theoretical efficiency in a model 10 kW direct carbon fuel cell using a coal based carbonate slurry", Electrochim. Acta, 329, 135131 (2020).

Appendix 3

MJ Glenn, JA Allen and SW Donne; "Carbon Electro-Catalysis in the Direct Carbon Fuel Cell Utilising Alkali Metal Molten Carbonates: A Mechanistic Review", J. Power Sources, 453, 227662 (2020).

Appendix 4

MJ Glenn, J Allen, SW Donne; "Silicate Formation in Ternary Alkali Metal Carbonate Melts", Energy & Fuels, 33, 12008-12015 (2019).

Appendix 5

MJ Glenn, JA Allen, SW Donne; "Carbon Gasification from a Molten Carbonate Eutectic", Energy Technology, 7, 1900602 (2019).

Appendix 6

MJ Glenn, B Mathan, MM Islam, Y Beyad, JA Allen, SW Donne; "Gas Atmosphere Effects Over the Anode Compartment of a Tubular Direct Carbon Fuel Cell Module", Energy & Fuels, 33, 7901-7907 (2019).

Appendix 7

JA Allen, M Glenn, P Hapugoda, R Stanger, G O'Brien and SW Donne; "An Investigation of Mineral Distribution in Coking and Thermal Coal Chars as Fuels for the Direct Carbon Fuel Cell", Fuel, 217, 11-20 (2018).

Appendix 8

S Moradmand, JA Allen, SW Donne; "Thermal and Electrochemical Impact of Kaolin on a Direct Carbon Fuel Cell", Fuel, in press (2020).

Appendix 9

S Moradmand, JA Allen, SW Donne; "Thermal behaviour of silica in contact with an alkali-metal carbonate mixture used in direct carbon fuel cell applications", in preparation (2020).

Appendix 10

Safety assessments.

Appendix 11

Video of DCFC construction.

SIGN-OFF

I, the undersigned, being a person duly authorised by the Grantee, certify that:

    (a) the above information is true and complete;

    (b) the expenditure of the Funding received to date has been solely on the Project; and

    (c) there is no matter or circumstances of which I am aware, that would constitute a breach by the Department of Regional NSW or, if applicable the End Recipient, of any term of the Funding Agreement between the Department of Regional NSW and the Grantee dated that has not been notified by the Grantee.

Signature:

Position: Professor of Chemistry

Name: Scott Donne

Date: 31 May, 2021

Analysis of theoretical efficiency in a model 10 kW direct carbon fuel cell using a coal based carbonate slurry

J.A. Allen [a, *], M. Glenn [b], S.W. Donne [b]

[a] Chemical Engineering Discipline, Faculty of Engineering and Built Environment, University of Newcastle, University Drive Callaghan, NSW, 2308, USA
[b] Chemistry Discipline, Faculty of Science and Information Technology, University of Newcastle, University Drive Callaghan, NSW, 2308, USA

ABSTRACT

A detailed mass and enthalpy balance of a direct carbon fuel cell has been carried out in order to understand achievable efficiency of a 10 kW analogy. Using literature input data, a steady state model has been built which allows assessment of the final fuel cell efficiency and sensitivity of this value to several variables including the extent of parasitic gasification of the fuel (reverse Boudouard reaction). It is shown that for a hybrid DCFC system, which utilises both primary (solid oxide membrane) and secondary (molten carbonate) electrolytes, a slurry based feed of coal and carbonate could provide enough waste heat from electrochemical inefficiency to both retain the molten feed temperature, as well as provide pre-heating for inlet air streams to achieve an overall system efficiency of over 70%. Higher system efficiencies may be possible, however will depend heavily on the cell design and specifically on increasing the electrochemical efficiency at the expense of waste heat generated. Additional parasitic power input is required in these cases. A base case of assumptions has been evaluated with sensitivity of the system efficiency compared for the carbon slurry loading, the carbon and oxygen conversion per pass of the fuel cell (fuel utilisation), equipment heat losses, amount of coal char ash present and the extent of carbon corrosion within the cell. Under the base case investigated, life cycle emissions of the technology have been estimated (using several assumptions) at 647 kg CO_2/MWh at 70% system efficiency, with no carbon storage, while emissions of 93 kg CO_2/MWh at 66% system efficiency are potentially achievable (dependent on accuracy of assumptions) if carbon dioxide is able to be effectively sequestered.

© 2019 Elsevier Ltd. All rights reserved.

1. Introduction

The direct carbon fuel cell (DCFC) is a future energy technology which has been known for some time as the most efficient process for electrical energy generation from carbon based sources [1]. The technology has an extremely high theoretical efficiency due to favourable thermodynamics of the reactions used. In practice, very few systems are able to reach their thermodynamic limits and the DCFC is no exception. In fact, there are several factors which contribute to the realisable efficiency of DCFC technology which must be considered when making direct comparisons to traditional coal fired power stations.

Primary among these considerations is the arrangement of the fuel cell. In more recent development of the DCFC, it has been

shown that very high electrochemical performance and fuel utilisation can be achieved with a fuel cell which incorporates a solid oxide membrane [2,3]. This allows transport of the oxidant to the fuel without physical contact between the two separate streams. Development work at the cathode of the DCFC matches that done on solid oxide fuel cell (SOFC) technology, however the temperature of operation is generally slightly lower than a SOFC [4]. It has also been demonstrated that high performance can be achieved using a number of arrangements in the anode compartment of the DCFC [5,6], particularly including use of molten carbonate salts as oxide carriers to enhance the triple phase reaction boundary at the anode [2,7]. In cases where carbonate salts are not used, the arrangement relies on chemical transformation of the carbon fuel to generate carbon monoxide, and subsequent electrochemical oxidation of the carbon monoxide formed to then complete the oxidation [8]. This later arrangement, although simplified in terms of the electrochemical engineering due to the generation of a fluidic electrochemical reactant, is expected to have much lower overall efficiency compared to an arrangement which allows direct

* Corresponding author. University Drive, University of Newcastle, Callaghan, NSW, 2308, USA.
E-mail address: j.allen@newcastle.edu.au (J.A. Allen).

Table of symbols

Symbol Meaning Units

a	Mean atomic weight g.mol-1
A, B, C	Empirical constants for calculation of gas heat capacities
c_{Pn}	Heat capacity of component n kJ.kg-1.K-1
E_n	Electrochemical potential under n condition V
F	Faradays constant C.mole-1
ΔH_{fusion}	ΔH_{vap} Heat of fusion or vaporisation of component stream undergoing phase change. kJ.kg-1
ΔH_n	Enthalpy change of component n from reference to process temperature kJ.h-1
$\Delta H_{rxn}(T)$	Molar enthalpy of reaction at temperature T kJ.mol-1
i_{op}	Operating current density mA.cm-2
L_c	Carbon loading in carbonate wt%
$\dot{m}_n$	Mass flow rate of component n kg.h-1
$\dot{n}_e$	Hourly molar requirement mol.h-1
n_x	Number of moles of component x
P_{peak}	Peak power density mW.cm-2
Q_n	Heat loss to surroundings from unit operations at reference point n kJ.h-1
R	Universal gas constant J.mol-1.K-1
$\Delta S_{(T)}$	Reaction entropy at temperature T J.K-1/mol-1
t	Time h
T	Temperature K
u_i	Atomic weight of element i g.mol-1
W_x	Electrical power with reference to x mW, W or kW

Greek letters

η_{conv}	Electrochemical conversion of carbon per pass of anode compartment wt%
η_{EC}	Electrochemical efficiency
η_{EC}	System efficiency
σ_{thermo}	Irreversible entropy loss J.K-1/mol-1
μ_n	Overpotential contribution of component n V
y_i	Mass fraction of element i (dry ash fee basis) wt%

electrochemical oxidation of the solid fuel itself. Where molten salts are employed, the question then becomes the delivery of carbon to the reaction site to which carbon, oxide and electrons must be able to be concurrently transferred.

In terms of scale up and practical commercialisation of the DCFC, the engineering and process aspects of the technology need to be considered in addition to the fundamental performance and behaviour at each electrode of the fuel cell. Indeed, practical engineering aspects could potentially overshadow consideration of power output in a real operating system. For example, a solid anode is likely the best approach in terms of reduction of parasitic side reactions (such as Boudouard corrosion) as well as elimination of mass transfer limitations of a DCFC system. However, efficient and effective formulation of a solid coal based anode of sufficient integrity and conductivity to allow electrochemical consumption is expected to be an energy intensive process, as is observed in the carbon electrodes consumed in the electrochemical production of aluminium - which undergo energy intensive processing before effective use. There are a number of alternative anode approaches which have been trialled in the literature including compressed beds, cages and carbon slurry with current collectors [9]. Good electrochemical performance has been observed for a number of these, although it is often difficult to eliminate limitations which also result from separate fuel and performance issues.

In terms of envisaging a continuous process, as opposed to a carbon battery approach, the most obvious choice is a slurry arrangement. Although a semi-continuous process could be realised with other arrangements, a truly continuous process could only really occur in the case of the particulate approach.

The slurry system approach has also seen a high degree of study in the literature and performance of various fuels, and fuel pretreatments in these mass transport limited conditions are commonly reported on [2,3,10−34]. The system does however have its own specific limitations, apart from mass transfer. Potentially the most problematic of these is the contact of carbon dioxide with the fuel, generating carbon monoxide in an endothermic reaction known as reverse Boudard gasification (C + CO_2 = 2CO). Since the system is loaded with carbon, and carbon dioxide is being generated while the fuel is being swept over the reaction site, there is an increased possibility of reaction compared to, for example, a solid anode system where the carbon is protected through polarisation [33].

A slurry fuel must also maintain a high enough temperature to keep the carbonate component molten, and for the cell to be operated in the best temperature range of both the cathode and the oxide conducting membrane, which both tend to have decreased performance with decreasing temperature.

In several references, heat generation within the DCFC is assumed to be more than enough to both maintain reaction and melt temperatures, often with additional 'waste heat' to spare [35]. Indeed the high efficiency of the carbon conversion process relies on the high performance of the fuel cell (in term of electrochemical efficiency) as well as its ability to generate heat. In terms of fuel cell thermodynamics, in fact these two parameters are working against each other. For example, a 1 kW system operating at 50% electrochemical efficiency will, in simple terms, generate 1 kW of waste heat. Since the DCFC is celebrated for its efficiency, in fact any increase in efficiency will be a loss in the waste heat generated. There also exist complications with parasitic side reactions since Boudouard corrosion is an endothermic process [36] which could consume heat as well as carbon reactant within the cell. The carbonate can be maintained at a high temperature (with expected heat losses through radiative heat) and recycled within the reactor, however carbon reactants must be introduced at room temperature and increased to reaction temperature − which is well above 600 °C. Greater use of heat however might be expected to originate in the cathodic compartment, where air must also be heated to reaction temperature before being introduced. Since conversion is never 100% for a single pass, and oxygen makes up a small portion of the air stream, the amount of air requiring constant heating might be expected to be very large. Radiative heat losses at elevated temperatures also have the potential to be significant.

To date, no study or assessment of an operating, molten carbonate based direct carbon fuel cell system from a heat and mass transfer approach has been considered, nor has any study satisfactorily demonstrated the possibility that such a system could realise promised efficiencies of the technology by providing enough waste heat to keep the cell and its components at the reaction temperature. This is surprising considering the abundance of literature which exists covering this topic for other high temperature fuel cells such as solid oxide systems [37,38]. This could be a result of the, to date, lab based focus on DCFC technology and lack of commercial or even demonstration scale operable units.

Previously modelling of DCFC systems attempt to model

overpotential, based on estimation of various contributions to polarisation within the cell, and therefore consider the overall electrochemical efficiency of the system. These works then investigate integration of other options with DCFC's to boost efficiencies, generally through collection and usage of waste heat [39,40]. The same source model has been used in these cases, which calculated very low electrochemical efficiencies, down to as little as 32% [41]. The model gives a very high ohmic resistance value due to packing of graphite particles in a packed bed arrangement, with no consideration of other DCFC arrangements or comparison to real bench scale measurements from other published works in the area. The design assumed in these studies is also outdated as it does not include a solid oxide membrane to separate oxygen reduction and carbon oxidation reactions. In these model cases, a large amount of waste heat will be available because the electrochemical efficiency is so low, and any gains in efficiency are at the expense of the original carbon conversion reaction. Indeed an efficiency of only 30−40% means DCFC technology is comparable to an average performance coal fired power station [42], and main advantages of the technology are therefore not realised. These models also unanimously fail to include the possibility of corrosive side reaction of the carbon dioxide through Boudouard gasification which also consumes heat, or the consideration of the impact of carbon/carbonate loading, carbon utilisation within the cell during steady state operation and heat capacity of inlet/outlet feeds for allowing maintenance of heat within the cell. Very little sensitivity analysis around the playoff between heat and electrical energy generation has been considered and could be considered to be the most crucial aspect of the technology uptake if its high efficiency is to be realised. Other more realistic models for DCFC systems are conversely focused on the Boudouard reaction as a major reaction pathway in a semi-solid oxide fuel cell set up (DC-SOFC) rather than a parasitic side reaction, and does not consider integration of molten carbonates into the system [43,44].

This work therefore includes a first overall process model of a direct carbon fuel cell operated in a continuous manner using a coal and ternary alkali metal carbonate (Li/Na/K) slurry fuel system. Since no such system exists for measurement, several assumptions regarding performances and other important variables have been taken from literature, and a sensitivity analysis of the overall efficiency of the system in response to variation in these and other parameters has been assessed. The overall efficiency of a DCFC system has been estimated under a number of operating scenarios using a set base case. The base case assumed is for a 10 kW system as this has been determined at the most likely entry point for a commercial unit which is able to be used in distributed energy applications.

2. Modelling approach

2.1. Process inclusions and layout of unit operations

The DCFC unit modelled has been assumed to be a 10 kW (output) cell which receives a pre-pyrolysed coal char (to ensure stability prior to DCFC use [45], full assumptions including coal char composition used in this work in Section 2.3 and Table 4). Unit

Table 1
Coefficients of Eqn (8) for determining gaseous heat capacity.

Constant	H_2O (g)	CO_2 (g)	CO (g)	O_2 (g)	N_2(g)
A	3.47	5.46	3.38	3.64	3.28
B	0.00145	0.00105	0.00056	0.00051	0.00059
C	12100	−115700	−3100	−22700	4000

Table 2
Enthalpy nomenclature and relevant material streams, in $kJ.h^{-1}$.

$\Delta H_{A,i}$	Inlet air stream (CA-1)
ΔH_{OT}	Oxide transferred to anode (equivalent oxygen enthalpy)
$\Delta H_{A,o}$	Outlet air stream (CA-2)
$\Delta H_{s,i}$	Inlet carbon slurry (AN-1)
ΔH_{EC}	Electrochemical Resistance heat (Q_{waste} converted to kJ/h carbon transformed, i.e. Eqn (22))
ΔH_B	Endothermic heat consumed for reverse Boudouard reaction
Q_2	Heat loss from equipment to surroundings (assumed value based on total input heat, see Eqn (7))
$\Delta H_{g,o}$	Outlet anode gas stream (AN-2)
$\Delta H_{s,o}$	Outlet carbon slurry stream (HT-1)

operations modelled, shown in Fig. 1, include a char/carbonate mixing tank, the DCFC module (broken into anode and cathode compartments) and a slurry holding tank.

It is assumed that a set amount of carbonate is removed for coal mineral recovery, and that this must be replaced with fresh/renewed carbonate powder provided at room temperature to the process (95% recycle rate used in all modelling). Equipment heat losses are assumed to occur from the char mixer and recycled slurry holding tank as well as from the anode compartment of the DCFC (the cathode is assumed to be located within the anode compartment and not exposed to the surroundings). No heat losses from transfer lines have been considered. An air pre-heater/blower would also be required for the process, however this has not been modelled other than accounting for the total heat required to pre-heat the required air flow to reaction temperature. The model does not consider heat recovery options other than to assess overall heat requirements, and how much may realistically be provided by process streams.

2.2. General mass and energy balance modelling

2.2.1. Basis and units

The process is assumed to be operating at steady state with an overall available electrical energy output of 10 kW. Mass flows are calculated on the basis of $kg.h^{-1}$ and energy flows in $kJ.h^{-1}$. The reference temperature used in the enthalpy balance is 20 °C.

2.2.2. Mass balance

The total mass of all substances taking part in a process remains constant. This law for steady state operation may be written as:

$$\dot{m}_{input} = \dot{m}_{output} \tag{1}$$

This is a simple and fundamental engineering principle which has been applied in this work to determine mass flows of the process. Mass balances have been carried out with full process integration of each unit operation. Generally, input gases have been broken down into their constituents in the mass balance according to known stoichiometry. For example, air is broken into inputs of oxygen and nitrogen in a 21:79 vol% ratio. Solids are not broken into chemical compositions however coal char has been broken into a mineral/ash fraction, plus an organic fraction, and water has also been specified separately. More details around mass balance carried out within the fuel cell and for specific reactions taking place have been discussed in Section 2.3.

2.2.3. Energy/enthalpy balance

At steady state operation, the law of conservation of energy and 1st law of thermodynamics suggests that the energy of a contained system is constant which may be written as:
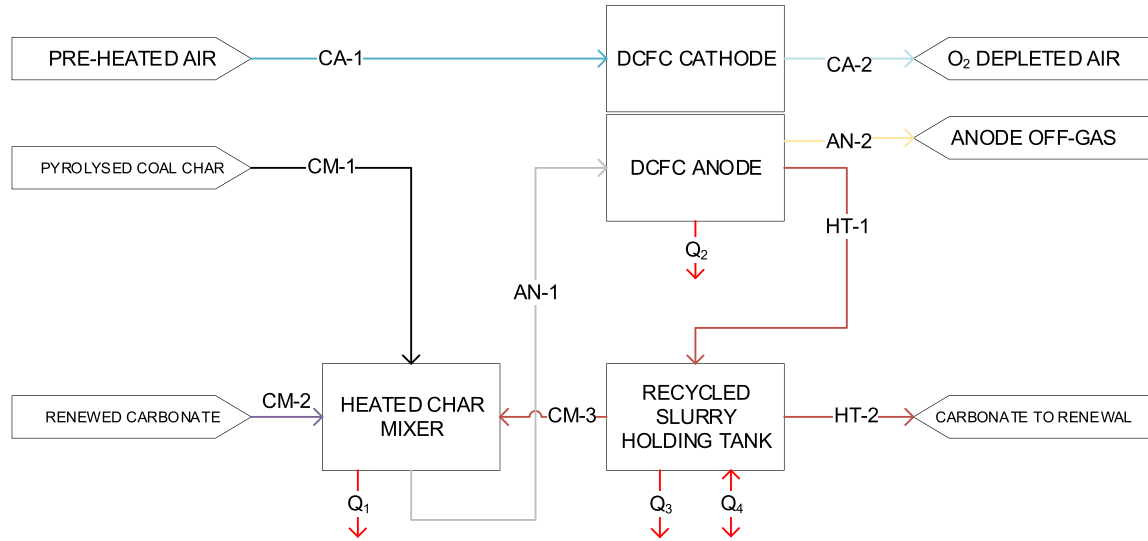
Fig. 1. Process model used for steady state assessment of mass and enthalpy flows for a slurry based direct carbon fuel cell system of 10 kW output.

$$\Delta U = E_{out} - E_{in} = Q - W \tag{2}$$

where U is the internal energy change of the system, Q is the heat supplied and W is the work done. This study uses the enthalpy value of the stream, expressed as heat, to carry out this energy balance and assumes ideal gas behaviour as well as constant pressure throughout. Enthalpy is a relative value which allows an effective energy balance to be carried out if consistent reference case is used. Exergy and work were not considered here and heat flow was always from hot to cold streams to ensure adherence to the second law of thermodynamics. Entropy was however considered in electrochemical assumptions (Section 2.3.3).

Using an enthalpy balance, the heat of a specific input or output stream is calculated based on the heat required to change the stream from the reference temperature to a process condition:

$$\Delta H_n = \dot{m}_n c_{Pn} \left(T_{process} - T_{reference} \right) \tag{3}$$

If a phase change occurs within this temperature range, heat of transformation (fusion or evaporation) must also be included. For example, since an ambient temperature has been chosen as the reference temperature in this case, both solid and liquid heat capacities as well as heat of fusion must be included in the enthalpy calculation of the ternary carbonate if the process stream is operated above the melting point of the eutectic as follows:

$$\Delta H_n = \dot{m}_n c_{Pn,liquid} \left(T_{process} - T_{melt} \right) + \dot{m}_n \Delta H_{fusion}$$
$$+ \dot{m}_n c_{Pn,solid} \left(T_{melt} - T_{reference} \right) \tag{4}$$

The same applies to phase changes for the water component considered here which undergoes evaporation in the temperature range of interest.

Heat capacity of a material may be a constant value which is not dependent on temperature, as indicated for Eqn (3), or it may have known temperature dependence, such as is the case for steam at constant pressure. In this work, a temperature independent heat capacity has been assumed, however has been taken as the average heat capacity of the material at process temperature and the heat capacity of the material at room temperature if there is known temperature dependence of this value:

$$c_{Pn} = \frac{c_{Pn} \left(T_{reference} \right) + c_{Pn} \left(T_{process} \right)}{2} \tag{5}$$

This can be assumed in cases where relatively small changes in heat capacity are observed, as is the case for components considered here. In the case of phase change, two average heat capacities are taken for each of the phases considered. Values for heat capacities and phase change of components have been taken from literature values in this work as outlined in Section 2.3.

In addition to enthalpy of components in and out, energy generation and consumption must also be calculated for each individual unit operation, which generally includes taking into account any reactions which are occurring within the unit operation, as well as irreversible heat losses from the equipment:

$$\Sigma \Delta H_{inputs} = \Sigma \Delta H_{outputs} + \Sigma \Delta H_{rxn} - Q_n \tag{6}$$

where Q_n is heat loss to surroundings. This has been included as a fixed percentage specified for each unit operation of the total heat change of the unit operation from inputs only:

$$Q_n = X\% \times \left(\Sigma \Delta H_{inputs} \right) \tag{7}$$

In order to carry out the modelling, first the mass transfer is calculated for each unit operation to have known mass flows for all streams. Following this, enthalpy calculations are carried out iteratively by setting the enthalpy change across a unit operation to zero by modifying the temperature of the output stream. No mechanical energy factors have been included in the balance which is assumed to take place at constant pressure.

2.3. Process model assumptions and justification of variables

2.3.1. Thermal properties of streams (heat capacity, heat of fusion and evaporation)

Since the model is enthalpy based, accurate values for materials heat capacity as well as phase change heats are required.

2.3.1.1. Gas heat capacities. Information for standard gases including carbon dioxide, carbon monoxide, oxygen, nitrogen and steam have been taken from a reference textbook [46] and calculation of molar heat capacity follows the formula:

$$c_{pn(molar)} = \left(A + BT + CT^{-2}\right) \times R \tag{8}$$

where R is the ideal gas constant ($J.mol^{-1}.K^{-1}$), T is the temperature (K) and A, B and C are unitless constants specific to the gas referred to. Table 1 gives constants for each gas stream included in the model.

Conversion from molar to mass based values from Eqn (8) must then be carried out using gas molecular weights.

2.3.1.2. Solid heat capacities. The coal char has been broken into mineral and organic fractions for the mass balance and heat capacity values have been used for each component separately. There have been many studies attempting to calculate and predict the heat capacity of coal [47,48], however these tend to be for raw coals and are highly dependent on the coal type, including consideration of the amount of ash present as well as relative fixed carbon and volatile ratios. When considering a temperature range which crosses the pyrolysis reaction temperature of the coal, heat capacity becomes difficult to measure. Since this model considers use of a pre-pyrolysed and presumably unchanging coal char, these relationships are not very accurate for prediction of heat capacity. An early and widely cited study by Merrick however allows for calculation of the ash-free portion of a carbon based material dependant on its ultimate analysis, i.e. elemental composition [49] and also gives heat capacity as a function of temperature. This correlation is based on Einstein form of the quantum theory specific heat description for solids, and not empirical data, with good agreement to experimental data observed by the author. The mean atomic weight (defined as a) is firstly calculated as follows:

$$\frac{1}{a} = \sum_{i=1}^{5} \frac{y_i}{u_i} \tag{9}$$

where $i = 1 - 5$ refers to elements carbon, hydrogen, oxygen, nitrogen and sulphur known from ultimate analysis on a dry ash free basis, y_i is the mass fraction of each and u_i is the respective atomic weights. The specific heat (in $J.kg^{-1}.K^{-1}$) can then be found using:

$$c_{p,coal\ char} = \frac{R}{a}\left(g_1\left(\frac{380}{T}\right) + 2g_1\left(\frac{1800}{T}\right)\right)$$
$$\text{where } g_1(z) = \frac{\exp(z)}{((\exp(z)-1)/z)^2} \tag{10}$$

The instantaneous specific heat of coal ash was also presented by Merrick based solely on the material temperature (°C for this relationship), which has been used in this work:

$$c_{p,mineral\ matter} = 754 + 0.586\ T \tag{11}$$

The final solid which is present in this balance is the ternary carbonate eutectic. It has been assumed that a small amount of carbonate must be continuously replaced during operation of the DCFC (95 wt% recycle used). A ternary carbonate eutectic has been used in this work since it has the lowest melting point and has also shown little variation in electrochemical performance compared to other possible carbonate combinations [50]. Kenisarin et al. provided a summary of the thermal properties of a number of phase change materials, including carbonate combinations [51], with data for carbonate properties taken from work of Marianowski et al. [52]. The solid ternary carbonate, of molar composition Li (43.5):Na (31.5):K (25.0) was reported to have a temperature independent heat capacity of $1.67\ J\ g^{-1}\ K^{-1}$, which has been used here for the solid component for the carbonate species.

2.3.1.3. Liquid heat capacities. Both liquid water and molten carbonate are considered as liquids within the process model. In the same work as the solid carbonate, a temperature independent value of $1.63\ J\ g^{-1}\ K^{-1}$ for liquid carbonate was presented by Kenisarin et al. [51] for the ternary eutectic. Heat capacity as a function of temperature was not investigated by these authors for the ternary system, however the work of Araki et al. [53] showed a linear response with temperature past the melting point of the binary $Li_2CO_3 - K_2CO_3$ (50:50 mol%) carbonate. This suggests a single value is able to be fairly assumed in this case.

The thermal properties of liquid water are well characterised and in this work the following temperature (in K) dependant relationship was used to find the molar heat capacity ($J.mol^{-1}.K^{-1}$) which can then be converted to mass based heat capacity using molecular weight of water [46]:

$$c_{p\ water(molar)} = \left(8.712 + 0.00125T - 0.00000018T^2\right) \times R \tag{12}$$

Water is assumed to be introduced with the char at a very low loading (2% moisture, carbonate is assumed to be introduced dry) and does not interact with the carbonate, being removed as steam in the anode off-gas as the char passes through the cell. Although a very small contribution overall, this value has been included to improve accuracy of modelling.

2.3.1.4. Phase change enthalpy. Two phase changes occur within the model including evaporation of water, and melting of carbonate. The evaporation of water is an accepted standard value which occurs at 100 °C and with a heat of vaporisation of $2442\ kJ\ kg^{-1}$ [46]. The heat of fusion of the ternary eutectic carbonate has been reported as $276\ kJ\ kg^{-1}$ [51], although the melting point of this material is somewhat contentious. Early work by Janz et al. reported a melt temperature of 398 °C [54], which is generally used as the standard melt temperature. However more accurate differential thermal analysis carried out on the melt has shown a lower melting point of 386 °C with this number also seen to be sensitive to dissolution of coal mineral components in the melt [55]. The melting point of the unmodified eutectic has been assumed to be 386 °C in this work.

2.3.2. Carbon conversion pathways

In order to model the consumption and conversion of carbon within the anode compartment, several dependant reactions must be considered, shown diagrammatically in Fig. 2.

The electrochemical conversion of carbon to form carbon dioxide gas (route C1 in Fig. 2) is the dominant reaction and is assumed to correlate to the output cell current with four electrons generated per mole of carbon consumed. The amount of carbon which is reacted electrochemically per pass of the anode compartment is expected to be heavily dependent on operational variables including current collector arrangement, slurry flow rate and velocity within the cell, turbulence as well as carbon loading and particle size. Sensitivity analysis of this variable has been carried out in this work in Section 3.2 and for a base case has been assumed to be 75 wt% conversion per pass (η_{conv}, sometimes also referred to as fuel utilisation efficiency) i.e. C1 = 75 wt% x (C1+C2+C3). Previous results in a slurry system suggested that up to 80% fuel utilisation is possible for a stationary slurry system [30], meaning 75% is expected to be achievable in a flow through system.

The carbon dioxide formed with this reaction is then free to interact with carbon entering the anode compartment. Since the operating temperature is high (>700 °C), it is expected that some reverse Boudouard gasification will occur within the cell. This will consume a portion of the carbon (C2) which is not electrochemically reacted, and will reduce the final amount of both carbon
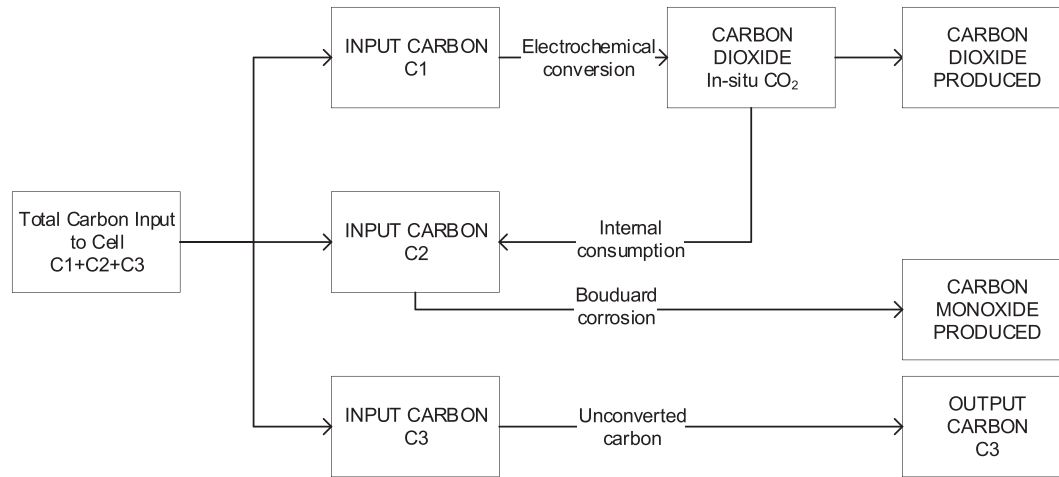
Fig. 2. Carbon conversion (carbon component of coal char only) within the DCFC anode compartment.

dioxide and unreacted carbon exiting the cell. This has been modelled as an assumed weight percentage of carbon dioxide which is reacted with the fuel, 10 wt% of the total carbon dioxide produced assumed to react with carbon in the cell as the base case. Carbon which is neither electrochemically nor chemically reacted then remains in the slurry (C3).

The carbon referred to here has been assumed to be proportional to the elemental carbon present within the ash free coal char, which, despite pre-pyrolysis, will still contain some oxygen, nitrogen and hydrogen components. The 'unreacted' portion of the coal char leaving the anode may be composed of a higher portion of these elements depending on their final fate within the anode chamber. However this has not been accounted for in the model and the recycled coal char is assumed to have the same dry ash free composition as the input char in order to allow steady-state operation to be achieved.

2.3.2.1. Management of coal mineral/ash within the model. Similarly to the non-carbonaceous portion of the ash-free char, the mineral matter within the char must also be accounted for in the model. Mineral matter is not expected to react within the cell, chemically or electrochemically, and instead will remain in the molten carbonate. Indeed it is expected that a portion of this will dissolve, as shown through previous investigations of mineral matter submersed in carbonate salts [55]. For the sake of steady state model operation however, the portion of mineral matter which remains in the recycled carbonate stream is assumed to be proportional to the amount of unreacted ash-free coal char in the specified ratio initially identified for the coal fuel, i.e. the ash percentage of the fuel assumed in the model. Therefore, the unreacted ash resulting from carbon conversion within the cell (from both chemical and electrochemical reactions) is assumed to be removed along with the carbonate removed in this case (i.e. stream HT-2).

2.3.3. Fuel cell heat generation and mass flow assumptions
2.3.3.1. Thermodynamics. The high thermodynamic efficiency of the electrochemical carbon oxidation reaction is a major selling point of the technology. Thermodynamically, all of the calorific value (chemical energy) of the fuel could be converted into electromotive force (i.e. $\Delta G/\Delta H \approx 1$), largely due to the very small entropy change which occurs. Four main overall reaction pathways are possible for carbon when using a solid oxide membrane separator, including two- and four-electron electrochemical reactions, as well as chemical reaction of carbon with reaction products; i.e.,
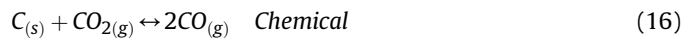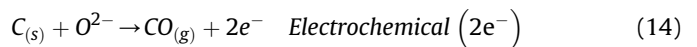
$$C_{(s)} + 2O^{2-} \rightarrow CO_{2(g)} + 4e^- \quad Electrochemical \left(4e^-\right) \tag{13}$$

$$C_{(s)} + O^{2-} \rightarrow CO_{(g)} + 2e^- \quad Electrochemical \left(2e^-\right) \tag{14}$$

$$CO_{(g)} + O^{2-} \rightarrow CO_{2(g)} + 2e^- \quad Electrochemical \left(2e^-\right) \tag{15}$$

$$C_{(s)} + CO_{2(g)} \leftrightarrow 2CO_{(g)} \quad Chemical \tag{16}$$

Oxygen is the oxidant in the DCFC, with oxide anions transferred to the anode via a solid electrolyte ionic conductor. The half-cell equations for oxygen include:

$$O_2 + 4e^- \rightarrow 2O^{2-} \quad Electrochemical \left(4e^-\right) \tag{17}$$
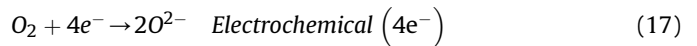
Thermodynamic calculations for the production of one product mole of gas should consider the change in Gibbs free energy (ΔG_{rxn}, kJ/mol) and electrochemical potential (E_{rxn}, V) using temperature dependent values of the entropy and enthalpy for each reactant and product species [56]. Equations used include:

$$\Delta G_{rxn} = \Delta H_{rxn} - T\Delta S_{rxn} \tag{18}$$

$$E_{rxn}(T) = -\frac{\Delta G_{rxn}}{nF} \tag{19}$$

where ΔH_{rxn} (kJ/mol) is the temperature dependent change in enthalpy of the reaction, ΔS_{rxn} (kJ/mol) the entropy change, T is the temperature (K), n the stoichiometric number of electrons involved, and F is Faradays constant (96485 J/mol/K). Results for the overall electrochemical potential of the three possible electrochemical reactions (Eqns (13)–(15) combined with Eqn (17) according to the number of electrons involved) and the Gibbs free energy change for the chemical reaction (Eqn (16)) are shown in Fig. 3.

The reversible potential in Fig. 3 [A] does not change significantly with temperature for the full four-electron oxidation of carbon to carbon dioxide, while reactions involving carbon monoxide are heavily temperature dependent. Indeed changes in the open circuit potential of the DCFC observed experimentally which vary from thermodynamically predicted values, and sensitivity of the open circuit potential to temperature, is often ascribed to the influence of carbon monoxide [57]. Chemical reaction of carbon to
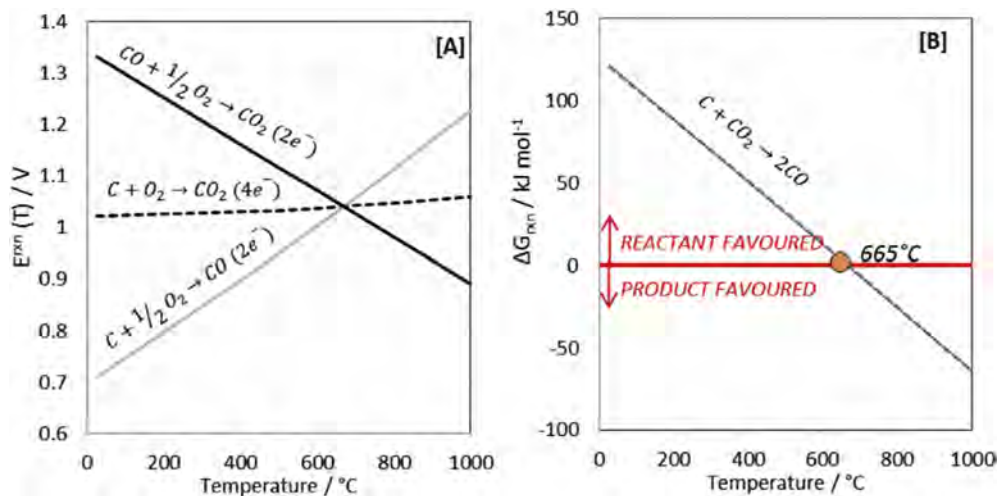
Fig. 3. [A] Overall electrochemical potential of reaction for production of 1 mol of product gas and [B] Gibbs free energy for chemical reaction to produce carbon monoxide (Bouduard reaction).

form carbon monoxide is also an area of great interest in both DCFC [58,59] and gasification applications [36]. Thermodynamically, this reaction becomes product favoured above 665 °C (Fig. 3 [B]). Kinetically, the reaction is slow without catalysts for thermal and coking coals investigated up to 900 °C [45], although impact of the Bouduard gasification reaction depends heavily on gasification environment, carbon type and catalysts used [36].

2.3.3.2. Electrochemical efficiency and performance. The final operational potential of the fuel cell (E_{op}) is dictated by a number of factors within the cell including ohmic (μ_{ohmic}), concentration (μ_{conc}) and activation (μ_{act}) overpotentials − which reduces the operating potential of the fuel cell and therefore the overall efficiency of the electrochemical reaction as follows [40]:

$$E_{op} = E° - \mu_{ohmic} - \mu_{act} - \mu_{conc} \tag{20}$$

$$\eta_{EC} = -\frac{E_{op} n_e F}{\Delta H_{rxn\ (T)}} \tag{21}$$

where n_e is the number of electrons transferred in the electrochemical reaction (Eqn (13)), F is Faraday's constant, $\Delta H_{rxn(T)}$ is the molar enthalpy of the reaction at a specific temperature (J.mol^{-1}) and $E°$ is the theoretical reversible potential.

However, in the case of high temperature fuel cells, this inefficiency is not necessarily 'wasted' as it introduces heat which may be required in the cell. In the case of SOFC's, generally more heat than required for the reaction is generated since a lower electrochemical efficiency is possible, and waste heat is therefore generated and preferably recovered during operation [37,38]. The amount of useable heat able to be generated in a fuel cell can be quantified using consideration of the overpotentials observed for an operating system, and fundamental consideration of system entropy [38]:

$$Q_{waste} = T(\Delta S_{(T)} - \sigma_{thermo}) \tag{22}$$

$$\sigma_{thermo} = \frac{n_e F}{T}(\mu_{ohmic} + \mu_{act} + \mu_{conc}) \tag{23}$$

where σ_{thermo} is the thermodynamic entropy production, essentially the irreversibility of the reaction, and Q_{waste} is the equivalent

'waste heat' generated per mole of carbon converted electrochemically (J.mol^{-1}).

Prediction of ohmic, activation and concentration overpotentials based on first principles is difficult and likely to be inaccurate at this stage of commercial development of the cell, and in particular in regards to realistic concentration overpotentials which will depend heavily on fuel cell design and how mass transfer of the carbon fuel is handled. In this modelling work therefore an estimation based on observed electrochemical performance on the lab scale is used, and a sensitivity analysis to this assumption carried out.

H° and S° are the standard enthalpy and entropy of formation which can be found as a function of temperature, applied to the Shomate Equation [60]. This can then be used to calculate the entropy and enthalpy of the reaction by balancing the products and reactants (same reaction applies to entropy calculation) as well as the number of moles of each involved in the reaction (shown as n and m here), i.e.:

$$\Delta H_{rxn(T)} = \sum n H°_{reactant} - \sum m H°_{products} \tag{24}$$

The relationship between Gibbs fee energy, enthalpy entropy and then reversible potential can then be used to calculate the expected $E°$ as a function of temperature.

$$E° = \frac{-(\Delta H_{rxn\ (T)} - T\Delta S_{(T)})}{n_e F} \tag{25}$$

The impact on operation of the overpotential has already been outlined above (i.e. determination of the amount of waste heat), however it also impacts on the operational current density through its relationship to the power density of the cell. Current density in particular is essential in determining flow rates of carbon fuel required to be input into the cell according to Eqn (13) (4 electrons generated per mole of carbon converted) and due to the interrelationship of power, current, potential, and charge i.e.:

$$P_{peak} = E_{op} \times i_{op} \tag{26}$$

$$\dot{n}_C = \frac{\dot{n}_e}{n_e} = \frac{Q}{n_e F} = \frac{i_{op} \times A \times t}{n_e F} = \frac{i_{op} \times \left(W_{total} \big/ P_{peak}\right) \times t}{n_e F} \tag{27}$$

where P_{peak} is the peak power density (mW.cm^{-2}), i_{op} is the operational current density (mA.cm^{-2}), $\dot{n}_C$ is the molar flow rate of

carbon (mol C.h^{-1}) for a set current density and assuming an overall output electrical power of the cell of W_{total} (mW in this equation) over a defined time period (1 h is the basis used here) to substitute for the reaction area, A (cm^2). $\dot{n}_e$ is the equivalent electron hourly need (mol e$^-$.h^{-1}) while n_e is the number of electrons involved in the oxidation reaction ($n_e = 4$ according to Eqn (13)).

It can be seen in Eqn (27) that the number of moles of carbon consumed (and therefore the mass feed rate of carbon, and ash-free coal char for a set carbon composition on a dry ash free basis) depends on the operational current density, which depends on the potential the cell is operated at for peak power density (Eqn (26)). Dependence on the total power output desired (10 kW in this case) and a reference time (feeds are calculated on an hourly basis in this work) are also included.

Literature studies evaluating DCFC performance have, to date, been limited to bench and lab scale cells. However consideration of the performance of these with focus on slurry arrangements can give a ball park figure for performance and would likely be conservative since further optimisation of a scaled up system would be able to be carried out. The maximum peak power density observed in a studies published to date using carbonate/carbon slurry arrangements is shown in Fig. 4 [A] as a function of operational temperature, while the measured open circuit potential for these systems is shown in Fig. 4 [B] along with theoretical reversible potential (E^o) calculated for electrochemical reactions possible within the cell as straight lines.

In some cases a very low initial open circuit potential is observed once reaction temperature is reached which suggests other side reactions, such as gasification, may be taking place within the cell. Some higher open circuit potentials extend beyond that expected even for electrochemical carbon monoxide formation, in particular that of Nabae et al. who reported an OCV of nearly 1.5 V at 800 °C [61]. The authors attributed this to utilisation of nickel catalysts and

subsequent electrochemical reactions, which are also commonly used by other authors. OCV variations can also originate from concentration overpotentials including those experienced at the cathode during oxygen reduction. The majority of papers published in this area also often report on a power density without specifying the area normalisation method used, i.e. cathode or anode current collection area, area of oxide membrane or other, meaning true power density is difficult to determine. This means a wide range of power densities have been reported which reflect no true relationship with temperature as might be expected considering observed changes in open circuit potential with temperature change [15]. In this work, power density of 150 mW cm^{-2} has been used as shown in Fig. 4 [A].

The operating voltage at peak power and subsequent current density is shown in Fig. 4 [C], with calculated electrochemical efficiency of this operational input (i.e. Eqn (25)) displayed in Fig. 4 [D]. In cases where operational data (such as potential/current at peak performance) were not specifically provided they were interpolated from potential-current graphs provided in the referenced works.

Surprisingly, little attention has been paid to electrochemical efficiency in the literature. Instead, discussion of carbon utilisation efficiency tends to dominate assessment of the performance of bench scale cells, which is mostly related to the influence of mass transfer limitations as well as reverse Boudouard consumption of fuel (see Fig. 2). This is also of merit, however a separate issue to electrochemical efficiency.

Generally, it is expected that as the operating current density increases the efficiency of the system will decrease, due to a number of factors including increased ohmic resistance. Ohmic resistance was determined to dominate in modelling of a specific DCFC set up by Liu et al. [41], where the ohmic resistance hinged on the thickness of the anode carbon bed, however in a hybrid system
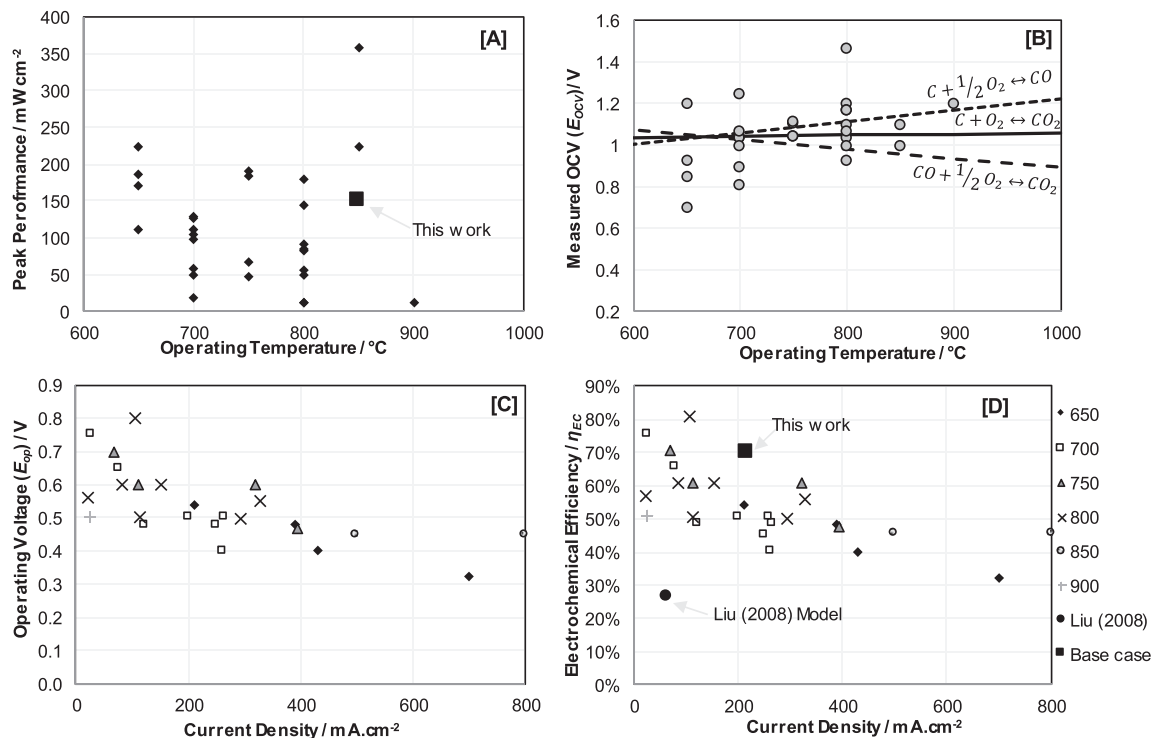
Fig. 4. [A] Literature reports for peak power density achieved in lab scale DCFC systems [B] measured open circuit voltage of lab scale systems [C] operating voltage and current density for peak power performance of literature systems [D] Calculated electrochemical efficiency (Eqn (25)) for literature systems. 650 °C [11,21,22,31], 700 °C [15,18,19,23,24,28,33], 750 °C [20,26,32,34], 800 °C [10,12−14,16,25,27,30,61], 850 °C [2,3], 900 °C [29].

this loss might be more reasonably expected to reside in the resistance introduced by the solid oxide membrane and in current collectors used at the anode and cathode. The model prediction for efficiency with current density given by Liu et al. [41] is shown in Fig. 4 [D], to be well below that obtained in real operating systems. It can be seen however in Fig. 4 [D] that the electrochemical efficiency observed in the majority of cases, and particularly in cells with high current density, is low, an average of only approximately 50% observed in the studies considered here — although this is still substantially higher than the very conservative efficiency calculated by Liu et al. [41]. In either case, the promised high theoretical efficiency of 100% of the system is not realised, which is potentially problematic for the uptake of the technology and in implications for overall system efficiency. This low efficiency could stem from a number of reasons, although it is most likely due to large losses in concentration overpotential, resistance imposed by the oxide membrane and sluggish activation of the carbon oxidation reaction [62].

2.3.3.3. Carbon loading. Limited work has also been carried out regarding the optimal carbon loading of the carbonate, in particular those which consider a flow-through model. As carbon loading is increased, it is expected that the viscosity of the melt will also increase to a point where the mixture no longer flows. Certainly this would be expected if the carbon composition dominated the carbonate component, as in the case of a 4:1, carbon:carbonate mixture as preferred by some investigations [13,14,16,20]. The loading will influence the effective carbon concentration and therefore the conversion expected per pass. A slurry loading of 40 wt% carbon has therefore been assumed in the base case to maintain presumably sufficient viscosity for flow, while also having a high carbon concentration and therefore conversion per pass although this will need further experimental work to confirm flow properties at this loading.

2.3.3.4. Endothermic Boudouard corrosion. As discussed in Section 2.3.2, the parasitic formation of carbon monoxide is likely to take place within the anode compartment. This becomes more prevalent at elevated temperatures and has been observed to occur for coal fuels both with and without a molten carbonate carrier [18].

The heat of the reaction of Eqn (14) is 184 kJ mol^{-1} at 850 °C using heats of reaction calculations discussed in Section 2.3.3 (Eqn (24)), the basis being moles of carbon consumed in the reaction.

This is an endothermic reaction and therefore the enthalpy of the corrosion is modelled as a loss within the anode compartment.

2.3.3.5. Modelling of oxygen/oxide cross over within the cell. Since the reaction includes a 1:1 mol ratio of oxygen to carbon the same molar flow rate of oxygen is required as carbon, needed for the electrochemical conversion (i.e. $\dot{n}_C = \dot{n}_{O_2}$). This is firstly converted to mass of oxygen converted per hour, and an additional conversion/utilisation assumption added. In some SOFC models up to 80% or higher conversion per pass is assumed [37,38], while here modelling 75 wt% conversion of oxygen is assumed to be realistic as an estimate in the base case. This will depend heavily on the final arrangement chosen for the cathode arrangement and design parameters. The total moles of oxygen required to be fed to the system can then be calculated, and, assuming air is made of 20.95 vol% oxygen with the balance made with nitrogen, the full air flow rate on a mass basis can be calculated.

The anode and cathode compartments have been modelled separately in this work, as shown in Fig. 1. The oxygen converted at the cathode must travel through the solid membrane as oxide, where it then reacts at the anode current collector interface to form carbon dioxide. It is assumed that the enthalpy of the oxygen being reacted at the cathode is transferred from the cathode to the anode and is available at the anode as a heat input in order to allow an overall heat balance on the fuel cell to be carried out. No other heat generation of transfer from the cathode is assumed and all electrochemical overpotential heating is assumed to reside in the anode and be available for slurry heating. The input used for the cathode operational temperature is set at 850 °C, assumed to be the operational temperature of the fuel cell.

2.3.3.6. Overall heat management/assumptions in the fuel cell. Heat management within the fuel cell as assumed in the model is shown in Fig. 5.

Anode and cathode are balanced separately with the enthalpy balance managed through modification of the output stream temperatures where both slurry and gas temperatures are assumed to be the same. The overall enthalpy balance for the anode and cathode are based on principles of conservation of heat (of all streams against a reference temperature of 20 °C) as follows:

$$\text{CATHODE:} \Delta H_{A,i} = \Delta H_{OT} + \Delta H_{A,o} \qquad (28)$$
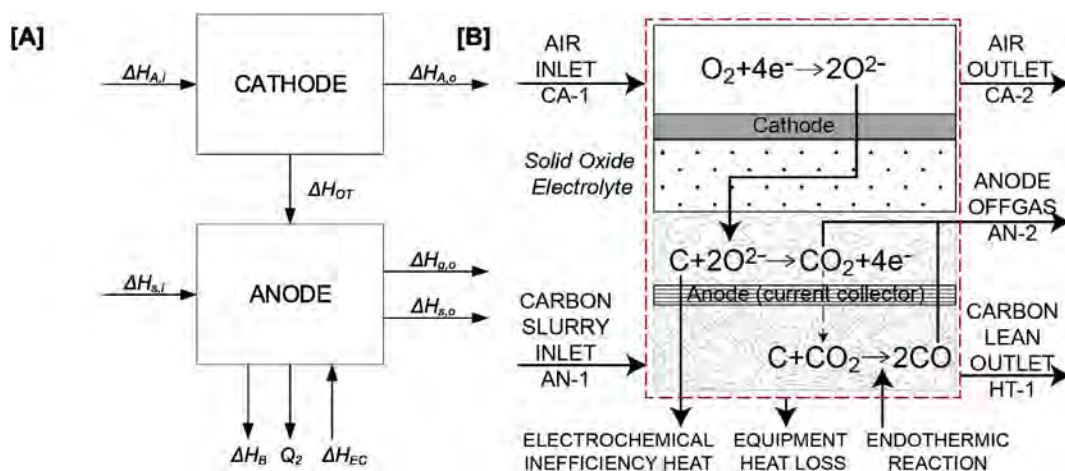
Fig. 5. [A] Enthalpy balance within the DCFC anode and cathode components [B] Physical/chemical representation of enthalpy balance.

ANODE: $\Delta H_{s,i} + \Delta H_{EC} + \Delta H_{OT} = \Delta H_B + Q_2 + \Delta H_{g,o} + \Delta H_{s,o}$

$$\text{(29)}$$

where enthalpy nomenclature and relevant material streams/ equations are defined in Table 2.

2.3.4. Heat recovery from streams and overall efficiency calculation

In order to gain an understanding of the total efficiency of the system, the total required input energy to the process must be known, and the amount of potential heat able to be recovered from within the process can be considered to meet this need. Note that this model is for steady state operation only and initial heat up of the fuel cell system is not considered. As discussed in Section 2.2.3, the enthalpy balance for the process has been carried out through referencing of heat for material streams from a reference temperature to the operational temperature. The reference temperature has been chosen to be ambient temperature to enable consideration of these heat flows into and out of the process also from a total heat transfer perspective.

Pyrolysed coal char and top-up carbonate are assumed to enter the process at the ambient reference temperature of 20 °C. The bulk of the slurry does not require heating at steady state since it is recycled. Instead heat loss from the slurry is considered in the model through irreversible equipment losses to the surroundings (i.e. Q_1, Q_2 and Q_3).

Air inlet to the cathode is modelled to be introduced at the reaction temperature, and this represents a significant heat input requirement of the process. The total enthalpy change of this stream from ambient temperature to the reaction temperature can be used to estimate the heat input required for this process, i.e. $\Delta H_{A,i}$ (kJ/h). In the base case, this value is close 7.5 kW which, for a 10 kW system, is a significant energy penalty.

Potential heat that may be available to meet this need from within the cycle include the outlet cathode air stream ($\Delta H_{A,o}$), the outlet anode gas stream ($\Delta H_{g,o}$) as well as any waste heat that may be generated from overheating of the carbonate slurry in the fuel cell.

In order to maintain the energy balance of the process, the temperature of the slurry entering the heated char mixer must be consistent, assumed to be 900 °C in the model to allow for expected cooling which occurs on introduction of the room temperature coal char and top-up carbonate, and is controlled in the model by assumptions in the recycled slurry holding tank. If the temperature of the slurry leaving the fuel cell is less than or equal to 900 °C, additional heat input is required for this unit operation, Q_4 (which is heat required in addition to the cathode inlet air stream enthalpy). If, however, the slurry leaves at an elevated temperature, then some of this heat must be removed and this can be included in the heat recovered from the process (also denoted as Q_4). It is more difficult to fully recover heat however for a relatively viscous and corrosive stream compared to a gas steam. Therefore the amount of heat able to be recovered from these streams has been assumed to be 75% of the gas streams, and only 50% of the slurry stream.

The total shortfall of the system (in kW, converted from kJ/h) can then be calculated as follows depending on the temperature of the carbon-lean slurry leaving the fuel cell anode compartment (stream HT-1):

$$W_{parasitic} = \frac{\Delta H_{A,i}}{3600} - 75\% \times \frac{\Delta H_{A,o}}{3600} - 75\% \times \frac{\Delta H_{g,o}}{3600} - 50\% \times \frac{Q_4}{3600} \quad \text{T}_{\text{slurry}} > 900°\text{C} \quad \text{(30)}$$

$$W_{parasitic} = \frac{\Delta H_{A,i}}{3600} + \frac{Q_4}{3600} - 75\% \times \frac{\Delta H_{A,o}}{3600} - 75\% \times \frac{\Delta H_{g,o}}{3600} \quad \text{T}_{\text{slurry}} \leq 900°\text{C}$$

$$\text{(31)}$$

The overall energy efficiency of the process, considering calorific value of input char can then be considered. The total input of coal char to the process is calculated from stream CM-1. Taking the actual carbon component of this stream (which depends on the elemental carbon content of the char, see Section 3.1), the total input heat which may be generated from the complete oxidation of the carbon can be calculated from the reaction enthalpy, calculated from first principles, of 383 kJ mol^{-1} of carbon entering the fuel cell system. This gives us the maximum possible energy which could theoretically be extracted from the coal (W_{cal}). The system has been designed to give a 10 kW output (W_{net}) which is the total design output (W_{total}) minus the parasitic losses incurred from heating, and therefore total efficiency of the system can be calculated from Eqn (32):

$$\eta_{system} = \frac{(W_{total} - W_{parasitic})}{W_{cal}} = \frac{W_{net}}{W_{cal}} \quad \text{(32)}$$

3. Model results

3.1. Base case model outputs and overall efficiency

A summary of important base case assumptions is outlined in Table 3 which have been used to build the base case of the model.

The base case has been built to incorporate assumptions for the cell which are possible in a best case scenario at the present time, while the sensitivity analysis in Section 3.2 will give an overview of efficiency outcomes based on variation of key assumptions. Total efficiency has been focused on as a key performance metric of the system at this stage since it is a major selling point of the technology. Carbon intensity of the process is also commented on and compared to other energy technology options in Section 3.3.1.

The model also depends to some extent on the composition of the coal char since this will influence both the amount of carbon feed required (carbon conversion only considers carbon component of the char as discussed in Section 2.3.3), as well as heat capacity values of the material streams as outlined in Section 2.3.1. The char properties chosen are a base case for slow pyrolysis of a moderate ash composition thermal coal char treated to a higher heating temperature (HHT) of 800 °C the char examined electrochemically in previous work [45,63]. Properties used here are shown in Table 4 while sensitivity analysis to coal ash composition is carried out in Section 3.2.2.

Overall power inputs for the base case model are compared in Fig. 6 [A], in units of kW.

The total input calorific value of carbon to the process is calculated from coal char required to be added to stream CM-1, which was found to have a feed rate of 2.0 kg/h of coal char in order to maintain an overall electrical energy output of 10 kW in the base case. The final efficiency of the process is:

$$\eta_{system} = \frac{W_{net}}{W_{cal}} = \frac{10.0}{14.22} = 70.4\%$$

The system efficiency is slightly higher than the electrochemical efficiency in the base case scenario. A higher efficiency than the electrochemical efficiency can be realised through the way the system efficiency is calculated. Electrochemical conversion

Table 3
Summary of base case assumptions.

η_{conv}	Carbon electrochemical conversion per pass (C1, Fig. 2)	75%	wt%
L_c	Feed Ratio Coal Char (db): Carbonate	40%	wt%
	Carbon dioxide reacted chemically per pass	5%	wt%
	Oxygen electrochemical conversion per pass	75%	wt%
η_{EC}	Electrical conversion efficiency/over potential for fuel cell	70%	
P_{peak}	Power density	150	mW.cm^{-2}
E^o	Thermodynamic reversible potential at 850 °C	1.05	V
E_{op}	Actual operating potential	0.70	V
i_{op}	Operating current	216	mA.cm^{-2}
W_{net}	Net output power	10	kW
	Equipment heat loss	5%	

Table 4
Coal char feed properties.

Coal char feed moisture	wt% (as received)	2.0%
Coal char ash composition	wt% (dry basis)	10.0%
C	wt% (dry ash free basis)	92.3%
H	wt% (dry ash free basis)	0.8%
N	wt% (dry ash free basis)	1.9%
O	wt% (dry ash free basis)	4.8%
S	wt% (dry ash free basis)	0.3%

efficiency depends on the current density generated from the amount of input char to the fuel cell (AN-1, C1 in Fig. 2), whereas the overall efficiency is calculated from the calorific value of input of coal char to the *process* (CM-1) — which is also intrinsically dependant on the carbon conversion rate per pass of the cell and the recycled potion of the slurry. Since the amount of coal char input to the DCFC depends on the recycle proportion in addition to the carbon conversion per pass, when the carbon conversion per pass increases, less overall input coal char is needed to the fuel cell, meaning slightly less carbon is required to be added to the system overall in a balance between the amount recycled and the amount consumed, and W_{cal} decreases also. There is also some calorific value lost in the carbonate dump stream of the process (HHV C, HT-2) and in the carbon monoxide generated through reverse Boudouard corrosion (HHV CO, AN-2).

Overall power into the system compared to power out is balanced as shown in Fig. 6 [B], in units of kW. This includes internal heat generation (from electrochemical inefficiency) and

consumption (from reverse Boudouard corrosion) of the process as well as irreversible equipment heat losses. It can be seen that the largest power input to the process is the cathode inlet gas, which is assumed to be heated from ambient temperature to the reaction temperature of the DCFC (850 °C) in the process. The amount of heat generated from electrochemical overpotential is less, but still substantial in comparison to heat losses assumed for the equipment of the process and to the power lost from Boudouard corrosion in this case (ΔH_B).

Parasitic power required to bring the cathode inlet flow to reaction temperature in the process is calculated as outlined in Section 2.3.4, Eqn (30) and the proportion of power recovered from each stream is shown in Fig. 6 [C]. A large amount is recovered from CA-2 while Q_4 gives only a small contribution to meeting this requirement. A marginal amount of parasitic power input is required to bring the cathode inlet stream to reaction temperature in this scenario (0.03 kW), being however mostly self-sustaining in terms of heating requirements.

Other important values in terms of operating temperatures and material feed rates are provided in Supplementary Material Table S1, in comparison of other key operational scenarios discussed in the following section.

3.2. Sensitivity analysis

3.2.1. Electrochemical fuel cell efficiency

The electrochemical efficiency of the fuel cell is a key performance metric for any fuel cell system. In this case 'efficiency' will
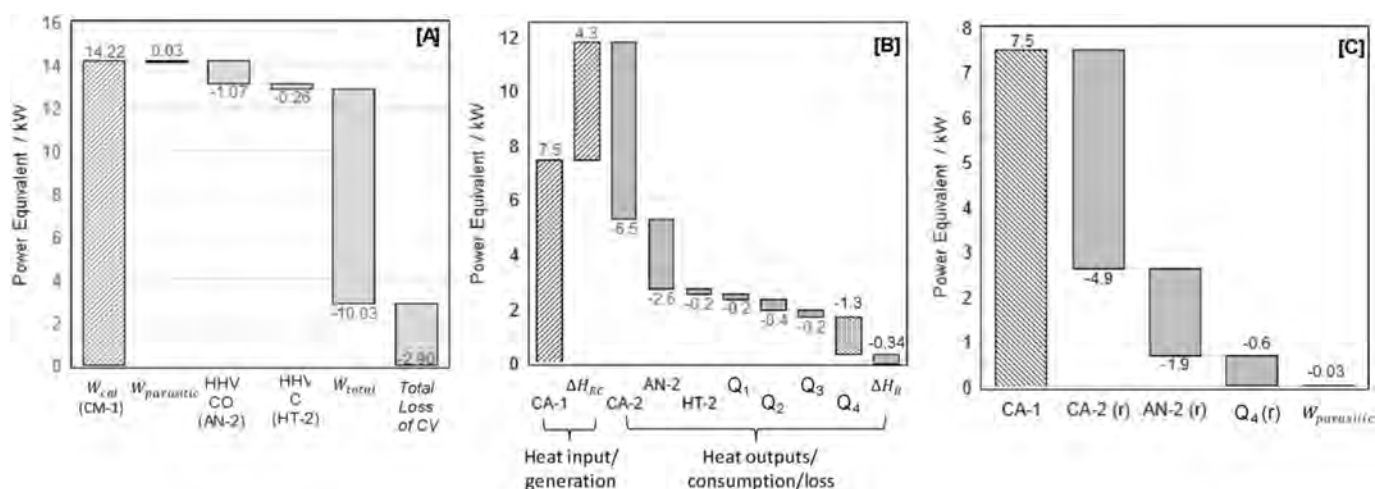
Fig. 6. Base case power requirements and outputs in kW [A] Calorific value (CV) and power input comparison for consideration of total CV loss across the system [B] Overall balance of all process heat inputs and outputs including heat generation and consumption as well as equipment heat loss (refer to Fig. 1 for process stream information) [C] Power recovery balance for providing heat to inlet cathode air stream including portions recovered from hot outlet streams (see Eqns (30) and (31)) and remaining additional input power required.

determine both the amount of coal feed and air flow required to achieve the operational output goal of the 10 kW cell, as well as the amount of waste heat generated in the system. This will have flow on effects for the parasitic power need and, as a result, on the overall system efficiency.

The final overall system efficiency as a function of the assumed electrochemical efficiency has been calculated for a balanced model, shown in Fig. 7, along with waste heat generated and parasitic power inputs calculated to be required for the process.

At low electrochemical efficiency, the final system efficiency is identical since the amount of waste heat generated allows for full recovery of energy and no additional heat inputs are required. The waste heat which is generated is calculated after removing that required for the cathode inlet stream and is calculated in the same way as $W_{parasitic}$ (i.e. Eqns (30) and (31)). It can be seen that for low electrochemical efficiency W_{rec} is substantial. For example in the 30% efficiency case if W_{rec} were able to be transformed directly into electrical energy, it would increase the efficiency by over 20%, as also indicated in Fig. 7. Since the amount of collectable heat would require further transformation before use, and incur losses, this is an upper bound on the possible efficiency for this scenario. Indeed other authors who have assumed efficiencies this low have tried a number of methods to realistically capture this waste heat, with only small efficiency gains (<5%) realised [39,40]. Parasitic input energy required for the process is not substantial, even in the case of only small amounts of waste heat generation, i.e. 90%. From this viewpoint it would therefore be far preferable, from an emissions perspective, to operate at high efficiency rather than operating a sub-performing cell in the hope of extracting useable waste heat —assuming the cell can be self-sustaining in terms of heat inputs. 70% electrochemical efficiency is the balance point of parasitic energy for the base case scenario and is likely achievable. 80% electrochemical efficiency is likely to be far more difficult to achieve
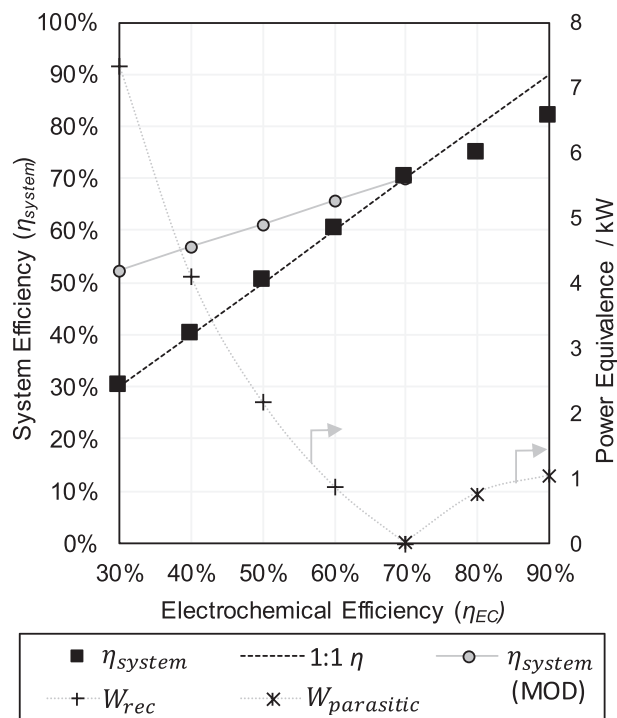
in a real system in the short term and without significant improvement to ohmic resistance introduced by solid oxide membranes and activation overpotential resulting from slow carbon oxidation kinetics. Some catalytic work has been done in this area [63], but more is needed to address this crucial operational parameter.

It can also be seen in Table S1 that the operational temperature of the anode side of fuel cell appears to be extremely high in this case. This is because the model does not remove this heat until the slurry holding tank. In reality, heat would need to be removed from the fuel cell itself to prevent such extreme overheating. This is not thought to present an issue for the model, however, as the calculation for fuel cell performance is still based on the set temperature of 850 °C, which is also what the cathode inlet and outlet streams are set at also.

3.2.2. Coal Char Ash, carbon and oxygen conversion per pass, and slurry loading

Several other inputs used in the model are based around assumptions which could impact on the final output of the model. Some of these have major impacts on outcomes, while others are more moderate. Moderate impacts have been found to include variation in:

- *Coal Char Ash loading (CCA)*: Impact of starting ash content of coal fuel, wt% on a dry basis. Ash displaces carbon component of fuel and means a higher feed rate of coal char is required for less electrochemical benefit.
- *Carbon Conversion Per Pass (CCPP):* The amount of carbon converted to carbon dioxide electrochemically depends on the final cell arrangement. The amount converted also translates to the amount recycled within the cell, and the amount required to be topped up on an hourly basis. When this number is higher than the electrochemical efficiency a higher overall system efficiency can be observed.
- *Oxygen Conversion Per Pass (OCPP)*: The amount of oxygen converted per pass will impact on the flow rate of air required to match the electrochemical output of the carbon oxidation, increasing the flow rate will impact on the amount of heat needed to bring the air stream to the reaction temperature of 850 °C.
- *Slurry Loading (SL):* The slurry loading impacts on the amount of carbon contained within the carbonate fed to cell, a more concentrated stream could have flow issues also, however these are not considered here and instead implications of conversion and recycle streams are investigated based on the slurry loading used.

In order to compare the impact of variation of these components, one variable at a time has been investigated while keeping others at the base case value. Limits of plus or minus 20% of the initial value have been investigated, as specified in Table 5.

Impact of the variation has been investigated through the final system efficiency measured (η_{system}), and the final energy balance of the process, i.e. whether additional parasitic energy input is required ($W_{parasitic}$) or whether a net heat output is observed for the process (W_{rec}). Results have been compared against the base case for all scenarios in Fig. 8.

It can be seen that increase from the base case in the SL and OCPP do not impact on the final system efficiency, but that these changes do result in an increase in the recoverable heat output of the process. OCPP in particular impacts this value since increased conversion translates directly to lowered flow rate and therefore a smaller amount of energy required to heat the stream to reaction temperature.


Fig. 7. Impact of electrochemical efficiency on overall system efficiency. η_{system} (MOD) is the efficiency of the system if the recovered heat (W_{rec}) of the system were able to be directly converted to an electrical energy ouput (i.e. Eqn (32) including addition of W_{rec} in the numerator).

Table 5
Values used in sensitivity analysis of moderate impact variables on system efficiency.

VARIATION	CCA	CCPP	OCPP	SL
	wt% (db)	wt% of DCFC inlet	wt% of DCFC inlet	wt% (db)
−20%		55%	55%	20%
−10%	0%	65%	65%	30%
Base	10%	75%	75%	40%
+10%	20%	85%	85%	50%
+20%	30%	95%	95%	60%

System efficiency increase beyond the base case is observed for an increase in the CCPP. This is a result of the way that system efficiency is calculated, as discussed earlier. Since the carbon conversion per pass increases, the amount of coal char required to be continuously topped up to the process decreases, along with the calorific value of this input, which is used to calculate W_{cal} and η_{system}. Since the output power does not change, this then increases the overall system efficiency beyond even the electrochemical efficiency of the cell.

Reduction in the CCA is not seen to impact on the efficiency, although slightly more waste heat is generated. Increase in CCA does have consequences for the parasitic energy required and therefore the final system efficiency. The base case used of 10 wt% ash is reasonable for coal char [45], slightly on the low side, and a higher value is equally likely depending on the coal source and type. As well as impacting on the carbonate contamination and recovery, as previously known [55], the char ash can also be seen here to have a direct negative impact on system efficiency also.

The largest reduction in system efficiency in these moderate cases however is seen to be the OCPP. Ideally no additional energy input or output for the system would be observed, as is the case for the base scenario where only a minor parasitic input is required. Waste heat is difficult to recover and does not easily translate to efficiency gains, while parasitic energy input may actually need to be higher than assumed here depending on the method of providing the heat due to the energy transformations involved. Large losses due to parasitic heat inputs required are seen for low oxygen conversions, reducing the system efficiency by almost 5% in the case of only 55% conversion of air.

3.2.3. Extent of Reverse Boudouard corrosion and equipment heat losses

Reverse Boudouard corrosion of carbon fuels is known to occur within molten carbonates under CO_2 atmospheres [18], particularly at elevated temperatures. The reaction is doubly problematic in the DCFC as it consumes both the carbon reactant in a side reaction which does not directly contribute to electrochemical performance, as well as consuming heat within the cell since it is an endothermic reaction. Consumption of the carbon within the cell through Boudouard corrosion means a greater input of coal char must be used to account for this loss. The carbon monoxide generated through the process does, however, represent a potential energy source and could be burnt to release its calorific value as heat or, preferably, electrochemically transformed, i.e.:

$$CO_{(g)} + O^{2-} \rightarrow CO_{2(g)} + 2e^- \tag{33}$$

Electrochemical oxidation of carbon monoxide has not been considered here and it is assumed that all CO formed will be present in the anode gas stream leaving the process (AN-2). Consideration of the impact of this reaction on the system efficiency is shown in Fig. 9, which also includes the potential collectable energy of the carbon monoxide generated, the parasitic energy input required and the amount of carbon consumed through the corrosion.

The amount of carbon consumed is calculated through the amount of the carbon component only of the coal char entering the DCFC anode compartment, i.e. C1+C2+C3 (Fig. 2). It can be seen that the corrosion increases the parasitic energy required to be input to the process, decreasing the system efficiency, however the biggest impact on the efficiency is actually realised through the increased amount of coal char which is required to be fed to the DCFC as a result of parasitic consumption. An increase in only 10% of the amount of carbon consumed through this reaction can be seen to change the efficiency of the system by more than 10%, which is significant. The amount of carbon monoxide produced is however substantial with almost 5 kW of additional potential energy in the form of carbon monoxide production. It may be possible in such cases, where carbon corrosion is observed to be substantial, to offset this loss through the use of a complimentary solid oxide fuel cell or through inbuilt DCFC design to convert the CO electrochemically formed within the cell, as is the case with DCFC systems which purposely use indirect carbon oxidation [5].

Equipment heat loss is also another avenue of large impact on system performance and generally represents the heat input required to maintain the carbonate slurry temperature. Operation at elevated temperatures means radiative heat loss from equipment could be substantial if not carefully managed. Losses from
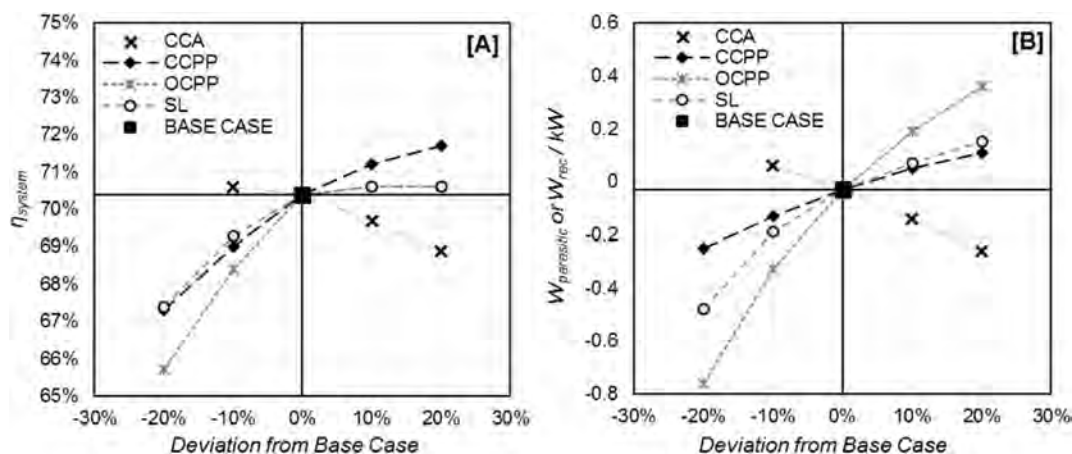
Fig. 8. Sensitivity analysis results for [A] system efficiency and [B] total parasitic power use ($W_{parasitic}$) or waste heat generation (W_{rec}).
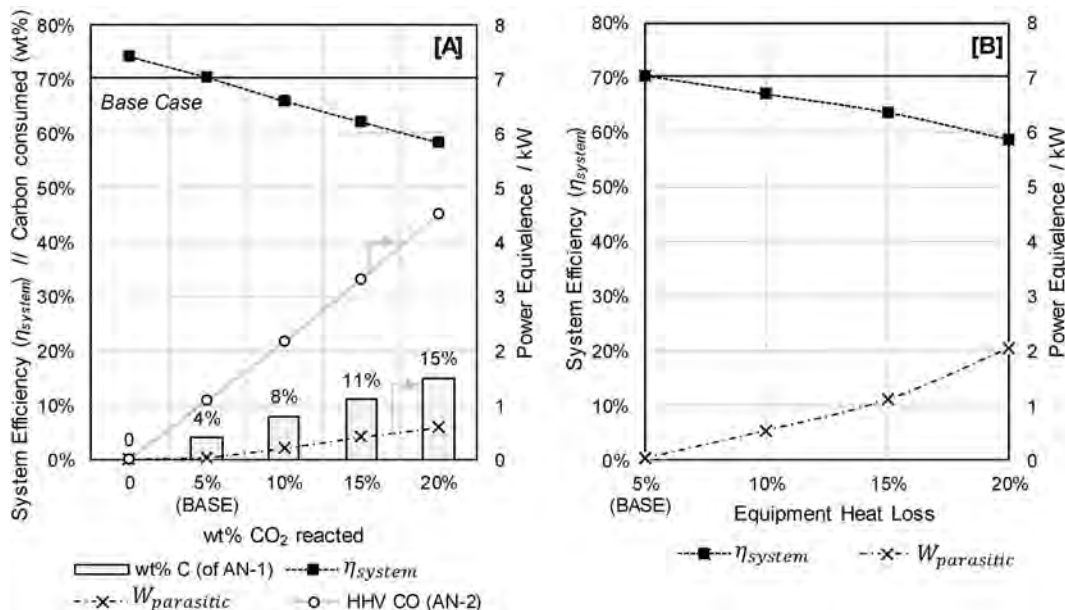
Fig. 9. Sensitivity of process outputs to [A] extent of reverse Bouduard corrosion within the anode compartment of the fuel cell including the calorific value representing the carbon monoxide generated during the process [B] heat loss of equipment including Q_1, Q_2 and Q_3 and resultant parasitic power use requirement for the process.

equipment only have been assumed here, however could also occur through transfer lines. As expected, shown in Fig. 9 [B] if equipment heat loss begins to exceed 5%, the amount of input parasitic energy required increases substantially, more than double observed for efficiency losses in the case of increased carbon corrosion in Fig. 9 [A]. In the case of Boudouard corrosion, the biggest impact on efficiency is related to consumption of the carbon reactant, while in the case of the heat loss this is mainly due to the additional parasitic energy required to heat the inlet cathode stream since far less excess heat is available. 20% loss was seen to be the furthest extent of heat loss possible since this means a decrease in the slurry temperature to less than 500 °C for stream AN-1 (Table S1), which is borderline acceptable considering the melting point of the eutectic at 386 °C [55].

3.3. Commercial DCFC challenges, opportunities and comparative emissions

Analysis shown here gives a range of performance values which could be expected in a carbon slurry DCFC arrangement. The biggest impact on the cell performance is seen clearly to reside in the electrochemical efficiency achievable for the system. Some promising results have been seen in this area, and an aim of minimum 70% electrochemical efficiency should be used in slurry systems based on achievable bench scale results to date. Increased efficiency can be reached by reducing the overpotential of the carbon oxidation reaction. This can be addressed through consideration of the contributions to overpotential including activation, ohmic and concentration polarisation. Use of catalysts [63] or mediators [28] could see improvement in activation polarisation. Improvement to ohmic polarisation requires careful cell design and improved solid oxide conductors in hybrid systems. Choice and use of current collectors at the anode and cathode will also likely impact heavily on this polarisation loss. Concentration overpotential can be addressed through optimisation of mass transport within the anode compartment, although will likely remain significant in a system reliant on delivery of a particulate fuel to the reaction surface. If these are able to be improved, then it can be

seen clearly here that, despite a reduction in the waste heat generated, better system efficiency and therefore emission intensity outcomes will be realised. Indeed a system which utilises all waste heat internally gives the best expected outcome for the system.

Electrochemical efficiency must also however be balanced with other sources of inefficiency in the system. As discussed here, the largest impacts apart from electrochemical efficiency can be seen to stem from the rate of oxygen conversion per pass, the extent of carbon corrosion and expected unrecoverable heat loss from equipment. An electrochemical efficiency of >90% along with large heat loss from equipment would mean substantial parasitic energy inputs are required, which would have a heavy impact on the overall system efficiency. Good management and understanding of carbon corrosion within the system is also essential and if unable to be kept within approximately 10% of carbon fed to the cell should consider recovery of carbon monoxide energy either within the system or in an additional external unit operation such as a solid oxide fuel cell on a smaller scale.

3.3.1. Carbon emissions

Carbon dioxide is produced in a pure stream in the process, although some contamination from carbon monoxide will be expected due to Boudouard corrosion, as discussed. Depending on the final use of the carbon dioxide stream, and final system performance, the carbon monoxide could be converted to carbon dioxide in a small solid oxide fuel cell system, or combusted in an oxygen adjusted carbon dioxide stream to generate increased waste heat for recovery. The amount of pure oxygen required would be expected to be very small, only required to offset the small amount of CO generated, and therefore efficiency losses from oxygen separation technologies would be expected to be minor and either additional electrical output from the fuel cell or heat generation for internal use could aid in offsetting this parasitic use. The presence of other contaminants is not expected in the flue stream. Sulphur components have been shown to demonstrate affinity for the molten alkali carbonate system [64] while the absence of nitrogen for combustion would be expected to eliminate any expectation of

Table 6

Comparative life cycle carbon emissions (kg CO_2/MWh) and process efficiency for DCFC technology compared to coal fired power plants with and without carbon capture and storage options, Average coal fired power station (CFPS) for sub-critical pulverised plant and state of the art ultra-supercritical coal fired power station (USC CFPS) included.

	DCFC (this work)		Average CFPS		USC CFPS	
	CO_2 emissions	Process efficiency	CO_2 emissions	Process efficiency	CO_2 emissions	Process efficiency
Thermal conversion only	567		976		749	
No CCS (LCA)	647	70%	1092	35%	837	46%
With CCS (LCA)	93	66%			243	35%

nitrous oxide emissions. Particulates are similarly not expected, although some small vaporisation of the carbonate stream might be expected and could be handled while cooling of the off-gas.

In the base case scenario, a carbon emission intensity of 567 kg CO_2/MWh has been calculated. The anode gas stream however does not require further processing as discussed for carbon dioxide capture, only compression and transport if the intention is to use carbon sequestration to limit emissions, which is known to constitute only a small portion of the energy needed for traditional coal fired power plants with carbon capture and storage options [42]. Alternatively, other emerging carbon dioxide utilisation and conversion processes could be employed [65]. Since a 10 kW DCFC is expected to be used in a distributed network, it is expected that the carbon dioxide would be compressed and stored on site until being transferred to a processing facility. No losses in the carbon dioxide captured from the fuel cell would be expected, unlike other carbon capture technologies which are often limited to capturing only 90% of carbon dioxide emissions through processes using MEA as chemical absorbent for example [42]. The emissions from the process would therefore be limited to those needed for auxiliary operations before and after the technology including transport and coal production, and other pre-processing. Carbon emission intensity (for the base case, this is slightly improved in the case of increased electrochemical efficiency if this is able to be realised as shown in Table S1) is compared to other low carbon technologies which utilise coal as a fuel in Table 6.

The estimate for carbon emissions from a DCFC system in Table 6 with no carbon capture for a life cycle assessment (LCA) assumes all CO_2 from the system (567 kg CO_2/MWh), plus the emissions given for the coal supply chain in the case of the high efficiency coal plant of Ref [42] (80 kg CO_2/MWh). This is potentially an overestimate since the higher efficiency of the DCFC means that less coal is required per MWh of electricity produced, reducing shipping and processing costs, although different pre-processing requirements will exist for the DCFC (including pyrolysis to remove volatile matter) which might be expected to increase the emissions slightly to offset this assumption. In the case of capture/sequestration emissions for a DCFC system, an estimate of the electrical energy required for the compression, transport and sequestration of the carbon dioxide have been taken from Ref. [41] and is calculated to contribute an additional 0.7 kW of parasitic energy to the 10 kW system and result in a reduced process efficiency of less than 5% as a result, as shown in Table 6. The emissions from this process in the case of capture and sequestration do not include any losses from the DCFC system, since no additional capture process is required, and include carbon emissions estimated in the case of the high efficiency plant for the coal supply chain (80 kg CO_2/MWh) plus the emissions resulting from the high efficiency plant with CCS (13 kg CO_2/MWh). Once again this is an overestimate since CCS equipment and inefficiencies are included. This means DCFC technology with effective carbon capture options could achieve an emission intensity of approximately 93 kg CO_2/MWh.

For comparison, life-cycle emissions from renewable sources including solar photovoltaic and wind energy have been estimated

in the ranges of 40−160 kg CO_2/MWh and 3−35 kg CO_2/MWh [66] respectively. If storage using commercial lithium ion batteries is included in this estimate, emissions (related to battery manufacture only) increase by 47 kg CO_2/MWh using figures supplied by Ref. [67] of 3.5 kg CO_2/kg Li-ion battery and energy density of 75 W h/kg. This makes carbon emissions from a DCFC system potentially comparable to those expected using renewable energy.

4. Conclusion

Mass and enthalpy balance modelling is shown here to be a useful tool to investigate theoretical overall system efficiency for a model direct carbon fuel cell system. The integrated process approach used here has allowed deeper understanding of the true interplay of several process variables on the energy balance, including electrochemical efficiency and the impact of Boudouard corrosion, while also demonstrating a more realistic understanding of the heat used internally in the process and consideration of additional parasitic energy use which may be required. The electrochemical efficiency of the DCFC system has been shown to be the most important value in determining the overall system efficiency. The balance point determined, where no additional heating was needed, was seen to be 70% electrochemical efficiency, which allows generation of enough waste heat within the system to allow almost complete self-heating of streams. This has not yet been observed on the bench scale for these systems, however looking at a range of literature data appears to be realistic if researchers are able to optimise activation, ohmic and concentration polarisation losses. Other major areas of optimisation include ensuring high oxygen conversion per pass to avoid excessive amount of parasitic energy to heat this stream, as well as limiting the corrosion of carbon through the reverse Boudouard reaction. If Boudouard corrosion becomes substantial, consideration of the anode off-gas treatment and recovery of calorific value of this steam will become important.

Although there is still much that needs to be proven with DCFC technology, the ability of this technology to reduce greenhouse gas emissions to the same level as renewable energy sources is shown to be theoretically possible here. If biomass based fuels were alternatively used, the technology would represent a net reduction in emissions if successfully combined with carbon dioxide removal processes since they are considered a carbon neutral fuel source. This all hinges on the achievable efficiency of the system and for a DCFC technology to be competitive with other low emission coal or even renewable energy types on an emission basis.

Appendix A. Supplementary data

Supplementary data to this article can be found online at https://doi.org/10.1016/j.electacta.2019.135131.

References

[1] R.D. Weaver, L. Nanis, Electrochemical oxidation of carbon in a molten car-bonate coal-air fuel-cell, J. Electrochem. Soc. 127 (1980). C410-C410.
[2] J.-Y. Lee, R.-H. Song, S.-B. Lee, T.-H. Lim, S.-J. Park, Y.G. Shul, J.-W. Lee, A performance study of hybrid direct carbon fuel cells: impact of anode microstructure, Int. J. Hydrogen Energy 39 (2014) 11749–11755.
[3] B. Ahmed, S.-B. Lee, R.-H. Song, J.-W. Lee, T.-H. Lim, S.-J. Park, Development of novel LSM/GDC composite and electrochemical characterization of LSM/GDC based cathode-supported direct carbon fuel cells, J. Solid State Electrochem. 18 (2014) 435–443.
[4] J. Hanna, W.Y. Lee, Y. Shi, A.F. Ghoniem, Fundamentals of electro- and ther-mochemistry in the anode of solid-oxide fuel cells with hydrocarbon and syngas fuels, Prog. Energy Combust. Sci. 40 (2014) 74–111.
[5] T.M. Gür, M. Homel, A.V. Virkar, High performance solid oxide fuel cell operating on dry gasified coal, J. Power Sources 195 (2010) 1085–1090.
[6] A. Jayakumar, R. Kungas, S. Roy, A. Javadekar, D.J. Buttrey, J.M. Vohs, R.J. Gorte, A direct carbon fuel cell with a molten antimony anode, Energy Environ. Sci. 4 (2011) 4133–4137.
[7] C.R. Jiang, J.J. Ma, A.D. Bonaccorso, J.T.S. Irvine, Demonstration of high power, direct conversion of waste-derived carbon in a hybrid direct carbon fuel cell, Energy Environ. Sci. 5 (2012) 6973–6980.
[8] T.M. Gür, Mechanistic modes for solid carbon conversion in high temperature fuel cells, J. Electrochem. Soc. 157 (2010) B751–B759.
[9] R. Agarwal, Design and Modeling of a Novel Direct Carbon Molten Carbonate Fuel Cell with Porous Bed Electrodes, Virginia Polytechnic Institute and State University, 2015.
[10] B. Cantero-Tubilla, C.C. Xu, J.W. Zondlo, K. Sabolsky, E.M. Sabolsky, Investi-gation of anode configurations and fuel mixtures on the performance of direct carbon fuel cells (DCFCs), J. Power Sources 238 (2013) 227–235.
[11] M. Chen, C. Wang, X. Niu, S. Zhao, J. Tang, B. Zhu, Carbon anode in direct carbon fuel cell, Int. J. Hydrogen Energy 35 (2010) 2732–2736.
[12] N.J. Cherepy, R. Krueger, K.J. Fiet, A.F. Jankowski, J.F. Cooper, Direct conversion of carbon fuels in a molten carbonate fuel cell, J. Electrochem. Soc. 152 (2005) A80–A87.
[13] A.C. Chien, A. Arenillas, C.R. Jiang, J.T.S. Irvine, Performance of direct carbon fuel cells operated on coal and effect of operation mode, J. Electrochem. Soc. 161 (2014) F588–F593.
[14] A.C. Chien, G. Corre, R. Antunes, J.T.S. Irvine, Scaling up of the hybrid direct carbon fuel cell technology, Int. J. Hydrogen Energy 38 (2013) 8497–8502.
[15] L. Deleebeeck, K.K. Hansen, HDCFC performance as a function of anode at-mosphere (N-2-CO2), J. Electrochem. Soc. 161 (2014) F33–F46.
[16] L. Deleebeeck, D. Ippolito, K.K. Hansen, Enhancing hybrid direct carbon fuel cell anode performance using Ag2O, Electrochim. Acta 152 (2015) 222–239.
[17] A. Elleuch, A. Boussetta, J. Yu, K. Halouani, Y. Li, Experimental investigation of direct carbon fuel cell fueled by almond shell biochar: Part I. Physico-chemical characterization of the biochar fuel and cell performance examination, Int. J. Hydrogen Energy 38 (2013) 16590–16604.
[18] A. Elleuch, K. Halouani, Y. Li, Investigation of chemical and electrochemical reactions mechanisms in a direct carbon fuel cell using olive wood charcoal as sustainable fuel, J. Power Sources 281 (2015) 350–361.
[19] A. Elleuch, J. Yu, A. Boussetta, K. Halouani, Y. Li, Electrochemical oxidation of graphite in an intermediate temperature direct carbon fuel cell based on two-phases electrolyte, Int. J. Hydrogen Energy 38 (2013) 8514–8523.
[20] A. Fuente-Cuesta, C. Jiang, A. Arenillas, J.T. Irvine, Role of coal characteristics in the electrochemical behaviour of hybrid direct carbon fuel cells, Energy En-viron. Sci. 9 (2016) 2868–2880.
[21] W. Hao, X. He, Y. Mi, Achieving high performance in intermediate tempera-ture direct carbon fuel cells with renewable carbon as a fuel source, Appl. Energy 135 (2014) 174–181.
[22] W. Hao, Y. Mi, Evaluation of waste paper as a source of carbon fuel for hybrid direct carbon fuel cells, Energy 107 (2016) 122–130.
[23] W. Hao, Y. Mi, A direct carbon fuel cell with a CuO–ZnO–SDC composite anode, RSC Adv. 6 (2016) 50201–50208.
[24] L. Jia, Y. Tian, Q. Liu, C. Xia, J. Yu, Z. Wang, Y. Zhao, Y. Li, A direct carbon fuel cell with (molten carbonate)/(doped ceria) composite electrolyte, J. Power Sources 195 (2010) 5581–5586.
[25] C. Jiang, J.T.S. Irvine, Catalysis and oxidation of carbon in a hybrid direct carbon fuel cell, J. Power Sources 196 (2011) 7318–7322.
[26] C. Jiang, J. Ma, A. Arenillas, J.T.S. Irvine, Hybrid direct carbon fuel cells with different types of mineral coal, ECS Trans. 57 (2013) 3013–3021.
[27] N. Kaklidis, V. Kyriakou, I. Garagounis, A. Arenillas, J.A. Menendez, G.E. Marnellos, M. Konsolakis, Effect of carbon type on the performance of a direct or hybrid carbon solid oxide fuel cell, RSC Adv. 4 (2014) 18792–18800.
[28] L. Kouchachvili, M. Ikura, Performance of direct carbon fuel cell, Int. J. Hydrogen Energy 36 (2011) 10263–10268.
[29] Y. Nabae, K.D. Pointon, J.T.S. Irvine, Electrochemical oxidation of solid carbon in hybrid DCFC with solid oxide and molten carbonate binary electrolyte,
[30] J. Ruflin, A.D. Perwich Ii, C. Brett, J.K. Berner, S.M. Lux, Direct carbon fuel cell: a proposed hybrid design to improve commercialization potential, J. Power Sources 213 (2012) 275–286.
[31] X.Y. Xu, W. Zhou, F.L. Liang, Z.H. Zhu, Optimization of a direct carbon fuel cell for operation below 700 degrees C, Int. J. Hydrogen Energy 38 (2013) 5367–5374.
[32] B. Yu, Y. Zhao, Y. Li, A SnO2-samarium doped ceria additional anode layer in a direct carbon fuel cell, J. Power Sources 306 (2016) 387–393.
[33] J. Yu, B. Yu, Y. Li, Electrochemical oxidation of catalytic grown carbon fiber in a direct carbon fuel cell using Ce0.8Sm0.2O1.9-carbonate electrolyte, Int. J. Hydrogen Energy 38 (2013) 16615–16622.
[34] J.S. Yu, Y.C. Zhao, Y.D. Li, Utilization of corn cob biochar in a direct carbon fuel cell, J. Power Sources 270 (2014) 312–317.
[35] T.M. Gür, Perspective—low-carbon electricity is great: what about "Less-Carbon"? J. Electrochem. Soc. 164 (2017) F1587–F1590.
[36] M.F. Irfan, M.R. Usman, K. Kusakabe, Coal gasification in CO2 atmosphere and its kinetics since 1948: a brief review, Energy 36 (2011) 12–40.
[37] F. Calise, M. Dentice d'Accadia, A. Palombo, L. Vanoli, Simulation and exergy analysis of a hybrid solid oxide fuel cell (SOFC)–Gas turbine system, Energy 31 (2006) 3278–3299.
[38] S.H. Chan, C.F. Low, O.L. Ding, Energy and exergy analysis of simple solid-oxide fuel-cell power systems, J. Power Sources 103 (2002) 188–200.
[39] Z. Yang, W. Peng, T. Liao, Y. Zhao, G. Lin, J. Chen, An efficient method exploiting the waste heat from a direct carbon fuel cell by means of a ther-mophotovoltaic cell, Energy Convers. Manag. 149 (2017) 424–431.
[40] M. Zhao, H. Zhang, Z. Hu, Z. Zhang, J. Zhang, Performance characteristics of a direct carbon fuel cell/thermoelectric generator hybrid system, Energy Convers. Manag. 89 (2015) 683–689.
[41] Q. Liu, Y. Tian, C. Xia, L.T. Thompson, B. Liang, Y. Li, Modeling and simulation of a single direct carbon fuel cell, J. Power Sources 185 (2008) 1022–1029.
[42] J. Koornneef, T. van Keulen, A. Faaij, W. Turkenburg, Life cycle assessment of a pulverized coal power plant with post-combustion capture, transport and storage of CO2, Int. J. Greenhouse Gas Control 2 (2008) 448–467.
[43] B.R. Alexander, R.E. Mitchell, T.M. Gür, Modeling of experimental results for carbon utilization in a carbon fuel cell, J. Power Sources 228 (2013) 132–140.
[44] H. Xu, B. Chen, P. Tan, H. Zhang, J. Yuan, J.T.S. Irvine, M. Ni, Performance improvement of a direct carbon solid oxide fuel cell through integrating an Otto heat engine, Energy Convers. Manag. 165 (2018) 761–770.
[45] J.A. Allen, M. Glenn, S.W. Donne, The effect of coal type and pyrolysis tem-perature on the electrochemical activity of coal at a solid carbon anode in molten carbonate media, J. Power Sources 279 (2015) 384–393.
[46] J.M. Smith, H.C.V. Ness, M.M. Abbott, Introduction to Chemical Engineering Thermodynamics, sixth ed., McGraw-Hill, New York, 2001.
[47] J. Deng, Q.-W. Li, Y. Xiao, C.-M. Shu, Experimental study on the thermal properties of coal during pyrolysis, oxidation, and re-oxidation, Appl. Therm. Eng. 110 (2017) 1137–1152.
[48] E. Melchior, H. Luther, Measurement of true specific heats of bituminous coals of different rank, and of a high-temperature coke, in the temperature range 30–350 °C, Fuel 61 (1982) 1071–1079.
[49] D. Merrick, Mathematical models of the thermal decomposition of coal: 2. Specific heats and heats of reaction, Fuel 62 (1983) 540–546.
[50] J.A. Allen, J. White, M. Glenn, S.W. Donne, Molten carbonate composition ef-fects on carbon electro-oxidation at a solid anode interface, J. Electrochem. Soc. 162 (2015) F1–F8.
[51] M.M. Kenisarin, High-temperature phase change materials for thermal energy storage, Renew. Sustain. Energy Rev. 14 (2010) 955–970.
[52] L. Marianowski, H. Maru, Latent heat thermal energy storage systems above 450 C, in: 12th Intersociety Energy Conversion Engineering Conference, 1977, pp. 555–566.
[53] N. Araki, M. Matsuura, A. Makino, T. Hirata, Y. Kato, Measurement of ther-mophysical properties of molten salts: mixtures of alkaline carbonate salts, Int. J. Thermophys. 9 (1988) 1071–1080.
[54] G.J. Janz, M.R. Lorenz, Solid-liquid phase equilibria for mixtures of lithium, sodium, and potassium carbonates, J. Chem. Eng. Data 6 (1961) 321–323.
[55] M.J. Glenn, J.A. Allen, S.W. Donne, Thermal investigation of a doped alkali-metal carbonate ternary eutectic for direct carbon fuel cell applications, En-ergy Fuel. 29 (2015) 5423–5433.
[56] P.J. Linstrom, W.G. Mallard, NIST Chemistry WebBook, NIST Standard Refer-ence Database Number 69, National Institute of Standards and Technology, Gaitherburg, MD, 2014.
[57] K. Hemmes, M. Cassir, A theoretical study of the carbon/carbonate/hydroxide (electro-) chemical system in a direct carbon fuel cell, J. Fuel Cell Sci. Technol. 8 (2011), 051005-051005.
[58] Y. Jiao, W. Tian, H. Chen, H. Shi, B. Yang, C. Li, Z. Shao, Z. Zhu, S.-D. Li, In situ catalyzed Boudouard reaction of coal char for solid oxide-based carbon fuel cells with improved performance, Appl. Energy 141 (2015) 200–208.
[59] C. Li, Y. Shi, N. Cai, Performance improvement of direct carbon fuel cell by introducing catalytic gasification process, J. Power Sources 195 (2010) 4660–4666.
[60] M.W. Chase Jr., NIST-JANAF thermochemical tables, J. Phys. Chem. Ref. Data Monogr. 9 (1998) 1–1951.
[61] Y. Nabae, K.D. Pointon, J.T.S. Irvine, Ni/C slurries based on molten carbonates as a fuel for hybrid direct carbon fuel cells, J. Electrochem. Soc. 156 (2009) B716–B720.

[62] J.A. Allen, J. Tulloch, L. Wibberley, S.W. Donne, Kinetic analysis of the anodic carbon oxidation mechanism in a molten carbonate medium, Electrochim. Acta 129 (2014) 389–395.

[63] J.A. Allen, M. Glenn, P. Hapugoda, R. Stanger, G. O'Brien, S.W. Donne, An investigation of mineral distribution in coking and thermal coal chars as fuels for the direct carbon fuel cell, Fuel 217 (2018) 11–20.

[64] V. Kaplan, E. Wachtel, I. Lubomirsky, Carbonate melt regeneration for efficient capture of SO 2 from coal combustion, RSC Adv. 3 (2013) 15842–15849.

[65] M. Ghoorah, B.Z. Dlugogorski, H.C. Oskierski, E.M. Kennedy, Study of thermally conditioned and weak acid-treated serpentinites for mineralisation of carbon dioxide, Miner. Eng. 59 (2014) 17–30.

[66] R. Turconi, A. Boldrin, T. Astrup, Life cycle assessment (LCA) of electricity generation technologies: overview, comparability and limitations, Renew. Sustain. Energy Rev. 28 (2013) 555–565.

[67] J. Sullivan, L. Gaines, A Review of Battery Life-Cycle Analysis: State of Knowledge and Critical Needs, Argonne National Laboratory (ANL), 2010.

Review article

Carbon electro-catalysis in the direct carbon fuel cell utilising alkali metal molten carbonates: A mechanistic review

Michael J. Glenn [a], Jessica A. Allen [b], Scott W. Donne [a],[*]

[a] *Discipline of Chemistry, Newcastle Institute for Energy and Resources, University of Newcastle, Callaghan, NSW, 2308, Australia*
[b] *Discipline of Chemical Engineering, Newcastle Institute for Energy and Resources, University of Newcastle, Callaghan, NSW, 2308, Australia*

HIGHLIGHTS

- The DCFC converts the chemical energy in carbon to electrical energy with >80% efficiency.
- Here we review the literature on interactions between various DCFC components.
- A novel electro-catalysis mechanism for the DCFC is proposed.
- This will assist in the design of catalysts and overall DCFC systems.

GRAPHICAL ABSTRACT
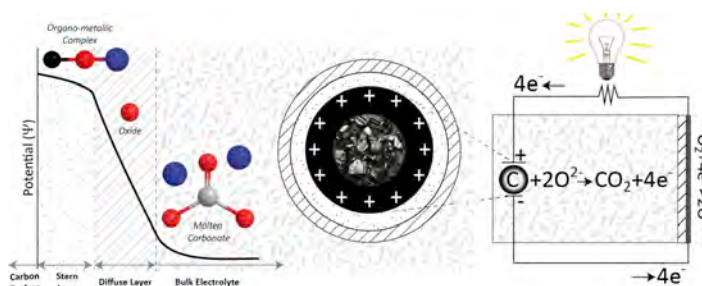
ABSTRACT

The direct carbon fuel cell (DCFC) is a promising technology projected to produce electrical energy from carbon with 100% theoretical efficiency, and realisable efficiencies of 80% observed on the lab scale. Recently this field has gained popularity with the development of a hybrid DCFC system incorporating aspects of both solid oxide and molten carbonate fuel cell systems. Interactions, including chemical and electrochemical reactions that can occur between the various reactants, products and electrolyte mediums in a DCFC; i.e., molten carbonate, carbon and CO_2, have been explored in a variety of other literature spheres over the past several decades without careful application of these concepts to a DCFC system. These interactions appear in the fields of molten salts for concentrated solar power, the molten carbonate fuel cell, and alkali metal carbonate catalysed biomass and coal gasification from CO_2. This review ties together several key pieces of information not limited to the DCFC literature, leading up to the apotheosis which is a novel electro-catalysis mechanism for the DCFC, which will aid in understanding of the system performance sensitivities as well as potentially catalyst and anode design development.

1. Introduction

The direct carbon fuel cell (DCFC) has been demonstrated to convert the chemical energy stored in carbon to electrical energy at a real efficiency of 80% [1]. This is a significant improvement over coal fired power stations, which are limited by the Carnot efficiency of thermal energy conversion, typically no higher than 46%, depending on the temperature able to be reached [2]. Further, the waste heat produced from the DCFC can be used in a bottoming cycle to maintain operational temperature, thus mitigating losses to the overall efficiency [3].

A commonly utilised version of the DCFC which will be the focus of this communication is a double electrolyte hybrid of the solid oxide fuel cell (SOFC) and molten carbonate fuel cell (MCFC), as shown in Fig. 1. The primary electrolyte of a hybrid DCFC is a solid oxide ion conductor similar to that used in SOFC; e.g., yttria stabilised zirconia (YSZ), scandium stabilised zirconia (SSZ), gallium doped cerium (GDC) or samaria-doped ceria (SDC) [4,5], while the secondary electrolyte is a molten salt mixture, often the Li_2CO_3/K_2CO_3 (62/38 mol%) eutectic or the $Li_2CO_3/Na_2CO_3/K_2CO_3$ (43.5/31.5/25 mol%) ternary eutectic [6].

A number of recent publications have shown promising results for the DCFC, with many authors attributing variations in performance to the kinetics of carbon oxidation [7]; i.e.,

$$C + 2O^{2-} \rightarrow CO_2 + 4e^- \tag{1}$$

The carbon oxidation reaction occurs at the anode of the DCFC and is generally thought to be rate limiting at operational temperatures between 500 and 700 °C in the context of full cell operation where oxygen reduction is occurring at the cathode [8]; i.e.,

$$O_2 + 4e^- \rightarrow 2O^{2-} \tag{2}$$

Lanthanum strontium manganate (LSM) [9]; e.g., $(La_{0.80}Sr_{0.20})_{0.95}MnO_3$, is a commonly used oxygen reduction catalyst above 750 °C. Below 800 °C poor oxide diffusion kinetics limit the performance of this material [10], which has been reported at high as 359 mW/cm² at 850 °C [11]. Below 750 °C lanthanum strontium cobalt iron (LSCF); e.g., $(La_{0.60}Sr_{0.40})_{0.95}Co_{0.20}Fe_{0.80}O_3$, has been used more recently [8], and found to consistently produce high performing DCFCs (225 mW/cm² at 650 °C [12]). Both LSM and LSCF are A-site deficient perovskite structures [13]. Silver has also been used as an oxygen reduction catalyst, which has the benefit of enhanced electrical conductivity [14], however the performance of these systems has been comparatively poor (50 mW/cm² at 800 °C [15] and 135 mW/cm² at 850 °C [16], respectively), which may be due to poor oxygen reduction kinetics and/or oxide diffusivity. Normalized units of mW/cm² have conveniently been used to compare the specific power of various electrode materials. However, this is a crude comparison because it does not take into consideration the voltage drop caused by the thermodynamic overpotential and resistive heating. This voltage drop scales with the electrode surface area and operating current, which is why larger electrodes operating well below the open circuit potential (OCP) produce less useable power, despite being constructed from power dense materials.

Carbon oxidation is at the heart of the DCFC, which is likely why so much attention revolves around this reaction. However, there are a number of other processes that also take place in this system, such as the reverse Boudouard reaction [17], carbonate decomposition [18], carbon activation [19], lithium intercalation [20], and even the potential formation of organometallic surface complexes [21,22]. While these processes do not contribute directly to current flow they all modify the system, which indirectly affects carbon oxidation, and ultimately performance. These other processes are often investigated separately, and are seldom discussed in the sphere of DCFC literature. This mechanistic review aims to address each of these factors and assess their impact on the performance of a hybrid DCFC.

2. Carbon conversion pathways

2.1. Thermodynamics of carbon conversion

The thermodynamics of both carbon electro-oxidation and gasification from CO_2 are dependent upon the operational temperature, as shown by Fig. 2. For both chemical and electrochemical conversion pathways the Gibbs free energy (ΔG_r; J.mol⁻¹) can be calculated from the entropy and enthalpy values at each specific temperature [23], as shown by Fig. 2. For the electrochemical conversion pathways, the electrochemical potential (E_r; V) can subsequently be calculated from knowing the Gibbs free energy value at each temperature; i.e.,

$$\Delta G_r = \Delta H_r - T\Delta S_r. \tag{3}$$

$$E_r = -\frac{\Delta G_r}{nF}. \tag{4}$$

where F is the Faraday constant (96485 J K⁻¹ mol⁻¹), T is the temperature (K), n the number of electrons involved in terms of the stoichiometric coefficient, ΔS_r (J.K⁻¹.mol⁻¹) the overall change in entropy, and ΔH_r (J.mol⁻¹) is the net change in enthalpy.

Fig. 2[A] and [B], both show that the thermodynamics of four-electron carbon oxidation (Eqn (1)) are not affected greatly by temperature. However, the partial electro-oxidation pathway is temperature dependent. The first step involves a two-electron oxidation to form carbon monoxide; i.e.,

$$C + O^{2-} \rightarrow CO + 2e^- \tag{5}$$
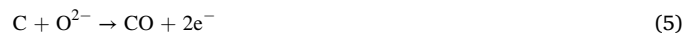
The intermediate CO species produced can be further oxidised to CO_2 in a subsequent two-electron process; i.e.,

$$CO + O^{2-} \rightarrow CO_2 + 2e^- \tag{6}$$
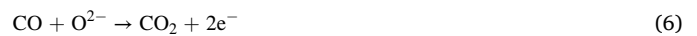
The first step (Eqn (5)) becomes more favourable with temperature, particularly above ~680 °C which is the intersection point in Fig. 2[A]. This pathway then competes with four-electron oxidation which is the desired process for performance optimisation. By contrast, the second partial electro-oxidation step (Eqn (6)) is diminished at higher temperatures. Making practical use of this reaction pathway presents a design challenge because the second step can only take place provided that
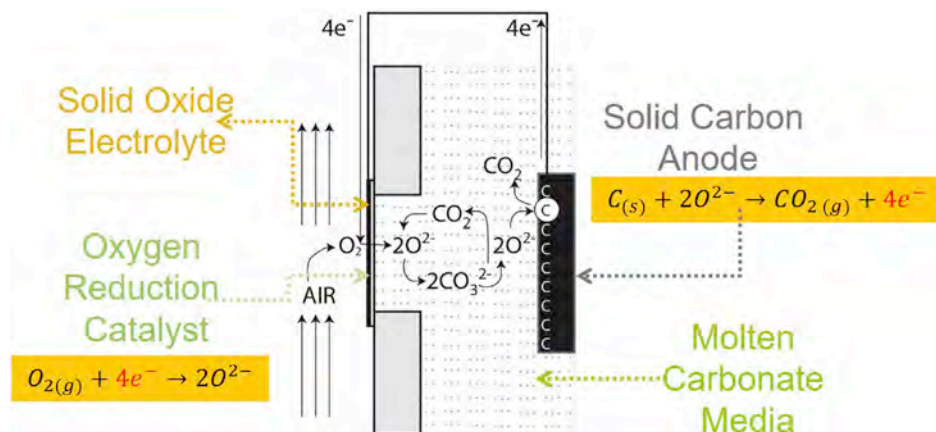
Fig. 1. DCFC Schematic with the associated electrochemical reactions included.
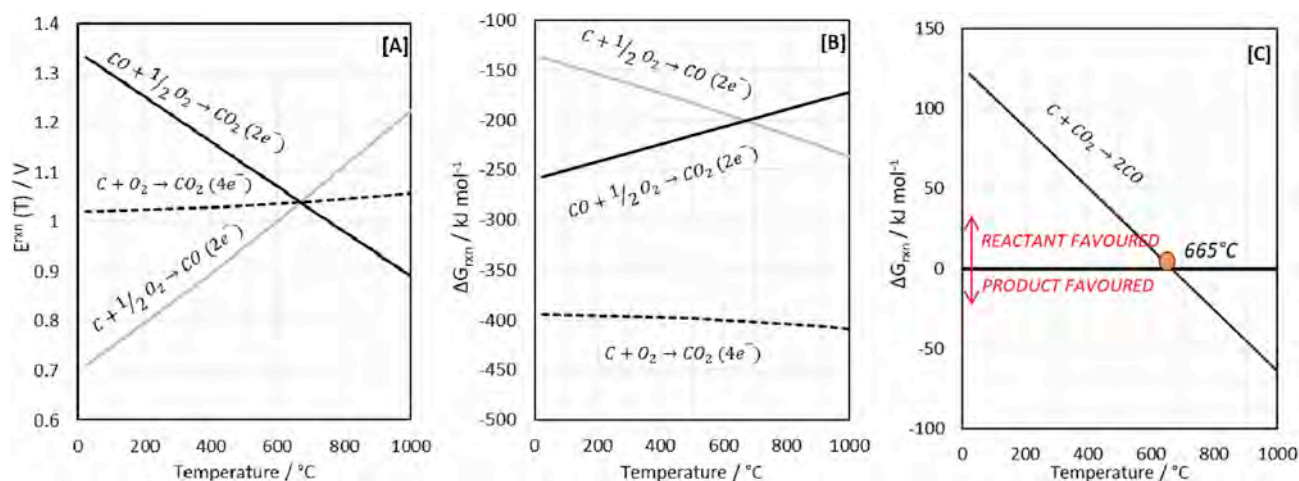
Fig. 2. [A] Overall electrochemical potential of reaction for the production of 1 mol of product gas; [B] Gibbs free energy for electrochemical reaction to produce of 1 mol of product gas; and [C] Gibbs free energy for chemical of reverse Bouduard reaction to produce of 1 mol of CO gas.

ample CO gas is available and sound contact can be established with the current collector.

In addition, the reverse Bouduard reaction may also take place, thus producing CO chemically; i.e.,

$$C(s) + CO_2(g) \rightarrow 2CO(g) \tag{7}$$

From Fig. 2[C], the thermodynamics of this reaction are heavily temperature dependent. The process only becomes theoretically spontaneous above 665 °C, however authors have reported this reaction taking place to a notable extent at temperatures as low as 500 °C in the presence of molten alkali metal carbonates [24]. It should be noted however that four-electron electro-oxidation (Eqn (1)) is thermodynamically favoured over the reverse Bouduard reaction (Eqn (7)) at DCFC operational temperatures; i.e., $\Delta G_r = -402 \text{ kJ mol}^{-1}$ versus -6 kJ mol^{-1} (Fig. 2) at 700 °C, respectively. Hence, under closed circuit conditions electro-oxidation is the thermodynamically preferred pathway for carbon consumption.

The reverse Bouduard reaction is typically described as parasitic in the sphere of DCFC literature [18] because it consumes fuel without leading to a current. Further, the reaction is endothermic, drawing 159.7 kJ mol^{-1} of carbon consumed [25]. Consequently, this incurs an energy penalty on the DCFC due to the additional heat input required to maintain a stable operating temperature. This issue is exacerbated by the specific heat capacity of these carbonate mixtures which is quite low for a molten salt over the DCFC operation temperature range. The specific heat capacity for the Li$_2$CO$_3$ (62 mol%)/K$_2$CO$_3$ (32 mol%) binary eutectic was measured using adiabatic scanning calorimetry (ASC) by Araki et al. [26] to be 1.60 kJ^{-1} kg^{-1}°C^{-1} between 500 and 800 °C.

2.2. Carbon electro-oxidation mechanism and kinetics

Long et al. [27] proposed a mechanism for catalysed graphite oxidation with alkali metal carbonates under CO$_2$ at elevated temperatures above 500 °C. Their mechanism takes into account the structure of graphite, which is comprised of six membered hexagonal sheets of graphene held together by π-stacking interactions. Crystalline graphite exhibits preferred orientation, which means that both the basal planes and the edges are exposed to the alkali metal carbonate reagent. Long et al. [27] suggests that the edges are more reactive, and it is at these sites that a redistribution of the π-electrons occurs weakening C–C bonds and strengthening C–O bonds.

Later, Cherepy et al. [28] proposed a six-step mechanism for the electro-oxidation of carbon in molten carbonate media. The mechanism shows oxide (O^{2-}) reacting with so-called 'surface reactive' carbon

(C_{SR}), over a series of steps that involve individual electron discharges, oxide adsorption or carbon dioxide evolution, which was also considered by Allen et al. [7]; i.e.,

$C_{SR} + O^{2-} \rightarrow C_{SR}O^{2-}$	Adsorption	(8)
$C_{SR}O^{2-} \rightarrow C_{SR}O^- + e^-$	Discharge	(9)
$C_{SR}O^- \rightarrow C_{SR}O + e^-$	Discharge	(10)
$C_{SR}O + O^{2-} \rightarrow C_{SR}O_2^{2-}$	Slow adsorption, RDS by Cherepy et al. [28]	(11)
$C_{SR}O_2^{2-} \rightarrow C_{SR}O_2 + e^-$	Discharge, RDS by Allen et al. [7]	(12)
$C_{SR}O_2^- \rightarrow CO_2(g) + e^-$	Discharge and gas evolution	(13)

Cherepy et al. [28] suggest that carbonate decomposition is analogous to cryolite decomposition because both reactions produce oxide; i.e.,

$$2[Al_2O_2F_4]^{2-} \rightarrow 2O^{2-} + 2[Al_2OF_4] \tag{14}$$

Their overall process depicts surface reactive carbon reacting with carbonate, not oxide, to form carbon dioxide and four electrons (Eqn (15)), however carbonate does not appear in any of their mechanistic steps.

$$C_{SR} + 2CO_3^{2-} \rightarrow 3CO_2 + 4e^- \tag{15}$$

Therefore, Cherepy et al. [28] implies that carbonate decomposition to form oxide occurs as a precursor and that it is not a rate limiting step in the process. Surprisingly few additional mechanistic studies have been carried out for the electrochemical oxidation of carbon. The majority of DCFC investigations use full cell set ups, or alternatively use arrangements where the carbon fuel is a slurry, thus introducing inherent mass transport limitations which may overshadow more sensitive mechanistic observations. A generic understanding of carbon oxidation kinetics has therefore been mostly collected without any attempt to understand underlying mechanistic principles.

3. Carbon gasification and associated processes

3.1. Gasification under varied gas atmospheres

The reverse Bouduard reaction is a specific type of carbon gasification that occurs using a CO$_2$ gasification agent [17], resulting in the production of basic alkali metal oxides. Alkali metal oxide activity increases molten carbonate basicity, which in linked to carbon electro-oxidation kinetics (Section 4), hence gasification sensitivities are worth investigating. In addition to reaction temperature, the reaction is highly sensitive to the addition of catalyst materials. Single alkali metal carbonates including Li$_2$CO$_3$, Na$_2$CO$_3$ and K$_2$CO$_3$ have all been used in

this role. McKee et al. [29] found Li_2CO_3 to be the most effective catalyst, however conflicting results have been reported, and a detailed reaction mechanism is lacking.

Wood et al. [22], first suggested that surface K–O–C complexes form during gasification. The presence of K–O–C surface complexes was demonstrated by alkylation with methyl iodide, and verified using nuclear magnetic resonance (NMR) spectroscopy [22,30]. However, a thermodynamic justification was not proposed for the carbothermic reduction of alkali metal cations at 700 °C to form these complexes. Furthermore, a mechanism that can account for the gasification behaviour has recently been provided [31] however the formation of surface complexes without the need for carbothermic reduction remains to be demonstrated.

Nagase et al. [32] compared the rate of the reverse Bouduard reaction when different alkali metal carbonates were added as a catalyst using thermogravimetric analysis (TGA), with the results summarised in Table 1. Single alkali metal carbonates have been examined in terms of their role as a reverse Bouduard reaction catalysts. However, the literature remains scarce on the catalytic activity of alkali metal carbonate mixtures, including mixtures used in DCFCs and molten carbonate fuel cells (MCFCs).

Kopyscinski et al. [33] suggested that carbon gasification occurs under N_2 when in the presence of K_2CO_3. Two reactions were proposed, one leading to CO_2 (Eqn (16)) and the other CO (Eqn (17)) with both resulting in the formation of potassium metal; i.e.,

$$K_2CO_3(s) + C(s) \rightarrow CO_2(g) + CO(g) + 2K(g) \tag{16}$$

$$K_2CO_3(s) + 2C(s) \rightarrow 3CO(g) + 2K(g) \tag{17}$$
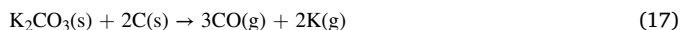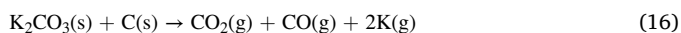
This study involved analysing demineralised coal by thermogravimetric analysis (TGA) under N_2 before switching the gas to CO_2 at 700 °C. Fourier transform infrared (FTIR) analysis revealed that the flue gas was comparatively richer in CO compared to CO_2, thus leading to the conclusion that Eqn (17) is the preferred pathway. Both Eqn (16) and Eqn (17) imply that carbothermic reduction has taken place, as K^+ is reduced to elemental K, which exists as a gas phase metal in the presence of carbon at temperatures above 759 °C [34].

Kopyscinski et al. [33] also found that the reverse Bouduard gasification was more facile for a system held under N_2 at 700 °C for an extended time period before being switched to CO_2, compared to the system held under CO_2 throughout the duration of the experiment. Carbonate decomposition (Eqn (22)) is expected to be enhanced under non-CO_2 atmospheres, and this has been confirmed by numerous studies [18,35–38]. Therefore, during isothermal conditions under nitrogen, carbonate decomposition would occur (Eqn (22)), leading to increased oxide activity in the melt. On switching to carbon dioxide, enhanced gasification is then observed. Although it was not discussed by the authors, these findings show that a higher O^{2-} activity in the melt leads to enhanced gasification. Further, it may also be that the active catalyst for the reverse Bouduard reaction is O^{2-} instead of CO_3^{2-}.

Nagase et al. [32] suggested a similar reaction scheme when using Na_2CO_3 as a reverse Bouduard gasification catalyst, claiming a disproportionation reaction leading to the production of Na which also exists as a gas phase metal above 883 °C [34] (Eqn (19)), and a liquid phase metal peroxide; i.e., Na_2O_2, through an Na_2O intermediate (Eqn (18)).

$$Na_2CO_3(l) + C(s) \rightarrow Na_2O(s) + 2CO(g) \tag{18}$$

$$2Na_2O(s) \rightarrow Na_2O_2(l) + 2Na(g) \tag{19}$$

Na_2O_2 can react with carbon to reform sodium oxide (Eqn (20)), which further reacts with CO_2 below 400 °C to reform sodium carbonate (Eqn (21)) [32]; i.e.,

$$Na_2O_2 + C \rightarrow Na_2O + CO \tag{20}$$

$$Na_2O + CO_2 \rightarrow Na_2CO_3 \tag{21}$$

Generally, carbothermic reduction does not take place below 2000 °C in the absence of a cathodic potential, with the lowest reported temperature being at least 800 °C [39]. Carbothermic reduction was proposed by Kopyscinski et al. [33] to account for the mass loss which could not be solely accounted for due to carbonate decomposition (Eqn (22)). At the temperatures investigated and under an inert gas atmosphere, irreversible loss of CO_2 as a gas had previously been suggested to occur [40]; i.e.,

$$CO_3^{2-} \leftrightarrow CO_2 + O^{2-} \tag{22}$$

As such, carbon consumption via a gasification mechanism was postulated, which was a modification on the hypothesis first proposed by Wood et al. [22].

Recent work has demonstrated that gasification can also take place form carbonate when carbon dioxide is absent, this is carbon gasification from carbonate and carbonate decomposition taking place in a single reaction (Eqn (23)) [31]. In this case the C^{4+} for the comproportionation reaction (Section 3.6) comes from carbonate instead of CO_2; i.e.,

$$CO_3^{2-} + C \leftrightarrow 2CO + O^{2-} \tag{23}$$
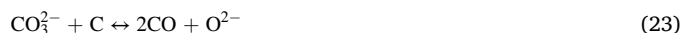
Therefore, carbon gasification from carbonate is possible without the requirement of carbothermic reduction.

3.2. Role of oxide species in gasification

For systems without added carbonate it has been widely reported that activation energy of gasification decreases with coal rank because the mineral matter in low ranking coals such as lignite catalyses gasification from CO_2 [17]. Raw coal has also shown sensitivity to the CO_2 partial pressure. The expected result would be that an increased partial pressure should cause the activation energy to decrease (Eqn (7)), however for lignite this correlation does not appear. Under pure CO_2, the activation energy has been calculated to be 247 kJ mol^{-1} versus 192 kJ mol^{-1} for 20 mol% CO_2. Further, the E_A value unexpectedly spikes at 40 mol% [41]. One possible explanation is that increasing CO_2 atmosphere deactivates the catalytic properties of the coal minerals. An example of this would be the reverse of carbonate decomposition (Eqn (22)); i.e., carbonate reformation, this is where oxide (dissolved in molten carbon or colloidal alkali metal oxides) react with CO_2 (dissolved in molten carbonate or in the overhead gas at the gas/liquid boundary).

It was suggested by Yu et al. that the intrinsic electric field generated by the potential difference between the anode and cathode in an operational DCFC may act to supress reverse Bouduard corrosion [42]. This claim was demonstrated by a shift in the CO_2:CO ratio from >20% CO_2 to <10% CO from flue gas analysis at 700 °C under current controlled conditions, in response to an increase in current density from 50 to 200 mA cm^{-2}.

Nabae et al. also reported an enhanced ratio of CO_2:CO when an external current was imposed compared to the current flow solely driven by the overpotential across the cell [43]. Weaver et al. also demonstrated a similar finding, when operating under isothermal conditions at 700 °C, in this case using coal chars [44].

An electric field exists when the dielectric is both polarisable and non-conductive. Once a current is passed between the electrodes the dielectric has broken down and the electric field collapses. Therefore, if the DCFCs electric field is suppressing reverse Bouduard gasification then it would only be effective under open circuit conditions.

**Table 1**
Rate of CO_2 conversion over single alkali metal carbonate catalysts.

Alkali Metal Carbonate	Turnover Rate (μmol.min^{-1} per mmol of Alkali Metal Carbonate)
Li_2CO_3	30
Na_2CO_3	36
K_2CO_3	36
Cs_2CO_3	35

A high current means a high reaction rate, therefore it is more likely that adsorbed CO quickly oxidises to CO_2 (Eqn (12)) before it can desorb as evolved CO gas. Thus, the ratio of CO_2:CO ratio in the flue gas stream increases.

3.3. Impact of oxide on electrode surface potential

Chen et al. [45] examined the wetting interactions of pristine graphite rods in a molten alkali metal carbonate mixture using contact angle measurements at temperatures in the range 520–560 °C. The Li_2CO_3/K_2CO_3 binary eutectic (62/38 mol%) was used, and it was found that the wettability increased significantly over time. Initially, there was no wetting interaction, however after 48 min wetting was observed to be initiated. Bubbling, said to be due to reverse Bouduard gasification was noted as the carbonate film crept along the carbon rod. The open circuit potential also shifted from 0.5 V to −0.81 V after just 160 s upon immersion, ascribed to CO surface adsorption by the authors (Eqn (24)). The OCP is sensitive to the adsorption of other species at the electrode surface also, hence adsorbed oxide would also be expected to affect the surface potential [46]; i.e.,

$$\psi_o = \frac{kT}{e}\left(a_{\text{adsorbed}} - a_{\text{bulk}}\right) \tag{24}$$

where ψ_o is the measured surface potential (V), k is the Boltzmann constant (1.38×10^{-23} m^2 kg s^{-2}.K^{-1}), T is temperature (K), a_{adsorbed} is the activity of adsorbed species, a_{bulk} is the activity of species in the bulk, and e is the charge on an electron; i.e., 1.60×10^{-19} C.

This is the second O^{2-} adsorption step in the electro-oxidation mechanism (Eqn (11)) because it directly proceeds the RDS [7], hence this shows how CO remains adsorbed long enough to have a measurable effect on carbonate wetting. This is in fact chemisorption, because the following step involves an electron discharge (Eqn (12)); i.e., breaking a chemical bond, before CO_2 is evolved (Eqn (13)) [28].

3.4. Carbon activation

Partial gasification of the carbon fuel has been linked to changes in the characteristics of the carbon [18]. These changes include increasing its wettability to molten alkali metal carbonates [45], and the process of producing activated carbon [19]. Activated carbon is a material that finds application in energy storage devices, such as electrical double layer capacitors, due to its high surface area of up to 3000 m^2 g^{-1} [47]. There are a variety of methods that can be used to chemically produce these materials, several of which employ basic conditions [48], including alkali metal carbonate media [49]. Coincidentally, whether operating under CO_2 or non-CO_2 atmospheres, carbon materials that are present in the DCFC may also undergo similar activation type reactions which are also employed in the synthesis of activated carbon. Under CO_2, the reverse Bouduard gasification is favoured above 700 °C, and this is catalysed by alkali metal carbonates as discussed in Section 2.1. These conditions are used to prepare activated carbon [19], because gasification increases both the micro porosity and the meso porosity of the material [50], leading to a surface area increase [51].

Under non-CO_2 atmospheres both Na_2CO_3 and K_2CO_3 have been used to activate carbon sources such as lignin [49] and even palm shells [52] under N_2 in the temperature range 500–800 °C. Under these conditions, gasification is also expected to take place, as noted above in Eqn (16) and Eqn (17). In the aforementioned studies raw biomass was used, hence some of the changes occurring in the material may have been due to volatile release. However, it is also likely that activated carbon is being produced in DCFC operation, even when coal char is being used as the fuel, due to the interactions between the carbon and the molten carbonate. This has direct implications on DCFC performance because voltammetry measurements are typically normalized in terms of a geometric surface of the electrode (mA.cm^{-2}) and not a Brunauer

Emmett Teller (BET) surface area [53].

Experimental evidence for the activation could be obtained by exposing a 2D carbon interface with a fixed geometric surface area to molten carbonate and measuring the BET surface area both before and after immersion in molten carbonate. The surface area increase should occur even under open circuit conditions since carbonate itself is a gasifying agent [31].

3.5. Organometallic complex formation

In the field of alkali metal carbonate catalysed gasification from CO_2, several authors have suggested that K–O–C sites form on the carbon surface when using K_2CO_3. This was first proposed by Wood et al. [22] and later a mechanism was developed by Kopyscinski et al. [33]. The formation of organometallic complexes was demonstrated via NMR [22], XRD [33] and light microscopy [33], however due to the small size of the complex the results were inconclusive [33].

The formation of these complexes coupled with a carbothermic reduction pathway has been able to explain why gasification occurs under N_2 in the presence of alkali metal carbonates. Despite the contributions of previous authors however, there remains a number of unanswered questions surrounding the these complexes, including the molecular geometry they adopt and whether the process is chemcial or electrochemical in nature.

A similar concept was proposed in the DCFC literature by Wang et al. [21], however these authors were working with a Li_2CO_3/K_2CO_3 binary mixture (62/38 wt%) that was purposefully doped with various transition metal oxides in separate experiments; i.e., Fe_2O_3, Co_3O_4, NiO, MnO_2, at the 0.1 wt% concentration level. Noticeable differences were that, instead of K–O–C complexes, Wang et al. [21] imply that M^{2+} cations facilitate the transfer of oxide to the carbon surface, where M^{2+} represents either Fe^{2+}, Co^{2+}, Ni^{2+} or Mn^{2+}. This model implies that electrostatic attraction between the cation and the oxide drive the interaction, as shown in Fig. 3. Wang et al. [28] suggest that there are two distinct pathways for electro-oxidation to occur, either directly via the aforementioned 6-step series of reactions proposed by Cherepy et al. [28] (Eqns (8)-(13)), or indirectly with the aid of a transition metal cation apparently complexed to the carbon surface (Fig. 3). The later pathway requires the availability of a suitable metal for organometallic complexation, which depending upon the arrangement may or may not be present. Therefore, it is worth reviewing different arrangements and how they impact on the electro-oxidation mechanism.

DCFC arrangements can be differentiated broadly into two categories; i.e., those that rely on chemically oxidising the fuel via Eqn (7) thus producing CO, before electro-oxidising CO to CO_2 via a two-electron process. The other variety is able to facilitate the four-electron oxidation directly from C to CO_2 (Eqn (1)), as shown in Fig. 4. Most authors agree that in cases where either alkali metal carbonates or alkali metal hydroxides are not utilised, the initial electro-oxidation step from C^0 to C^{2+} (Eqn (5)) does not take place, nor does the complete four-electron oxidation pathway suggesting the oxidation pathway is at least partially driven by gasification [10].

Fig. 4 shows nickel being used as an anode current collector where it is in contact with the carbon fuel, which is quite common for DCFC arrangements [8,10,23]. It should be noted that nickel is a very effective catalyst for the reverse Bouduard reaction. It has been reported by Nagase et al. [32] that the reaction rate for the reverse Bouduard reaction at 800 °C in an uncatalysed system is comparable to a nickel catalysed system at 400 °C, which is even below the temperature dependant thermodynamic limit for the reaction (Section 2.1).

In many carbonate-absent systems carbon is pressed up against the anode, which is often a mixture of a solid oxide electrolyte such as YSZ and nickel. This traps the CO gas in place long enough so that it cannot be evolved out of the system before it can react with oxide that has diffused through the solid oxide electrolyte. It is highly unlikely in this case that the three-phase boundary of carbon, oxide conductor; e.g.,
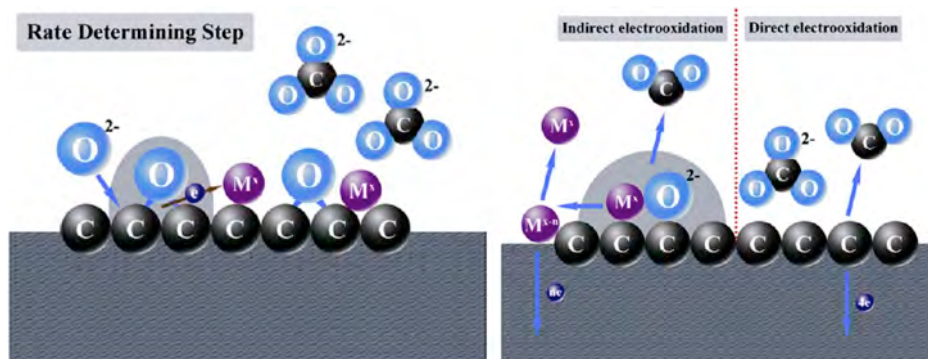
Fig. 3. Illustration showing how metal cations can mediate electro-oxidation [21].
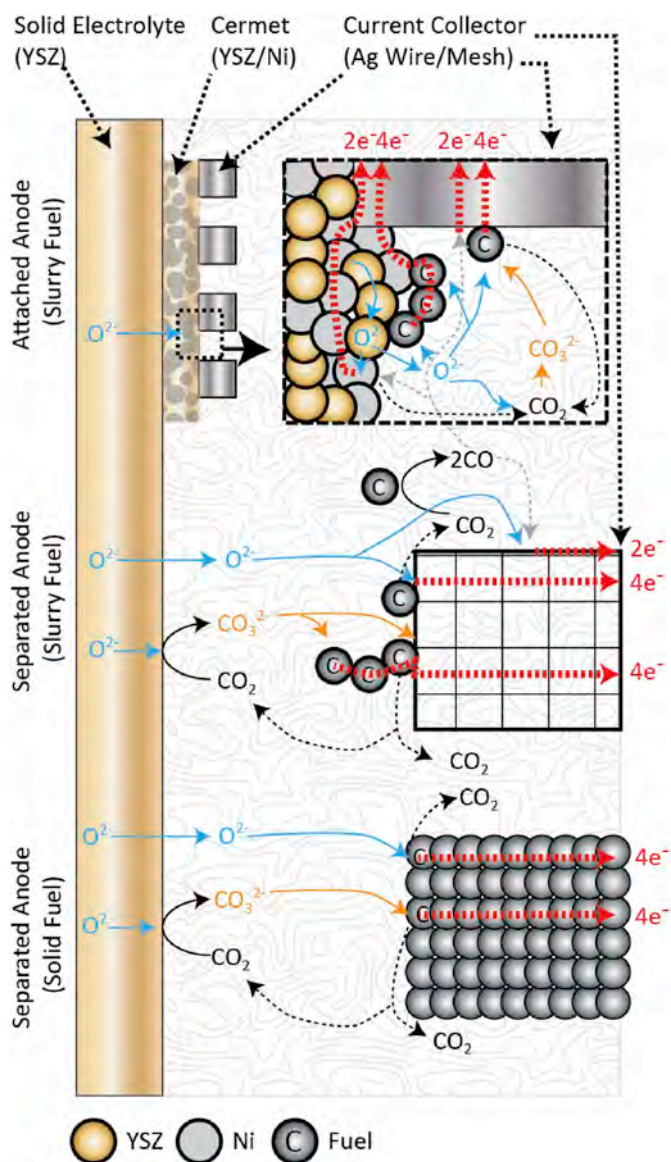
Fig. 4. Reaction pathways diagram for a carbonate containing DCFC arrangement, shown with a solid YSZ solid membrane and a nickel current collector.

YSZ, and a current collector such as nickel would allow for the complete electrochemical oxidation of the carbon.

In cases where hydroxides are used they are ultimately converted to carbonates under a CO_2 atmosphere via Eqn (25); i.e.,

$$2OH^- + CO_2 \rightarrow CO_3^{2-} + H_2O \tag{25}$$

Therefore, carbonate is ultimately used as both the electrolyte in the DCFC and as a source of oxide ions for direct electro-oxidation. However, several studies have shown that mixtures with a higher lithium carbonate content typically exhibit an enhanced performance, with the Li_2CO_3/K_2CO_3 binary eutectic exhibiting superlative overall performance [6,54]. This indicates that the Li^+ cation is potentially playing some role in the overall reaction kinetics [54].

3.6. Organometallic complex formation via electrochemical reaction

Electrochemical formation of organometallic species has not previously been considered in DCFC literature. However, it is proposed here that the role of the alkali metal cations and the potential formation of organometallic complexes should be considered mechanistically. There are two possible ways organo-metallic complexes could be stabilised, either via an electrostatic attraction force between the alkali metal cation and oxide, or via π-back bonding leading to the formation of a coordination complex. The latter possibility would involve CO acting as a carbonyl ligand, where the lone pair of electrons donates to the metal via a Lewis acid-base neutralization reaction. Here the carbon is the donor atom, hence the bond order would be M:C≡O:, as opposed to the electrostatic interaction which would produce a different order of attachment; i.e., M-O-C. Coordination compounds typically require metals that contain d-orbital electrons, such as transition metals [55]. There are however some examples in the literature where alkali metals cations have been used in this way [56,57]. Further, the crystal field splitting parameter for the carbonyl ligand (CO) is very low, meaning that it tends to form stable coordination compounds [58]. That being said, previous authors including Wood et al. [22] and Kopyscinski et al. [33] have suggested that the attachment order is M-O-C. Kopyscinski et al. and Wood et al. limited their investigations to the chemcial transformation of carbon in the presence of molten carbonates, and did not consider an electrochemical transformation pathway for the formation of organometallic complexes.

There are a three reactions which could produce organometallic complexes electrochemically, all of which involve comproportionation. In each case the carbon from the fuel is oxidised to form C^{2+}, while at the same time the C^{4+} from the carbonate is reduced to also form C^{2+}. Another well understood example of comproportionation is the reverse Boudard reaction (Eqn (7)). Of course, the reverse Boudard reaction (Eqn (7)) is chemical in nature and not electrochemical, because the overall reaction does not produce or consume electrons. That being said the individual redox processes that constitute the net comproportionation reaction (Eqn (27-28)) are electrochemical in nature [18]. In this example C^{4+} comes from CO_2 instead of the CO_3^{2-}, however the concept is similar (see Eqns (8-13). Eqn (26) shows the reverse Boudard reaction in terms of oxidation states; i.e.,

$$C^0 + (C^{4+}) (O^{2-})_2 \leftrightarrow 2(C^{2+}) (O^{2-}) \tag{26}$$

The individual half-cell reactions involving carbon from both the fuel (C^0) (Eqn (27)) and carbonate (C^{4+}) (Eqn (28)) are:

$$C^0 \leftrightarrow C^{2+} + 2e^- \tag{27}$$

$$C^{4+} + 2e^- \leftrightarrow C^{2+} \tag{28}$$

Combining the above redox reactions (Eqn (27-28)) gives the overall comproportionation of carbon; i.e.,

$$C^0 + C^{4+} \leftrightarrow 2C^{2+} \tag{29}$$

This concept can be applied to demonstrate how the formation of organometallic complexes might be possible via three separate reactions; i.e., α (Eqn (30)), β (Eqn (31)) and γ (Eqn (32)):

(α-electrochemical)	$M_2CO_3 + 3C + M_2O \rightarrow 4 [M - CO]^+ + 4e^-$	(30)
(β-electrochemical)	$2M_2CO_3 + 3C \rightarrow 4 [M - CO]^+ + CO_2 + 4e^-$	(31)
(γ-electrochemical)	$M_2CO_3 + 2C \rightarrow 2 [M - CO]^+ + CO + 2e^-$	(32)

The organometallic product ($[M - CO]^+$) from Eqns (25)-(27) contains C^{2+}, thus emphasising the electro-oxidation from the fuel (C^0) to C^{2+}.

Eqns (30)-(32) are thermodynamically driven by an electrochemical potential (E_r; V), however other factors can also impact on these reactions. For instance, Eqn (30) involves alkali metal oxides (M_2O), and is therefore dependent upon carbonate decomposition occurring beforehand (Eqn (22)). Eqn (31) produces CO_2 gas, therefore, the reaction it may be supressed under a CO_2 atmosphere due to Le Chatelier's principle. Despite this, Nagase et al. [32] suggested that redox reactions of the type discussed here are almost independent of the CO_2 pressure. Eqn (32) produces CO gas, however given that the partial pressure of CO in the DCFC anode compartment is low, this would not be expected to affect the equilibrium position of Eqn (32) appreciably.

The order of attachment of the atoms; i.e., either M:C≡O: or M:O≡C:, does not affect the comproportion reaction. However, it does impact upon the molecular geometry given that these complexes adsorb to the surface of the carbon. Whereas M:C≡O: requires a curved shape so that carbon can occupy the center of the complex whilst also constituting part of the electrode, M:O≡C: can form a linear complex that extends out into the carbonate melt. Therefore, the M:O≡C: linear complex is more plausible than the M:C≡O: configuration.

The surface reactive carbon shown in the electro-oxidation mechanism of Cherepy et al. [28] is suggested here to take the form of these organometalic complexes. There are several reasons for this; firstly, carbon is chemically bound to oxide, which is the other reactant in electro-oxidation, and secondly, the complex bears an overall +1 charge which would logically increase its affinity for the polar molten carbonate media, thus lowering the interfacial surface energy, which can therefore explain the enhanced wetting reported by Chen et al. with time [45].

3.7. Organometallic complex formation via chemical reaction under CO_2

As mentioned, the formation of organometallic complexes may occur from either a chemical or an electrochemical reaction. It is important to note that the wetting phenomenon reported by Chen et al. [45] was triggered under open circuit conditions, where there is no current flow. Hence a chemical pathway must also exist for the formation of these complexes. Under a CO_2 atmosphere this is possible by combining reactions α, β and γ with the CO_2 to CO reduction reaction; i.e.,

$$CO_2 + 2e^- \leftrightarrow CO + O^{2-} \tag{33}$$

The electrons required for the CO_2 reduction reaction come from reactions α, β and γ (Eqn (30)-(32)). The overall reactions for the formation of organometallic complexes via chemical reaction pathways are:

(α-chemical)	$M_2CO_3 + 3C + M_2O + 2CO_2 \rightarrow 4 [M - CO]^+ + 2CO + 2O^{2-}$	(34)
(β-chemical)	$2M_2CO_3 + 3C + CO_2 \rightarrow 4 [M - CO]^+ + 2CO + 2O^{2-}$	(35)
(γ-chemical)	$M_2CO_3 + 2C + CO_2 \rightarrow 2 [M - CO]^+ + 2CO + O^{2-}$	(36)

Eqns (34)-(36) may all be considered as gasification reactions which are analogous to the Bouduard reaction (Eqn (7)), because they convert CO_2 and carbon to CO. However, noticeable differences are these reactions lead to the production of organometallic complexes and oxide, both of which enable facile electro-oxidation of the C^{2+} bound in the complex to C^{4+}. Hence this gasification pathway can be thought of as a method of functionalising the system prior to being operated as the anode compartment within a DCFC. Further, this also provides a mechanism to increase the oxide activity under a CO_2 atmosphere. However, this may be only temporary as oxide readily reacts with CO_2 to reform carbonate due to Le Chatelier's principle [36–38], which is the reverse of the carbonate decomposition reaction (Eqn (22)). If oxide can react to electro-oxidise C^{2+} in the complex before it has a chance to react with CO_2 then this would increase specific power, however this is dependent upon the reaction kinetics of both process and which is more facile to be specific. Claes et al. [41] suggested that the kinetics of CO_2 diffusion may limit the rate of both chemical and electrochemical reactions within molten carbonates, which is intuitive; however, this remains to be verified experimentally.

The formation of organometallic complexes could be verified by removing unconsumed fuel from the anode chamber after electro-oxidation in molten carbonate before washing off the solid carbonate with warm water. A cross-section of the formerly exposed to the C/CO_3^{2-} interface should then be analysed by a surface technique for materials characterisation capable of detecting O-M and M − C bonds; e.g., Fourier transform infra-red spectroscopy (FTIR), Raman spectroscopy, x-ray photoelectron spectroscopy (XPS) or x-ray adsorption fine structure (XAFS).

4. Carbonate decomposition, oxide activity and system behaviour

4.1. Carbonate decomposition

Given that electro-oxidation is thought to involve an oxide species, the decomposition of carbonate (Eqn (22)), is a very important process for DCFC performance, despite often being overlooked or assumed to be trivial. Activity of oxide is likely to depend heavily on the equilibrium shown in Eqn (22), which also details the irreversible decomposition reaction which occurs when CO_2 is able to be irreversibly removed from the system. Carbonate decomposition can be triggered by reducing the CO_2 partial pressure [35,41]; i.e., Henry's Law, or by lowering the net pressure under a CO_2 atmosphere [59].

Olivares et al. [35] examined the decomposition of a ternary alklai metal carbonate mixture up to 1000 °C under three separate gases; i.e., Ar, air and CO_2. Decomposition via Eqn (22) was influenced by both the CO_2 partial pressure and temperature, with higher temperaratures and low CO_2 partial pressures leading to enhanced decomposition. The extent of decomposition was very slight (5.1%) even for the system under Ar at 1000 °C. However, several authors have reported enhanced decomposition in the presence of carbon [18,32,60–62], suggesting that carbon is a catalyst for carbonate decomposition. Mims and Pabst showed that K_2CO_3 mixed with coal decomposed at 500 °C under N_2 [60, 61], whereas the decomposition temperature for unmodified K_2CO_3 is above 1600 °C [63]. Similarly, McKee et al. [62]. showed that Na_2CO_3 mixed with coal decomposed at 500 °C under N_2. In both the aforementioned studies carbonate decomposition was demonstrated by thermogravimetric analysis. The issue for these earlier works is that the mass loss could be due to either carbonate decomposition, or the reverse Bouduard reaction, or even a combination of both. Two subsequent

studies, however, by separate authors have shown that both processes are likely to be taking place.

Peng et al. [18] examined the solid Li_2CO_3/K_2CO_3 binary eutectic under two different gases; i.e., 95% N_2 + 5% CO_2 and 100% CO_2, separately using scanning electron microscopy (SEM) with energy dispersive spectroscopy (EDX) after thermal fusion at 750 °C with a graphite rod. For the system under 100% CO_2 the O signal was even throughout the entire sample, indicating a uniform distribution of carbonate crystals. However, for the system fused under 95% N_2 + 5% CO_2 the distribution of the O signal was uneven, indicating that a mixture of both carbonate and oxide crystals were present. Thus demonstrating that under a CO_2 depleted atmosphere, carbonate decomposition takes place, with carbon as a catalyst.

As discussed in Section 3.1 Kopyscinski et al. [33] found that mass loss under N_2 exceeded the total amount of carbonate added. Therefore, gasification under N_2 can also occur, however the exact nature of this reaction either via carbothermic reduction proposed earlier; i.e., Eqns (16) and (17), or a comproportionation as discussed here and presented in Eqns (30)-(32) remains a topic for continued investigation.

4.2. Oxide activity

Peng et al. [18] suggested that the activity of oxide would be influenced by the decomposition of carbonate, which would in turn increase the basicity of the melt. Dissolved O^{2-} carries a lone pair of electrons, thus increasing the basicity under the Lewis definition. Conversely, dissolved CO_2 is increases the acidity of the melt [41], by supressing carbonate decomposition due to Le Chatelier's principle. Claes et al. [41] measured the solubility limit of CO_2 in the ternary eutectic at 700 °C using potentiometric titration, in which case it was found to be $(9.5 \pm 1.0) \times 10^{-2}$ mol L^{-1} atm^{-1} [41]. Dissolved CO_2 reacts with oxide to form carbonate, which is the reverse of carbonate decomposition (Eqn (22)). It was hypothesized in two separate investigations that carbonate can further react with oxide to form di-carbonate ions (Eqn (38)) [41] and multiple-carbonate ions (Eqn (37)) [64]. These suggestions came from potentiometric titration [41] and an in-situ pressure monitoring reactor [64], respectively.

$$CO_2 + CO_3^{2-} \leftrightarrow C_2O_5^{2-} \tag{37}$$

Peng et al. [18] hypothesized that the activity of oxide is orders of magnitude greater at the carbon interface compared with conditions in the bulk, however this statement was not supported by evidence. These inferences carry significant implications for DCFC operation because (i) potential for carbon activation, and (ii) electro-oxidation by oxide rather than carbonate.

Firstly, a higher oxide activity may potentially impact the formation of activated carbon through gasification. Chemical activation of carbon is routinely carried out on an industrial scale using strong bases such as KOH [48]. Further, the aforementioned conditions used to prepare activated carbon using alkali metal carbonate reagents show a high efficacy at elevated temperatures (500–800 °C) under N_2 [49,52], which has also been suggested to promote oxide activity in the melt [18].

The second consequence of a higher oxide activity is the impact it likely has upon carbon electro-oxidation. Cherepy et al. [28] indicated that both surface reactive carbon and oxide are involved throughout every step of the electro-oxidation mechanism. Therefore the rate of electro-oxidation is dependent upon the availability of these species, specifically the one which is in least supply. If surface reactive C^{2+} is to be substituted with the aforementioned organometallic complexed carbon, then the Cherepy et al. mechanism can be amended to show how organometallic complexes are involved in electro-oxidation from C^{2+} to C^{4+}. The first three steps in the Cherepy mechanism show the oxidation from C^0 to C^{4+}, hence they can be replaced with organometallic complex formation either electrochemically under a non-CO_2 atmosphere (Eqn (30)-(32)), or chemically under CO_2 and at OCP (Eqns (34)-(36)). The

last three step in the Cherepy mechanism may then be replaced with:

$[M - CO]^+ + O^{2-} \rightarrow [M - CO_2]^-$	Slow adsorption	(38)
$[M - CO_2]^- \rightarrow [M - CO_2] + e^-$	Fast discharge	(39)
$[M - CO_2] \rightarrow M^+ + CO_2 + e-$	Fast discharge and evolution	(40)
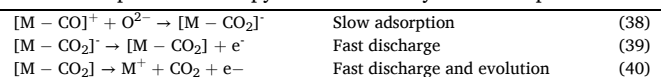
Direct electro-oxidation may be possible from both oxide (Eqns (39)-(41)) or carbonate species (Eqns (42)-(43)); i.e.,

$$C + CO_3^{2-} \rightarrow 3CO_2 + 4e^- \tag{41}$$

However, oxidation from CO_3^{2-} is likely to be kinetically slower, which has not generally been discussed as an issue in the literature. It is expected to be slower because the carbonate anion is comparatively larger than oxide, leading to steric interference with the carbon surface. The radius of carbonate and the van der Waals radius of oxide anions are 2.05–2.44 Å [65] and 1.4 Å [66], respectively. Carbonate is a resonance structure where the C–O bond order rapidly alternates between 1 and 2, hence this bond distance represents an average value over a time scale [67]. Therefore, comparing the radius of a polyatomic ion with a van der Waals radius of a single anion is not exact. The carbonate anion is physically larger than oxide, occupying an area of up to 2.10 $Å^2$ if oriented flat at the electrode surface. Carbonate adopts a trigonal planar geometry with a C–O bond distance of 1.28 Å and bond angles of 120° [18]. From these known dimensions trigonometry was used to calculate the O–O and bond distance in the carbonate anion, which was found to closely match the Tobolsky parameter calculation reported by Ward et al. (2.13 Å) [68].

Due to size differences, oxide is expected to be able to physically pack more efficiently than carbonate at the electrode/electrolyte interface, which is the boundary between the molten carbonate and the fuel. This may be a reason why Peng et al. [18] suggest that oxide activity is at its highest at the electrode interface, as opposed to being evenly dispersed throughout the bulk.

To be clear, the initial two-electron oxidation step from C^0 to C^{2+} takes place along with organometallic complex formation, and it is a comproportionation reaction involving both the carbon fuel and the carbonate. Therefore, carbonate and not oxide is required for this first step to take place. Following this, the two-electron oxidation from C^{2+} to C^{4+} can take place from either carbon or carbonate, however the reaction from oxide is likely to be kinetically favoured.

4.3. Electrical double layer and oxide diffusion

Charge density can be related to the formation of an electrical double layer (EDL) at the interface between the electrode and the electrolyte via the Poisson–Boltzmann Equation [53]; i.e.

$$\frac{d^2\varphi}{dx^2} = -\frac{1}{\varepsilon\varepsilon_o}\rho \tag{42}$$

where ρ is the charge density (C.m^{-3}), φ is the potential (V), x represents the distance (m) from the electrodes surface, ε is the electrolyte dielectric constant, and ε_o is the permittivity of free space (8.854 × 10^{-12} kg^{-1} m^{-3} s^4.A^2). Integrating charge density with respect to distance in one dimension gives an expression for the electric field ($\bar{\varepsilon}$); i.e.,

$$\bar{\varepsilon} = -\frac{d\varphi}{dx} = \frac{1}{\varepsilon\varepsilon_o}\int \rho dx \tag{43}$$

Integrating the electric field over distance in one dimension produces an expression to calculate the potential (φ); i.e.,

$$\varphi = -\int \bar{\varepsilon} dx \tag{44}$$

Therefore, an electrical double layer is expected to be produced at the surface of the carbon electrode during steady state electrochemical oxidation.

There are several species that may contribute to the electrical double

layer in the case of carbon electro-oxidation in molten carbonates. Firstly, the adsorption of organometallic complexes which bear a +1 positive charge (Eqns (30)-(32)). Another contribution is the reported phenomenon of lithium ion intercalation into carbon [69–74], which contributes to the overall positive charge at the electrode. Lithium intercalation (lithiation [75]) has been proposed to occur in DCFC anode half-cells operating at 600 °C using graphite as a fuel with a range of carbonate compositions, both binary and ternary [6]. Necessary conditions for the lithium intercalation are an activity gradient of Li^+ between the carbon electrode and the molten electrolyte, the availability of sufficiently sized vacant sites, including a short hopping distance between the sites, and overall charge neutrality. Taking graphite as a standard material, the separation distance between the individual graphene sheets which act as interstitial sites is 3.35 Å [76]. This is very large by comparison the size of the Li^+ cation is 1.52 Å [77], therefore lithium intercalation is plausible. On the nanoscale, interstitial lithiation occurs in-between two C^{2+} ions at the electrode/electrolyte interface and two carbon atoms which are one row removed from the interface; i.e.,

$$2 \, nC + 2nC^{2+} + nLi^+ \rightarrow C_{4n}Li_n^{5n+} \tag{45}$$

The two C^{2+} ions at the part of an organometallic complex (Eqn (47)), which is illustrated in Section 4.4.

$$2 \, nC + 2n[M - CO]^+ + nLi^+ \rightarrow n[M_2LiC_4O_2]^{2+} \tag{46}$$

In order to maintain charge neutrality over the electrode/electrolyte interfacial area, negatively charged oxide might adsorb directly to the surface, forming a Stern layer. This also serves to facilitate electro-oxidation by eliminating any possibility of a diffusion limitation.

Oxide diffusion in alkali metal carbonate media is a critical component of this electrical double layer hypothesis. Spedding et al. [78] measured trace ion diffusion coefficients for Na^+, K^+ and CO_3^{2-} in the binary Li_2CO_3/K_2CO_3 eutectic using the open ended capillary method. The diffusion coefficients have been summarised in Table 2. From this table the diffusion of CO_3^{2-} is much slower than both of the alkali metal cations, which is an expected result given the larger size of the carbonate anion. In general the diffusivity of individual ions increases as the van der Waals ionic radius decreases, because smaller ions can more freely hop between vacant sites. However, when examining the diffusivity of the individual alkali cations in molten carbonate mixtures, the opposite trend is noted, such that $K^+ > Na^+ > Li^+$, and the van der Waals ionic radii of these alkali metal cations is 2.8 Å [34], 2.27 Å [77] and Li 1.52 Å [77], respectively. This trend only applies to mixtures, and not the parent materials; i.e., individual Li_2CO_3, Na_2CO_3 and K_2CO_3, and it is known as the Chemla effect. This phenomena has been reported by Janz et al. [65] when examining Na_2CO_3/K_2CO_3 binary mixtures and Janssen et al. [79] looking at Li_2CO_3/K_2CO_3 binary mixtures. The Chemla effect occurs in certain mixtures of molten salts when the smaller cations are drawn closer to significantly larger anions which restricts the mobility (μ) of the cation.

Molten salts characteristically exhibit strong bonds between the individual ions of opposing charges. Both melting temperature and viscosity are indicators of interionic bond strength. The melting temperature of the ternary eutectic has been reported to be within the range between 380 and 397 °C by four separate authors; i.e., Glenn et al. [80] (387 °C), Janz et al. [81] (397 °C), Tamaru et al. [82] (390 °C) and Volkova et al. [83] (380 °C). In terms of transport properties viscosity is

differentiated from the diffusion coefficient of a single ion in that the former describes the movement of ions pairs; i.e., $[M^+CO_3^{2-}]$, in the case of molten carbonates. Janz et al. [65] measured the viscosity (η, poise) of the ternary eutectic over a range of temperatures (483–600 °C) using an oscillating viscometer. The viscosity values presented in this work were measured below the typical DCFC operation temperature range, hence the data was extrapolated using an exponential model to 700 °C where the viscosity is projected to be 1.03×10^{-2} g cm^{-1} s^{-1}. This viscosity is quite high, thus indicating that strong intermolecular dipole-dipole interactions are in effect.

The diffusion of oxide ions in molten carbonate media has not been measured, however Chen et al. [45] suggests that oxide selectively diffuses to the crest of the meniscus front, which is the interface with the carbon fuel.

The density (ρ; g.cm^{-3}) of the ternary eutectic was measured by Ward et al. [68] using a capillary type MgO conductance cell to be 1.99 g cm^{-3} at 720 °C. However, what is of most interest here is the charge density for oxide ions, which is comparatively greater compared to carbonate. Both are divalent anions, however the mass of carbonate is almost four-fold greater than oxide; i.e., 60 g mol^{-1} versus 16 g mol^{-1}, respectively. Therefore, the force experienced due to the electric field would be greater for oxide (Eqn (45)), thus causing it to selectively diffuse to the fuel/electrolyte interface.

The mechanism for oxide ions diffusion through molten alkali metal carbonate media has not been explored in the literature. One possibility is that it may follow a model which is similar to the way that protons diffuse through aqueous media; i.e., the Grotthuss mechanism [84]. Janz and Lorenz hypothesized that the movement of ion pairs; i.e., $[M^+CO_3^{2-}]$, within the molten carbonate media may follow a Grotthuss-type mechanism [59]; however, this is a different to the transport of oxide through molten carbonates. Fig. 5 illustrates a Grotthuss mechanism analogue which has been visualised for the diffusion of oxide ions in molten carbonate media. The exact state an individual oxide anion begins in is arbitrary given that the occupancy positions are interchanging. The letters (a)–(f) in Fig. 5 simply represent a sequence of steps whereby O^{2-} is depicted as hopping from one CO_3^{2-} to the next. In this way carbonate acts as a vehicle via which oxide is able to diffuse through the melt with expedience. The dashed lines represent dipole-dipole interactions between the carbonate anions and the corresponding alkali metal cations in the melt.

One consequence of this mechanism would be that no species can physically diffuse through a carbonate melt more quickly than an oxide anion. This has implications for DCFC system designs that include the use of chemical mediators and shuttles [85] as it is expected that the same effect could be enabled through increasing oxide activity in the melt to a greater effect. This is not to say that the diffusion process is particularly expedient compared to the diffusion of protons through water for example, however it does represent a physical limitation of the molten carbonate system. The reason for this comes directly from the Grotthuss mechanism, which explains why protons are able to diffuse through aqueous media at an unparalleled rate [86].

4.4. Electrical double layer effects on DCFC behaviour

The effect of adsorbed oxide anions at the electrode interface would be to enable facile electro-oxidation, which should be affected by both the oxide activity in the melt and the applied potential. In this sense the Stern layer can be thought of as means by which oxide is made readily available prior to electro-oxidation, thus eliminating any diffusion limitation on the reaction rate. When examining voltammetric data from DCFC half-cell experiments the current increases as expected with potential. However, Fig. 6 shows that the extent of this increase varies significantly when the electrode is modified, particularly when a polarising potential above 0.2 V is applied. From this figure the current density for three different electrodes can be rated as graphite < coal < coal + catalyst. Graphite is a uniform crystalline material which exhibits

Table 2
Trace ion diffusion coefficients (cm^2.s^{-1}) for Na^+, K^+ and CO_3^{2-} in the ternary alkali metal carbonate eutectic around the DCFC operational temperature range 654 ± 44 °C.

Ion Species	Trace Ion Diffusion Coefficients Range ($\times 10^5$ cm^2 s^{-1})
Na^+	2.20–2.35
K^+	1.98–2.08
CO_3^{2-}	4.93–5.20
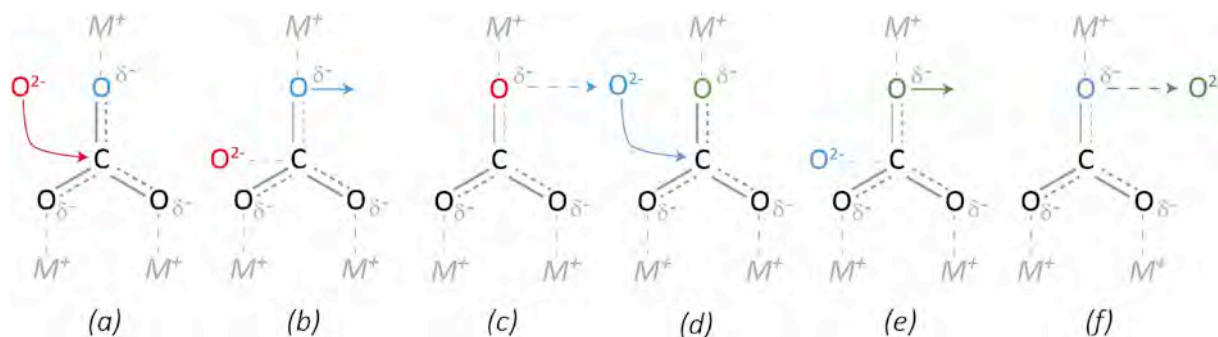
Fig. 5. Proposed mechanism for oxide conduction in molten alkali metal carbonates.

preferred orientation, hence the electro-oxidative activity has been demonstrated to be lower compared to coal which is amorphous [87]. Further, graphite is an allotrope of sp^2 hybridised carbon with delocalised π-electrons; i.e., $(sp^2)^3$ and 2p), which enable high electrical conductivity; however, for this reason it is also an ineffective dielectric, hence the breakdown potential is lower than amorphous carbon; e.g., coal char.

The catalyst referred to in Fig. 6 is Kaolin ($Al_2O_3 \cdot 2SiO_2$), which is a clay species found naturally in thermal coals [88]. Kaolin is both an electrical insulator and high polarisable due to its heteroatoms which impart a net dipole moment across the molecule, therefore it is an effective dielectric and the EDL can be charged to a higher potential. Fig. 6[A] shows that electrodes doped with kaolin consistently produced the highest current density, particularly at more anodic potentials where the fuel is polarised. Fig. 6[B] and [C] show that a current spike at ~0.25 V is only present for the electrodes doped with kaolin or coal, where the latter has been shown to contain oxide donating mineral species; e.g., calcite ($Ca(CO_3)$), illite ($K_{0.6}(H_3O)_{0.4}Al_{1.3}Mg_{0.3-}Fe^{2+}_{0.1}Si_{3.5}O_{10}(OH)$) and siderite ($Fe(CO_3)$) etc [88], thus hinting that oxide activity is key to charging the double layer capacitor (DLC).

The EDL is comprised of adsorbed oxide at the $C_{(s)}/CO_3^{2-}{}_{(l)}$ interface which charges the DLC, and the current spikes in Fig. 6 are caused by dielectric breakdown. Logically, a more effective dielectric allows the DLC to be charged to a higher voltage before sudden discharge. There is a positive correlation between the maximum charging voltage, EDL charge density (Eqn (42)) and the amount of energy released upon discharge ($E = \frac{1}{2}CV^2$). The discharge reaction is carbon electro-oxidation from oxide (Eqn (5) – (6)) which is occurring during charging, however because the rate of oxide diffusion to the EDL exceeds the charge transfer kinetics (Fig. 5) then the DLC will continue to charge

until it reaches its theoretical breakdown voltage, which is dictated by the dielectric medium.

A mechanism describing the role of Kaolin as a carbon electro-oxidation catalyst has been proposed recently by Allen et al. [88]. In summary, Kaolin dissolves in the carbonate melt which leads to enhanced interfacial contact area with the fuel via a wetting phenomenon. Thus, Kaolin effectively mediates oxide transfer to the electrode/electrolyte interface. This catalysis pathway is driven by favourable interactions between the molten carbonate and the fuel, which are mediated through the Kaolin. In order to clearly show this, several key literature findings must be considered.

It has been shown that the addition of 5 wt% Kaolin to the ternary eutectic depresses the melting point by 11 °C, thus demonstrating that colligative properties are in effect, and therefore dissolution occurs [80]. In addition, several authors have reported that Kaolin reacts irreversibly upon dissolution to form alkali alumina silicates such as Kaliophilite ($KAlSiO_4$) under CO_2 gasification conditions when mixed with K_2CO_3 and coal char [89–91]. Tulloch et al. [92] examined interactions between coal char and various coal minerals using SEM. It was determined that Kaolin displayed the greatest degree of mixing and contact between the graphite and minerals pre-immersion in molten carbonate. Given that carbon acts as a heterogeneous catalyst for carbonate decomposition (Section 4.1), then dissolved Kaolin; i.e., an alkali aluminosilicate, logically enhances the catalytic effect leading to a greater oxide activity at the electrode/electrolyte interface, and therefore the availability of oxide for electro-oxidation is enhanced. Further, Kaolin facilitates organometallic complex formation by bringing carbon and carbonate in contact, which also contributes to an enhanced rate of electro-oxidation. These effects increase at high polarising potentials (>0.2 V), where under these conditions oxide is drawn to the electrode surface, as Fig. 7
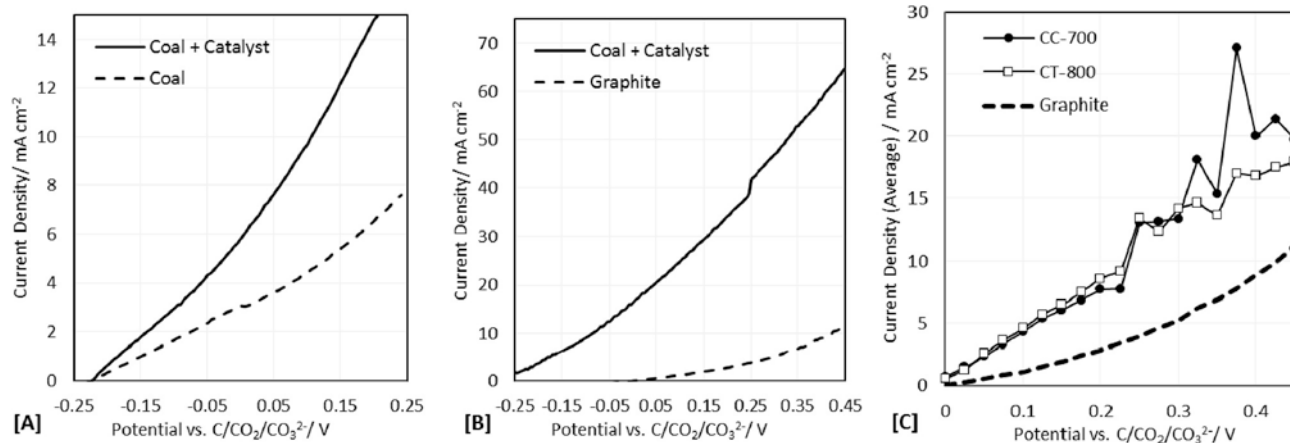
Fig. 6. Linear sweep voltammograms held at 600 °C and swept anodically at a rate of at 5 mV s^{-1} for various electrodes; i.e., unmodified graphite, 70 wt% graphite +30 wt% coal or 70 wt% graphite +25 wt% coal +5 wt% catalyst (Kaolin). CC-700 and CC-800 denote a coking coal pyrolyzed at 700 °C and 800 °C, respectively [88,89].

illustrates. From left to right the carbon electrode is positively charged due to lithiation (Eqns (47)-(48)) and the presence of C^{2+} from two-electron oxidation. Organometallic complexes are adsorbed to the electrode surface which bear an overall charge +1 charge per complex. A Stern layer of oxide is also adsorbed to the surface, thus maintaining charge neutrality over the electrode/electrolyte interface. The diffuse layer consists of an oxide concentration gradient, which gradually decreases with increasing distance away from the electrode surface. In the bulk, carbonate and alkali metal cations are randomly dispersed in the ratio 2:1 for M^+ and CO_3^{2-}, respectively. The maximum potential (ψ; V) is at the electrode/electrolyte interface and decreases moving away towards the bulk, which is given by Eqn (46). Theoretically, in the limit as the distance (x; m) from the electrode surface approaches infinity, the potential moves towards 0 V.

## 5. Additional factors affecting DCFC operation

5.1. Doping with metal oxides

Doping the carbonate melt with metal oxides has been demonstrated to improve the performance over the course of several independent studies [21,93], including Cs_2O due to its role in mediating the shuttle mechanism (Section 4.3) [94,95].

Two studies aimed at examining the performance increase when doping molten carbonate media with metal oxide species have shown great performance improvements. A ternary carbonate eutectic was doped with 20 wt% $CsVO_2$–MoO_3 [93]. In this case, the performance enhancement was attributed to the formation of a chemically produced intermediate species which enhanced the overall reaction kinetics. It is important to mention here that this loading (20 wt%) is very high, and that the communication was brief. Further investigation would be ideal to explain and substantiate these findings.

Wang et al. experimented with doping a carbonate melt by adding 0.1 wt% of transition metal oxides capable of donating oxide anions; i.e., Fe_2O_3, Co_3O_4, NiO, and MnO_2 [21]. Here the net increase in oxide anion concentration was calculated to be between 7.2×10^{-4} and 1.71×10^{-3}

Fig. 7. Electrical double layer at the interface between the carbon electrode (left) and the molten carbonate electrolyte (right). Oxide is adsorbed at the Stern Layer and organometallic complexes are protruding from the electrode interface out into the bulk.

mol per 100 g depending upon the dopant species added, and assuming 100% dissociation in solution. In the case of NiO this assumption is uncertain, because a number of different authors indicate that only partial dissolution occurs in molten carbonates [96,97]. Wang et al. reported doubling of the current density at the same polarisation compared to the control. It is important to note that these experiments were performed under N_2 not CO_2 [21]. These authors do not state why N_2 was chosen over CO_2. A critical review of this study might suggest that the exercise of adding these dopant species may actually have no overall effect upon the oxide anion concentration under CO_2. The reason being the system equilibrium will shift to counteract any changes. Given that the alkali metal carbonate media is an abundant source of oxide anions, far exceeding any contributions coming from the dopant species, what effectively limits carbonate dissociation is the CO_2 saturation coming from the gas atmosphere [98]. Adding oxide-donating dopants may initially cause a small spike in the net O^{2-} ion concentration, however the presence of dissolved CO_2 at the saturation limit would cause the system to counteract the changes via carbonate formation. In this case the dopant species are expected to simply react with CO_2 to form carbonate variants of the metal oxides that were initially added (Eqn (48)); i.e.,

$M^{2+} + O^{2-} + CO_2 \leftrightarrow MCO_3$	(M = Fe, Co, Ni, Mn)	(47)
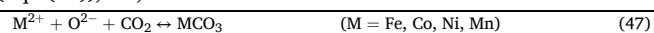
Deng et al. [64] measured the solubility of Li_2O in the ternary eutectic to be very low at 0.835 mol_{CO_2}/mol_{Li_2O} at 550 °C using a reactor with in-situ pressure monitoring. The undissolved Li_2O particles were found to be suspended at the gas-liquid interface, due to their lower density compared to the molten carbonate. Interestingly, the reaction between Li_2O and CO_2 to form Li_2CO_3 (Eqns (49)-(50)) was found to be exothermic from thermodynamic calculations [64].

$Li_2O(l) + CO_2(g) \leftrightarrow Li_2CO_3(l)$	($\Delta H_{723\ K} = -207.8$ kJ mol^{-1})	(48)
$Li_2O(s) + CO_2(g) \leftrightarrow Li_2CO_3(l)$	($\Delta H_{723\ K} = -214.6$ kJ mol^{-1})	(49)
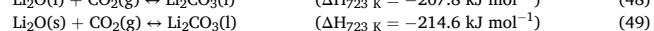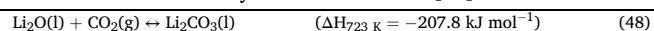
This may be advantageous for the DCFC as the addition of alkali metal oxides under a CO_2 atmosphere generates heat, thus offsetting the energy penalty brought on by the reverse Bouduard reaction which is an endothermic process (159.7 kJ mol^{-1}) [25].

5.2. Solid oxide electrolyte considerations

YSZ remains the most commonly used solid oxide electrolyte, due to its high oxide conductivity, mechanical strength, comparatively lower cost and thermal expansion coefficient that is well matched with LSM (10×10^{-6} °C^{-1} over the range 25–1000 °C [99]). However, YSZ does not exhibit low temperature (<750 °C) oxide anion conductivity to make it comparable with SDC, GDC and especially BiO_3 based materials (0.37 S cm^{-1} at 700 °C [5]) [4], however the mechanical strength of YSZ is unparalleled (Table 3). 3YSZ (3 mol% Y_2O_3 + 97 mol% ZrO_2) and 8YSZ (8 mol% Y_2O_3 + 92 mol% ZrO_2) are the two most commonly used blends, with the former (3YSZ) exhibiting four-fold the mechanical strength, yet only one third the mechanical strength of the latter (8YSZ), as shown in Table 3 [5]. Thinner membranes lead to an enhanced oxide diffusivity, hence performance optimisation is often a balance between mechanical strength and oxide conductivity. Literature surveys show that majority of high performing cells incorporate a membrane thickness of <1 mm [8].

Both zirconia and YSZ can undergo temperature induced phase

Table 3
Mechanical strength and ionic conductivity of YSZ blends at 800 °C [5].

Blend	Mechanical Strength (MPa)	Ionic Conductivity (S.cm^{-1})
8YSZ	250–300	0.052
3YSZ	1100–1150	0.018
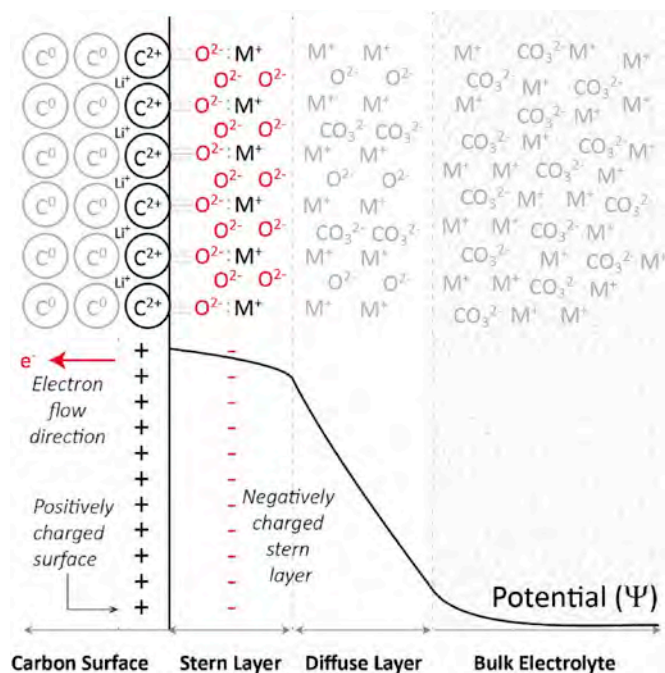
transitions which are influenced by the yttria loading [100], from monoclinic (<1170 °C) to tetragonal (1170–2350 °C) to cubic (2350–2680 °C) [5,101]. The tetragonal phase exhibits superior ionic conductivity; hence, sintering is recommended to be kept below 1600 °C to avoid entering the tetragonal-cubic phase transition. Applying thin surface layer of YSZ nanoparticles mixed with LSM to a YSZ substrate prior to sintering can optimise the surface area at the triple phase boundary [10]; i.e., O_2/LSM/YSZ, and lead to better adhesion to the substrate via the formation of a YSZ + LSM intergrowth layer [102]. YSZ also has very poor thermal conductivity (2.2 W mK^{-1} [103]), even to the point where it is used as a resistive heating element [104], however this can present a challenge for DCFC systems that rely upon transferring heat across a YSZ membrane.

5.3. Atmospheric gas selection

The selection of which gas atmosphere to utilise during DCFC operation should be guided by a number of factors that must be considered [105]. Most importantly air should be kept well away from the fuel, as this leads to spontaneous combustion at DCFC operating temperatures, which can quickly consume the carbon. This can be achieved by passing a stream of CO_2 over the anode compartment or another inert gas such as N_2 or Ar.

For practical DCFCs maintaining a CO_2 partial pressure over the carbonate compartment prevents total carbonate decomposition, otherwise the DCFC will not be able to operate long enough to produce significant energy. Total carbonate decomposition leaves behind a mixture of alkali metal oxide crystals which cannot serve as an electrolyte due to being dispersed in the solid phase [63].

Carbonate decomposition is inversely correlated with both the net pressure under a pure CO_2 atmosphere and the CO_2 partial pressure under a mixed gas atmosphere, due to Henry's law [41]. Janz et al. [59] and Spedding et al. [78] quantified the extent of carbonate decomposition in response to varying the CO_2 pressure above the ternary eutectic over a range of temperatures 700–950 °C (see Section 4.3).

The kinetics of the reverse Bouduard gasification are positively correlated with CO_2 partial pressure for thermal coals [17], hence mixing CO_2 with another inert gas can be an effective method of controlling this parasitic reaction. Also, the open circuit potential (OCP) has been shown to be 0.1–0.3 V higher under N_2 compared with CO_2, where the reverse Bouduard reaction (Eqn (7)) can take place [10]. Logically, this may translate to a higher peak power potential, and therefore more efficient operation. Of course, power can be calculated from the product of current and potential; i.e.,

$$P = V \times I \tag{50}$$

Efficiency losses due to heat conversion are proportion to the operating current; i.e.,

$$P_{loss} = I^2 \times R \tag{51}$$

Assuming that peak power is constant, then operating at a higher potential requires a lower current which would therefore mitigate losses through inefficiency. Hence mixing a small amount of N_2 or another inert gas with CO_2 may enhance efficiency.

For three-electrode studies of the anode half-cell a graphite reference and counter electrode have traditionally been employed [6,87,92]. In these cases CO_2 has been utilised for the reference electrode reactions (Eqn (1) and (42)), however there are other reversible carbon oxidation and reduction pathways that do not utilise CO_2 [106,107]; i.e.,

$$CO_3^{2-} + 4e^- \leftrightarrow C + 3O^{2-} \tag{52}$$

For the aforementioned reasons it is therefore recommended that the experimenter select the appropriate gas type, mixture and partial pressure tailored for their specific arrangement.

5.4. Electro-catalysis mechanism

Combining each of the factors that affect DCFC performance an integrated electro-catalysis mechanism can be devised (Fig. 8). This takes into account the mechanism of each process and how it impacts on other processes for both CO_2 and CO_2-depleted atmospheres. The solid line in this figure represents the catalytic effect, while the dashed line shows an inhibitory response. Gasification triggers carbon activation, the formation of organometallic complexes and carbonate decomposition. Carbonate decomposition under CO_2-depleted atmospheres causes an increase in oxide activity, which in turn enhances gasification, thus creating a positive feedback loop.

Carbon activation and lithiation, organometallic complex formation and an elevated oxide activity all contribute to the formation of an EDL. The EDL facilitates electro-oxidation by providing a source of oxide at the Stern layer which is used to further oxidise C^{2+} to C^{4+} and eliminate the possibility of a diffusion limitation.

It should also be noted that electro-oxidation and gasification consume the carbon fuel. In fact, they are in direct competition. Of these two processes electro-oxidation is the process which contributes to the current response, hence controlling gasification is paramount to performance optimisation. Gasification may contribute to initiating conditions that are ideal for facile electro-oxidation, however once these conditions are established it ultimately becomes parasitic. In addition, the formation of charged organometallic complexes may also suppress gasification due to the associate effect of the electric field. This would be especially true once a complete surface overage of the electrode is established. For these reasons controlled gasification pre-treatments may be an option to explore for future works.

6. Conclusion

This review has shown how information scattered throughout the literature in separate research spheres all contributes to performance in the DCFC. It is important to be aware of the ways in which the system can behave, and the effects that each of these behaviours exert. The aim of this work has been to increase awareness in the sphere of DCFC literature for the purpose of both advancing understanding and for system optimisation.

Outcomes of this communication are:

(i) Various processes including electro-oxidation, gasification, carbon activation and carbonate decomposition which occur in the DCFC have been discussed, including their interdependency with comments being made regarding possible performance effects.
(ii) The formation of organometallic complexes was explored in the context of the DCFC, and the role they may place in the electro-oxidation mechanism.
(iii) Electro-oxidation from either carbonate or oxide were considered as separate pathways, going against the literature paradigm that implies spontaneous carbonate decomposition (autodissociation) is occurring under a CO_2 atmosphere.
(iv) Oxide activity has been considered as an important parameter which can be used to explain the performance of various fuels and potential triggered spikes from voltammetry data in the literature.
(v) Electrical double layer formation has been suggested under conditions that lead to an enhanced oxide activity; e.g., a CO_2-depleted atmosphere, kaolin doped fuel and polarising potential >0.2 V.

Declaration of competing interest

The authors declare that they have no known competing financial interests or personal relationships that could have appeared to influence the work reported in this paper.
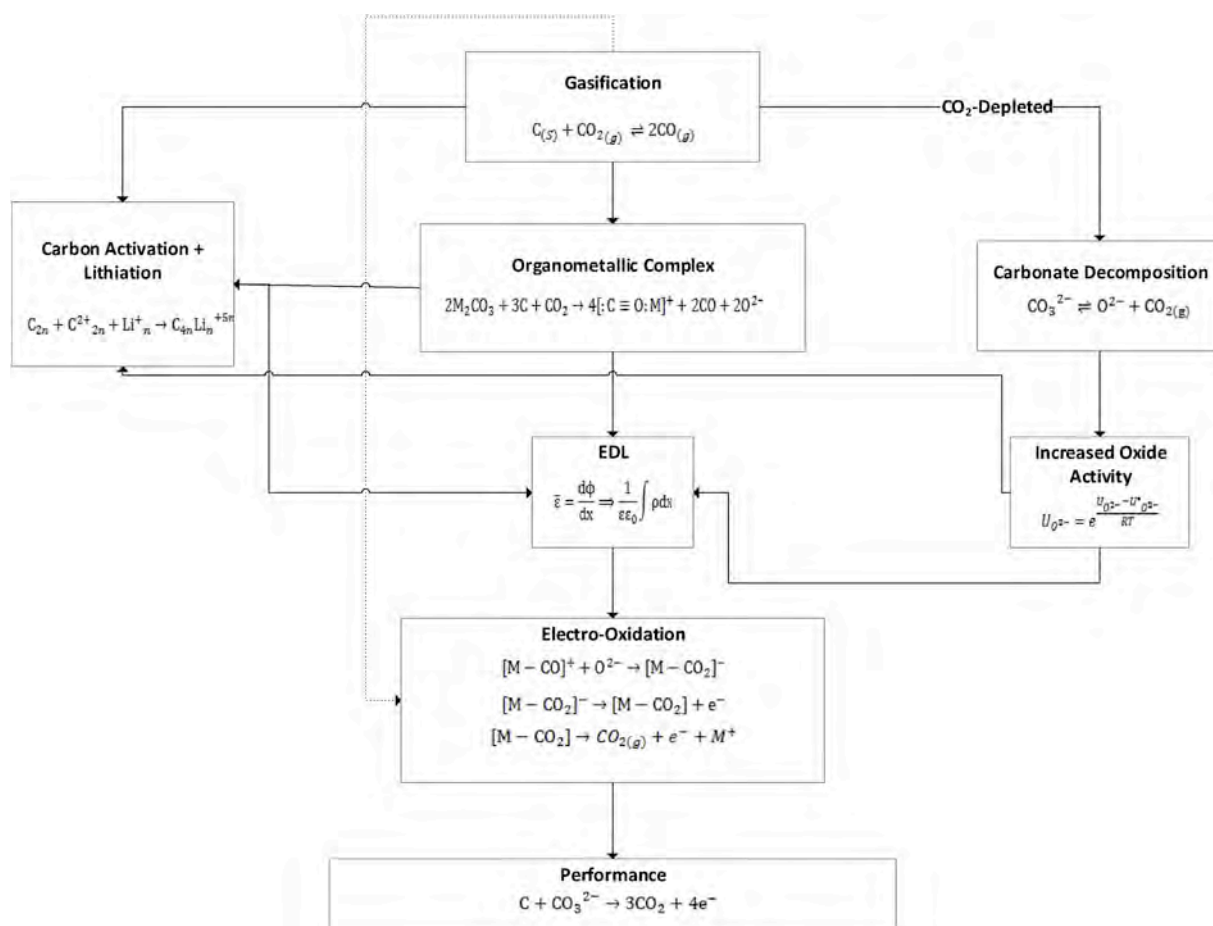
Fig. 8. Electro-catalysis mechanism for the DCFC under both CO_2 and CO_2-depleted atmospheres. Solid lines indicate an enhanced response, whereas dashed lines represent in inhibitory response.

References

[1] J.F. Cooper, Direct conversion of coal derived carbon in fuel cells, in: S. Basu (Ed.), Recent Trends in Fuel Cell Science and Technology, Anamaya Publishers, New Delhi, India, 2007.

[2] P. Freund, Making deep reductions in CO2 emissions from coal-fired power plant using capture and storage of CO2, Proc Inst Mech Eng A J Power Energy 217 (1) (2003) 1–7.

[3] T.M. Gür, Perspective—low-carbon electricity is great: what about "less-carbon"? J. Electrochem. Soc. 164 (14) (2017) F1587–F1590.

[4] H. Yokokawa, et al., Recent developments in solid oxide fuel cell materials, Fuel Cells 1 (2) (2001) 117–131.

[5] S. Badwal, F. Ciacchi, Oxygen-ion conducting electrolyte materials for solid oxide fuel cells, Ionics 6 (1–2) (2000) 1–21.

[6] J. Allen, et al., Molten carbonate composition effects on carbon electro-oxidation at a solid anode interface, J. Electrochem. Soc. 162 (1) (2015) F76–F83.

[7] J.A. Allen, et al., Kinetic analysis of the anodic carbon oxidation mechanism in a molten carbonate medium, Electrochim. Acta 129 (2014) 389–395.

[8] C. Jiang, et al., Challenges in developing direct carbon fuel cells, Chem. Soc. Rev. 46 (10) (2017) 2889–2912.

[9] C. Li, Y. Shi, N. Cai, Performance improvement of direct carbon fuel cell by introducing catalytic gasification process, J. Power Sources 195 (15) (2010) 4660–4666.

[10] A.C. Rady, et al., Review of fuels for direct carbon fuel cells, Energy Fuels 26 (3) (2012) 1471–1488.

[11] J.-Y. Lee, et al., A performance study of hybrid direct carbon fuel cells: impact of anode microstructure, Int. J. Hydrogen Energy 39 (22) (2014) 11749–11755.

[12] W. Hao, X. He, Y. Mi, Achieving high performance in intermediate temperature direct carbon fuel cells with renewable carbon as a fuel source, Appl. Energy 135 (2014) 174–181.

[13] S.J. Skinner, Recent advances in Perovskite-type materials for solid oxide fuel cell cathodes, Int. J. Inorg. Mater. 3 (2) (2001) 113–121.

[14] R.A. Matula, Electrical resistivity of copper, gold, palladium, and silver, J. Phys. Chem. Ref. Data 8 (4) (1979) 1147–1298.

[15] Y. Tang, J. Liu, Effect of anode and Boudouard reaction catalysts on the performance of direct carbon solid oxide fuel cells, Int. J. Hydrogen Energy 35 (20) (2010) 11188–11193.

[16] Y. Xie, Y. Tang, J. Liu, A verification of the reaction mechanism of direct carbon solid oxide fuel cells, J. Solid State Electrochem. 17 (1) (2013) 121–127.

[17] M.F. Irfan, M.R. Usman, K. Kusakabe, Coal gasification in CO 2 atmosphere and its kinetics since 1948: a brief review, Energy 36 (1) (2011) 12–40.

[18] F. Peng, et al., Direct Carbon Fuel Cells–Wetting behavior of graphitic carbon in molten carbonate, Int. J. Hydrogen Energy 41 (41) (2016) 18858–18871.

[19] F. Rodriguez-Reinoso, M. Molina-Sabio, M. Gonzalez, The use of steam and CO2 as activating agents in the preparation of activated carbons, Carbon 33 (1) (1995) 15–23.

[20] J. Rosolen, F. Decker, Stress in carbon film electrodes during Li+ electrochemical intercalation, J. Electrochem. Soc. 143 (8) (1996) 2417–2421.

[21] C.Q. Wang, et al., Significant improvement of electrooxidation performance of carbon in molten carbonates by the introduction of transition metal oxides, J. Power Sources 233 (2013) 244–251.

[22] B.J. Wood, R.D. Brittain, K. Lau, A study of the role of alkali metal salts as char gasification catalysts by Knudsen cell mass spectrometry, Carbon 23 (1) (1985) 73–77.

[23] S. Giddey, et al., A comprehensive review of direct carbon fuel cell technology, Prog. Energy Combust. Sci. 38 (3) (2012) 360–399.

[24] C.L. Spiro, et al., Significant parameters in the catalysed CO 2 gasification of coal chars, Fuel 62 (3) (1983) 323–330.

[25] J.G. Peacey, W.G. Davenport, The Iron Blast Furnace: Theory and Practice, Elsevier, 2016.

[26] N. Araki, et al., Measurement of thermophysical properties of molten salts: mixtures of alkaline carbonate salts, Int. J. Thermophys. 9 (6) (1988) 1071–1080.

[27] F. Long, K. Sykes, The catalysis of the oxidation of carbon, J. Chim. Phys 47 (1950) 361–378.

[28] N.J. Cherepy, et al., Direct conversion of carbon fuels in a molten carbonate fuel cell, J. Electrochem. Soc. 152 (1) (2005) A80–A87.

[29] D.W. McKee, et al., Catalysis of coal char gasification by alkali metal salts, Fuel 62 (2) (1983) 217–220.

[30] B. Wood, et al., Mechanism of catalytic gasification of coal char, in: Quarterly Technical Progress Report No. 3, 1 April-30 June 1981, SRI International, Menlo Park, CA (USA), 1981.

[31] Glenn, M.J., J.A. Allen, and S.W. Donne, Carbon gasification from a molten carbonate eutectic. Energy Technol. 0(0).

[32] K. Nagase, et al., Kinetics and mechanisms of the reverse Boudouard reaction over metal carbonates in connection with the reactions of solid carbon with the metal carbonates, Phys. Chem. Chem. Phys. 1 (24) (1999) 5659–5664.

[33] J. Kopyscinski, et al., K 2 CO 3 catalyzed CO 2 gasification of ash-free coal. Interactions of the catalyst with carbon in N 2 and CO 2 atmosphere, Fuel 117 (2014) 1181–1189.

[34] A. Gordon, F. Tristan, SI Chemical Data, John Wiley & Sons Incorporated, 1998.

[35] R.I. Olivares, C. Chen, S. Wright, The thermal stability of molten lithium–sodium–potassium carbonate and the influence of additives on the melting point, J. Sol. Energy Eng. 134 (4) (2012) 041002.

[36] P. Lorenz, G. Janz, Electrochemical reduction of oxygen in carbonate and carbonate-halide melts, J. Electrochem. Soc. 118 (10) (1971) 1550–1553.

[37] D.W. McKee, Mechanisms of the alkali metal catalysed gasification of carbon, Fuel 62 (2) (1983) 170–175.

[38] B. Jalan, Y. Rao, A study of the rates of catalyzed boudouard reaction, Carbon 16 (3) (1978) 175–184.

[39] B.V. L'vov, Mechanism of carbothermal reduction of iron, cobalt, nickel and copper oxides, Thermochim. Acta 360 (2) (2000) 109–120.

[40] J. Kopyscinski, et al., K2CO3-catalyzed CO2 gasification of ash-free coal: kinetic study, Energy Fuels 27 (8) (2013) 4875–4883.

[41] P. Claes, D. Moyaux, D. Peeters, Solubility and solvation of carbon dioxide in the molten Li2CO3/Na2CO3/K2CO3 (43.5 : 31.5 : 25.0 mol-%) eutectic mixture at 973 K I. Experimental part, Eur. J. Inorg. Chem. (4) (1999) 583–588.

[42] J. Yu, B. Yu, Y. Li, Electrochemical oxidation of catalytic grown carbon fiber in a direct carbon fuel cell using Ce 0.8 Sm 0.2 O 1.9-carbonate electrolyte, Int. J. Hydrogen Energy 38 (36) (2013) 16615–16622.

[43] Y. Nabae, K.D. Pointon, J.T. Irvine, Electrochemical oxidation of solid carbon in hybrid DCFC with solid oxide and molten carbonate binary electrolyte, Energy Environ. Sci. 1 (1) (2008) 148–155.

[44] R. Weaver, et al., Direct Electrochemical Generation of Electricity from Coal, Report May 16, 1977–February 15, SRI, Menlo Park, CA 94025, 1979. SAN-0115/ 105-1.

[45] C.C. Chen, et al., Wetting behavior of carbon in molten carbonate, J. Electrochem. Soc. 159 (10) (2012) D597–D604.

[46] M. Kosmulski, Surface Charging and Points of Zero Charge, vol. 145, CRC Press, 2009.

[47] T. Otowa, Y. Nojima, T. Miyazaki, Development of KOH activated high surface area carbon and its application to drinking water purification, Carbon 35 (9) (1997) 1315–1319.

[48] H. Marsh, F.R. Reinoso, Activated Carbon, Elsevier, 2006.

[49] J.i. Hayashi, et al., Preparation of activated carbon from lignin by chemical activation, Carbon 38 (13) (2000) 1873–1878.

[50] J.F. Cooper, J.R. Selman, Analysis of the carbon anode in direct carbon conversion fuel cells, Int. J. Hydrogen Energy 37 (24) (2012) 19319–19328.

[51] W.-Y. Wen, Mechanisms of alkali metal catalysis in the gasification of coal, char, or graphite, Catal. Rev. Sci. Eng. 22 (1) (1980) 1–28.

[52] D. Adinata, W.M.A.W. Daud, M.K. Aroua, Preparation and characterization of activated carbon from palm shell by chemical activation with K 2 CO 3, Bioresour. Technol. 98 (1) (2007) 145–149.

[53] A.J. Bard, et al., Electrochemical Methods: Fundamentals and Applications, vol. 2, Wiley, New York, 1980.

[54] B. Cantero-Tubilla, et al., Investigation of anode configurations and fuel mixtures on the performance of direct carbon fuel cells (DCFCs), J. Power Sources 238 (2013) 227–235.

[55] J.D. Lee, Concise Inorganic Chemistry, John Wiley & Sons, 2008.

[56] E. Weiss, Structures of organo alkali metal complexes and related compounds, Angew. Chem. Int. Ed. 32 (11) (1993) 1501–1523.

[57] J.W. Steed, First-and second-sphere coordination chemistry of alkali metal crown ether complexes, Coord. Chem. Rev. 215 (1) (2001) 171–221.

[58] A.L. Companion, M. Komarynsky, Crystal field splitting diagrams, J. Chem. Educ. 41 (5) (1964) 257.

[59] G.J. Janz, M.R. Lorenz, Molten carbonate electrolytes: physical properties, structure, and mechanism of electrical conductance, J. Electrochem. Soc. 108 (11) (1961) 1052–1058.

[60] C.A. Mims, J.K. Pabst, Alkali catalyzed carbon gasification I. Nature of the catalytic sites, Prepr. Am. Chem. Soc. Div. Pet. Chem. 180 (1980) 258–262.

[61] C.A. Mims, J.K. Pabst, Alkali-catalyzed carbon gasification. II. Kinetics and mechanism, United States, Am. Chem. Soc., Div. Fuel Chem., Prepr. 25 (1980). CONF-800814-P2.

[62] D. McKee, D. Chatterji, The catalytic behavior of alkali metal carbonates and oxides in graphite oxidation reactions, Carbon 13 (5) (1975) 381–390.

[63] G.J. Janz, Molten Salts Handbook, Elsevier, 2013.

[64] B. Deng, et al., Kinetic and thermodynamic characterization of enhanced carbon dioxide absorption process with lithium oxide-containing ternary molten carbonate, Environ. Sci. Technol. 50 (19) (2016) 10588–10595.

[65] G.J. Janz, F. Saegusa, Molten carbonates as electrolytes: viscosity and transport properties, J. Electrochem. Soc. 110 (5) (1963) 452–456.

[66] A. Bondi, Van der Waals volumes and radii, J. Phys. Chem. 68 (3) (1964) 441–451.

[67] A. Streitwieser, et al., Introduction to Organic Chemistry, vol. 643, Macmillan, New York, 1992.

[68] A.T. Ward, G. Janz, Molten carbonate electrolytes: electrical conductance, density and surface tension of binary and ternary mixtures, Electrochim. Acta 10 (8) (1965) 849–857.

[69] E. Jacques, et al., The effect of lithium-intercalation on the mechanical properties of carbon fibres, Carbon 68 (2014) 725–733.

[70] H. He, et al., Dynamic study of Li intercalation into graphite by in situ high energy synchrotron XRD, Electrochim. Acta 92 (2013) 148–152.

[71] A. Satoh, N. Takami, T. Ohsaki, Electrochemical intercalation of lithium into graphitized carbons, Solid State Ion. 80 (3) (1995) 291–298.

[72] P. Bernardo, et al., Influence of graphite surface properties on the first electrochemical lithium intercalation, Carbon 49 (14) (2011) 4867–4876.

[73] V.A. Sethuraman, et al., Surface structural disordering in graphite upon lithium intercalation/deintercalation, J. Power Sources 195 (11) (2010) 3655–3660.

[74] Q. Xu, et al., Electrochemical investigation of lithium intercalation into graphite from molten lithium chloride, J. Electroanal. Chem. 530 (1) (2002) 16–22.

[75] S.-C. Wang, et al., The contribution of functional groups in carbon nanotube electrodes to the electrochemical performance, Electr. Mater. Lett. 10 (1) (2014) 241–245.

[76] S. Reich, C. Thomsen, Raman spectroscopy of graphite, Phil. Trans. R. Soc. Lond. A: Maths. Phys. Eng. Sci. 362 (1824) (2004) 2271–2288.

[77] G.H. Aylward, T.J.V. Findlay, SI Chemical Data, Wiley, New York, 1973.

[78] P. Spedding, R. Mills, Trace-ion diffusion in molten alkali carbonates, J. Electrochem. Soc. 112 (6) (1965) 594–599.

[79] J. Tissen, G. Janssen, P.v.d. Eerden, Molecular dynamics simulation of binary mixtures of molten alkali carbonates, Mol. Phys. 82 (1) (1994) 101–111.

[80] M.J. Glenn, J.A. Allen, S.W. Donne, Thermal Investigation of a Doped Alkali Metal Carbonate Ternary Eutectic for Direct Carbon Fuel Cell Applications, Energy & Fuels, 2015.

[81] G.J. Janz, M.R. Lorenz, Solid-liquid phase equilibria for mixtures of lithium, sodium, and potassium carbonates, J. Chem. Eng. Data 6 (3) (1961) 321–323.

[82] S. Tamaru, M. Kamada, Brennstoffketten, deren Arbeitstemperatur unterhalb 600° C liegt, Zeitschrift für Elektrochemie und angewandte physikalische Chemie 41 (2) (1935) 93–96.

[83] L. Volkova, Phase diagram of K2CO3-Na2CO3-Li2CO3, Izvest. Sibirsk. Oldel. Akad. Nauk. SSSR 7 (1958) 33–35.

[84] N. Agmon, The grotthuss mechanism, Chem. Phys. Lett. 244 (5) (1995) 456–462.

[85] T.M. Gür, Mechanistic modes for solid carbon conversion in high temperature fuel cells, J. Electrochem. Soc. 157 (5) (2010) B751–B759.

[86] P. Atkins, J. De Paula, Atkins' Physical Chemistry, Oxford University Press, 2014.

[87] J. Allen, M. Glenn, S. Donne, The effect of coal type and pyrolysis temperature on the electrochemical activity of coal at a solid carbon anode in molten carbonate media, J. Power Sources 279 (2015) 384–393.

[88] J.A. Allen, et al., An investigation of mineral distribution in coking and thermal coal chars as fuels for the direct carbon fuel cell, Fuel 217 (2018) 11–20.

[89] G. Bruno, et al., Water-insoluble compounds formed by reaction between potassium and mineral matter in catalytic coal gasification, Fuel 67 (1) (1988) 67–72.

[90] K. Formella, et al., Interaction of mineral matter in coal with potassium during gasification, Fuel 65 (10) (1986) 1470–1472.

[91] L. Kühn, H. Plogmann, Reaction of catalysts with mineral matter during coal gasification, Fuel 62 (2) (1983) 205–208.

[92] J. Tulloch, et al., Influence of selected coal contaminants on graphitic carbon electro-oxidation for application to the direct carbon fuel cell, J. Power Sources 260 (2014) 140–149.

[93] J. Liu, et al., A novel electrolyte composed of carbonate and CsVO 3–MoO 3 for electrochemical oxidation of graphite, Electrochem. Commun. 38 (2014) 12–14.

[94] D. Ippolito, L. Deleebeeck, K.K. Hansen, Effect of CeO2 addition on hybrid direct carbon fuel cell performance, J. Electrochem. Soc. 164 (4) (2017) F328–F332.

[95] D. Fini, et al., Evaluation of Sc2O3–CeO2–ZrO2 electrolyte-based tubular fuel cells using activated charcoal and hydrogen fuels, Electrochim. Acta 259 (2018) 143–150.

[96] S. Scaccia, Investigation on NiO solubility in binary and ternary molten alkali metal carbonates containing additives, J. Mol. Liq. 116 (2) (2005) 67–71.

[97] C.E. Baumgartner, NiO solubility in molten Li/K carbonate under molten carbonate fuel cell cathode environments, J. Electrochem. Soc. 131 (8) (1984). United States.

[98] S. White, U. Twardoch, The solubility and electrochemistry of alkali metal oxides in the molten eutectic mixture of lithium carbonate-sodium carbonate-potassium carbonate, J. Appl. Electrochem. 19 (6) (1989) 901–910.

[99] H. Hayashi, et al., Thermal expansion coefficient of yttria stabilized zirconia for various yttria contents, Solid State Ion. 176 (5) (2005) 613–619.

[100] J. Ilavsky, J.K. Stalick, Phase composition and its changes during annealing of plasma-sprayed YSZ, Surf. Coat. Technol. 127 (2) (2000) 120–129.

[101] P.K. Schelling, S.R. Phillpot, D. Wolf, Mechanism of the cubic-to-tetragonal phase transition in zirconia and yttria-stabilized zirconia by molecular-dynamics simulation, J. Am. Ceram. Soc. 84 (7) (2001) 1609–1619.

[102] K.-t. Lee, Development of Perovskite and Intergrowth Oxide Cathodes for Intermediate Temperature Solid Oxide Fuel Cells, 2006.

[103] K. Schlichting, N. Padture, P. Klemens, Thermal conductivity of dense and porous yttria-stabilized zirconia, J. Mater. Sci. 36 (12) (2001) 3003–3010.

[104] K. Tabata, et al., Zirconia Refractory Heating Element, 1991 (Google Patents).

[105] M. Glenn, et al., Gas atmosphere effects over the anode compartment of a tubular direct carbon fuel cell module, Energy Fuels 33 (8) (2019) 7901–7907.

[106] H.V. Ijije, R.C. Lawrence, G.Z. Chen, Carbon electrodeposition in molten salts: electrode reactions and applications, RSC Adv. 4 (67) (2014) 35808–35817.

[107] M. Ingram, B. Baron, G. Janz, The electrolytic deposition of carbon from fused carbonates, Electrochim. Acta 11 (11) (1966) 1629–1639.

# Silicate Formation in a Ternary Alkali Metal Carbonate Melt

Michael Glenn,[†] Jessica A. Allen,[‡] and Scott W. Donne*,[†]

[†]Discipline of Chemistry and [‡]Discipline of Chemical Engineering, University of Newcastle, Callaghan, NSW 2308, Australia

ABSTRACT: Studies have shown that doping carbonates with silica destabilizes the liquid phase by reducing the temperature window over which the mixture resides in a molten state. This work demonstrates that liquid-phase disruption is caused by silicate formation in the melt due to reactions between carbonate and silica. These results were verified using differential thermal analysis (DTA), X-ray diffraction, and thermogravimetric analysis, all of which pointed to the same conclusion. The exact amount of silica produced was measured using DTA, which precisely matched the theoretical yield. These results are particularly relevant to the direct carbon fuel cell (DCFC) when carbonate is used as an electrolyte and coal char is used as a fuel, given that silica is an abundant mineral in high-rank coals. In this situation, liquid-phase disruption would destabilize the carbonate electrolyte, thus having a deleterious impact on the DCFC.

1. INTRODUCTION

1.1. Direct Carbon Fuel Cell (DCFC). The DCFC uses a carbonaceous fuel, which is oxidized directly to CO_2 when coupled with an oxygen cathode.[1] The overall reaction of the DCFC is identical to that used in a coal fired power station, i.e.,

$$C(s) + O_2(g) \rightarrow CO_2(g) \ (\Delta H = -394 \text{ kJmol}^{-1} \text{at} 25 \text{ °C}) \tag{1}$$
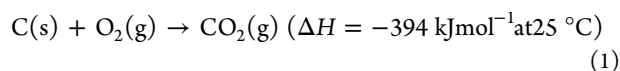
In the DCFC, the chemical process described by eq 1 can be separated into corresponding half reactions, i.e.,

$$C + 2CO_3^{2-} \rightarrow 3CO_2 + 4e^- \text{ (anode reaction)} \tag{2}$$

$$2CO_2 + O_2 + 4e^- \rightarrow 2CO_3^{2-} \text{ (cathode reaction)} \tag{3}$$
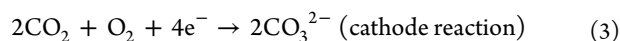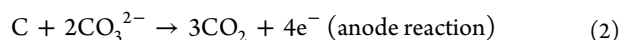
where the carbonate ion (CO_3^{2-}) is essentially an oxide ion carrier. The advantage of the DCFC over coal-fired power stations is that there is only one energy transformation step involved, i.e., chemical to electrical, which means that the efficiency of the process is very high. Thermodynamically, this process is ∼100% efficient; however, practically it is ∼80% efficient due to losses caused by the electrochemical over-potential and resistive heating in the electrical components,[2] which both cause a voltage drop and heat production during operation. Despite these inefficiencies, the DCFC can still operate at twice the efficiency of a coal-fired power station.[3] In addition, the heat produced can be used to maintain the operating temperature of the fuel cell (500−800 °C)[4] and make the system autogenous without the need for an external heat source after the initial preheating.[5]

1.2. Direct Carbon Fuel Cell Electrolyte. DCFCs can use molten salt electrolytes,[6] which allows for a three-dimensional current collector to be used rather than being confined to a two-dimensional surface with a lower area available for carbon electro-oxidation, e.g., a solid oxide electrolyte such as yttria-stabilized zirconia.[7] This can be either a molten alkali metal carbonate mixture[8] or an alkali metal hydroxide mixture.[9] It should be noted that molten carbonate mixtures are used most often,[7,8] in particular the

ternary eutectic composed of Li_2CO_3, Na_2CO_3, and K_2CO_3 in the ratio 43.5−31.5−25.0 mol %, respectively,[10] which melts at 387 °C.[11] Other common electrolytes are Li_2CO_3−K_2CO_3 (38:62 mol %[8]) and Li_2CO_3−Na_2CO_3 (60:40 mol %[12]). It is through this molten carbonate electrolyte that oxide ions are transported from the cathode to the anode. There is also the possibility that the carbonate will decompose, thus forming oxide anions at or near the surface of the carbon electrode,[13] i.e.,

$$M_2CO_3 \leftrightarrow M_2O + CO_2 \tag{4}$$

Under a positive CO_2 pressure, the reverse reaction, i.e., carbonate formation, has been demonstrated to occur by several authors.[14−16] Hence, many DCFC configurations apply a positive CO_2 pressure within the anode compartment.[17]

1.3. Alkali Metal Carbonate Mixtures and Applications. Alkali metal carbonates find application mainly in three domains, namely, (i) fuel cells (FC) such as the DCFC[18,19] and molten carbonate fuel cell,[20] (ii) concentrated solar power (CSP) fluids,[21−23] and (iii) catalysts for carbon gasification from both steam and CO_2.[14,24,25][14,24,25] When coal is used as a DCFC fuel, mineral matter can transfer to the carbonate melt, which alters the thermal properties of the system.[11,21,26]

The ternary eutectic is often used in both FC and CSP fluid applications due to the benefit of having a lower melting point and therefore requiring a lower energy input to achieve a molten state. Olivares et al.[21] demonstrated that a ternary carbonate mixture containing Li_2CO_3, Na_2CO_3, and K_2CO_3 in the proportions 32.1−33.4−34.5 wt %, respectively, produced a single differential scanning calorimetry peak at the melting temperature. Interestingly, the addition of 10 wt % NaOH lowered the melting point of the mix by 75 °C.[21] Furthermore, the melt was more susceptible to thermal decomposition under non-CO_2 atmospheres.[21] Sang et al.[26] added 9 wt % $CaCO_3$ to the ternary eutectic, which showed no evidence of lowering the melting point, and hence liquid phase disruption was not

evident. However, repeated thermal cycling, which has been demonstrated to facilitate sample homogenization was not employed.

For CSP and DCFC applications, it is preferable to conduct material characterization on molten carbonates rather than solid crystals; however, the literature on the examination of molten mixtures remains scarce.[27] This is due to the highly corrosive nature of the melts,[28] and their tendency to thermally decompose (eq 4) evolving CO_2,[21,27,29][21,27,29] and even vaporize at temperatures >700 °C.[21] Another issue is that Li^+ ions intercalate into the structure of the several materials, e.g., platinum.[30,31] Therefore, characterization should be conducted under a positive CO_2 pressure and corrosion-resistant materials, e.g., nickel alloys, used.[28] Bates et al.[32] examined molten carbonate samples at 500 °C using Fourier transform infrared and Raman spectroscopy using a quartz tube to contain the samples. However, it was reported in subsequent studies that quartz is readily soluble in alkali metal carbon melts;[11,33] hence, the samples examined by Bates et al.[32] were likely contaminated by dissolved quartz. Coyle et al.[28] demonstrated that many commercially available alloys containing chromium and titanium dissolve in the molten $Na_2CO_3-K_2CO_3$ (60:40 mol %) binary eutectic and the ternary carbonate eutectic when held at 900 °C. Carbonate-induced corrosion was confirmed by analyzing the corrosion products using backscattered scanning electron microscopy (SEM) and energy-dispersive X-ray spectrometry.[28]

1.4. Alkali Metal Carbonates for Direct Carbon Fuel Cell Applications. Thermal coal is made up of three broad components, i.e., ~40−65 wt % amorphous carbon, 10−30 wt % mineral matter,[34] and ~25−30 wt % volatiles (CO_2, NO_x, SO_x).[35−38] In the context of the DCFC where coal is used as the fuel, there is contact between the coal and the molten carbonate media, particularly in a slurry arrangement where particulates are intimately mixed with the eutectic.[39] Wang et al.[40] suggested that this close contact causes interactions between the coal mineral matter and the carbonate media, and the literature would indicate that the inclusion of anthracitic coal minerals can have a catalytic effect upon electro-oxidative kinetics of the DCFC anode reaction.[41] Minerals examined include a selection of metal oxides,[42] semimetal oxides,[41] and clays,[43] which have been applied in a slurry-type DCFC arrangement, where the carbon fuel is in close contact with the molten carbonate. Given that oxide ions act as an intermediate in the carbon oxidation pathway,[13] the enhanced carbon electro-oxidation in the presence of these impurities suggests that that dissolved oxide ions may be drawn to the carbon surface from within the molten carbonate. Additionally, the increased activity of oxide ions due to the dissolution of oxide-containing impurities has also been reported to improve the electro-oxidation kinetics.[42] This is beneficial to the DCFC operation because it enhances the electro-oxidation reaction rate and therefore the specific power of the system.[42]

Another study examined the effects of seven different species (TiO_2, SiO_2, $CaCO_3$, $CaSO_4$, Fe_2O_3, FeS, and $Kaolin$) common to the mineral matter of Australian bituminous coals[11] when added to the ternary carbonate eutectic at the 5 wt % level. The thermal effect of these additions were examined using differential thermal analysis (DTA), where it was demonstrated that the dissolution of the contaminants led to liquid-phase disruption, the extent of which varied with contaminant. Modeling of the melting process was carried out using different heating rates, which allowed the determination of the activation energy for melting in the presence of various contaminants. It was demonstrated that the contaminants can dramatically affect the activation energy and the kinetics of the melting process.[11]

It is important to understand the interaction between molten carbonate and silica because silica has been identified as the most abundant mineral found in Australian bituminous coals by low-temperature ashing studies.[43,44] Therefore, this study examines the thermal and crystallographic changes that occur when the ternary eutectic is doped with silica. It is hypothesized that there will be a chemical interaction between the carbonate and the silica, leading to destablization of the liquid phase.

2. EXPERIMENTAL METHODS

2.1. Carbonate Preparation. Carbonate mixtures were prepared from reagent-grade purity compounds (>99% purity). Lithium carbonate (Li_2CO_3), sodium carbonate (Na_2CO_3), and potassium carbonate (K_2CO_3) were sourced from Sigma Aldrich. Before use, all materials were dried in an alumina crucible at 150 °C for at least 2 h before being cooled in a dessicator and stored in an air-tight container.

A 200 g batch of the ternary eutectic (43.5 mol % Li_2CO_3, 31.5 mol % Na_2CO_3, and 25.0 mol % K_2CO_3) was prepared by initially mixing with a mortar and pestle. To ensure thorough mixing, the sample was ball-milled (Fritsch, Pulverisette) using four intervals of 10 min in both clockwise and counter-clockwise directions at 200 rpm, with a 2 min rest period between milling periods. Following this, the mixture was heated up to 600 °C in air to melt and hence homogenize the mixture. The melt was kept at 600 °C for 4 h and then cooled down to ambient temperature; after which it was removed from the crucible, broken up, and ground to a fine powder using a mortar and pestle.

2.2. Silica Contamination. Mixtures were prepared and doped with quartz (≥99.9%; Sigma-Aldrich) at 1, 2, or 5 wt % concentration levels. The pretreatment prior to analysis involved using a mortar and pestle to grind the silica into a fine free-flowing powder and then passing the sample through a 300 μm sieve, prior to being thoroughly mixed with the ternary eutectic using a mortar and pestle.

2.3. Differential Thermal Analysis and Thermogravimetric Analysis (TGA). A Perkin Elmer Diamond thermogravimetric and differential thermal (TGA/DTA) analyzer was used to carry out all thermal analysis experiments. Here, both the DTA and TGA data were collected simultaneously as the experiment was conducted. A sample mass between 4 and 8 mg was used for all TGA/DTA analysis experiments. Aluminum crucibles were used to allow for heating up to 600 °C and good thermal contact between the pans and the platinum plate underneath. Multiple heating and cooling cycles were employed at ±150 °C, around the melting point of the carbonate sample. A similar mass of α-Al_2O_3 was used as the reference material for DTA measurements. To initially equilibrate the sample, the instrument was held for 1 min at 25 °C under flowing N_2 (20 mL min^{-1}) inside the TGA/DTA instrument. A heating rate of 5 °C min^{-1} was applied from 25 to 600 °C and then held isothermally for 10 min. Six subsequent heating and cooling cycles were carried out in the temperature range 350−600 °C at 5 °C min^{-1}, with 10 min equilibration periods allowed in between heating and cooling profiles. Thermal cycling was carried out to homogenize the sample, thus ensuring reproducible results.

2.4. Structural Characterization. The structure of each mixture after thermal fusion was examined by means of powder X-ray diffraction (XRD). A Philips X'Pert MPD system equipped with a Cu anode to generate Cu Kα radiation (1.5418 Å) was used. Each diffraction pattern was recorded in the 2θ range of 10−90°, with an equivalent 2θ step size of 0.008° and a count time of 45 s.

3. RESULTS AND DISCUSSION

3.1. Differential Thermal Analysis of the Unmodified Eutectic.
The unmodified eutectic was examined by DTA as a control before comparing the response to the silica-doped systems, as shown in Figure 1. The figure shows that heating
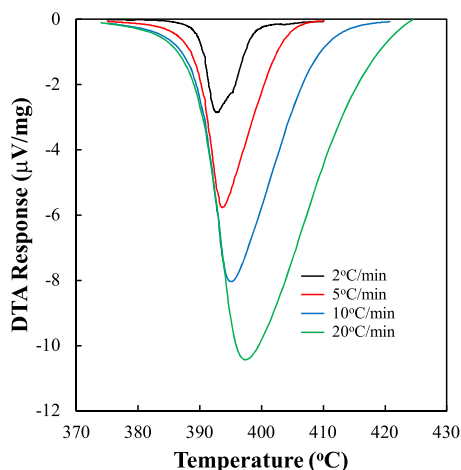
Figure 1. Normalized and baseline-corrected DTA result for the melting of the unmodified eutectic. Heating rates examined here are 2, 5, 10, and 20 °C min^{-1}, with a N$_2$ purge at 20 mL min^{-1}.

the unmodified eutectic gave rise to a single DTA peak startting at 387 °C, indicating that the eutectic has melted.[45] There is also a positive correlation between scan rate and peak position, such that faster scan rates appear to induce melting at a slightly higher temperature. The combination of poor heat transfer and slow melting kinetics both contribute to this effect. However, the melting point is an intrinsic system property that is entirely separate from heating rate. In addition, the area bound by the curve increases with scan rate, which is also due to the way in which the data have been plotted, i.e., normalized response (μV mg^{-1}) versus temperature (°C). The enthalpy associated with melting is irrespective of the scan rate, which can be seen when the response from the same mixture is plotted as normalized response (μV mg^{-1}) versus time (min).[11]

3.2. Raw Differential Thermal Analysis.
When 5 wt % silica was added to the unmodified eutectic, the melting point was elevated from 387 to 401 °C[11] and the formation of two distinct peaks separated by ~40 °C was observed (Figure 2). This figure shows that the DTA response shifts drastically from cycle 1 to cycle 2. There are is a split peak featured in cycle 1, which is due to both melting and dissolution processes, i.e., the lower temperature shoulder is due to melting of the carbonate phase and the higher temperature shoulder is due to the dissolution of silica. From cycle 2 onward, two distinct peaks emerge, which are separated by ~40 °C. The lower-temperature peak occurs at 401 °C, which represents the melting of the carbonate phase, followed by a dissolution process at higher temperatures.

3.3. Chemical Potentials.
It was demonstrated in a previous study that the dissolution of each contaminant led to liquid-phase disruption, the extent of which varied with dopant type.[11] Phase disruption was demonstrated by a melting point depression phenomenon, which is a colligative property of solutions.[46] Dopants that exhibited a particularly high degree of phase disputation were kaolin and silica, in contrast to
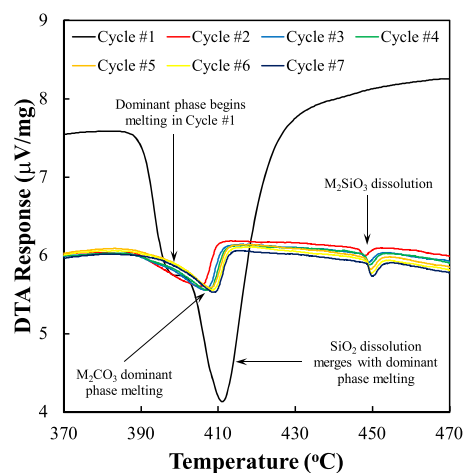
Figure 2. Raw DTA response for the eutectic doped with 5 wt % silica. The peaks are labeled, thus indicating the processes that they each represent. The solid series represents cycle 1 and the hashed series represent cycles 2−7.

species such as calcium sulfate and titanium dioxide, which had minimal impact.

In the prototypical case, contaminant addition caused the chemical potential (μ) of the liquid to be lower relative to that of the solid.[11] Silica was the only additive that raised the melting point of the mixture, thus stabilizing the chemical potential of the solid phase relative to the melt. A study by Kim et al.[47] demonstrated that mixing Na$_2$CO$_3$ with silica in the ratio 2:1 caused thermal decomposition under air at ~800 °C, in contrast with unmodified Na$_2$CO$_3$, which decomposed at a much higher temperature (~1100 °C), thus showing destablization of the liquid phase in the presence of silica. Figure 3 shows a combined chemical potential diagram for
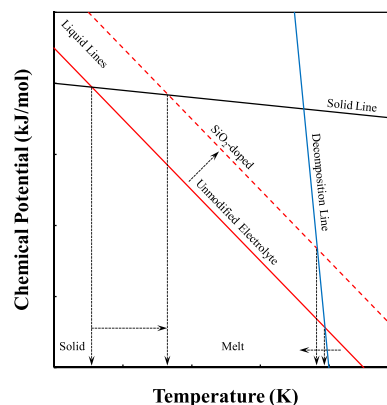
Figure 3. Chemical potential diagram for alkali metal carbonates doped with silica.

alkali metal carbonates doped with silica. This figure shows that the melting temperature of the carbonate increases when contaminated with silica[11] and the decomposition temperature decreases;[47] therefore, the temperature window over which alkali metal carbonates reside in a molten state is diminished when silica is added, i.e., the chemical potential of the liquid phase is destabilized.

3.4. Silica Dissolution: A Kinetically Slow Process.
There are several possible explanations for the liquid-phase disruption, such as slow dissolution of silica, a polymorphic

Table 1. Phase Transitions that Silica Undergoes When Heated under Atmospheric Pressure Including the Unit Cell Configuration and Density of Each Solid Phase[48]

temperature (°C)	573	870	1470	1705	1713
polymorph	α-quartz	β-quartz	β-tridymite	β-cristobalite	molten silica
unit cell	trigonal	hexagonal	hexagonal	cubic	NA
density (g cm^{-3})	2.65	2.53	2.25	2.2	NA
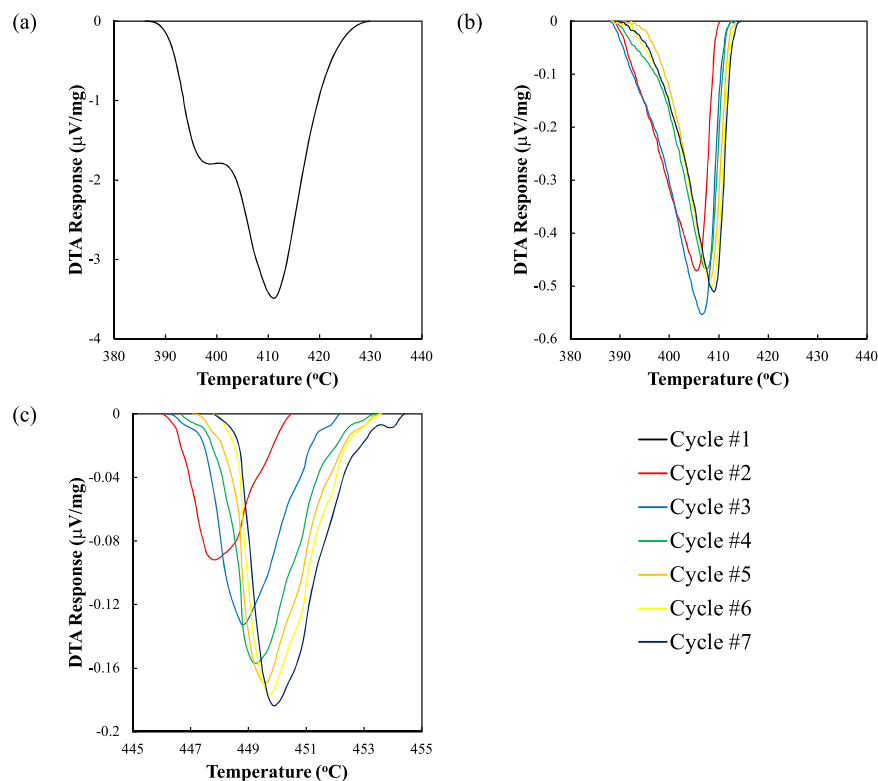
Figure 4. Background-corrected and normalized DTA response (μV mg^{-1}) for the ternary Li, Na, and K carbonate eutectics deliberately contaminated with 5 wt % SiO$_2$. (a) First melt with a heating rate of 20 °C min^{-1}; (b) peak 1 for heating cycles 2−7, for which the heating rate was 5 °C min^{-1}; and (c) peak 2 for heating cycles 2−7, for which the heating rate was also 5 °C min^{-1}.

inversion, or silicate formation in the melt. Several studies have reported extremely slow dissolution of silica, which can take hours or even days if left unagitated at a temperature slightly above the melting point.[29] Kracek et al.[29] reported that a ternary carbonate mixture containing Na$_2$CO$_3$ and K$_2$CO$_3$ with 60−75 wt % SiO$_2$ (quartz) held at 700 °C required over 48 h to fully dissolve the sample. When the same mixture was held at 540 °C, this time period was extended to 10 days, during which the quartz did not even completely dissolve.[29] Therefore, to facilitate dissolution, the samples were briefly held at 1200 °C.[29]

In our case, therefore, the silica would not have completely dissolved during the first cycle (Figure 2). The drastic change after the first cycle indicates that most of the silica has dissolved, and therefore, thermal cycling facilitates silica dissolution.

3.5. Detailed Examination of Silica Dissolution. The second higher-temperature DTA peak shown in Figure 2, which is present from cycle 2 onward, occurs at ~442 °C, which is 40 °C higher than the melting point. This may have been due to a polymorphic inversion within the silica, given that quartz can transition between polymorphs in response to varied temperature and pressure conditions. Table 1 shows the phase transitions that silica undergoes when heated under

atmospheric pressure, including the unit cell configuration and density of each solid phase.

A mixture containing Li$_2$CO$_3$ and Na$_2$CO$_3$ has been reported to catalyze the phase transition from quartz to tridymite, thus lowering the inversion temperature to 870 ± 10 °C[49] instead of 1470 °C.[48] However, this is still well above the highest heating temperature examined in this study (600 °C); hence, this possibility is unlikely.

Another possible explanation for this secondary peak is that the alkali metal carbonates are reacting with silica to produce alkali metal silicates and CO$_2$, i.e.,

$$Li_2CO_3 + SiO_2 \rightarrow Li_2SiO_3 + CO_2 \ (\Delta G = -88.5 \ kJ \ mol^{-1}) \tag{5}$$

$$Na_2CO_3 + SiO_2 \rightarrow Na_2SiO_3 + CO_2 \ (\Delta G = -4.56 \ kJ \ mol^{-1}) \tag{6}$$

$$K_2CO_3 + SiO_2 \rightarrow K_2SiO_3 + CO_2 \ (\Delta G = -39.4 \ kJ \ mol^{-1}) \tag{7}$$

$$M_2CO_3 + SiO_2 \rightarrow M_2SiO_3 + CO_2 \ (\Delta G < 0$$

$$kJ \ mol^{-1} at \ 500 \ ^\circ C) \tag{8}$$
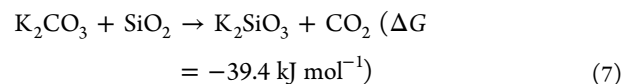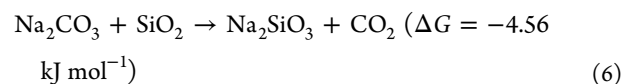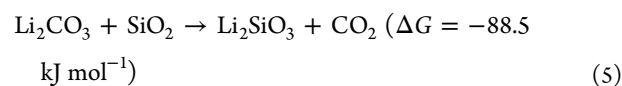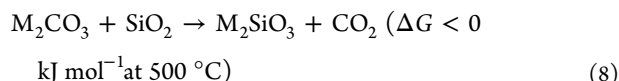
where M in the generic reaction in eq 8 denotes an alkali metal species, Li, Na, or K. McKee et al.[25] found that alkali metal silicates were produced from reactions between silica containing coal minerals and alkali metal carbonates (5 wt %) at 1000 °C. Kracek et al.[50] examined separate mixtures of $Na_2CO_3–K_2CO_3–SiO_2$ and $Li_2CO_3–Na_2CO_3–SiO_2$. Complex phase equilibria were discovered for various composition and temperature conditions, including the formation of the intermediate compound $NaLiSiO_3$.[50] Devyatkin et al.[51] suggested that silicates could emerge from mixtures between alkali metal carbonates and silica. These silicates were predicted to form spontaneously based on thermodynamic considerations, i.e., ΔG in eqs 5−7.[51] However, consideration was not extended to the kinetic time frame over which these species would form under specified temperature conditions, nor the possibility of intermediate compound formation as addressed above, e.g., $NaLiSiO_3$.[50]

Under a flowing non-CO_2 atmosphere, silicate formation is irreversible because there is no CO_2 to carry out the reverse reaction. Therefore, the second peak is due to silicate dissolution into the molten carbonate rather than silicate formation. Figure 4 shows DTA plots for the eutectic doped with 5 wt % silica that have been baseline-corrected and normalized. From this figure, it can be seen that the DTA melt response for the first melt scan is fundamentally different in shape and is much more intense by comparison to the subsequent cycles. The data for the first heating cycle consist of two overlapping peaks separated by ∼5 °C, with the twin peaks initiated at ∼397 and 407 °C (Figure 4A). Therefore, the four parent materials, i.e., Li_2CO_3, Na_2CO_3, K_2CO_3, and SiO_2, did not form a homogeneous phase at this point. This also shows that silica dissolution does not occur immediately. The second shoulder of the split peak at 407 °C is likely caused by silica dissolution; however, some silica remains undissolved. From the second heating cycle onward, there are two well-defined peaks separated by ∼40 °C, the first peak is due to carbonate phase melting (Figure 4B) and the second due to silicate dissolution (Figure 4C). The fused materials were not examined by SEM to confirm the formation of alkali metal silicates; however, the literature clearly demonstrates that these are the only products that can be formed.[52−54]

Figure 5 shows XRD patterns for pure silica, the unmodified eutectic, and eutectic samples purposefully contaminated with silica. The formation of alkali metal silicate species is indicated by the vertical lines marked on the XRD patterns in Figure 5. Specifically, peaks at 26°2θ and 32.5°2θ evidence the presence of lithium silicate.[55] The low-intensity peak at 22.5°2θ indicates that sodium silicate is present.[56] Also, the peak at 31.5°2θ, marked by the rectangle in Figure 5, corresponds to an intense peak in the potassium silicate pattern.[57] The peak at 31.5°2θ is also present in the pattern of the unmodified eutectic; however, its intensity is lower. Therefore, this peak position corresponds to overlapping peaks from the unmodified eutectic and quartz. Despite this, there is a clear correlation between potassium silicate loading and peak intensity.

Kim et al.[47] presented a disordered XRD pattern of a thermally fused binary mixture containing Na_2CO_3 and SiO_2 in the ratio 2:1, showing that crystal-phase disruption had
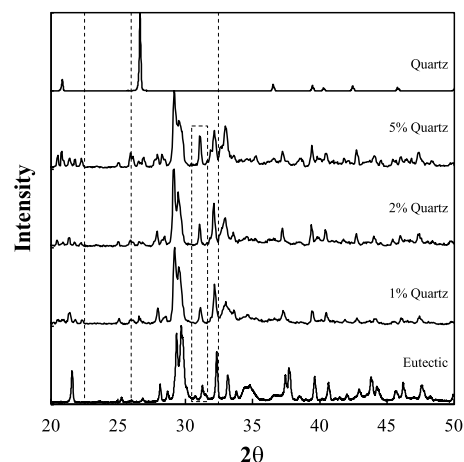
Figure 5. XRD patterns of pure quartz (top), eutectic with 5 wt % quartz, eutectic with 2 wt % quartz, eutectic with 1 wt % quartz, and the unmodified eutectic (bottom).

occurred. However, it is noticeable that for a quaternary mixture fused from Li_2CO_3, Na_2CO_3, K_2CO_3, and SiO_2 (Figure 5), the degree of disruption is comparatively more intense due to the greater number of silicate compounds that can form.

3.6. Thermal Analysis and Peak Areas. The formation of silicate compounds was also demonstrated by calculating the area bounded by the baseline-corrected DTA data (Figure 6), which was used as a semiquantitative measure of the process enthalpy, e.g., melting and/or dissolution. This method is valid for comparing peaks occurring over a similar temperature windows that were conducted at an identical scan rate. Ye et al.[58] used this method to examine the melt characteristics of a $NaCO_3–NaCl$ eutectic, and it has also been applied in other literature studies.[11]

Figure 6 shows a systematic increase in the area of peak 2 with cycle number; however, this not the case for peak 1. This indicates that more silicate is progressively dissolved with thermal cycling. With 5 wt % silica added to the mixture (corresponding to 8.06 mol %), and after silicate formation has proceeded to completion, silicate species should account for ∼8.06 mol % of the sample product. However, this silicate percentage in the sample product is expected to be slightly greater due to CO_2 evolution (eq 8), which is also a form of carbonate decomposition.

Figure 7 shows the mass loss with thermal cycling using TGA. Here, the mass loss occurs between cycles 2 and 5 caused by CO_2 evolution (eq 8), which is both carbonate decomposition and silicate formation. Mass loss ceases after cycle 5, which shows that all the silicate has reacted with carbonate to form silicate monomers. At this point, silicate compounds should theoretically account for 9.71 mol % of the sample product. Figure 8 plots the peak area ratio for peak 2 (silicate dissolution) compared to peak 1 (carbonate melting) versus cycle number. The values are plotted as a percentage because the area above peak 1 was much larger than that above peak 2 (Figure 6). From Figure 8, the area ratio increases progressively from 4.2 to 9.0 mol % between cycles 2 and 4, meaning that the amount of dissolved silicate increases. This percentage value then plateaus at ∼10% between cycles 5 and 7, showing that all the silica has reacted with carbonate to form silica. This value matches the theoretical amount of silicate

(a)

(b)
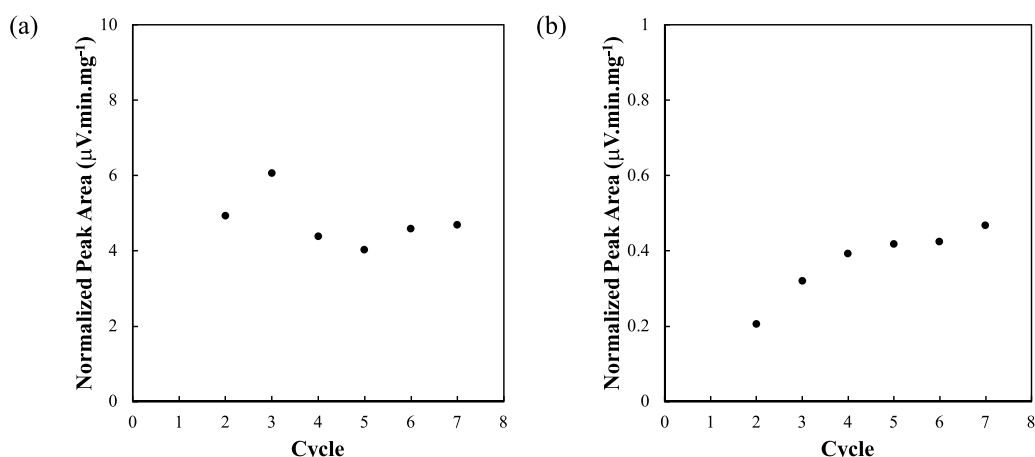
Figure 6. Integrated area under the baseline-corrected DTA response (μV min mg^{-1}) for the eutectic doped with 5 wt % silica. (a) Area values for peak 1 (carbonate melting) and (b) area values for the peak 2 (silicate dissolution).
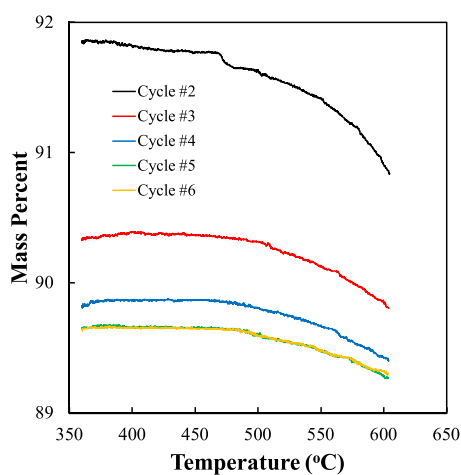
Figure 7. TGA response of the eutectic samples doped with 5 wt % silica. Melt cycles 2−6 have been plotted.
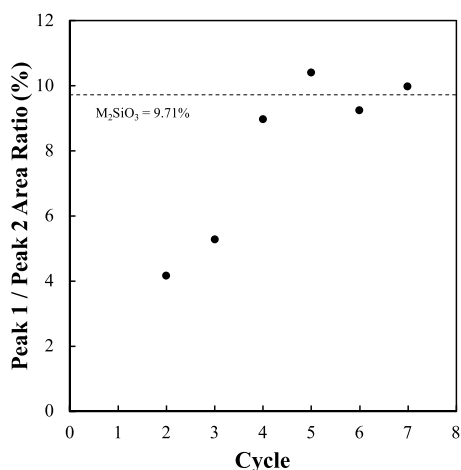
Figure 8. Plot of the peak area (peak 1/peak 2 or carbonate melting to silicate dissolution) as a function of cycle number. The horizontal line in inserted at 9.71% and represents the theoretical amount of silicate present after the silica has reacted with carbonate.

produced after all the silica has reacted to form silicate monomers (9.71 mol %).

Analyzing the flue gas by gas chromatography or Fourier transform infrared spectroscopy would be useful to confirm CO_2 production; however, there is already conclusive evidence from TGA, DTA, XRD, and the literature suggesting that the product gas is CO_2.[52−54]

4. CONCLUSIONS

The effects of doping a ternary carbonate eutectic with silica was explored by DTA, XRD, and TGA, whereby it was demonstrated that the parent reagents react to form silicate. Calculating the area bound by the DTA peaks showed the exact quantity of silica produced, which closely corresponds to the expected yield (9.71 mol %). The presence of silicate in the carbonate mixture destabilizes the liquid phase, leading to (i) melting point elevation and (ii) depression of the decomposition point of the carbonate mixture. It was also discovered that thermal cycling can be used to facilitate the dissolution of silica in molten alkali metal carbonates.

These findings impact the DCFC when molten carbonates are used as electrolytes and coal is used as a fuel because coal often contain substantial amounts of silica, which destabilizes the molten carbonate phase. This is exacerbated when coal is continuously fed into the system and the fixed carbon is consumed either by electro-oxidation or gasification, thus leaving behind large amounts of mineral matter.

■ AUTHOR INFORMATION

Corresponding Author
*E-mail: scott.donne@newcastle.edu.au. Phone: +61 2 4921 5477. Fax: +61 2 4921 5472.

ORCID [ⓘ]
Jessica A. Allen: 0000-0003-1916-4964
Scott W. Donne: 0000-0001-9389-7870

Notes
The authors declare no competing financial interest.

■ REFERENCES

(1) Li, C.; Shi, Y.; Cai, N. Effect of contact type between anode and carbonaceous fuels on direct carbon fuel cell reaction characteristics. *J. Power Sources* **2011**, *196*, 4588−4593.

(2) Cooper, J. F. Direct Conversion of Coal Derived Carbon in Fuel Cells. In *Recent Trends in Fuel Cell Science and Technology*; Basu, S., Ed.; Anamaya Publishers: New Delhi, India, 2007.

(3) Bugge, J.; Kjær, S.; Blum, R. High-efficiency coal-fired power plants development and perspectives. *Energy* **2006**, *31*, 1437−1445.

(4) Basu, S. Future Directions of Fuel Cell Science and Technology. In *Recent Trends in Fuel Cell Science and Technology*; Springer, 2007; pp 356−365.

(5) Gür, T. M. Perspective—Low-Carbon Electricity Is Great: What about "Less-Carbon". *J. Electrochem. Soc.* **2017**, *164*, F1587−F1590.

(6) Lan, R.; Tao, S. A simple high-performance matrix-free biomass molten carbonate fuel cell without CO_2 recirculation. *Sci. Adv.* **2016**, *2*, No. e1600772.

(7) Rady, A. C.; et al. Review of Fuels for Direct Carbon Fuel Cells. *Energy Fuels* **2012**, *26*, 1471−1488.

(8) Allen, J.; et al. Molten Carbonate Composition Effects on Carbon Electro-Oxidation at a Solid Anode Interface. *J. Electrochem. Soc.* **2015**, *162*, F76−F83.

(9) Zecevic, S.; Patton, E. M.; Parhami, P. Direct electrochemical power generation from carbon in fuel cells with molten hydroxide electrolyte. *Chem. Eng. Commun.* **2005**, *192*, 1655−1670.

(10) Janz, G. J.; Lorenz, M. R. Solid-Liquid Phase Equilibria for Mixtures of Lithium, Sodium, and Potassium Carbonates. *J. Chem. Eng. Data* **1961**, *6*, 321−323.

(11) Glenn, M. J.; Allen, J. A.; Donne, S. W. Thermal Investigation of a Doped Alkali Metal Carbonate Ternary Eutectic for Direct Carbon Fuel Cell Applications. *Energy Fuels* **2015**, No. 1027.

(12) Morita, H.; et al. Performance analysis of molten carbonate fuel cell using a Li/Na electrolyte. *J. Power Sources* **2002**, *112*, 509−518.

(13) Cherepy, N. J.; et al. Direct conversion of carbon fuels in a molten carbonate fuel cell. *J. Electrochem. Soc.* **2005**, *152*, A80−A87.

(14) McKee, D. W. Mechanisms of the alkali metal catalysed gasification of carbon. *Fuel* **1983**, *62*, 170−175.

(15) Lorenz, P.; Janz, G. Electrochemical Reduction of Oxygen in Carbonate and Carbonate-Halide Melts. *J. Electrochem. Soc.* **1971**, *118*, 1550−1553.

(16) Jalan, B.; Rao, Y. A study of the rates of catalyzed boudouard reaction. *Carbon* **1978**, *16*, 175−184.

(17) Jain, S. L.; et al. Solid state electrochemistry of direct carbon/air fuel cells. *Fuel Cells Bull.* **2008**, *2008*, 10−13.

(18) Jiang, C.; et al. Demonstration of high power, direct conversion of waste-derived carbon in a hybrid direct carbon fuel cell. *Energy Environ. Sci.* **2012**, *5*, 6973−6980.

(19) Rady, A. C.; et al. Direct carbon fuel cell operation on brown coal. *Appl. Energy* **2014**, *120*, 56−64.

(20) Dicks, A. L. Molten carbonate fuel cells. *Curr. Opin. Solid State Mater. Sci.* **2004**, *8*, 379−383.

(21) Olivares, R. I.; Chen, C.; Wright, S. The thermal stability of molten lithium−sodium−potassium carbonate and the influence of additives on the melting point. *J. Solar Energy Eng.* **2012**, *134*, No. 041002.

(22) Wu, Y.-t.; et al. Experimental study on optimized composition of mixed carbonate salt for sensible heat storage in solar thermal power plant. *Solar Energy* **2011**, *85*, 1957−1966.

(23) Ren, N.; et al. Experimental study on optimized composition of mixed carbonate for phase change thermal storage in solar thermal power plant. *J. Therm. Anal. Calorim.* **2011**, *104*, 1201−1208.

(24) Wen, W.-Y. Mechanisms of alkali metal catalysis in the gasification of coal, char, or graphite. *Catal. Rev.* **1980**, *22*, 1−28.

(25) McKee, D. W.; et al. Catalysis of coal char gasification by alkali metal salts. *Fuel* **1983**, *62*, 217−220.

(26) Sang, L.; et al. Study on Modification of Ternary Carbonates with Additives. *Energy Procedia* **2015**, *69*, 1023−1028.

(27) Braunstein, J.; Mamantov, G.; Smith, G. P. *Advances in Molten Salt Chemistry*; Springer Science & Business Media, 2013; Vol. 3.

(28) Coyle, R.; Thomas, T. M.; Lai, G. Exploratory corrosion tests on alloys in molten salts at 900 °C. *J. Mater. Energy Syst.* **1986**, *7*, 345−352.

(29) Kracek, F. The Ternary System: K2SiO3—Na2SiO3—SiO2. *J. Phys. Chem. A* **1932**, *36*, 2529−2542.

(30) Jacques, E.; et al. The effect of lithium-intercalation on the mechanical properties of carbon fibres. *Carbon* **2014**, *68*, 725−733.

(31) Tobishima, S.-i. et al. Secondary Lithium Battery. U.S. Patent US47374241988.

(32) Bates, J.; et al. Raman spectra of molten alkali metal carbonates. *J. Phys. Chem. A* **1972**, *76*, 1565−1571.

(33) Devyatkin, S. Electrochemistry of silicon in chloro-fluoride and carbonate melts. *J. Min. Metall., Sect. B* **2003**, *39*, 303−307.

(34) Vassilev, S. V.; Tascón, J. M. Methods for characterization of inorganic and mineral matter in coal: a critical overview. *Energy Fuels* **2003**, *17*, 271−281.

(35) Van Krevelen, D. Graphical-statistical method for the study of structure and reaction processes of coal. *Fuel* **1950**, *29*, 269−284.

(36) Kabe, T. et al. *Coal and Coal-Related Compounds: Structures, Reactivity and Catalytic Reactions*; Elsevier, 2004; Vol. 150.

(37) Gorbaty, M. L.; Larsen, J. W.; Wender, I. *Coal Science*; Academic Press, 2013.

(38) Smith, K. L. et al. *The Structure and Reaction Processes of Coal*; Springer Science & Business Media, 2013.

(39) Watanabe, H.; Furuyama, T.; Okazaki, K. Enhancing the efficiency of direct carbon fuel cells by bubbling Ar gas in carbon/carbonate slurry. *J. Power Sources* **2015**, *273*, 340−350.

(40) Wang, C. Q.; et al. Significant improvement of electrooxidation performance of carbon in molten carbonates by the introduction of transition metal oxides. *J. Power Sources* **2013**, *233*, 244−251.

(41) Li, X.; et al. Evaluation of raw coals as fuels for direct carbon fuel cells. *J. Power Sources* **2010**, *195*, 4051−4058.

(42) Cao, D.; Sun, Y.; Wang, G. Direct carbon fuel cell: Fundamentals and recent developments. *J. Power Sources* **2007**, *167*, 250−257.

(43) Tulloch, J.; et al. Influence of selected coal contaminants on graphitic carbon electro-oxidation for application to the direct carbon fuel cell. *J. Power Sources* **2014**, *260*, 140−149.

(44) Ward, C. R. Analysis and significance of mineral matter in coal seams. *Int. J. Coal Geol.* **2002**, *50*, 135−168.

(45) Suddhasatwa, B. *Recent Trends in Fuel Cell Science and Technology*; Springer Press: NY, 2007.

(46) Atkins, P.; De Paula, J. *Atkins' Physical Chemistry*; Oxford University Press, 2014.

(47) Kim, J.-W.; Lee, Y.-D.; Lee, H.-G. Decomposition of Na2CO3 by Interaction with SiO2 in Mold Flux of Steel Continuous Casting. *ISIJ Int.* **2001**, *41*, 116−123.

(48) Devine, R. A.; Duraud, J.-P.; Dooryhée, E. *Structure and Imperfections in Amorphous and Crystalline Silicon Dioxide*; John Wiley & Sons Inc, 2000.

(49) Fenner, C. N. The stability relations of the silica minerals. *Am. J. Sci.* **1913**, *214*, 331−384.

(50) Kracek, F. C. Phase equilibrium relations in the system, Na2SiO3-Li2SiO3-SiO2. *J. Am. Chem. Soc.* **1939**, *61*, 2863−2877.

(51) Devyatkin, S. V.; Pisanenko, A. D.; Shapoval, V. I. Chemical and electrical behavior of carbonate melts containing silicon oxide. *Russ. J. Appl. Chem.* **2002**, *75*, 562−564.

(52) Massuyeau, M.; Gardés, E.; Morizet, Y.; Gaillarda, F. A model for the activity of silica along the carbonatite−kimberlite−mellilitite−basanite melt compositional joint. *Chem. Geol.* **2015**, *418*, 206−216.

(53) Bourgue, E.; Richet, P. The effects of dissolved CO2 on the density and viscosity of silicate melts: a preliminary study. *Earth Planet. Sci. Lett.* **2001**, *193*, 57−68.

(54) Moussallam, Y.; Florian, P.; Corradini, D.; Morizet, Y.; Sator, N.; Vuilleumier, R.; Guillot, B.; Iacono-Marziano, G.; Schmidt, B.; Gaillard, F. The molecular structure of melts along the carbonatite−kimberlite−basalt compositional joint: CO2 and polymerisation. *Earth Planet. Sci. Lett.* **2016**, *434*, 129−140.

(55) Koryakina, N.; Kuznetsov, V.; Belov, N. Hydrothermal crystallization in the Li 2 O-Sc 2 O 2-SiO 2-H 2 O system. *Kristallografiya* **1972**, *17*, 228−229.

(56) Kahlenberg, V.; et al. X-ray powder diffraction data for δ-Na$_2$Si$_2$O$_5$. *Powder Diffraction* **2000**, *15*, 139−141.

(57) Bernet, K.; Hoppe, R. Zur Kristallstruktur von K4 [SiO4]. *Z. Anorg. Allg. Chem.* **1990**, *589*, 129−138.

(58) Ye, L.; et al. The thermal physical properties and stability of the eutectic composition in a Na 2 CO 3−NaCl binary system. *Thermochim. Acta* **2014**, *596*, 14−20.

Carbon Gasification from a Molten Carbonate Eutectic

Michael J. Glenn, Jessica A. Allen, and Scott W. Donne*

This investigation explores the impact of using a ternary alkali metal carbonate eutectic, i.e., Li_2CO_3, Na_2CO_3, and K_2CO_3 (43.5: 31.5: 25 mol%, respectively), as a catalyst for carbon gasification under CO_2 and non-CO_2 atmospheres. Gasification under CO_2, i.e., the reverse Boudouard reaction, is a well-understood process with considerable commercial interest. However, in the context of direct carbon fuel cell (DCFC) operations, it is a parasitic reaction because it consumes fuel without producing power. In this study, the effect on carbon gasification of a common DCFC electrolyte is examined. Thermogravimetric analysis shows gasification occurring in the absence of a CO_2 atmosphere, which has significant implications for DCFCs using alkali metal carbonates as the secondary electrolyte. A combined reaction mechanism is proposed which entails gasification from carbonate and carbonate decomposition.

1. Introduction

Molten carbonates are useful in a range of applications, including as heat storage mediums in concentrated solar power (CSP) technology[1] and as ionic conductors in high-temperature fuel cells, such as the molten carbonate fuel cell (MCFC) and direct carbon fuel cell (DCFC).[2,3] Evidence has also been shown as to the catalytic nature of single alkali metal carbonates during the gasification of carbonaceous fuels.[4–8] Some work on pyrolysis and gasification of biomass feedstocks has been carried out using molten carbonates as both a heat transfer medium and a catalytic reaction environment.[9]

In all applications, both the reaction chemistry of these carbonates and their thermal properties are of considerable importance. In the DCFC, best performance has been observed for those which use a hybrid arrangement comprising a primary electrolyte, such as a solid oxide conductor, along with a secondary molten carbonate electrolyte.[10] The carbonates enable a high level of contact between the solid oxide electrolyte used in the arrangement, e.g., yttria-stabilized zirconia (YSZ)[2] or

Dr. M. J. Glenn, Prof. S. W. Donne
Discipline of Chemistry
University of Newcastle
Callaghan, NSW 2308, Australia
E-mail: scott.donne@newcastle.edu.au

Dr. J. A. Allen
Priority Research Centre for Frontier Energy Technology and Utilization
Discipline of Chemical Engineering
Faculty of Engineering and Built Environment
University of Newcastle
Callaghan, NSW 2308, Australia

The ORCID identification number(s) for the author(s) of this article can be found under https://doi.org/10.1002/ente.201900602.

samaria-doped ceria (SDC)[11] and the carbon fuel medium. Several arrangements are possible in this regard, as shown in **Figure 1**, which also indicates potential reaction pathways in solid oxide—DCFCs (SO-DCFCs).

Figure 1 shows nickel being used as an anode current collector where it is in contact with the carbon fuel, which is quite common for DCFC arrangements.[12–14] It should be noted that nickel is a very effective catalyst for the reverse Boudouard reaction. It has been reported by Nagase et al.[15] that the reaction rate for the reverse Boudouard reaction at 800 °C in an uncatalyzed system is comparable with a nickel-catalyzed system at 400 °C, which is even below the temperature-dependant thermodynamic limit for the reaction.

Four main overall reaction pathways are possible for carbon in an SO-DCFC arrangement when using a solid oxide membrane separator, including two- and four-electron electrochemical reactions, as well as the chemical reaction of carbon with reaction products, i.e.,

$$C(s) + 2O^{2-} \rightarrow CO_2(g) + 4e^- \quad \text{Electrochemical (4e}^-) \quad (1)$$

$$C(s) + O^{2-} \rightarrow CO(g) + 2e^- \quad \text{Electrochemical (2e}^-) \quad (2)$$

$$CO(g) + O^{2-} \rightarrow CO_2(g) + 2e^- \quad \text{Electrochemical (2e}^-) \quad (3)$$

$$C(s) + CO_2(g) \leftrightarrow 2CO(g) \quad \text{Chemical} \quad (4)$$

Oxygen is the oxidant in the DCFC, with oxide anions transferred to the anode via a solid electrolyte ionic conductor. Equation (5) shows the half-cell equation for the oxygen reduction reaction, i.e.,

$$O_2(g) + 4e^- \leftrightarrow 2O^{2-} \quad \text{Electrochemical (4e}^-) \quad (5)$$
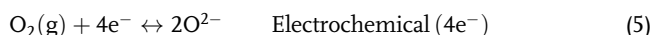
Thermodynamic calculations for the generation of one mole of product gas should consider the change in Gibbs free energy (ΔG_r; $J\,mol^{-1}$) and electrochemical potential (E; V) using temperature-dependent values of entropy and enthalpy for each reactant and product species,[16] i.e.,

$$\Delta G_r = \Delta H_r - T\Delta S_r \quad (6)$$

$$E = \frac{\Delta G_r}{nF} \quad (7)$$

where ΔH_r ($J\,mol^{-1}$) is the temperature-dependent change in enthalpy of the reaction, ΔS_r ($J\,K^{-1}.mol^{-1}$) is the entropy change, T is the temperature (K), n is the stoichiometric number of electrons involved, and F is Faraday's constant (96486.7 $C\,mol^{-1}$).

Figure 1. Reaction pathways diagram for a carbonate-containing SO-DCFC arrangement, shown with a solid YSZ solid membrane and a nickel current collector.

Results for the overall electrochemical potential of the three possible electrochemical reactions (Equation (1)–(3) combined with Equation (5) according to the number of electrons involved) and the Gibbs free energy change for the chemical reaction (Equation (4)) are shown in **Figure 2**.

The reversible potential in Figure 2a does not change significantly with temperature for the four-electron oxidation from carbon to carbon dioxide, whereas reactions involving carbon monoxide are heavily temperature dependent. Differences in experimental observations of the open-circuit potential (OCP) for DCFC systems often vary from thermodynamically predicted values. Sensitivity of the OCP to temperature is often ascribed to the influence of carbon monoxide.[17] Gasification of carbon to form carbon monoxide is also an area of great interest in both DCFC[18,19] and gasification applications.[20] Under N_2, OCP has been shown to be 0.1–0.3 V higher than under CO_2,[21–23] where the reverse Boudouard reaction (Figure 2c) can take place.[12]

Thermodynamically, the reaction in Equation (4) becomes product favored above 665 °C (Figure 2c). However, under closed circuit conditions, above 665 °C, four-electron electro-oxidation (Equation (1)) is thermodynamically favored over the reverse Boudouard reaction (Equation (4)) at DCFC operational temperatures, i.e., $\Delta G_r = -402\,\mathrm{kJ\,mol^{-1}}$ versus $-6\,\mathrm{kJ\,mol^{-1}}$ (Figures 2b,c) at 700 °C, respectively. However, the impact of the Boudouard gasification reaction depends heavily on the gasification environment, catalysts used, temperature, and carbon type including particle size.[20] Kopyscinski et al.[8] showed that in the presence of a K_2CO_3 catalyst, heating to 700 °C under N_2 before switching to CO_2 causes more facile gasification compared with a system which remains under CO_2 for the full duration of the experiment.

It can be seen in Figure 2 that there are several oxidation pathways that may occur in molten carbonates which are in addition to those described by Equation (1)–(4), the difference being that electro-oxidation occurs with direct involvement from carbonate rather than from oxide species, i.e.,

$$C + 2CO_3^{2-} \rightarrow 3CO_2 + 4e^- \qquad \text{Electrochemical}\,(4e^-) \qquad (8)$$

$$CO + CO_3^{2-} \rightarrow 2CO_2 + 2e^- \qquad \text{Electrochemical}\,(2e^-) \qquad (9)$$

$$CO_3^{2-} \leftrightarrow CO_2 + O^{2-} \qquad \text{Chemical} \qquad (10)$$
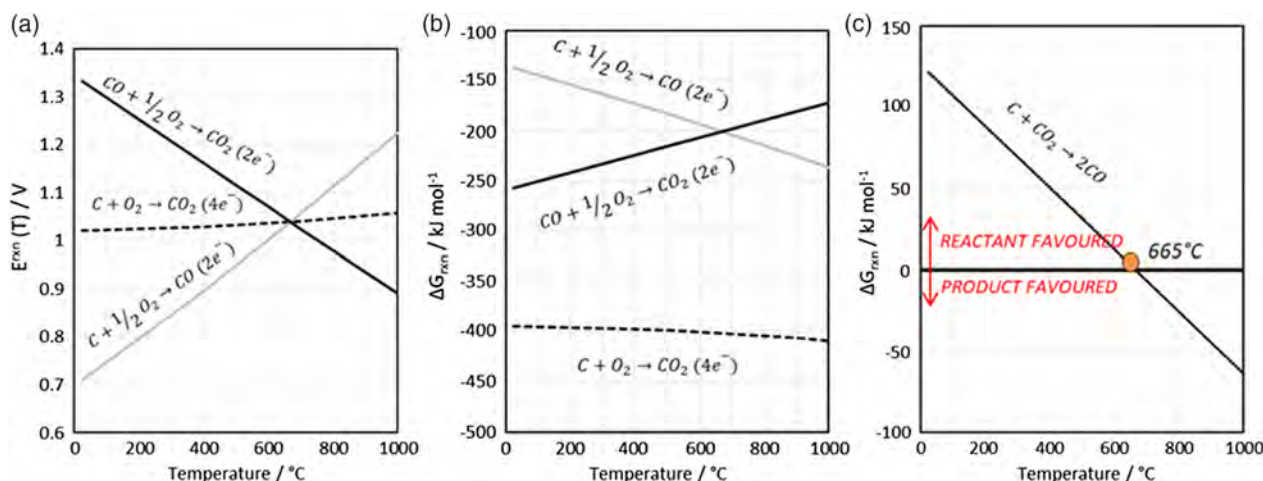
Figure 2. a) Overall electrochemical potential of a reaction for the production of 1 mol of product gas, b) Gibbs free energy for an electrochemical reaction to produce 1 mol of product gas, and c) Gibbs free energy for chemical of reverse Boudouard reaction to produce 1 mol of carbon monoxide gas.

Previous work has examined the catalytic effect of binary mixtures containing Na_2CO_3 and K_2CO_3,[24,25] whereas other studies have examined ternary carbonate mixtures.[26–28] Increasing the number of components used to make up a mixture generally lowers the melting point, which has been demonstrated to improve the gasification rate.[28] The current working hypothesis to explain this is that upon melting, the catalyst is dispersed more evenly over the char and penetrates pores,[26,28] which is a physical mechanism. However, it has also been noted that carbonate chemically decomposes to form oxides during gasification,[25,28] which the literature hypothesis does not address. Klopper et al.[25] suggested that alkali metal carbonates thermally decompose to form alkali metal oxides during gasification (Equation (11)), i.e.,

$$M_2CO_3\,(l) \rightarrow M_2O(s) + CO_2\,(g) \qquad (11)$$
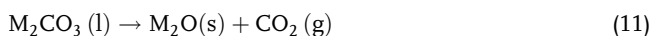
where M represents the alkali metal (i.e., Li, Na, or K). However, the decomposition temperatures reported by these authors are actually melting temperatures, i.e., 891 and 851 °C for K_2CO_3 and Na_2CO_3, respectively.[29] Single alkali metal carbonates, and even mixtures, barely decompose under a CO_2 atmosphere up to 900 °C.[30] Therefore, another hypothesis involving a chemical mechanism is required to explain how carbonate mixtures enhance gasification and also why they decompose to oxides at the same time.

In this work, chemical side reactions which may occur in molten carbonates have been investigated to understand their potential influence on the electrochemical oxidation of carbon fuels. The possible catalytic influence of alkali metal carbonates on chemical reactions of a bituminous coal char has been investigated under both N_2 and CO_2 atmospheres using thermogravimetric analysis (TGA). The effect of both temperature and alkali metal carbonate loading has been investigated to observe the relative impacts of each variable on the transformation of a stabilized coal char–based feedstock. Results are discussed in terms of a combined mechanism which considers both carbonate decomposition and gasification from carbonate.

2. Results

2.1. Coal Characterization and Gasification Limitations

The samples both before (raw) and after pyrolysis (CT-800) were analyzed by Fourier-Transform Infrared Spectroscopy (FTIR). **Figure 3** shows the FTIR spectra which were collected from the solid materials after they were cooled down to ambient temperatures. Previous investigations from this lab have shown that the mineral content in this raw coal sample is 29.0 wt%, with quartz showing up as the most abundant mineral by far at 85.4 wt%, thus constituting 24.8 wt% of the coal char sample.[31]

Figure 3 shows that post pyrolysis, coal becomes considerably more graphitic in nature, as evidenced by the apparent lack of functionality when comparing the above spectra. Many of the bands present in raw coal (Figure 3a) come from carbon functionalities including both aliphatic (2900 and 1040 cm^{-1}) and aromatic groups (1617 and 800 cm^{-1}). Heteroatoms are also present in the form of both silicon- and oxygen-containing functionalities, evidenced by the bands at 500 and 1040 cm^{-1}. These functionalities are most likely due to the presence of SiO_2 or clays such as quartz and montmorillonite present in both raw and pyrolyzed coal samples.[32]

The degree to which gaseous CO_2 reacts with solid carbon in the DCFC, i.e., reverse Boudouard gasification (Equation (4)), is dictated by a number of variables such as carbon fuel, gaseous atmosphere, and the applied electric field, which polarizes the fuel, thus possibly suppressing carbon corrosion.[33]

When considering the kinetics of carbon gasification from CO_2 (Equation (4)), it is important to consider whether the process is activation or diffusion limited. Depending on the specific conditions imposed, either factor could be limiting and is mutually exclusive.[34] Important dictating factors to consider are the relatively low temperature (500–800 °C),[35] which limits the rate of activation, and a low particle size (<45 μm), thereby facilitating effective diffusion.[34,35]

Of course, if a greater quantity of carbon materials is consumed in response to the addition of a catalyst or even a higher
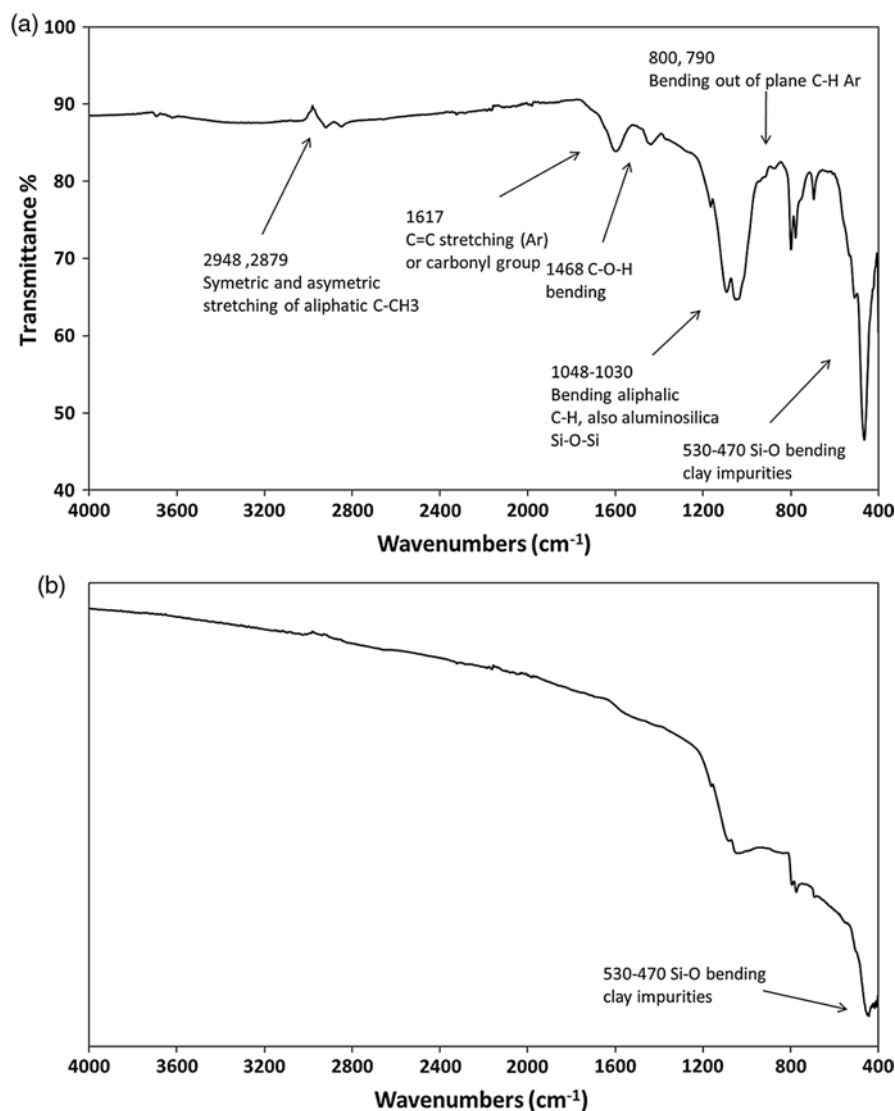
Figure 3. FTIR spectra of a) raw IV coal prior to pyrolysis and b) CT-800 post pyrolysis. Bands have been identified and are labelled on each spectrum.

imposed temperature, then these results too would suggest that the system is activation limited. This is because temperature has a much greater influence on the rate of an activation-controlled gasification process compared with a diffusion-limited system. The diffusion kinetics can be described by the Chapman–Enskog theory, which dictates that a large temperature increase causes only a relatively minor enhancement in the rate of gaseous diffusion.[36]

2.2. A Varied Temperature Study on Coal

The effects of heating coal char under N_2 and CO_2 were investigated for several higher heating temperatures (HHTs) using a coal char prepared under identical conditions (see Section 2.1). The procedure used was the same for each experiment with regions identified in **Table 1**.

Table 1. Varied temperature study—regions and conditions imposed.

Region	Process	Control	Gas
R1	Dehydration (0–220 °C)	Temperature ramp (10 °C min^{-1})	N_2
R2	Inert atmosphere (220 °C –HHT)	Temperature Ramp (10 °C min^{-1})	N_2
R3	Inert atmosphere (HHT)	Isothermal (120 min)	N_2
R4	Gasification (HHT)	Isothermal (120 min)	CO_2

TGA data were normalized to be on a dry basis (db) after R1. This assumed all water, including physically and chemically bound water, is removed by 220 °C. R2 therefore starts with a mass of 100 wt% (db) for all samples at a temperature of 220 °C. Results for mass change with temperature and time for R2, R3, and R4 described in Table 1 are shown in **Figure 4**a,b, respectively.
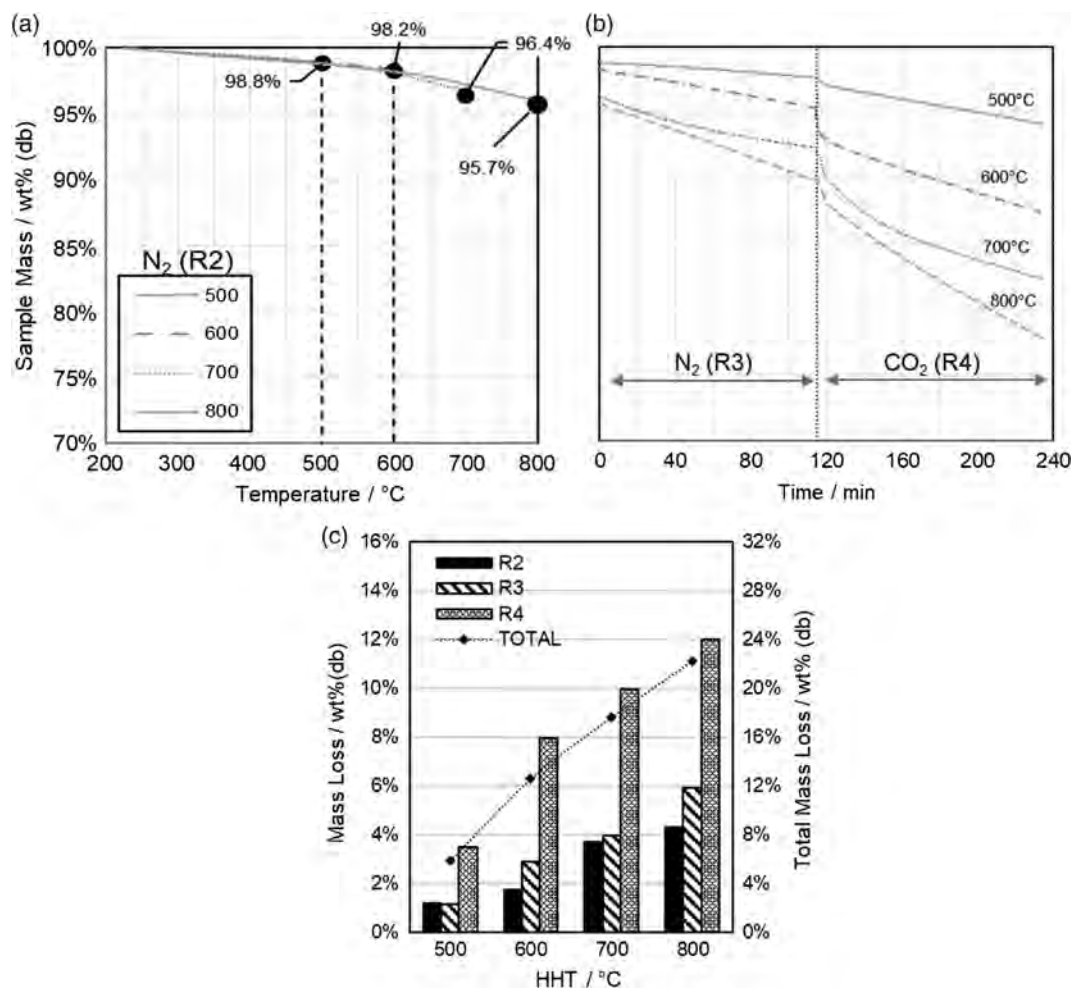
Figure 4. Varied HHT study on CT(800) coal char. Mass loss during a) temperature ramp to different HHTs and b) isothermal regions under N_2 for 2 h and CO_2 for 2 h. c) Mass loss (db) in R2, R3, and R4. Region descriptions indicated in Table 1.

During temperature ramp to the HHT of the investigation, mass change was minor and followed an almost identical trend for all samples, and the maximum mass loss was observed for a HHT of 800 °C. The coal char used was previously pyrolyzed at 800 °C, which suggested there should be no further mass loss before this temperature. However, it can be seen that increasing mass losses with increasing temperature occurred in both R2 and R3 under N_2 atmosphere as shown in Figure 4c.

Pyrolysis is therefore likely to still continue for this coal, pointing to a kinetically slow process in this instance because initial coal pyrolysis was performed at a slow heating rate of 5 °C min^{-1} and a residence time of 60 min at this temperature. Poor diffusion has been demonstrated to prevent complete devolatilization of coal samples during pyrolysis,[37] which may have been a factor in the initial pyrolysis experiment carried out;[31,38] however, mass loss overall is relatively small under N_2; i.e., ≈10 wt% of the initial mass measured even after holding at 800 °C for 2 h.

It can also be clearly observed in Figure 4 that when CO_2 was introduced (R4) at a higher temperature, particularly above 650 °C, greater weight loss occurred in that region. This is an expected result given that reaction kinetics for carbonaceous fuels in these conditions have been shown to improve with increased temperature,[39] and it is known that Boudouard gasification is thermodynamically favored above 665 °C (Figure 4). As discussed later, sensitivity of mass loss with different HHTs strongly suggests that the system is activation limited.

2.3. Alkali Metal Carbonate Catalysis

Coal gasification by CO_2 has been studied extensively.[39] Less frequent are examinations of the gasification of coal under CO_2 in the presence of alkali metal carbonates,[7,8] even fewer for gasification of processed coal chars.[5] Here, a systematic analysis of the effect of the ternary alkali metal carbonate eutectic has been investigated with coal char. The eutectic has been added in varying amounts to determine the effect of catalyst loading on the gasification response, following the same TGA procedure as outlined in the Experimental Section. When including alkali metal carbonates, it is important to consider that the eutectic melts at ≈400 °C[40–42]; hence, R2 was divided into two sub-regions to reflect this, i.e., R2A and R2B, which represent pre- and post-melting.

**ADVANCED
SCIENCE NEWS**
www.advancedsciencenews.com

Energy Technology
Generation, Conversion, Storage, Distribution
www.entechnol.de

Similarly to Section 2.3, sample mass was normalized for the temperature at which all physical and chemical moisture was assumed to have been removed (220 °C at the start of R2). Mass change over all regions, separated into temperature ramp and isothermal conditions, is shown in **Figure 5**.

After carbonate melting (R2B), mass loss increases substantially for carbonate loadings above 10 wt%, with this trend continuing for isothermal conditions under N_2. Response to a CO_2 gas atmosphere (R4) is also dependent on carbonate loading. A breakdown of mass loss in each region, as well as overall sample mass loss, is shown in Figure 5c.

Looking specifically at the conditions under N_2 (R2-R3), Figure 5 shows that enhanced mass loss occurred when adding carbonate, compared with the unmodified coal char control. This trend was particularly evident for the addition of 20 wt% molten carbonate loading (44.64 wt%).

Under CO_2, there is a positive correlation between mass loss and carbonate loading up to 20 wt% carbonate where a decline in comparative mass loss occurs (see R4 in Figure 5c). However, since mass loss under N_2 is much greater for this loading, the total mass loss for the 20 wt% sample is still larger than other samples. Total mass of the sample decreased by over 60 wt%, which is much larger than any mass loss observed without carbonate present even at higher temperatures (Figure 5). This has not previously been observed when using the ternary eutectic, and the extent of mass loss increase with carbonate addition is clearly significant, compared with what had been previously observed for either carbonate in the absence of carbon[30] or vice versa (as shown in Figure 4). However, similar observations have been seen in the recent literature when using K_2CO_3 as a catalyst. Kopyscinski et al.[7] noted that the mass lost under N_2 could not be accounted for purely due to carbonate decomposition, and a demonstrably larger mass loss in the presence of the catalyst was measured when heating under N_2 before switching to CO_2, compared with simply holding under CO_2 for the duration of the experiment.[8]
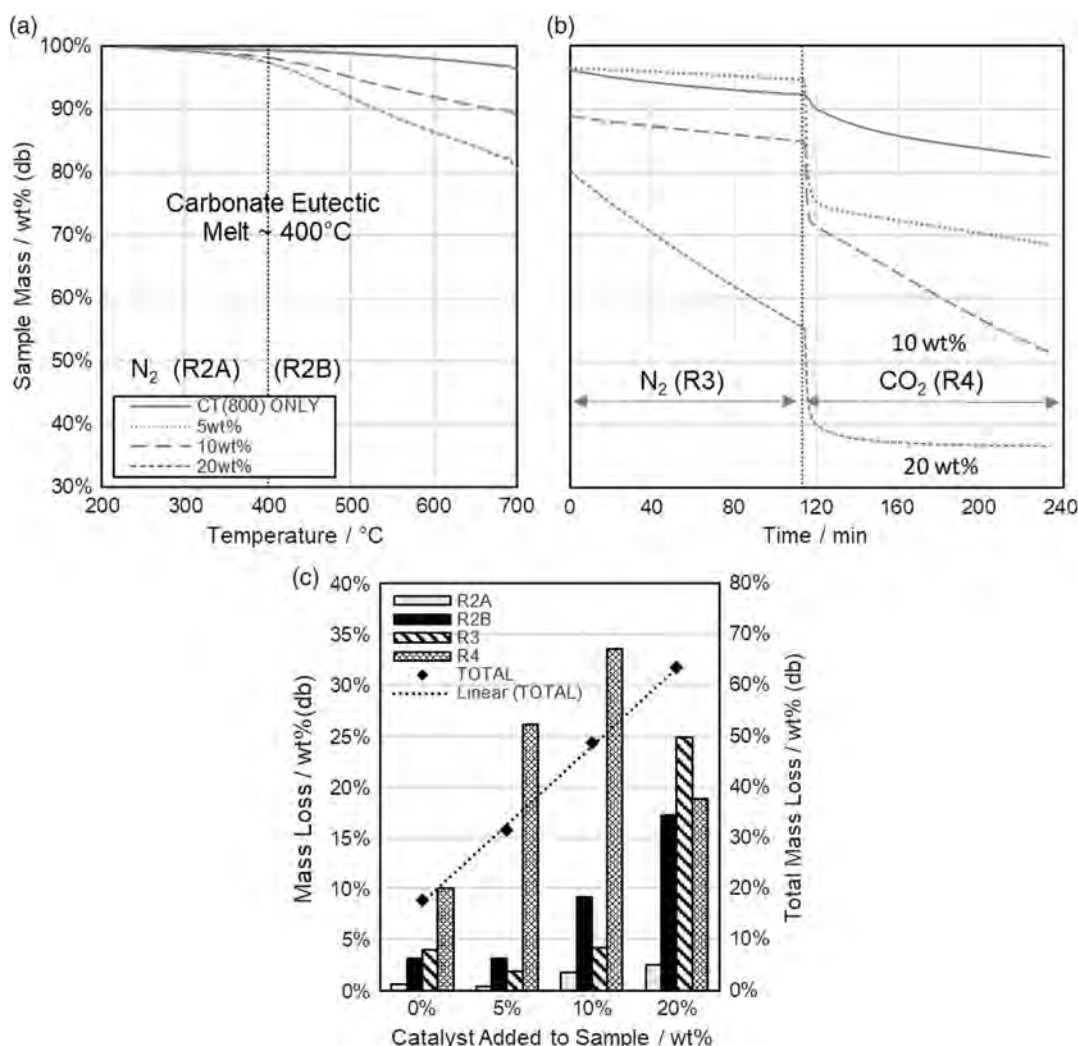
Figure 5. CT(800) coal char mass change for alkali metal carbonate catalyzed study under nitrogen and carbon dioxide atmospheres (as indicated) under a) temperature ramp and b) isothermal conditions, 700 °C. c) Sample mass loss for R2A, R2B, R3, and R4 as well as total sample mass loss between 220 and 700 °C.

2.4. High-Temperature Catalysis Study

The addition of a small amount of alkali metal carbonates (5 wt%) is seen in Section 2.4 to significantly enhance mass loss under CO_2 atmospheres, increasing from just under 10 wt% change to more than double this amount. The mass loss under N_2, i.e., R2A + R2B + R3, was seen to be similar, when comparing the control to the 5 wt% catalyst loading, i.e., 7.69 wt% versus 5.34 wt%, respectively. Since the amount of the alkali metal catalyst is also minor, under CO_2 (R4), virtually all mass loss can be attributed effectively to the reverse Boudouard reaction rather than decomposition via Equation (10). The effect of temperature was therefore investigated with and without a small carbonate loading of 5 wt% when heating to either 700 or 800 °C in separate experiments (**Figure 6**).

Mass loss under N_2 in all cases observed in Figure 6c is shown to be relatively small and similar for all cases under the conditions imposed. However, it is evident that less mass was lost when carbonate was present compared with the control for the system heated to 700 °C, which is consistent with previous findings (Section 2.4). The observation is likely due to the reported tendency of alkali metal carbonates to inhibit the rate of the pyrolysis process.[7,8]

A significant difference in behavior under CO_2 atmospheres was observed, with the largest mass loss overall observed for gasification of coal char at 800 °C in the presence of 5 wt% carbonate, shown clearly in Figure 6. The shape of mass loss curves is also very different for the coal char taken to 800 °C, and a similar effect is seen without carbonate addition for this temperature in Figure 6. Initially, the gasification reaction appears to begin more slowly in this case; however, there is also no plateau in mass loss as observed after an initially fast mass loss for other gasification temperatures. Overall however, the influence of the carbonate catalyst can be seen to have a much higher impact on mass loss than increasing the reaction temperature by 100 °C. In the case of gasification at 800 °C, the extent of gasification is almost triple in the presence of 5 wt% carbonate compared with that without.
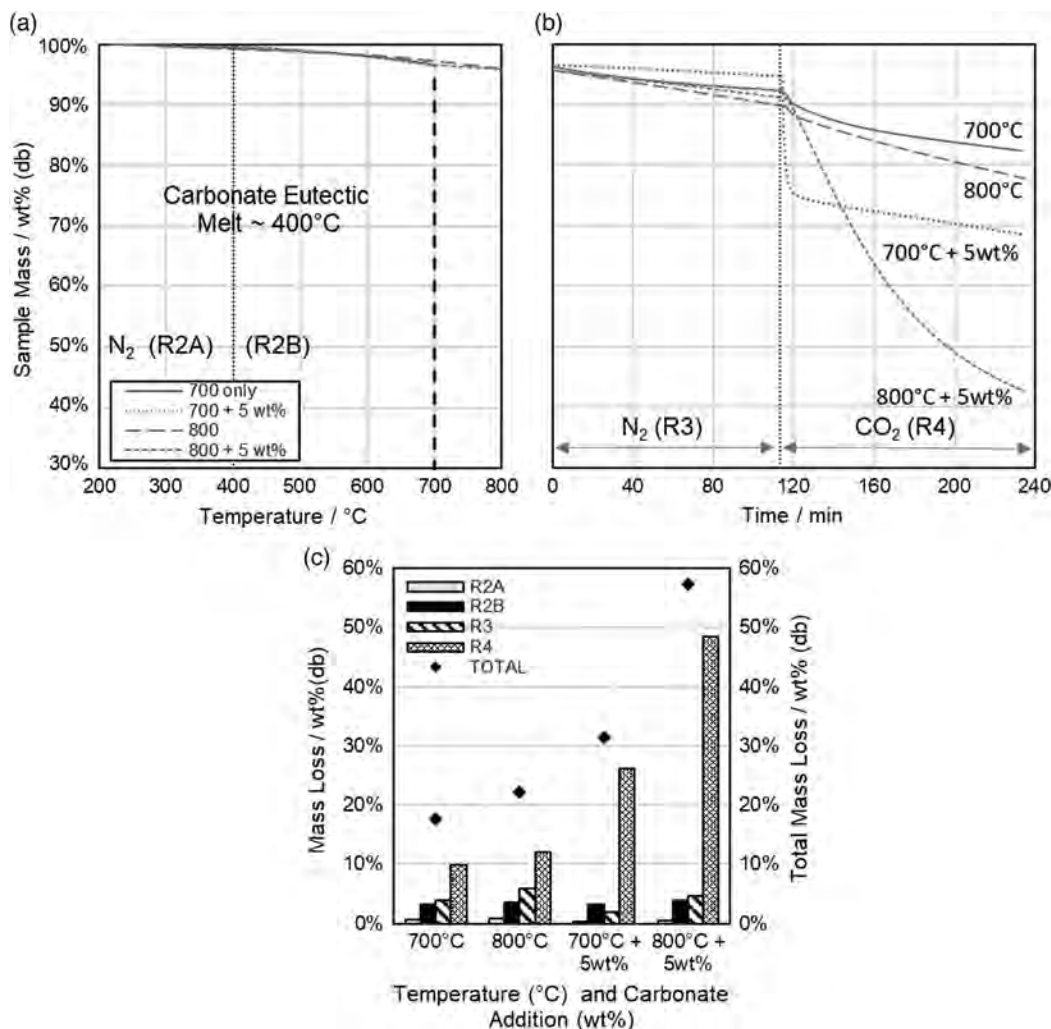

Figure 6. CT(800) coal char mass change for high-temperature alkali metal carbonate catalyzed study under nitrogen and carbon dioxide atmospheres (as indicated) under a) temperature ramp and b) isothermal conditions, 700 or 800 °C. c) Sample mass loss for R2A, R2B, R3, and R4 as well as total sample mass loss between 220 and 700 °C or 220–800 °C.

3. Discussion

3.1. Carbon Gasification from CO$_2$: Uncatalyzed Mechanism

It is vital to consider that the gasification mechanism likely shifts depending upon whether or not carbonate is present as a catalyst. The mechanism illustrated below Equation (12)–(16), describes uncatalyzed carbon gasification. This mechanism comes from the results presented in Section 2.3 and the relevant literature dealing with carbon gasification from CO$_2$.[39]

$$CO_2 (g) + C_{SR} (s) \leftrightarrow 2CO(g) \tag{12}$$

$$CO_2 (g) \overset{C_{SR}}{\leftrightarrow} CO_2(ads) \tag{13}$$

$$CO_2 (ads) \overset{C_{SR}}{\leftrightarrow} CO(ads) + O(ads) \tag{14}$$

$$C_{SR} + O(ads) \rightarrow CO(ads) \tag{15}$$

$$CO(ads) \rightarrow CO(ads) \tag{16}$$
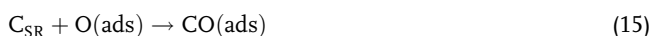
Equation (12)–(16) show an intuitive reverse Boudouard gasification mechanism, which involves CO$_2$ initially adsorbing onto the surface of carbon, before disassociating into CO(ads) and O(ads). In this mechanism, O(ads) acts as an intermediate species, not as a catalyst. Surface reactive carbon (C$_{SR}$) is a notation used by Cherepy et al.[43] as part of their DCFC electro-oxidation mechanism to denote a carbon site able to undergo facile electrochemical oxidation. Equation (12)–(16) show C$_{SR}$ depicted as a heterogeneous catalyst initially and not a reactant, until when directly reacting with O(ads) to produce CO(ads), in which case carbon is consumed during the process.

These suggestions are supported by the literature findings of Franke and Meraikib, who hypothesized that for the catalyzed system, alkali metals intercalate into the carbon substrate acting as an electron donor, thus promoting chemisorption of CO$_2$ at the carbon surface.[44,45] The adsorbed carbonyl group (CO(ads)) can then desorb, evolving as CO(g), and the adsorbed oxygen species (O(ads)) reacts with the carbon substrate to form CO(ads), before also desorbing from the surface. Peng et al.[46] suggests that CO produced during the reverse Boudouard reaction is physisorbed to the carbon surface and that oxide is chemically adsorbed.

An important distinction between the mechanism proposed here and the Peng et al.[46] mechanism is that here oxide was substituted with the intermediate species O(ads). The oxide comes from carbonate decomposition, and for the uncatalyzed pathway, O(ads) is produced as a result of the breakdown of CO$_2$. In terms of charge, C^{4+} in CO$_2$ undergoes a two-electron reduction to C^{2+} in the form of CO, whereas one of the oxides (O^{2-}) in CO$_2$ undergoes a two-electron oxidation to O(ads), thus completing the redox couple, as shown in Equation (14). While chemisorption may be possible, there are no valance electrons available for the O(ads) species to chemisorb to the carbon surface; therefore, physisorption is more likely.

3.2. Carbonate Decomposition and Gasification Under CO$_2$-Depleted Atmospheres

Under N$_2$, mass loss exceeds the amount of carbonate present for the 10 and 20 wt% carbonate loadings; therefore, an explanation is required to rationalize carbon consumption under a CO$_2$-free atmosphere. This is evident from Section 2.4 that when carbonate is added to the coal char at a level above 5 wt%, mass loss in regions R2B and R3 (under N$_2$ gas) increases substantially. In the case of carbonate loading at 20 wt%, this is particularly evident where it is seen that the majority of mass loss for the sample occurs prior to the injection of gaseous CO$_2$.

Although some of this mass loss is likely due to continued pyrolysis of the coal char (as discussed in Section 2.5), the enhancement observed for a loading of 20 wt% is far more than what could be expected for coal pyrolysis.[37,47] An additional mass loss reaction must therefore take place which is linked to carbonate addition. This mass loss could be due to either gasification in the absence of CO$_2$, carbonate decomposition, or a combination of both.

Reverse Boudouard gasification (Equation (4)) does not occur under a CO$_2$-depleted atmosphere, because CO$_2$ is a reactant. However, it is worth examining the reverse Boudouard reaction to determine whether an alternative gasification pathway can proceed without gaseous CO$_2$ being present. The reverse Boudouard reaction (Equation (4)) is chemical in nature and not electrochemical, because the overall reaction does not produce or consume electrons. That being said the individual redox processes that constitute the net comproportionation reaction (Equation (18) and (19)) are electrochemical in nature.[46]

Equation 17 shows the reverse Bouduard reaction in terms of oxidation states, and in this example, the source of C^{4+} comes from CO$_2$, i.e.,

$$C^0 + (C^{4+})(O^{2-})_2 \leftrightarrow 2(C^{2+})(O^{2-}) \tag{17}$$
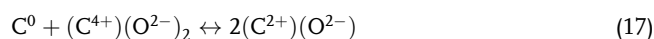
The individual half-cell reactions involving carbon from both the fuel (C^0) and CO$_2$ (C^{4+}) are shown below, i.e.,

$$C^0 \leftrightarrow C^{2+} + 2e^- \tag{18}$$

$$C^{4+} + 2e^- \leftrightarrow C^{2+} \tag{19}$$

Combining the above redox reactions gives the overall comproportionation of carbon, i.e.,

$$C^0 + C^{4+} \leftrightarrow 2C^{2+} \tag{20}$$

Now, the absence of CO$_2$ effectively removes C^{4+} from the reaction scheme; however, an alternative source of C^{4+} can be substituted from carbonate in an alkali metal salt system[15], i.e.,

$$CO_3^{2-} + C \leftrightarrow 2CO + O^{2-} \tag{21}$$

Equation (21) can be used to explain the results which have been presented here, because it essentially shows two processes taking place in a single reaction, i.e., gasification from carbonate and carbonate decomposition, both of which result in mass loss. As discussed in Section 2.4, the extent of mass loss increases above 400 °C when the carbonate melts, thus implying that

**ADVANCED
SCIENCE NEWS**
www.advancedsciencenews.com

Energy Technology
Generation, Conversion, Storage, Distribution
www.entechnol.de

the reaction rate of Equation (21) also increases when the carbonate melts. Gasification is typically investigated with steam or CO_2 as the gasifying agent;[39] however, there is no explicit reason as to why gasification with carbonate as a gasification agent would not be possible. Furthermore, this concept can be applied to several key literature findings to help shed a new perspective on what is taking place. Gasification from carbonate may be kinetically more labile given that molten carbonate is intimately mixed with the char, as opposed to CO_2, which must first diffuse into the slurry. This can explain the results of Yoshida et al.,[24] who show that the rate of gasification is greater for a carbonate-catalyzed system but that the total amount of CO produced is limited by the availability of carbon.

Carbonate decomposition (Equation (11)) under nitrogen to the extent observed in the case of 20 wt% loading contradicts the findings of Olivares et al. who reported that carbonate decomposition is negligible (5.1%) under non-CO_2 atmospheres (Ar) up to a temperature of 1000 °C.[30] However, it has previously been suggested by McKee and Chatterji[4,48] that carbonate decomposition is enhanced by the presence of graphite. These authors examined the thermal decomposition of Na_2CO_3 at 600 °C and concluded that, in the presence of graphite, the thermodynamic equilibrium shifted in favor of the decomposition products, indicated by the presence of CO_2 in the flue gas stream. This has also been suggested for K_2CO_3, where, in the presence of coal char under N_2 at 500 °C,[49,50] the decomposition temperature for unmodified K_2CO_3 is >1600 °C.[29] These findings demonstrate carbonate decomposition is enhanced in the presence of carbon even under a CO_2-depleted atmosphere. Also, Peng et al. showed enhanced metal oxide formation at the carbon–carbonate interface after fusing under essentially a N_2 gas mix (95% N_2 + 5% CO_2) using the energy-dispersive X-ray spectroscopy (EDX) analysis versus 100% CO_2 where only carbonate crystals were present.[46] In the aforementioned cases, traditional carbonate decomposition from auto-dissociation via Equation (11) may occur in conjunction with the combined mechanism (gasification from carbonate plus carbonate decomposition) via Equation (21), thus providing multiple reaction pathways and leading to enhanced decomposition kinetics, as well as enhanced mass consumption through CO_2 evolution.

3.3. Carbothermic Reduction

Previous work has suggested that gasification under N_2 or more generally CO_2-depleted atmospheres is possible via a carbothermic reduction mechanism.[8,51,52] Kopyscincki et al.[53] investigated the effect of mixing K_2CO_3 with ash-free coal chars while heating under a N_2 atmosphere. The authors observed mass loss at 700 °C, a temperature much higher than expected for volatile matter removal from the carbon source. It is useful to note that under these conditions, potassium carbonate would not have been molten (melt temperature of K_2CO_3 is 891 °C[54]). Nondispersive FTIR analysis of the flue gas during mass loss revealed the generation of both CO and CO_2, although CO was found to account for the majority of mass loss. This lends support to the combined mechanism described above (Equation (21)), i.e., gasification from carbonate plus carbonate decomposition, which shows CO as a product gas. The authors

suggest that the K_2CO_3 may be reduced by the carbon present to release CO and additionally CO_2, i.e.,

$$K_2CO_3 \, (s) + C(s) \rightarrow CO_2 \, (g) + CO(g) + 2K(s) \tag{22}$$

$$K_2CO_3 \, (s) + 2C(s) \rightarrow 3CO(g) + 2K(s) \tag{23}$$
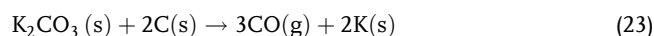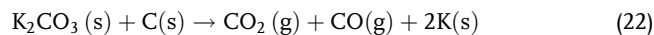
These are examples of carbothermic reduction reactions, where the carbothermic reduction product (K) is denoted as a solid; however, potassium metal melts above 759 °C;[55] hence, the phase is temperature dependent. Carbothermic reduction involves reduction of a metal in the presence of carbon at elevated temperatures. In this case, the alkali metal cation (M^+) is reduced to the elemental state, i.e.,

$$M^+ + e^- \rightarrow M \tag{24}$$

While the carbonaceous fuel is oxidized to C^{2+}, i.e.,

$$C^0 \rightarrow C^{2+} + 2e^- \tag{25}$$

The overall carbothermic reduction reaction is therefore

$$2M^+ + C \rightarrow C^{2+} + 2M \tag{26}$$

In general, carbothermic reduction only occurs at temperatures above 2000 °C.[56] Logically, the activation temperature varies according to the species being reduced. However, according to L'vov et al.,[56] the highest temperature carbothermic reduction has been reported at is 800 °C. Both Kopyscincki et al.[53] and Wood et al.[52,57] have suggested carbothermic reduction as a way of explaining their mass loss results under CO_2-depleted atmospheres in the presence of carbonate; however, a thermodynamic justification was absent from both communications. Instead the approach has been to search for the evidence of the carbothermic reduction product, i.e., metallic alkali metals.

To demonstrate the existence of the carbothermic reduction product, Kopyscincki et al.[8] used in situ X-ray powder diffraction (XRD) together with optical microscopy, with the idea being that if the product is present, then the reaction must necessarily have taken place. The XRD data itself, while interesting, is not unequivocally convincing. In almost all cases, the authors speculate about the nature of what exactly each pattern might be showing. The authors speculate that the size of the proposed K—O—C intermediate species is less than 5 nm, and therefore it cannot be detected by XRD.

Wood et al. proposed a mechanism to explain K_2CO_3-catalyzed gasification of carbon, which involved carbothermic reduction of K^+ to metallic K.[51,52] According to these authors, the potassium metal went on to form nucleophilic K—O—C surface sites which adsorbed to the carbon substrate. This was suggested to lead to a redistribution of electron density, in effect weakening C—C bonds while strengthening adjacent K—C bonds to the substrate. The K—O—C bonds were implied to be relatively weak, as this led to the evolution of CO gas, which is an enhanced gasification response.

The presence of K—O—C surface complexes was detected by alkylation with methyl iodide and examined using nuclear magnetic resonance spectroscopy (NMR).[51,52] Wood et al. claim that free radicals were produced when K_2CO_3 was heated with

**ADVANCED
SCIENCE NEWS**

www.advancedsciencenews.com

Energy Technology
Generation, Conversion, Storage, Distribution

www.entechnol.de

carbon at temperatures above 500 °C, thus forming reactive aliphatic fragments.[51,52]

3.4. Enhanced Gasification After Switching to a CO_2 Atmosphere

Kopyscinski et al.[8] showed that allowing an isothermal period under N_2 at 700 °C before switching to CO_2 caused a greater mass loss compared with holding under only CO_2 for an equivalent time frame. A mechanism was proposed whereby carbonate supplies surface-bound oxygen, which is capable of reacting with and gasifying carbon.[8] This surface-bound oxygen comes from the breakdown of adsorbed carbonate, which is different to the adsorbed oxygen shown in Equation (10)–(14), that resulted from the breakdown of adsorbed CO_2 in the uncatalyzed reaction pathway.

Kopyscinski et al.[8] go on to postulate the formation of a series of C—O—K and C—K surface complexes, which illustrate the system behavior under various temperature and atmospheric conditions. **Figure 7** shows carbonate adsorbing to the carbon surface at 700 °C, before being cleaved at the O—C bond, leaving behind a surface C—O—K complex (Figure 7a). CO is evolved, leaving behind atomic K on the surface, i.e., the carbothermic reduction product (Figure 7b).

It is evident from Figure 7 that the carbon substrate lowers the activation energy required for carbothermic reduction (Figure 7b). Under CO_2 at 700 °C, the system is shown to acquire a peroxide (O^-),[58] and K is reoxidized back to K^+ (Figure 7c(i)). This last step explains the decreased activity when heated under CO_2 compared with heating under N_2 then switching to CO_2.

In this mechanism, the source of peroxide is suggested to come from CO_2 breakdown, leaving behind carbon and oxide (O^{2-}), before oxide is oxidized to peroxide (O^-).[8] However, two species are being oxidized, i.e., K^+ and O^{2-}, and there is no corresponding species which is reduced to complete the redox couple. Under N_2 at temperatures exceeding 800 °C which is above the melting point of potassium, i.e., 759 °C,[55] potassium evaporation is shown (Figure 7c(ii)). When the system is cooled under CO_2, carbonate reformation is shown occurring as a surface process (Figure 7c(iii)), which is expected given that Equation (11) is reversible.[4,59,60]

Weighing up the totality of the evidence, it can be said that carbothermic reduction at 700 °C may be possible; however, unequivocal evidence is lacking at this time. Instead, gasification from carbonate and carbonate decomposition (Equation (21)) appears to be more a probable explanation for the observed mass loss under a CO_2-depleted atmosphere. It is apparent that the kinetics of the Boudouard reaction are facilitated after the gas atmosphere has been switched to CO_2 from N_2 at elevated temperatures (700 °C) after a 2 h isothermal period. This may be due to an enhanced oxide activity in the melt coming from carbonate decomposition, given that adsorbed oxide anions are thought to be involved in the carbonate-enhanced gasification mechanism.[46]

4. Conclusions

It has been demonstrated that in the presence of a ternary molten alkali metal carbonate eutectic, gasification under a CO_2-depleted atmosphere is possible. The reaction is similar to the reverse Boudouard reaction; however, the source of the C^{4+} comes from carbonate rather than carbon dioxide. In addition to gasification, this reaction also results in carbonate decomposition, thus increasing the oxide activity in the melt. Because carbonate is consumed during gasification, it is not a catalyst; its role is to enable an alternative reaction pathway. The enhanced mass loss when switching to CO_2 at an elevated temperature (700 °C) from a CO_2-depleted atmosphere is likely due to the enhanced oxide activity in the melt, which feeds directly into the gasification mechanism in the form of surface-bound oxygen or an oxygen ion that adsorbs to the carbon.

These findings are significant for DCFC applications because alkali metal carbonate mixtures are often used to enhance the design and the electro-oxidation mechanism. Gasification is generally regarded as a parasitic process that consumes fuel without passing current, and carbonate decomposition leads to the instability of the cell. It is therefore hoped that understanding these reactions in greater detail will support future researchers in making significant improvements to their DCFC designs.
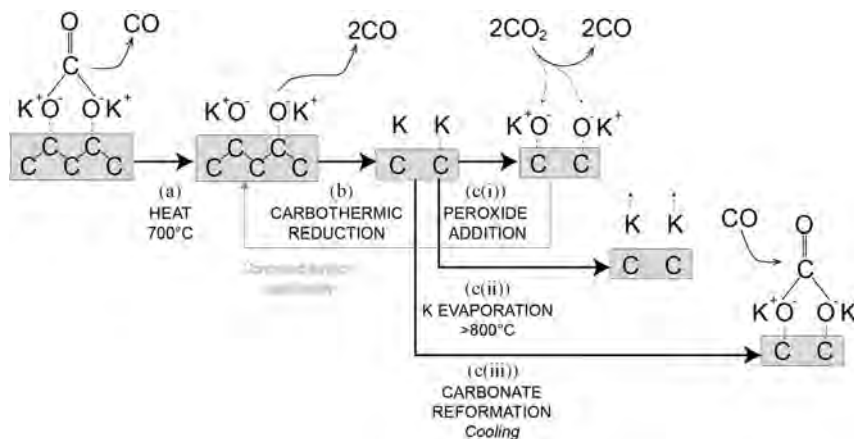

Figure 7. Reaction scheme of an ash-free coal heated under a N_2 or CO_2 atmosphere. The illustration above was appropriated from the original published version.[8]

**ADVANCED
SCIENCE NEWS**

www.advancedsciencenews.com

Energy Technology
Generation, Conversion, Storage, Distribution

www.entechnol.de

5. Experimental Section

Coal Char Preparation: The coal char used in this study was sourced from a mine located in Victoria, Australia, and was ranked as bituminous,[31,38] and it was pyrolyzed beforehand at 800 °C under N_2. The coal sample was initially milled and sieved repeatedly to obtain a particle size of less than 45 μm. A stainless-steel bowl and balls were used for milling in a Fritsch planetary monomill (Idar-Oberstein, Germany), coupled with a shaker sieve platform that was used for particle size separation. Several batches were milled in ≈200 mg increments until the required quantity was obtained for a full sample set. The mass of coal per batch was dictated by the device recommendations when using the stainless-steel mixing bowl that came with the instrument. The temperature was maintained under 100 °C throughout milling to avoid thermal degradation of the material during this procedure.

The milled coal samples were weighed, then placed into alumina crucibles before being inserted into a tube furnace under flowing nitrogen at 40 mL min^{-1}. The heating program initially entailed heating from ambient temperature to 110 °C at a rate of 10 °C min^{-1}, followed by a 1 h isothermal period. Post dehydration, the sample was then heated to 800 °C at a heating rate of 6 °C min^{-1}, where it was held isothermally for 4 h. The furnace was then switched off and allowed to cool to ambient temperature under flowing nitrogen. The samples were not removed from the inert atmosphere until the temperature was below 100 °C. The solid coal samples were analyzed by FTIR to examine changes in terms of the functional groups present both before and after pyrolysis. The FTIR instrument was a Perkin Elmer Frontier Spectrum Two, which used an attenuated total reflectance (ATR) crystal as a sampling accessory, and the wavenumber range examined was 400–4000 cm^{-1}. Detailed results from mineral liberation analysis and coal grain analysis on this coal char were also provided in previous work where coal was designated as CT-800.[31]

Alkali Metal Carbonate Preparation: Carbonate mixtures were prepared from reagent grade purity compounds (>99% purity). Lithium, sodium, and potassium carbonates were sourced from Sigma-Aldrich and before use were dried in an alumina crucible at 150 °C, for at least 24 h to remove water.

Carbonate mixtures were prepared by mixing first each specific composition using a mortar and pestle. The most commonly used composition was the ternary eutectic for which the molar composition is 43.5% Li_2CO_3, 31.5% Na_2CO_3, and 25.0% K_2CO_3. To ensure thorough mixing, the sample was passed through a ball mill (Fritsch, Pulverisette) following mortar and pestle mixing. Milling was carried out over four intervals of 10 min, in both clockwise and counter-clockwise directions at 200 rpm, with a 2 min rest period between milling periods. Following this, the mixture was heated up to 600 °C under CO_2 to initially melt and hence homogenize the mixture. The melt was kept at 600 °C for 4 h, then cooled down to ambient temperature, after which it was removed from the crucible, broken up, and ground to a fine powder using a mortar and pestle.

TGA of Coal Chars: A TA Instruments Q50 thermogravimetric analyzer was used for TGA. In these experiments, coal char was examined under reverse Boudouard gasification conditions. TGA was enabled to allow flue gas to be analyzed in an FTIR (Varian IR-660) to allow off-gas sampling. A total of 24 scans were measured per spectrum over the range 400–4000 cm^{-1} with a resolution of 2 cm^{-1}. FTIR operating conditions consisted of a gas cell length of 10 cm and temperature of 800 °C and a heat transfer line (Pike Technologies). Approximately, 10 mg of sample material was weighed out onto a platinum pan. The gas flow rate into the TGA was held constant at 200 mL min^{-1}; however, the gas was switched from N_2 to CO_2 and back to N_2 at the completion of each experiment. When heating ramps were imposed, the rate used was 10 °C min^{-1}. Specifically, the method involved heating from ambient to a desired temperature between 500 and 800 °C (varied between individual experiments) under N_2, then holding isothermally at that temperature for 2 h. The gas was then switched to CO_2 while still in the isothermal period, and the system was held isothermally for another 2 h. Finally, the gas was switched back to N_2, and the system was cooled down to 40 °C.

[1] N. Ren, Y. T Wu, T. Wang, C. F. Ma, *J. Therm. Anal. Calorim.* **2011**, *104*, 1201.
[2] C. Jiang, J. Ma, A. D. Bonaccorso, J. T. S. Irvine, *Energy Environ. Sci.* **2012**, *5*, 6973.
[3] A. C. Rady, S. Giddey, A. Kulkarni, S. P. S. Badwal, S. Bhattacharya, B. P. Ladewig, *Appl. Energy* **2014**, *120*, 56.
[4] D. W. McKee, *Fuel* **1983**, *62*, 170.
[5] D. W. McKee, C. L. Spiro, P. G. Kosky, E. J. Lamby, *Fuel* **1983**, *62*, 217.
[6] C. L. Spiro, D. W. McKee, P. G. Kosky, E. J. Lamby, D. H. Maylotte, *Fuel* **1983**, *62*, 323.
[7] J. Kopyscinski, R. Habibi, C. A. Mims, J. M. Hill, *Energy Fuels* **2013**, *27*, 4875.
[8] J. Kopyscinski, M. Rahman, R. Gupta, C. A. Mims, J. M. Hill, *Fuel* **2014**, *117*, 1181.
[9] B. J. Hathaway, J. H. Davidson, *Sol. Energy* **2017**, *142*, 224.
[10] A. D. Bonaccorso, C. Jiang, J. Ma, J. T. S Irvine, *Int. J. Hydrogen Energy* **2016**, *41*, 18788.
[11] X. Xu, W. Zhou, Z. Zhu, *RSC Adv.* **2014**, *4*, 2398.
[12] A. C. Rady, S. Giddey, S. P. S. Badwal, B. P. Ladewig, S. Bhattacharya, *Energy Fuels* **2012**, *26*, 1471.
[13] C. Jiang, J. Ma, G. Corre, S. L. Jain, J. T. S. Irvine, *Chem. Soc. Rev.* **2017**, *46*, 2889.
[14] S. Giddey, S. P. S. Badwal, A. Kulkarni, C. Munnings, *Prog. Energy Comb. Sci.* **2012**, *38*, 360.
[15] K. Nagase, T. Shimodaira, M. Itoh, Y. Zheng, *Phys. Chem. Chem. Phys.* **1999**, *1*, 5659.
[16] P. J. Linstrom, W. G. Mallard, Eds. *NIST Chemistry WebBook, NIST Standard Reference Database Number 69*, National Institute of Standards and Technology, Gaitherburg, MD **2011**.
[17] K. Hemmes, M. Cassir, *J. Fuel Cell Sci. Tech.* **2011**, *8*, 051005.
[18] Y. Jiao, W. Tian, H. Chen, H. Shi, B. Yang, C. Li, Z. Zhao, Z. Zhu, S. D. Li, *Appl. Energy* **2015**, *141*, 200.
[19] C. Li, Y. Shi, N. Cai, *J. Power Sources* **2010**, *195*, 4660.
[20] M. F. Irfan, M. R. Usman, K. Kusakabe, *Energy* **2011**, *36*, 12.
[21] L. Deleebeeck, K. K. Hansen, *J. Electrochem. Soc.* **2014**, *161*, F33.
[22] A. Elleuch, J. Yu, A. Boussetta, K. Halouani, Y. Li, *Int. J. Hydrogen Energy* **2013**, *38*, 8514.
[23] C. Jiang, J. Ma, A. D. Bonaccorso, J. T. S. Irvine, *Energy Environ. Sci.* **2012**, *5*, 6973.
[24] S. Yoshida, J. Matsunami, Y. Hosokawa, O. Yokota, Y. Tamaura, *Energy Fuels* **1999**, *13*, 961.
[25] L. Klopper, C. Strydom, J. Bunt, *J. Anal. Appl. Pyrol.* **2012**, *96*, 188.

**ADVANCED
SCIENCE NEWS**

www.advancedsciencenews.com

Energy Technology
Generation, Conversion, Storage, Distribution

www.entechnol.de

[26] A. Sheth, P. Agrawal, Y. D. Yeboah, *Catalytic Gasification of Coal Using Eutectic Salt Mixtures*, **1998**.

[27] A. Sheth, Y. D. Yeboah, A. Godavarty, Y. Xu, P. K. Agrawal, *Fuel* **2003**, *82*, 305.

[28] Y. D. Yeboah, Y. Xu, A. Sheth, A. Godavarty, P. K. Agrawal, *Carbon* **2003**, *41*, 203.

[29] G. J. Janz, *Molten Salts Handbook*, Elsevier, Burlington **2013**.

[30] R. I. Olivares, C. Chen, S. Wright, *J. Solar Energy Eng.* **2012**, *134*, 041002.

[31] J. A. Allen, M. J. Glenn, P. Hapugoda, R. Stanger, G. O'Brien, S. W. Donne, *Fuel* **2018**, *217*, 11.

[32] J. Tulloch, J. A. Allen, L. Wibberley, S. W. Donne, *J. Power Sources* **2014**, *260*, 140.

[33] J. Yu, B. Yu, Y. Li, *Int. J. Hydrogen Energy* **2013**, *38*, 16615.

[34] L. Lahaye, P. Ehrburger, *Fundamental Issues in Control of Carbon Gasification Reactivity*, Vol. 192, Springer Science & Business Media, Dordrecht **2012**.

[35] D. Ye, J. Agnew, D. Zhang, *Fuel* **1998**, *77*, 1209.

[36] J. H. Ferziger, H.G. Kaper, *Mathematical Theory of Transport Processes in Gases*, North-Holland, Amsterdam **1972**.

[37] G. R. Gavalas, K. A. Wilks, *AIChE J.* **1980**, *26*, 201.

[38] J. A. Allen, M. J. Glenn, S. W. Donne, *J. Power Sources* **2015**, *279*, 384.

[39] M. F. Irfan, M. R. Usman, K. Kusakabe, *Energy* **2011**, *36*, 12.

[40] G. J. Janz, M. R. Lorenz, *J. Chem. Eng. Data* **1961**, *6*, 321.

[41] L. Volkova, *Izvest. Sibirsk. Oldel. Akad. Nauk. SSSR* **1958**, *7*, 33.

[42] S. Tamaru, M. Kamada, *Zeitschrift für Elektrochemie und angewandte physikalische Chemie* **1935**, *41*, 93.

[43] N. J. Cherepy, R. Krueger, K. J. Fiet, A. F. Jankowski, J. F. Cooper, *J. Electrochem. Soc.* **2005**, *152*, A80.

[44] F. Franke, M. Meraikib, *Carbon* **1970**, *8*, 423.

[45] M. Meraikib, F. Franke, *Chem. Ing. Tech.* **1970**, *42*, 834.

[46] F. Peng, Y. Li, P. Nash, J. F. Cooper, S. J. Parulekar, J. R. Selman, *Int. J. Hydrogen Energy* **2016**, *41*, 18858.

[47] P. Arendt, K. H. van Heek, *Fuel* **1981**, *60*, 779.

[48] D. McKee, D. Chatterji, *Carbon* **1975**, *13*, 381.

[49] C. A. Mims, J. K. Pabst, *ACS Div. Pet. Chem.* **1980**, *180*, 258.

[50] C. A. Mims, J. K. Pabst, *ACS Div. Fuel Chem.* **1980**, *25*, CONF-800814-P2.

[51] B. J. Wood, B. L. Chan, R. H. Fleming, R. D. Brittain, K. M. Sancier, D. R. Sheridan, H. Wise, *Mechanism of Catalytic Gasification of Coal Char*. Quarterly Technical Progress Report No. 3, 1 April–30 June 1981, SRI International, Menlo Park CA **1983**.

[52] B. J. Wood, R. D. Brittain, K. Lau, *Carbon* **1985**, *23*, 73.

[53] J. Kopyscinski, M. Rahman, R. Gupta, C. A. Mims, J. M. Hill, *Fuel* **2014**, *117*, 1181.

[54] G. Janz, *Molten Salts Handbook*, Academic Press Inc., New York **1967**, p. 248.

[55] G. Aylward, T. Findlay, *SI Chemical Data*, 4th ed., Wiley **1998**.

[56] B. V. L'vov, *Thermochim. Acta* **2000**, *360*, 109.

[57] B. J. Wood, B. L. Chan, R. H. Fleming, R. D. Brittain, K. M. Sancier, D. R. Sheridan, H. Wise, *Mechanism of Catalytic Gasification of Coal Char*, Quarterly Technical Progress Report, 1 January–31 March 1981.

[58] S. W. Smith, W. Vogel, S. Kapelner, *J. Electrochem. Soc.* **1982**, *129*, 1668.

[59] P. Lorenz, P. G. Janz, *J. Electrochem. Soc.* **1971**, *118*, 1550.

[60] B. Jalan, Y. Rao, *Carbon* **1978**, *16*, 175.

1900602 (12 of 12)

Gas Atmosphere Effects Over the Anode Compartment of a Tubular Direct Carbon Fuel Cell Module

Michael Glenn,[†] Bobby Mathan,[†] Md Monirul Islam,[†] Yaser Beyad,[†] Jessica A. Allen,[‡] and Scott W. Donne*,[†] [iD]

[†]Discipline of Chemistry and [‡]Discipline of Chemical Engineering, University of Newcastle, Callaghan, NSW 2308, Australia

ABSTRACT: This study examines the performance of a tubular direct carbon fuel cell (DCFC) with varying gas atmosphere. DCFC performance is higher under a CO_2 atmosphere when compared with a N_2 atmosphere, where mass transport limitations in the anode compartment and the additional two-electron oxidation pathway from CO contribute. This hypothesis is verified by comparing the slurry arrangement to a solid working anode where mass transport is not required. In order to maximize the carbon utilization efficiency, operating below the thermodynamic temperature limit for reverse Boudouard gasification (700 °C) is recommended with agitation in slurry-based systems. For a maximum power output, operating under CO_2 at higher temperatures (>800 °C) and passing the CO containing flue gas over an oxygen reduction cathode achieve optimal results.

INTRODUCTION

Fossil fuel-based energy generation has been used extensively across the globe for energy generation for many decades due to their ready availability and low cost. In the Australian context, large centralized coal-fired power stations provide over 80% of Australia's power, with the remaining demand covered by more renewable technologies such as hydroelectric, solar, and wind. However, the future of energy production will be very different and definitely less reliant on fossil fuels, which are essentially a finite resource rapidly approaching their complete consumption. A more immediate concern is that the consumption of fossil fuels leads to significant greenhouse gas emissions, which have been definitively linked to climate change.[1] In the immediate future, where the transition from fossil fuel-based energy generation to renewable energy generation is occurring, there is a distinct need for both low emission and more efficient coal utilization technologies to ensure a successful transition.[2]

A promising transitional technology is the direct carbon fuel cell (DCFC). This is a high-temperature fuel cell system whereby carbon (coal) is used to generate electrical energy directly, rather than in a coal-fired power station (CFPS) where a number of energy transformation steps are required. This is a distinct advantage of the DCFC in that it leads to a substantial increase in the operating efficiency from 35 to 40% in a CFPS to ~80% in the DCFC, a 50% reduction in CO_2 emissions, zero SO_x, NO_x, and particulate emissions, as well as decentralized energy generation.[3] When fueled by chars, the CO_2 flue gas coming from the DCFC anode chamber can be sequestered with 100% capture rates without the need for costly post-combustion capture processes.[4]

Coal combustion in a CFPS (eq 1) transforms the chemical energy stored in coal into heat, which, with subsequent transfer to a heat transfer fluid such as steam, provides the ability to turn a turbine generator. In this process, there are three energy transformations (chemical → thermal → kinetic → electrical), each of which incurs an energy penalty. The conversion from heat to kinetic energy limits the maximum theoretical

efficiency to just ~46%, that is, the Carnot efficiency.[5] Alternatively, the DCFC uses the same overall reaction (eq 1) but carries out the conversion of chemical into electrical energy in a single electrochemical process, that is

$$\text{overall: } C + O_2 \rightarrow CO_2 \tag{1}$$

$$\text{anode: } C + 2O^{2-} \rightarrow CO_2 + 4e^- \tag{2}$$

$$\text{cathode: } O_2 + 4e^- \rightarrow 2O^{2-} \tag{3}$$
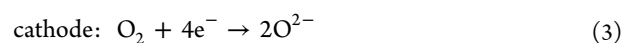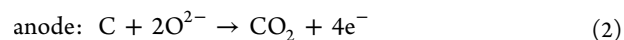
Typically, the DCFC is supported by oxide ion conducting electrolytes such as yttria-stabilized zirconia (YSZ; primary electrolyte), and a molten carbonate electrolyte (e.g., a eutectic of Li_2CO_3, Na_2CO_3, and K_2CO_3) can also be used as a secondary electrolyte. The thermodynamic efficiency of the electrochemical conversion of carbon into CO_2 is ~100%.[6] However, there are efficiency penalties due to various overpotentials associated with the anodic and cathodic half reactions as well as resistive heating in the current collectors, which decreases the overall efficiency to ~80%.[7] Internal resistance causes the cell voltage to drop during high current operation, thus producing heat. System overpotential is made up of contributions from ohmic losses (η_{ohmic}) arising from the series resistance, concentration overpotential (η_{conc}) arising from fuel loading and mass transport limitations, and activation overpotential (η_{act}) arising from anodic and cathodic charge transfer limitations,[8] that is

$$V = E - \eta_{ohmic} - \eta_{conc} - \eta_{act} \tag{4}$$

where V is the measured cell voltage (V) and E is the expected thermodynamic cell potential (V).

In addition to the four-electron oxidation of carbon to CO_2 in eqs 1−3, CO generated from the reverse Boudouard

reaction (eq 5) can be electrochemically oxidized to CO_2, that is

$$C + CO_2 \leftrightarrow 2CO \tag{5}$$

$$CO + O^{2-} \rightarrow CO_2 + 2e^- \tag{6}$$
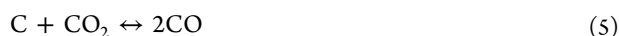
This is a competing two-electron process that decreases the overall energy density of the DCFC. It is critical to keep O_2 away from the anode chamber while operating the DCFC to avoid carbon combustion, which rapidly consumes the fuel without passing charge. To achieve this, gases such as CO_2 or N_2 are flowed over the anode chamber.[7,9] CO_2 can participate in the Boudouard reaction (eq 5), thus producing CO that can alter the dominant reaction pathway from a four-electron process to a two-electron process[10,11] and potentially also agitate the slurry. In addition, a positive CO_2 pressure suppresses carbonate decomposition (eq 7),[12] thus keeping the secondary electrolyte invariant, that is

$$CO_3^{2-} \leftrightarrow CO_2 + O^{2-} \tag{7}$$

In a study by Olivares et al.[12] the extent of carbonate decomposition was reduced from 5.4 wt % to just 1.4 wt % under non-CO_2 and CO_2 atmospheres, respectively. When the molten carbonate decomposes, it leaves behind a soluble alkali metal oxide product; however, if the decomposition is too severe, this may impede the flowability of the carbon/carbonate slurry. This would interrupt the continuous operation of the fuel cell, thus reducing it to a batch process, that is, a carbon battery.

The literature is yet to come to consensus on whether operating under CO_2 or N_2 leads to an enhanced performance. Elleuch et al.[13] and Jiang et al.[14] report a higher power density under CO_2, while Deleebeeck et al.[6] reposted the opposite. However, the open circuit potential (OCP) has been shown to be consistently higher (~0.15 V) under N_2.[6,13,14]

Slurry arrangements are often utilized where the particulate fuel (carbon) is suspended in a molten carbonate electrolyte. The advantage of using a molten carbonate secondary electrolyte is that it increases the electroactive surface area of the triple phase boundary at the anode interface, that is, C (fuel)/CO_3^{2-} (electrolyte)/Ag (current collector). This is because the current collector can extend out into the bulk of the molten slurry in three dimensions.[10,15] By contrast, a solid oxide electrolyte is confined to a two-dimensional interface and therefore has a lower surface area for a given anode chamber volume. In addition, using small carbon particulates (<200 μm) further increases the surface area available to electro-oxidation.

A drawback when using slurry arrangements is that physical diffusion of the carbon particles to the current collector can limit the rate of charge transfer. To mitigate this diffusion limitation, slurry arrangements are often agitated during operation. Li et al. reported a clear correlation between the rate of stirring and the measured current density using a slurry arrangement, thus demonstrating that mass transport was the rate-limiting factor.[16] For a solid anode arrangement, carbonaceous pellets or rods are used as both the fuel and the current collector. In this case, the active surface area is simplified to a two-phase boundary, where the fuel is in constant contact with the electrolyte, thus eliminating the possibility of a mass transfer limitation.

This study examines the performance of a tubular 8 mol % yttria-stabilized zirconia (8YSZ) cell using a thermal coal char as the fuel, lanthanum strontium manganite (LSM), that is, $(La_{0.80}Sr_{0.20})_{0.95}MnO_3$, as the cathode catalyst, and a ternary alkali metal carbonate eutectic as the secondary electrolyte over the temperature range of 700−860 °C. The performance was compared when changing the gas atmosphere over the anode compartment between CO_2 and N_2 in separate experiments, which influences the gasification characteristics of the carbonaceous fuel.[17] Variations to the gasification characteristics of the fuel were investigated using thermogravimetric analysis (TGA). Different anode arrangements were also explored, comparing a slurry arrangement to a solid graphite rod, with the latter serving as both the fuel and the current collector.

■ EXPERIMENTAL SECTION

Thermogravimetric Analysis. Approximately 10 mg of sample (either carbon material individually or a carbon-eutectic mixture) was weighed into a 20 μL alumina crucible, which was in turn loaded into the thermogravimetric analyzer (TGA; Netzsch STA 2500 Regulus). The sample was heated to 220 °C at 10 °C/min where it was held isothermally for 10 min to remove both surface and structural water. The resultant TGA data was normalized to the mass at 220 °C once the sample was dry. The temperature was then ramped to 700 °C at 10 °C/min before again being held isothermally for 10 min, after which the temperature was again ramped further to 800 °C at the same heating rate and held for further 10 min. The final heating stage was to 860 °C at 10 °C/min. Either CO_2 or N_2 was flowed over the sample at 40 mL/min in separate experiments. The same heating profile and sample were used for all the TGA experiments to ensure consistency between the results.

Cathode Fabrication. 8YSZ tubes were purchased from Lianyungang Highborn Technology Co., China, with dimensions of inner diameter = 9.5 mm, outer diameter = 12.5 mm (wall thickness = 1.5 mm), and length = 100 mm. The cathode paste was modified from a stock mixture containing LSM powder in a terpineol-based ink (Fuel Cell Materials), for which the solid loading was ~65 wt %. 8YSZ powder was added to the stock mixture to make up a 1:1 mol ratio of 8YSZ/LSM. A hand mortar was used to ensure that a homogeneous mixture was produced.

The modified mixture was coated onto 8YSZ tubes using a foam brush, and care was taken to ensure that the coating was both even and thin. The electrodes were then heated to 1300 °C at a rate of 1 °C/min where the temperature was held for 1 h before being cooled to ambient temperature. Silver wire (outer diameter = 0.35 mm; Goodfellow) was then wrapped around the tubes and adhered in place using silver paste, which was cured in a drying oven at 100 °C for 1 h. The silver wire on the outside of the tubes was used as a cathode current collector. Care was taken to ensure that the electrode fabrication process was consistent between the individual tubes. Figure 1 shows an example of the cathode assembly.

Anode Preparation. A slurry was made up of a thermal coal char intimately mixed with a ternary alkali metal carbonate eutectic, that is,

Figure 1. Cathode electrode with a silver wire current collector wrapped around the periphery.

Li_2CO_3, Na_2CO_3, and K_2CO_3 (43.5: 31.5:25 mol %, respectively),[18] which made up the fuel and secondary electrolyte, respectively. Preparation of the coal char involved pyrolyzing a thermal coal by heating to 800 °C at 5 °C/min then holding isothermally for 2 h, all under N_2 in a tube furnace. The eutectic was prepared from dry reagents of the individual carbonates, which were thermally fused at 600 °C for 2 h before being ball milled. Further details of both the coal char[19] and eutectic[20] preparation have been reported in previous studies.

A 1:1 mixture of coal char and eutectic was weighed out and ball milled from dry reagents to ensure thorough mixing. Approximately 3 g of slurry was inserted into the 8YSZ tube, and a silver coil was used as the anode current collector. When using a solid graphite rod (Sigma-Aldrich), the unmodified eutectic was employed without a coal char mixed in, and the silver coil was replaced with a silver wire connected atop the graphite rod without touching the eutectic. All current and power density values were normalized with respect to the anode current collector, that is, 3.4 and 3.6 cm² for the silver coil and the graphite rod, respectively. As with cathode fabrication, care was taken to ensure that the anode preparation was consistent between experiments.

Cell Arrangement. The tubular electrode was positioned in the center of an alumina crucible (outer diameter = 84 mm; height = 60 mm) and held in place using a base plate with a hole (diameter = 17 mm) purposely positioned to accommodate the electrode. An air gas line was fed into the cathode chamber from below through another hole in the base plate, and a second gas line was positioned atop the electrode feeding directly into the anode compartment. Either CO_2 or N_2 was passed through the anode gas line depending on the individual experiment, and the flow rate for all gases was held at 40 mL/min. Electrical connections to the potentiostat (Solartron SI 1287 Electrochemical Interface) were made outside the rear of furnace, and a two-electrode setup was employed. Figure 2 shows the cell arrangement.
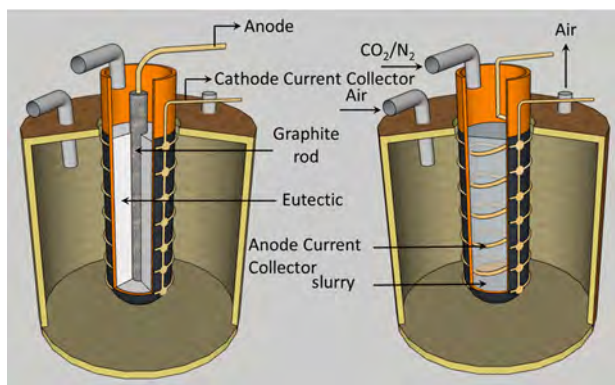
Figure 2. Schematic of the test cell.

Electrochemical Test Protocol. The open circuit potential (OCP) was measured as the cell was heated from ambient temperature to the desired operational temperature (700−860 °C) at ~3 °C/min. Once the operational temperature was reached, the potential was swept from the open circuit potential (0.8−1.1 V) to the short circuit potential (0.0 V) at 5 mV/s. Chronologically, the linear sweep voltammograms (LSVs) were measured in ascending temperature order, that is, 700 °C initially, then 800 °C, and lastly 860 °C. A 10 min isothermal period was allowed at each temperature prior to measuring a voltammogram to allow to the sample and control temperatures to equilibrate.

RESULTS

Gasification Characteristics. *TGA Response for Unmodified Coal Char.* Examining the gasification characteristics of the anode chamber gives an indication of the types of

chemical reactions that can take place under open circuit conditions. It is useful to gain an understanding of the system in a simplified context before introducing the electrochemical reactions that can occur under closed circuit conditions as is the case during voltammetry. The unmodified coal char was analyzed by TGA in order to quantify the amount of gas released und CO_2 compared with N_2.

Figure 3 demonstrates a distinct contrast in the mass loss profiles of the coal char under CO_2 versus N_2. The
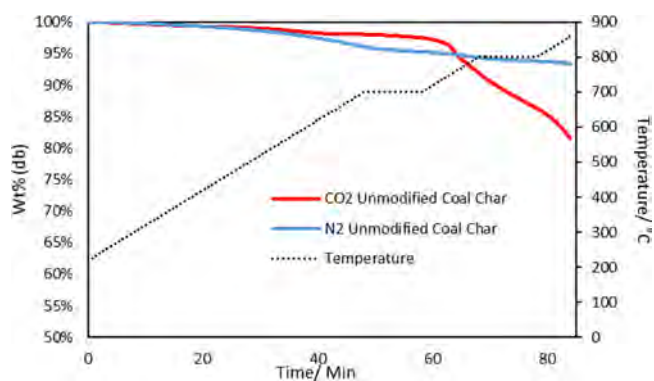
Figure 3. TGA of coal char heated to 860 °C under CO_2 and N_2 in separate experiments.

thermodynamic limit for reverse Boudouard gasification (eq 5) is just below 700 °C,[21] which is why a sudden mass loss (18 wt %) occurs under CO_2 at that temperature. This is noticeably different to the behavior under N_2, which shows a gradual mass loss with temperature (7 wt %) that can be attributed to volatilization. Despite being pyrolyzed at 800 °C, the char can undergo continued volatilization due to a diffusion limitation, which inhibits the pyrolysis kinetics.[19,22]

TGA Response for Slurries. Figure 4 compares the TGA results of the coal char slurry with the eutectic (1:1 ratio)
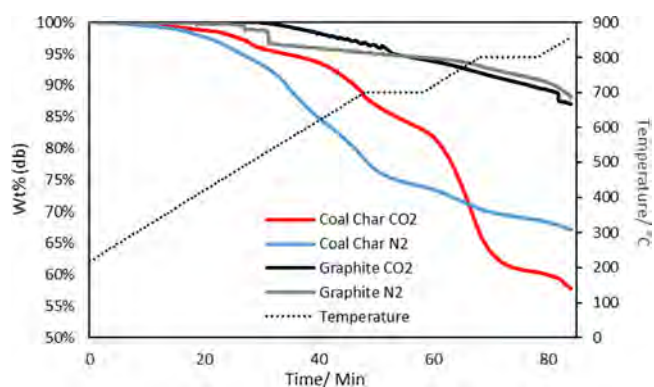
Figure 4. TGA of a 50/50 wt % coal char/ternary eutectic slurry and a 50/50 wt % graphite/ternary eutectic slurry heated to 860 °C under CO_2 and N_2 in separate experiments.

compared to a graphite slurry (1:1 ratio) under both CO_2 and N_2 and shows that the mass loss is significantly greater for coal char compared to graphite, that is, 35−42 wt % versus 9−10 wt %, respectively. This is because graphite is a much more stable form of carbon and is therefore less reactive than coal char, which is essentially amorphous.[23,24]

Now examining the coal char slurries, Figure 4 shows that reverse Boudouard gasification (eq 5) is taking place in the

coal char slurry under CO_2, as evidenced by the sharp mass loss above 700 °C. Below 700 °C, some portion of the mass loss can be attributed to volatilization, as seen in Figure 3; however, there is also a difference of ~10 wt % between the slurry and the unmodified coal char, indicating that the carbonate is playing a role in the mass loss processes. This difference can be attributed to a combination of carbonate decomposition (eq 7) and gasification from carbonate,[25] that is

$$CO_3^{2-} + C \leftrightarrow 2CO + O^{2-} \tag{8}$$

This is a comproportionation reaction because C^{4+} in carbonate reacts with C^0 in carbon to produce $2C^{2+}$ in the form of CO gas, which is evolved. Under N_2, it is evident that the sharp mass loss at 700 °C is absent (Figure 4), thus proving that reverse Boudouard gasification (eq 5) only occurs under CO_2 above ~700 °C. Unlike the reverse Boudouard process, gasification from carbonate (eq 8) does not depend upon gaseous CO_2 diffusing into the slurry. Further, carbonate decomposition (eq 7) has been shown to be more significant under inert gas atmospheres compared to carbon dioxide gas in molten carbonate salts at low temperatures.[12] This is why, at low temperatures, the mass loss under N_2 is greater, compared to higher temperatures (>800 °C) when CO_2 diffusion no longer dictates the reverse Boudouard gasification kinetics.

Comparing the total mass loss under CO_2 to N_2 for the coal char slurry (Figure 4), that is, 42 wt % versus 33 wt %, respectively, it is evident that the difference is not substantial. However, the total amount of gas evolved would be ~6-fold greater under CO_2, which is calculable from the reaction stoichiometry.

Electrochemical Analysis. *Varying the Overhead Gas in a Slurry Arrangement.* The OCP was recorded as the cell was heated at 3 °C/min from the point where the carbonate became molten to the operational temperature (400−700 °C). Figure 5 compares the OCP under CO_2 versus N_2 for the
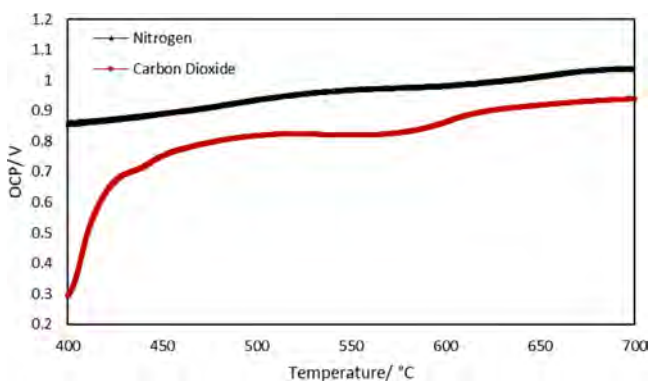
Figure 5. Open circuit potential versus temperature for a slurry arrangement under CO_2 compared with N_2.

slurry configuration. This figure shows that the OCP was higher under N_2 compared with CO_2, which is consistent with the previous findings.[6,13,14] This can be deduced directly from the Nernst equation for this system because CO_2 is the product of the overall electrochemical reaction.[6] Another reason for this may be due to gas adsorption on the current collector, which alters the surface potential.[26] The solubility of CO_2 in molten carbonate is $(9.5 \pm 1.0) \times 10^{-2}$ mol L^{-1} atm^{-1},[27] and this value would increase at lower temperatures.

Voltammetry. While the DCFC is operating under closed circuit conditions, both chemical (eqs 5 and 8) and electrochemical reactions (eqs 2, 3, and 6) can take place. Linear sweep voltammetry was used to measure the electrochemical performance of the cells, and the maximum power density was calculated from i−V data. Figure 6 compares a slurry arrangement under CO_2 and N_2 in separate experiments to determine the impact of the anode sweep gas on performance.

This figure shows that the power density is higher under CO_2 compared to N_2 at elevated temperatures (800−860 °C). The OCP was found to be 0.01−0.03 V higher under N_2 over the range of 700−860 °C, respectively; however, the peak power potential was virtually unaffected when the overhead gas was changed, that is, 0.57 ± 0.01 V versus 0.58 ± 0.02 V for CO_2 and N_2, respectively. A higher peak power potential translates to an enhanced efficiency, because less energy is lost through resistive heating (eq 4), which is a parasitic process.

Figure 7a examines the relationship between peak power and operational temperature. From this figure, it can be seen that, at 700 °C, the peak power under N_2 is slightly higher than under CO_2, that is, 1.1 mW/cm^2 versus 2.1 mW/cm^2 for CO_2 and N_2, respectively. At 800 °C, the trend is reversed as the performance under CO_2 exceeds that under N_2, that is, 8.0 mW/cm^2 versus 4.7 mW/cm^2. As the temperature increased to 860 °C, this trend was enhanced as the gap widened, that is, 18.4 mW/cm^2 versus 8.6 mW/cm^2 for CO_2 and N_2, respectively, which is almost a 2-fold difference in the opposite direction.

Reverse Boudouard gasification can take place under CO_2 atmosphere (eq 5), leading to the formation of CO gas bubbles. These gas bubbles may agitate the slurry in an otherwise quiescent system, thus facilitating mass transport of the coal char particulates to the current collector. The thermodynamic temperature limit for the reverse Boudouard gasification is 665 °C,[21] and the Gibbs free energy reduces significantly with temperature.[28] Both the rate of bubble formation and the bubble size are expected to increase with temperature, which can explain the heightened temperature sensitivity when operating under CO_2. These results therefore suggest that the low temperature (700 °C) performance is limited by mass transport in the anode compartment. Deleebeeck et al.[6] showed that the polarization resistance (R_p) decreased under CO_2 using electrochemical impedance spectroscopy (EIS), thus also hinting at a mass transport limitation on the anode side.

Comparing a Slurry Arrangement to a Solid Anode. In order to test this hypothesis, the experiments were replicated using a solid graphite working electrode, which replaced the coal char in the slurry (Figure 7b). The solid graphite rod served as both the fuel and the current collector, thus eliminating the system dependency on mass transport of carbon to the anode current collector.

Figure 7b shows that the performance under CO_2 exceeds that under N_2 over the entire temperature domain investigated (700−860 °C). Furthermore, the relative difference in performance did not fluctuate appreciably as the temperature increased. This is because mass transport is not required for a solid anode arrangement.

Flowing N_2 over the cell effectively removes CO_2 produced from electro-oxidation (eq 2) before it has a chance to react chemically with carbon to form CO (eq 5). The chemically generated CO can then react electrochemically to form CO_2
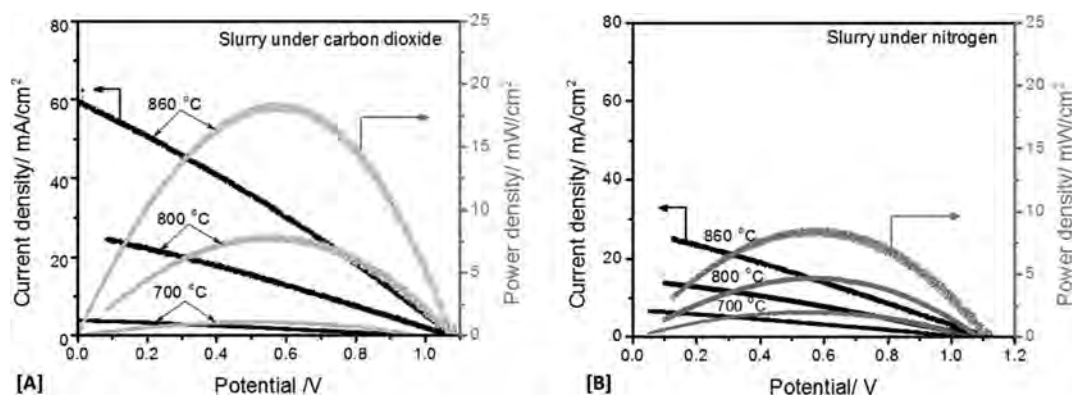
Figure 6. Current density (mA/cm^2) and power density (mW/cm^2) versus potential (V) for slurry arrangements under (A) CO$_2$ and (B) N$_2$ between 700 and 860 °C.
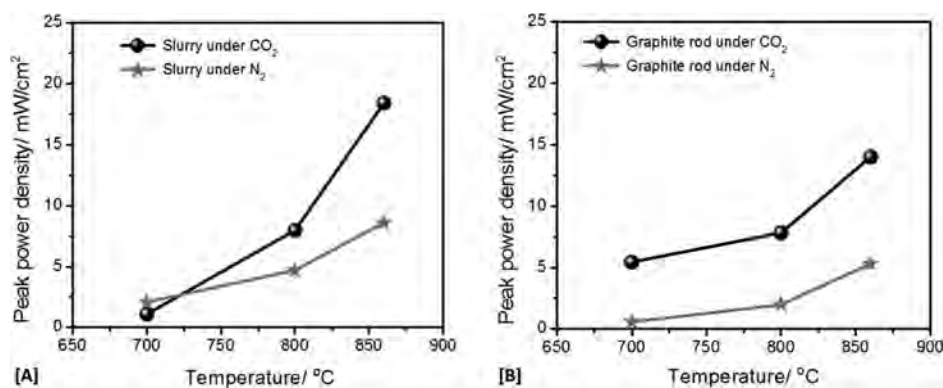
Figure 7. Peak power density (mW/cm^2) versus temperature (°C) for (A) a slurry arrangement and (B) a solid anode arrangement under CO$_2$ compared to N$_2$.
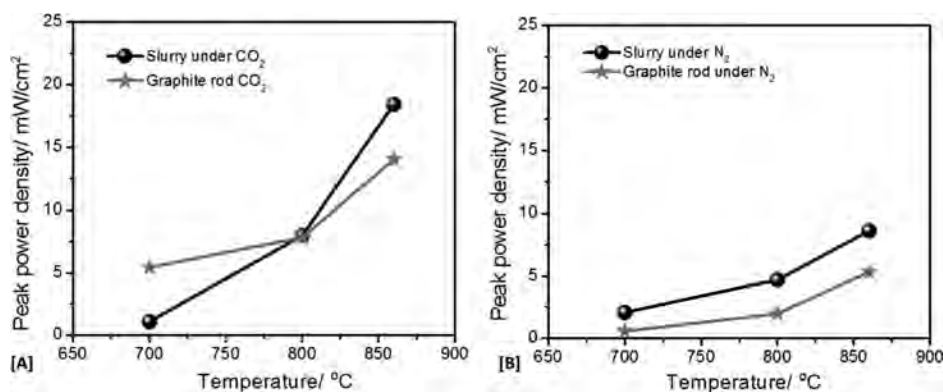
Figure 8. Peak power density (mW/cm^2) versus temperature (°C) for a slurry compared to a solid anode arrangement under (A) CO$_2$ and (B) N$_2$.

via two-electron oxidation (eq 6). In this way, CO supplies another form of fuel in addition to carbon, which contributes to the overall performance.

Figure 8a compares the slurry arrangement to the solid anode when operating under CO$_2$. This figure shows that, at low temperatures (700 °C), the solid anode performs better than the slurry; however, at intermediate temperatures (800 °C), the performance is approximately equivalent, and at high temperatures (860 °C), the trend is reversed, as slurry outperforms the solid anode. Previous studies have shown that the electro-oxidative activity of coal char is higher than graphite due to the amorphous nature of the char.[19,22] At 700 °C, mass transport limits the performance of the slurry arrangement; however, at higher temperatures (800−860 °C),

mass transport is no longer the limiting factor, because the system becomes activation-limited. Under activation-limited conditions, the performance discrepancy can be attributed to intrinsic differences between the graphite and coal char fuels and possibly the higher interfacial surface area of small carbon particulates in contact with the current collector.

Figure 8b shows that the slurry arrangement performs better than the solid anode under N$_2$. The opposite results might have been predicted given that mass transport is expected to be severely limited under N$_2$. The best explanation for this result can be attributed to intrinsic differences in the electro-oxidative activity between the coal char and graphite, where the coal char is the more electrochemically active material.[22]

■ DISCUSSION

Clearly, the effects of the reverse Boudouard reaction are enhancing the performance of the slurry arrangement at higher temperatures when the system is under CO_2. There are two ways in which gasification can enhance the performance, that is, agitating the fuel particles, which facilitates mass transport, or generating CO, which can act as a fuel itself by undergoing two-electron oxidation to CO_2 (eq 6). It is also possible that the results displayed here are due to a combination of both phenomena taking place.

The kinetics of two-electron oxidation from CO (eq 6) are more facile than four-electron oxidation from carbon (eq 2),[11,29] because CO is a gaseous fuel, which can both diffuse and react much faster than solid carbon. Therefore, as long as the reaction rate is over double that of the four-electron process, the power output of the cell will be greater. The trade-off is that the energy efficiency is only half that of the four-electron reaction at best, with additional losses coming from CO, which escapes without reacting further.

Therefore, the decision upon which reaction pathway to emphasize comes down to a question of whether efficiency or power is the main goal. For maximum efficiency, operating under a non-CO_2 atmosphere at temperatures below 700 °C prevents reverse Boudouard gasification. However, gasification form carbonate can still occur below 700 °C (eq 8). Hence, the only way to deactivate gasification and ensure that only four-electron oxidation takes place is to remove carbonate from the system. Gasification consumes the carbon fuel without generating a current, and it is therefore a parasitic process that lowers the overall carbon utilization efficiency.

To prevent diffusion limitations, a solid working anode can be used instead of a slurry. However, while the solid anode arrangement appears to offer an enhanced performance on the laboratory scale, there are logistical advantages to using a slurry when upscaling to a pilot scale module, such as supplying the fuel and enabling a continuously operating system. Therefore, to prevent a diffusion limitation when using a slurry arrangement, the anode compartment can be agitated using an impeller or a sparge gas, in which case the cell becomes activation limited. However, operating below 700 °C drastically inhibits the kinetics of both carbon oxidation at the anode (eq 2) and oxygen reduction at the cathode (eq 3). This means that, while efficiency is optimized, the power output will inevitably be poor.

Conversely, to optimize the power output, operating above 800 °C under a CO_2 atmosphere is clearly preferable. The efficiency losses due to the two-electron oxidation pathway must be accepted; however, the CO that escapes out of the cell can be utilized by implementing a direct carbon fuel cell/solid oxide fuel cell (DCFC-SOFC) hybrid design. This can be achieved by passing the flue gas coming out of the anode chamber across an oxygen reduction cathode, which electrochemically converts CO to CO_2, such as a long narrow YSZ tube with an oxygen reduction catalyst on the outside, in which case hot air (>800 °C) flows over the tube through a plenum. This is also referred to as an integrated gasification fuel cell system,[11] where the DCFC anode compartment also acts as a reformer supplying fuel for the SOFC.

When assessing the potential of the DCFC to replace the CFPS, it is important to differentiate the concepts of energy from the power and thermodynamic efficiency from the overall efficiency. CFPS has a low thermodynamic efficiency but a very high power output due to the facile kinetics of the combustion reaction; therefore, the overall efficiency is still positive. By contrast, the DCFC has a very high thermodynamic efficiency; however, the power output is less due to the slow kinetics of the redox reactions at the electrodes.

The key to making the DCFC economically viable is producing enough power to sustain the operational temperature without the required external heat input, that is, autogenous operation. Therefore, even if the carbon utilization efficiency is maximized, the energy balance can never be positive unless the power output exceeds the heating requirements. Improving both the power output and heating efficiency are two critical research areas that can pave the way to mass adoption of the DCFC.

■ SUMMARY AND CONCLUSIONS

The following are key points arising from this work:

(i) Operating the anode compartment under CO_2 gives rise to a higher power density than N_2 when using a slurry arrangement above 700 °C;

(ii) Without proper means of agitation, mass transport of the particulate fuel to the current collector in the anode compartment appears to be the rate-limiting factor dictating the performance for slurry arrangements;

(iii) Solid working anodes perform better than slurry arrangements when mass transport is the rate-limiting factor;

(iv) Two-electron oxidation from CO to CO_2 can significantly improve the power output at the cost of reducing the carbon utilization efficiency;

(v) To optimize the carbon utilization efficiency, operating below 700 °C in the absence of carbonate is recommended; and

(vi) For a maximum power, operate above 700 °C under CO_2, with a carbonate secondary electrolyte, and pass the CO containing flue gas over an oxygen reduction cathode.

■ AUTHOR INFORMATION

Corresponding Author
*E-mail: scott.donne@newcastle.edu.au.

ORCID ⓘ
Scott W. Donne: 0000-0001-9389-7870

Author Contributions
The manuscript was written through contributions of all authors. All authors have given approval to the final version of the manuscript.

Notes
The authors declare no competing financial interest.

■ REFERENCES

(1) Pearse, G.; Burton, B.; McKnight, D. *Big Coal: Australia's Dirtiest Habit.* 2013: NewSouth.

(2) Ezeh, A. C.; Bongaarts, J.; Mberu, B. Global population trends and policy options. *Lancet* **2012**, *380*, 142−148.

(3) Jiang, C.; et al. Hybrid direct carbon fuel cells with different types of mineral coal. *ECS Trans.* **2013**, *57*, 3013−3021.

(4) Campanari, S.; Gazzani, M.; Romano, M. C. Analysis of direct carbon fuel cell based coal fired power cycles with CO2 Capture. *J. Eng. Gas Turbines Power* **2013**, *135*, No. 011701.

(5) Bugge, J.; Kjær, S.; Blum, R. High-efficiency coal-fired power plants development and perspectives. *Energy* **2006**, *31*, 1437−1445.

(6) Deleebeeck, L.; Hansen, K. K. HDCFC performance as a function of anode atmosphere (N2-CO2). *J. Electrochem. Soc.* **2013**, *161*, F33−F46.

(7) Jiang, C.; et al. Challenges in developing direct carbon fuel cells. *Chem. Soc. Rev.* **2017**, *46*, 2889−2912.

(8) Zhao, M.; et al. Performance characteristics of a direct carbon fuel cell/thermoelectric generator hybrid system. *Energy Convers. Manage.* **2015**, *89*, 683−689.

(9) Rady, A. C.; et al. Review of Fuels for Direct Carbon Fuel Cells. *Energy Fuels* **2012**, *26*, 1471−1488.

(10) Nabae, Y.; Pointon, K. D.; Irvine, J. T. S. Electrochemical oxidation of solid carbon in hybrid DCFC with solid oxide and molten carbonate binary electrolyte. *Energy Environ. Sci.* **2008**, *1*, 148−155.

(11) Cao, T.; et al. Recent advances in high-temperature carbon−air fuel cells. *Energy Environ. Sci.* **2017**, *10*, 460−490.

(12) Olivares, R. I.; Chen, C.; Wright, S. The Thermal Stability of Molten Lithium-Sodium-Potassium Carbonate and the Influence of Additives on the Melting Point. *J. Sol. Energy Eng.* **2012**, *134*, 041002.

(13) Elleuch, A.; et al. Electrochemical oxidation of graphite in an intermediate temperature direct carbon fuel cell based on two-phases electrolyte. *Int. J. Hydrogen Energy* **2013**, *38*, 8514−8523.

(14) Jiang, C. R.; et al. Demonstration of high power, direct conversion of waste-derived carbon in a hybrid direct carbon fuel cell. *Energy Environ. Sci.* **2012**, *5*, 6973−6980.

(15) Xu, X.; et al.. Optimization of a direct carbon fuel cell for operation below 700 C. international journal of hydrogen energy, 2013. *38*(13): p. 5367−5374, DOI: 10.1016/j.ijhydene.2013.02.066.

(16) Li, X.; et al. Factors That Determine the Performance of Carbon Fuels in the Direct Carbon Fuel Cell. *Ind. Eng. Chem. Res.* **2008**, *47*, 9670−9677.

(17) Irfan, M. F.; Usman, M. R.; Kusakabe, K. Coal gasification in CO 2 atmosphere and its kinetics since 1948: a brief review. *Energy* **2011**, *36*, 12−40.

(18) Janz, G. J.; Lorenz, M. R. Solid-Liquid Phase Equilibria for Mixtures of Lithium, Sodium, and Potassium Carbonates. *J. Chem. Eng. Data* **1961**, *6*, 321−323.

(19) Allen, J.; Glenn, M.; Donne, S. The effect of coal type and pyrolysis temperature on the electrochemical activity of coal at a solid carbon anode in molten carbonate media. *J. Power Sources* **2015**, *279*, 384−393.

(20) Glenn, M. J.; Allen, J. A.; Donne, S. W. Thermal Investigation of a Doped Alkali Metal Carbonate Ternary Eutectic for Direct Carbon Fuel Cell Applications. *Energy Fuels* **2015**, *29*, 5423.

(21) Giddey, S.; et al. A comprehensive review of direct carbon fuel cell technology. *Prog. Energy Combust. Sci.* **2012**, *38*, 360−399.

(22) Allen, J. A.; et al. An investigation of mineral distribution in coking and thermal coal chars as fuels for the direct carbon fuel cell. *Fuel* **2018**, *217*, 11−20.

(23) McNaught, A.; Wilkinson, A.; IUPAC. *Compendium of chemical terminology ("gold book")*, 2nd ed. Blackwell Scientific Publications, Oxford. XML on-line corrected version created by Nic M, Jirat J, Kosata B, 1997.

(24) Thrower, P. A. *Chemistry & Physics of Carbon*. Vol. 25. 1996: CRC Press.

(25) Nagase, K.; et al. Kinetics and mechanisms of the reverse Boudouard reaction over metal carbonates in connection with the reactions of solid carbon with the metal carbonates. *Phys. Chem. Chem. Phys.* **1999**, *1*, 5659−5664.

(26) Chen, C. C.; et al. Wetting Behavior of Carbon in Molten Carbonate. *J. Electrochem. Soc.* **2012**, *159*, D597−D604.

(27) Claes, P.; Moyaux, D.; Peeters, D. Solubility and solvation of carbon dioxide in the molten Li2CO3/Na2CO3/K2CO3 (43.5 : 31.5 : 25.0 mol-%) eutectic mixture at 973 K I. Experimental part. *Eur. J. Inorg. Chem.* **1999**, *1999*, 583−588.

(28) Glenn, M. J.; Allen, J. A.; Donne, M. M. Carbon Electro-Catalysis in the Direct Carbon Fuel Cell Utilising Alkali Metal Molten Carbonates: A Mechanistic Review. *J. Power Sources*, **2019**, in press.

(29) Nürnberger, S.; et al. Direct carbon conversion in a SOFC-system with a non-porous anode. *Energy Environ. Sci.* **2010**, *3*, 150−153.
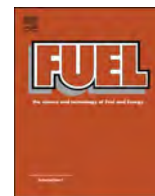
Full Length Article

An investigation of mineral distribution in coking and thermal coal chars as fuels for the direct carbon fuel cell

Jessica A. Allen[a,*], Michael Glenn[b], Priyanthi Hapugoda[c], Rohan Stanger[a], Graham O'Brien[c], Scott W. Donne[b]

[a] University of Newcastle, Discipline of Chemical Engineering, Priority Research Centre for Frontier Energy Technology and Utilisation, University Drive, Callaghan 2308, Australia
[b] University of Newcastle, Discipline of Chemistry, University Drive, Callaghan 2308, Australia
[c] QCAT CSIRO, Pullenvale 4069, Australia

ARTICLE INFO

ABSTRACT

For the first time, a combination of coal grain analysis (CGA) and mineral liberation analysis (MLA) has been applied to coal chars prepared at different pyrolysis temperatures. Information collected from these powerful techniques is used here to assess electrochemical activity of coal chars in a solid anode of the direct carbon fuel cell. Mineral distribution and consideration of particle size gives very useful information in terms of showing differences between chars of differing origin, although major differences in mineral distribution between pyrolysis HHT are not observed here. As a result of this analysis, it is proposed that electrochemical performance of coal chars at solid anodes in molten carbonate appear to be dependent on several, interlinked factors. The physical properties of the char including its porosity, resistivity, surface area and crystalline structure have previously been demonstrated to affect electrochemical oxidation of carbons, and these factors are also observed to be important here. Further, however, the prevalence, size and type of mineral matter in the coal char and its contact with char particles also is suggested to play an equally important role. The mechanism of this interaction may include alteration of previously observed sensitivities, such as mineral enhanced gasification of the coal char leading to carbon morphology changes. Additional influences of mineral matter are suggested here to include modification of surface polarity and subsequent contact between carbon and molten carbonate electrolyte (effectively enhancing surface area), or the ability of mineral components to act as a shuttle for active species.

1. Introduction

Coal remains a critical commodity globally, and coal fired power stations (CFPS) supply the majority of electrical energy demands to many nations, including Australia, China and the US [1]. The efficiency of CFPSs however are highly limited due to the energy transformations which occur. The most efficient CFPS currently are those using supercritical steam conditions and are able to achieve an efficiency of ~40%. This efficiency limitation is true for all fossil fuels used to extract energy through combustion methods. Fuels cells offer an alternative energy transformation pathway where chemical energy is transformed directly to electrical energy through electrochemical pathways. The direct carbon fuel cell (DCFC) has been developed in order to extend the application of fuel cells beyond gaseous fuels to include solid carbon fuels, such as coal. This technology has a theoretical efficiency of 100%, although more realistic estimates of efficiency specify values in the range of 60–80%, which is heavily dependent on cell arrangement and fuel used [2,3].

The DCFC has several existing technical challenges to overcome before commercialisation can be realised. Many of these issues are related to practical arrangement and operation of a DCFC cell, including allowance for possible parasitic reactions which may occur for particular arrangements (i.e., reverse Boudouard gasification) [4]. The most critical challenge for progress in the DCFC however is likely to be the slower kinetics observed for the electro-oxidation of carbon fuels (relative to combustion in air). This behaviour limits the overall performance of the DCFC and mechanisms underpinning this behaviour are poorly understood. It has, however, been shown that catalysts can be successfully integrated with a solid fuel to enhance electrochemical performance significantly [5]. In particular, naturally occurring clays in raw coal materials, such as kaolinite, have been shown to activate performance of graphite by up to 50% [5]. Quartz, also often present in

high concentrations in some coals, has shown the opposite effect, inhibiting electrochemical activity [5–7].

The importance of surface oxygen-functional groups has also been emphasised for coal chars, which has been seen to change as a function of pyrolysis highest heating temperature (HHT) [8,9]. The importance of surface area, porosity, carbon structure and surface functionalisation on the electrochemical performance of carbon materials has further been established in the literature when assessing slurry-type systems [7,9–12]. These studies generally use pure carbon materials which are not fossil fuel or biomass derived and therefore have no mineral component. In a particulate carbon arrangement, ash-free carbons have been shown to have high activity when they have a high mesoporous surface area and a high O/C ratio, these characteristics altered through acid and base washing treatments of activated carbons [10,12]. The importance of bulk lattice disorder and electrical conductivity of carbon fuels was also demonstrated early on by Cherepy et al. [11] and the importance of fuel conductivity has also been investigated in solid carbon anode arrangements subsequently [13,14].

It was found in a previous investigation that the thermal pre-treatment of raw coal effects the resultant coal char electrochemical activity. Assessment of physical properties of chars, including resistivity, BET surface area and chemical activity towards oxidation (reflective of surface functional groups) showed that although these important properties do clearly play a role in the activity of coal char, another variable also appears to impact on the activation of the char [13]. It was suggested that the inorganic minerals present and their distribution within the coal chars was instead causing kinetic activation, which was pyrolysis temperature dependant. Certainly the role of coal mineral constituents has been investigated when using coal chars in the DCFC, for example in the work of Tulloch et al. [5] as well as Li et al. [6]. Further, the role of metallic species present in the coal in the gasification process for a gas-fed DCFC has also been investigated [15]. It is clear that some species have catalytic roles in the electrochemical oxidation reaction while some appear to inhibit or, alternatively, indirectly effect electrochemical performance through impacting on the chemical conversion of the carbon to gaseous fuel carbon monoxide. These studies have generally not considered the link between the different types of char which are formed from different coals and the impact that the proportion of these catalytic species in different minerals, or the size of these minerals in the resultant char, may have on char electrochemistry.

In this work, previously studied coal chars [13] have been further analysed using advanced characterisation techniques including mineral liberation analysis (MLA) and coal grain analysis (CGA) to determine if indeed the mineral content plays a critical electrochemical role on the coal char used. One active and one inactive coal char of each parent coal was investigated and results are presented here. Kaolin doped electrodes have also been investigated to determine interfacial effects on observed kinetics.

CGA is a technique which has been developed by the Commonwealth Scientific and Industrial Research Organisation (CSIRO, Australia) to identify maceral components in coal particles using optical imaging [16,17]. The technique can also be applied to coal chars to determine the 'type' of char according to a standard identification system developed by Benfell et al. [18]. Investigation of coal chars as opposed to raw coal macerals is a very new application of CGA analysis under development, having only recently been applied to chars produced using an entrained flow gasifier [19]. This technique is made more powerful through integration of MLA data where the coal char is formed into a solid block and the same block is analysed in both CGA and MLA analysis. MLA uses a scanning electron microscope (SEM) and energy dispersive spectroscopy (EDS) X-ray analysis to complete an automated scan of a set area and identify mineral components present. The MLA software also identifies particle size and prevalence and gives quantitative information about mineral matter present in coal chars. Through manual analysis, MLA and CGA images

can be matched to give qualitative information about the integration of carbonaceous and inorganic mineral matter [17]. Although this technique is normally applied to raw coals [16], it is also highly relevant in the investigation of coal chars since it has been proposed that the distribution and type of mineral matter present in the coal char is likely to be of high importance in determining electrochemical activity in the direct carbon fuel cell [13].

2. Material and methods

2.1. Coal preparation and electrochemistry

Detailed information regarding preparation of coal char and testing of char in a half-cell assembly has been presented in previous work [13]. Chars were produced from raw coals by firstly ball milling the raw coal to reduce particle size, then sieving to a size of less than 45 μm in an iterative process until all raw coal was in the correct size range. Chars are produced by slow pyrolysis (heating rate 6–10 °C/min) under constant nitrogen flow (100 mL/min). Chars were held at the pyrolysis higher heating temperature (HHT) for 4 h before cooling to room temperature and gently separating particles with a mortar and pestle. Chars are identified here by their raw parent coal char type (Coking – C and thermal – T) as well as the HHT to which they were taken.

Working electrodes were produced by mixing 25 wt% of coal chars with graphite (SFG44, Timrex Switzerland) and compressing to form a pellet which was fixed in an alumina tube. Graphite working and counter electrodes were used within a pre-fused molten carbonate ternary eutectic of Li_2CO_3, K_2CO_3 and Na_2CO_3 which was also ball milled to ensure homogenisation prior to initial fusing. A carbon dioxide gas environment was used to form a stable and reproducible reference system (see Ref [5] for full details).

Kaolinite catalyst added was procured from Sigma Aldrich and dried under air at 110 °C before sieving to a particle size less than 32 μm. For the coal mixed electrode, the catalyst was firstly mixed with the char (mortar and pestle) and then the homogenous catalyst/char mixture was combined with graphite prior to pressing into an electrode. A distributed kaolinite electrode was made using graphite and sieved kaolinite via mixing with a mortar and pestle. A bulk kaolinite electrode was made by pressing kaolin into a solid disc and then cutting the solid disc into a square. The kaolin chunk was then placed at the bottom of the die press with graphite power loaded over the top before pressing into an electrode where the kaolinite chunk was exposed on one side. Electrode pellets were fixed to an alumina tube and tested as working electrodes.

Electrochemical experiments were carried out after heating the cell assembly containing pre-fused carbonate eutectic to the reaction temperature. Electrodes were held in the assembly under carbon dioxide flow until the eutectic became molten (less than 400 °C), after which they were inserted into the carbonate fluid. The system was allowed to equilibrate at open circuit for at least 10 min before carrying out linear sweep voltammetry scans from the open circuit potential to 0.5 V versus the reference, conducted at 5 mV/s.

2.2. Advanced analysis techniques

Two techniques were used to characterise the carbon and mineral compositions of the char samples on a particle basis. The CSIRO developed coal grain analysis (CGA) technique and the automated SEM-based MLA technique.

The optical reflected light imaging and analysis system, Coal Grain Analysis (CGA) developed in CSIRO provides reflectance and composition information on individual coal particles using a Zeiss Axio Imager reflected light microscope coupled with Coal Characterisation Imaging System (CCIS) software. This software was also developed by the CSIRO. This system was used to collect high resolution (1 pixel = 1 μm) colour images with the objective to determine the particle composition

and size information for the char samples analysed.

The Mineral Liberation Analyser (MLA) is a scanning electron microscope (SEM) based system built with computer software that automates microscope operation and data acquisition for automated mineralogy. This provides various quantitative data sets including modal mineralogy, porosity, grain size and shape, mineral associations and digital textural maps that are collected on polished surfaces of rocks. Part of the novelty of this work is in applying the MLA technique to thermally pre-heated samples, where the minerals may not be present in their original form.

Petrographic samples were prepared using representative samples mixed with resin, and then cut and polished to create the surface used for the analysis. The optical images were collected for the char samples for the mineral characterization work (CGA). Following CGA, these samples were carbon coated and contiguous SEM images were collected over the same area using the MLA (Mineral Liberation Analyser) scanning electron microscope system located at the JKMRC (Brisbane, Australia). This enabled the same particles to be matched from both image sets and hence allowed the mineral particles in the optical images to be accurately identified

For the optical image, the individual coal particles are higher reflecting than the mounting resin giving information about the whole char particle without identification of mineral matter, while MLA images provide detail on the minerals in the sample while being unable to provide detail on the coal (or char) particles. The techniques are therefore highly complementary and an example of a matched segment using each technique for CC-700 char is shown in Fig. 1.

It can be seen in Fig. 1 that often minerals which are easy to observe using MLA are often more difficult to discern from CGA output, including kaolinite (B) and quartz (A).

Table 1
Coal Char Properties [13]

COAL CHAR	CC-700	CC-900	CT-700	CT-800
C/wt% (db)	79.8	83.2	64.7	65.5
H/wt% (db)	2.40	1.43	1.03	0.54
N/wt% (db)	1.76	1.22	1.39	1.29
S/wt% (db)	0.22	0.09	0.21	0.24
O/wt% (db)	4.78	2.55	4.16	3.41
Ash/wt% (db)	11.1	11.6	28.6	29.0
Pyrolysis Yield (db)/wt%	80.8	77.9	76.5	76.5
Resistivity/ mΩ.cm^{-1}	2271	2	267	31
BET SA/m^2. g^{-1}	69	37	96	98
Average Current Density at 0.1 V vs C/ CO_2/CO_3^{2-}/ mA cm^{-2}	15.35 ± 2.73	4.15 ± 0.93	5.02 ± 2.75	14.64 ± 4.16

3. Results

3.1. Coal physical and electrochemical properties

Results found previously for coal chars investigated here are presented in Table 1.

These chars were selected for further analysis due to differences in electrochemical performance and are of different origin with different pre-treatments carried out (presented in detail in [13]). For ashless carbon sources, it has been shown clearly that electrochemical activity in slurry-type arrangements can be linked to carbon functionalisation and BET surface area [9–12]. It can be seen in Table 1 that there is no clear dependence on these simplified properties in the case of coal chars investigated here. In particular, the thermal coal used shows a substantial difference in electrochemical performance between 700 and 800 °C HHT despite little to no change in chemical composition or BET surface area resulting from pyrolysis conditions. Since the only major change appeared to be in the electrical resistance of these chars, it could be suggested that electrical conductivity is key to performance in a solid electrode, such as those used in this work, as might be expected for an electrochemical reaction involving the transfer of electrons through the carbon material, which also acts as the current collector in a solid electrode. However, CT-700 has a 10-fold lower resistance than CC-700 and yet this coal char demonstrated improved electrochemical performance at the same polarisation as other chars investigated. Potentially, electrical conductivity could vary differently with temperature for these chars, however this is expected to be a relatively small change. It was therefore thought that electrochemical observations may be explained through differences in the mineral component of the coal chars investigated, in particular, the particle size of the char. Mineral content and specific identification of mineral components were concluded to be key to determining electrochemical activity. A mixture of CGA/MLA analysis techniques were used in order to investigate this further.

3.2. Char particle size and classification

3.2.1. Particle size

Raw coals were prepared via ball-milling and sieving to less than 45 μm as outlined in [13] and Section 2.1. However, once the initial raw coal was sieved, it was then pyrolysed and used with no further treatment other than gentle separation of particles with a mortar and pestle. Char particle size was therefore measured using CCIS software to give a realistic reflection of the final char size used in electrochemical investigations, also reflective of the samples analysed for mineral distributions. Results for each coal type and HHT are shown in Fig. 2[A].

It can be seen in Fig. 2[A] that particle size of chars do not match

Fig. 1. Output image set for CC-700 of [A] CGA Optical Analysis and [B] SEM based MLA characterisation where (A)-(E) denote specific matched particles.
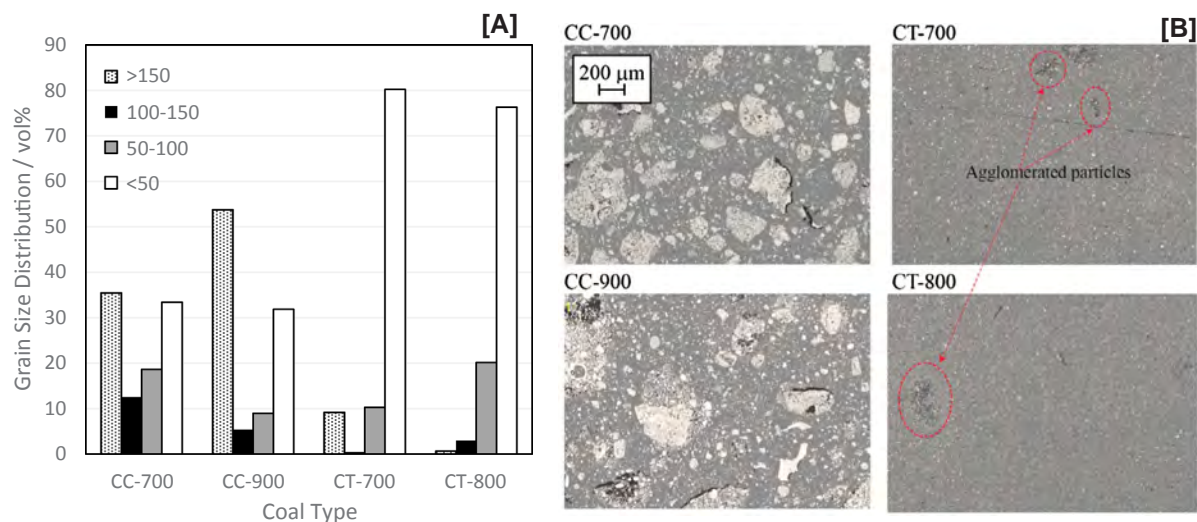
Fig. 2. [A] Coal char particle size distribution (in μm) and [B] optical image of coal chars embedded in resin.

raw coals, which were sieved to below 45 μm size. This is especially true in the case of the coking coals investigated where particle sizes of larger than 150 μm are common, indeed outnumbering smaller particles in the case of CC-900. Thermal coals show smaller particles with the majority in the expected size region, however they do include a few larger particles. Differences between the two different types of coals used can be clearly seen in optical images taken of the coal chars embedded in resin as per Section 2.2, shown in Fig. 2[B].

The size distribution of the chars is related to the coal type, with the coking coal able to fuse particles together, and the thermal coal tending to retain a similar size to the original coal. Some examples of possibly agglomerated particles in the thermal coal char are circled in Fig. 2[B]. These are visually very different to the large particle seen to dominate in CC chars. From an industrial perspective, electrochemical chars produced from a coking coal will likely require further size reduction after heating to overcome the inherent thermoplasticity. By comparison, the size of the thermal coal chars could be controlled from the original feed material.

3.2.2. Char classification

Char morphology can be classified as one of three char groups which depend on the apparent void space of the char analysed [18,19]. All coal chars investigated in this work were found using CCIS software to be Group III chars with characteristically low porosity and angular shape. Void space for these chars is less than 40%. It has previously been shown that Group III chars tend to originate from a coal with high inertinite content and are less likely to form from parent coals with high volatile composition, such as lignite [19]. However, the char classification system was designed for high heating rate chars (where vitrinite chars tend to swell significantly). The low heating rate chars in this study are unlikely to display the same level of thermo-swelling and hence may require a different char classification for electro-chemical purposes.

Using CCIS software, the amount of mineral content was also estimated for each char and this is compared to results found using standard ash analysis methods via proximate analysis techniques in Table 2.

The CGA prediction for mineral matter is quite close to that of the

measured ash amount using traditional methods. Underestimation using the CGA technique is normal as some of the very fine mineral grains (less than 1 μm) cannot be discriminated from the resin matrix whilst visible minerals require a density correction to convert from volumetric to mass basis. This depends on the mineralogy of the sample since different minerals contribute different amounts of ash. Alternatively, the traditional ash analysis method using in proximate analysis could lead to overestimation due to the measurement of the oxidised version of mineral components. Potentially the difference is due to a combination of these effects.

3.3. Char mineral composition and distribution

3.3.1. Char composition

Using MLA software, minerals were identified in each coal char from a representative sample of char embedded in resin which is cut and polished at the surface using the same sample prepared for CGA analysis. A normalisation procedure using libraries of known mineral compositions was used in order to identify mineral components in the chars as these were expected to be different to raw coal minerals present in the database. MLA analysis yielded a range of different particles, the relative weight percent of which was calculated by the software. This method allows detailed identification of minerals present in the char without thermally or chemically altering the char. Therefore, results reflect real concentrations observed in an electrode composed of this char. This method also allows differentiation of complex minerals such as kaolin compared to quartz. These minerals cannot be differentiated through normal ash analysis where elemental compositions are determined through ashing and overall elemental balance assuming oxides of each element. A combination of quartz, clays, carbonates and other minor mineral components were found in each char type, as shown in Table 3.

It can be seen in Table 3 that the majority of the mineral component for each char type is quartz and clay (including, kaolinite, illite and chlorite in this category) which make up a combined total of more than 90 wt% of the total inorganics. Carbonates, iron minerals, phosphates, manganese bearing compounds and rutile make up a combined total of less than 10%, in some cases less than 5 wt%.

Thermal and coking coal chars investigated show very different compositions, although only small differences can be seen between char HHT. The thermal coal used here clearly has a high quartz content, more than 85% of the mineral component is identified as silica. Between 700 and 800 °C this does not appear to change drastically, with the biggest changes being a slight decrease in silica and increase in illite

Table 2
Ash estimate from traditional and advanced methods.

	CC-700	CC-900	CT-700	CT-800
CGA Prediction	9.7%	11.7%	24.3%	25.7%
Proximate Analysis	11.1%	11.6%	28.6%	29.0%

Table 3
Minerals present in coal chars analysed according to MLA.

Mineral (wt%)	Composition	CC-700	CC-900	CT-700	CT-800
Quartz	(SiO_2)	34.15	41.42	86.25	85.43
Kaolinite	$Al_2Si_2O_5(OH)_4$	21.90	15.53	0.86	0.55
Illite	$K_{0.6}(H_3O)_{0.4}Al_{1.3}Mg_{0.3}Fe^{2+}_{0.1}Si_{3.5}O_{10}(OH)_2 \cdot (H_2O)$	31.33	34.30	10.95	11.87
Chlorite	$(Mg,Al,Fe)_{12}[(Si,Al)_8O_{20}](OH)_{16}$	6.16	4.17	0.79	0.87
Calcite	$Ca(CO_3)$	0.25	0.01	0.00	0.00
Siderite	$Fe^{2+}(CO_3)$	1.19	0.39	0.02	0.02
Pyrite	Fe_2S_2	2.03	0.27	0.00	0.01
Fe	Fe	0.63	1.46	0.14	0.25
Apatite	$Ca_5(PO_4)(F,Cl,OH)$	1.58	1.19	0.00	0.00
Manganite	$Mn^{3+}O(OH)$	0.02	0.00	0.37	0.80
MnSulfate	$MnSO_4$	0.03	0.00	0.37	0.10
MnS	MnS	0.00	0.00	0.03	0.00
Rutile	TiO_2	0.73	1.25	0.22	0.10
Total		100.00	100.00	100.00	100.00

when increasing temperature from 700 to 800 °C.

Coking coals however do show a noticeable change in mineral composition with pyrolysis temperature. When the HHT is increased to 900 °C, the amount of kaolinite present in the mineral component drops by more than 5 wt%, while the amount of quartz increases by the same amount. The decomposition of kaolinite has been reported to involve several temperature dependant steps, forming metakaolinite (AS_2, or $Al_2O_3.2SiO_2$) and even quartz at elevated temperatures [20], i.e.;

$$Al_2O_3. 2SiO_2. 2H_2O \xrightarrow{450-700°C} Al_2O_3. 2SiO_2 + 2H_2O \quad (1)$$

$$2(Al_2O_3. 2SiO_2) \xrightarrow{925-1050°C} 2Al_2O_3. 3SiO_2 + SiO_2 \quad (2)$$
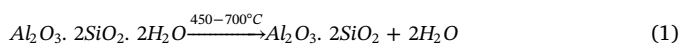
The decomposition temperature of kaolinite has been seen to be dependent on the type of coal due to differences in initial kaolinite composition [20]. Results shown for the CC-char heated at 900 °C see a decrease in the kaolinite measured and increase in quartz, which suggests the decomposition reaction shown in Eqs. (1) and (2) is likely occurring at the slightly lower temperature of 900 °C.

The total amount of mineral present in each char as a whole should also be considered since the mineral component of the coking and thermal coals investigated here are different. The overall weight percent of combined clays and quartz are compared in Fig. 3[E].

Carbonates and other minerals make up a very small portion of both coal char types initially, although during electrochemical analysis the coal chars are submersed in a carbonate electrolyte. Overall, each char has a similar amount of clay (~5 wt%) although CC chars are dominated by kaolinite while CT chars include mostly illite. The larger overall mineral content, combined with the high percentage of quartz in

CT char inorganics, reveals far more total quartz in CT chars than CC chars.

3.3.2. Ash particle size

Where inhibition was observed by quartz contamination of a solid graphite electrode, particle sizes in the 10–20 µm size range were used [5]. In the case of the CT chars, particle size of the quartz is much smaller, the majority in the 0–5 µm range, and almost exclusively less than ~ 15 µm, as shown in Fig. 4[B] (note spatial resolution of equipment is 0.1–0.2 µm).

CC chars also contain a comparatively small amount of quartz and some of this is present in larger particle sizes than the CT chars, extending out to 40 µm in size (Fig. 4[A]). This can also be seen for clay distribution where the distribution of clay in the CC chars includes larger particles than seen in CT chars.

The interfacial area expected for the quartz and clay minerals has also been calculated using the particle size distribution and density of the mineral and chars. Mineral density was calculated based on the combination of clays present in proportions seen in Table 3, while char density was measured by compressing char under the same conditions as electrode pellet formation (740 MPa) and measuring resultant volume. Density of chars ranged from 1.43 to 1.78 g/cm^3. Particles are assumed to be spheres with diameters of the specified particle size. Results for the surface area of mineral matter contacting the char per square centimetre are shown in Fig. 3[B].

The interfacial area of quartz and clay is reflective of the weight percentage. There is large contact area observed with quartz for the CT chars, reflective of the smaller particle size of the quartz in this case. For
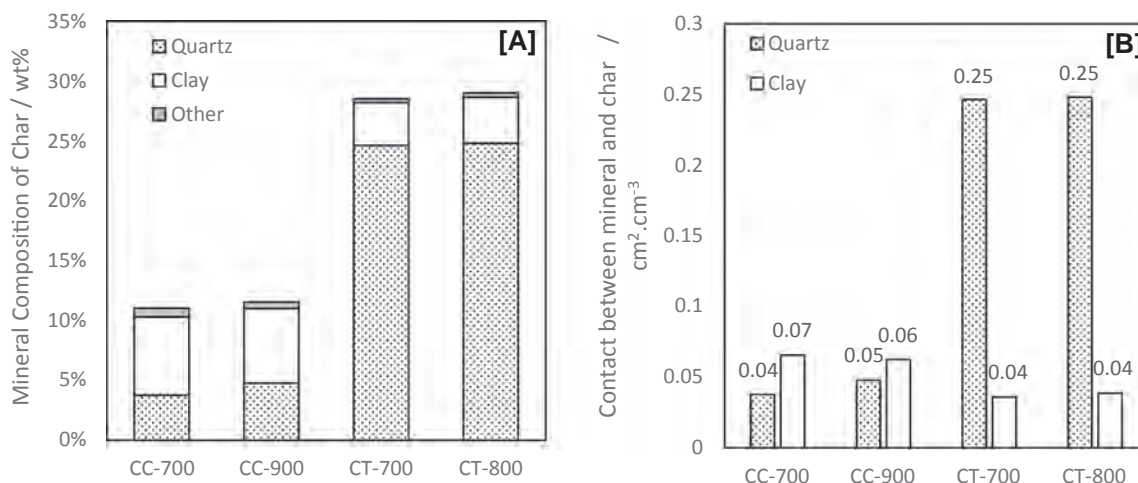

Fig. 3. [A] Main mineral composition of inorganic matter present in CT and CC chars [B] Comparative contact area of SiO_2 and clays for thermal and coking coals.
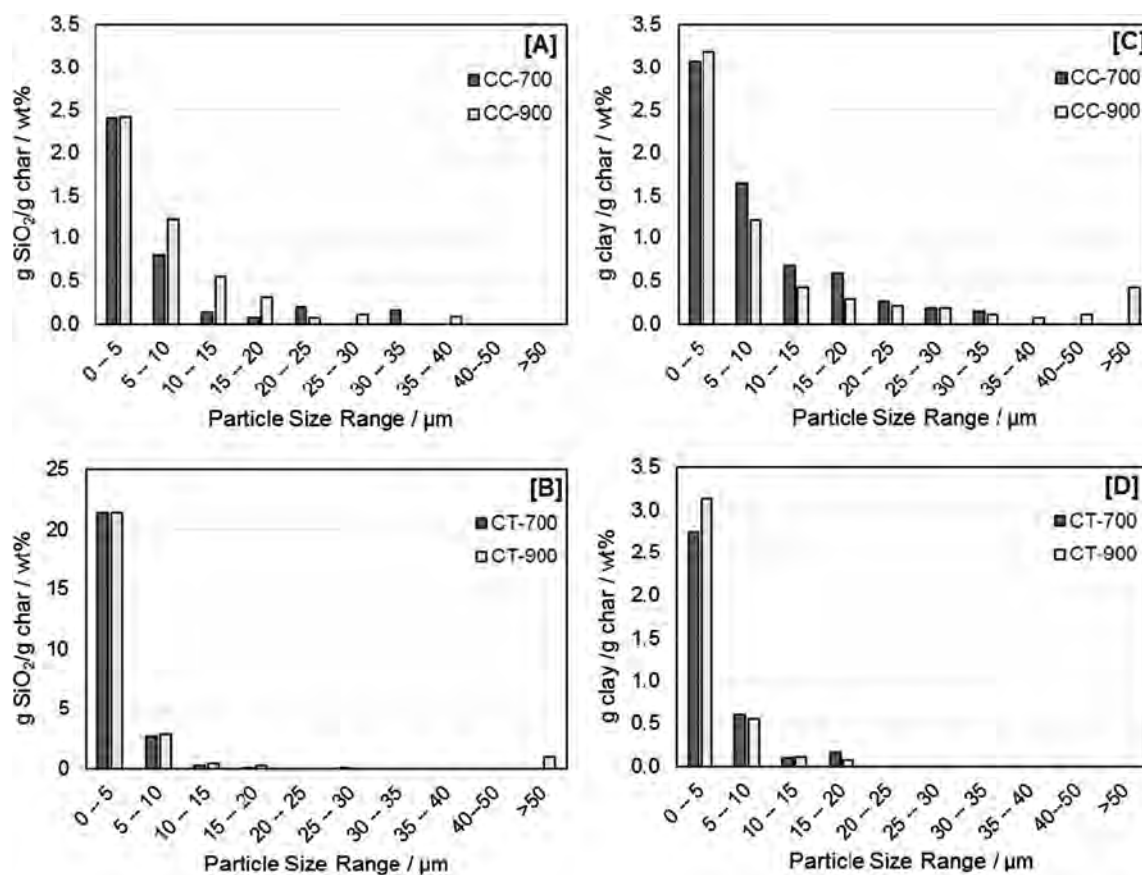
Fig. 4. Particle size distribution of SiO_2 and clay minerals in thermal and coking coals from MLA.

CC-chars there is higher contact area with clays. No major differences can be observed between pyrolysis temperatures for coal chars of the same parent coal origin other than a slight increase in quartz contact area between CC-700 and CC-900.

3.3.3. Mineral distribution

Combining optical images and mineral liberation analysis enables mineral distribution within the char to be observed and to qualitatively understand contact between char and minerals. Several example particulates for CT-700 and CC-700 are shown in Fig. 5[A] and [B] respectively. No major differences were observed between char HHT for each char type.

Qualitative analysis of a representative sample of particulates shows some trends and interesting observations for different coal chars investigated here. Mineral particles in the case of CT coals are far less closely intermixed with the carbon component than with CC chars, as well as being smaller, as expected from particle size and mineral size distributions (Figs. 2 and 4 respectively). Quartz is also prevalent in CT chars, although MLA data is difficult to match directly with optical images as quartz is not clearly delineated in optical sampling, being grey similar to the background colour. Intimate contact with char however does not appear to occur with quartz to the same extent as clay components, and smaller char particles in the case of CT-chars also means very little intimate contact can be observed.

CC-chars however show very close intermixing and association of char with minerals, especially in the case of clays. Here, particles as well as mineral components are larger, although minerals are, for the vast majority, still smaller than the raw coal sieve size of 45 μm (Fig. 4).

3.4. Electrochemical investigation

3.4.1. Impact of minerals

To determine the electrochemical effect of kaolinite mineral on coal chars, CT-700 coal was mixed with 5 wt% kaolinite and tested in a graphite based electrode for activity. Results for both the initial, unmodified CT-700 char and kaolin modified CT-700 char electrode are shown in Fig. 6 along with the normalised electrochemical performance of all coal chars presented here, details provided in previous work [13], for reference.

It was seen previously [5] that kaolinite increases the comparative electrochemical performance of graphite substantially when normalised for the amount of kaolin present. In Fig. 6[A], no normalisation has occurred other than for the somewhat arbitrary geometric surface area of the electrode, and yet the observed current density is seen to be more than double at $0.2\,V$ vs. $C/CO_2/CO_3^{2-}$ ($6.46\,mA.cm^{-2}$ for CT-700, $14.61\,mA\,cm^{-2}$ for CT-700 with kaolinite). Clearly, electrochemical performance of CT-700 can be greatly enhanced through the addition of relatively small amounts of kaolinite, and this is observed to a greater degree than increased performance when combining with graphite in a similar ratio [5]. The increase does not quite give comparable performance to the highest performing chars (CT-800 and CC-700) as shown in Fig. 6[B], but is regardless seen to be a step change in performance compared to both CT-700 and CC-900.

The effect of quartz is more difficult to understand. Inhibition by quartz addition has been observed previously [5,6], however CT-800, which still includes a large amount of quartz, shows high activity. This could be a result of distribution within the electrode, quartz particle size and association with coal char or, most likely, total amount of quartz present in the solid electrode. In this case a maximum of 25 wt% of the char is quartz and only 25 wt% of the electrode is char, meaning approximately ~6 wt% quartz total in the electrode. In the previously
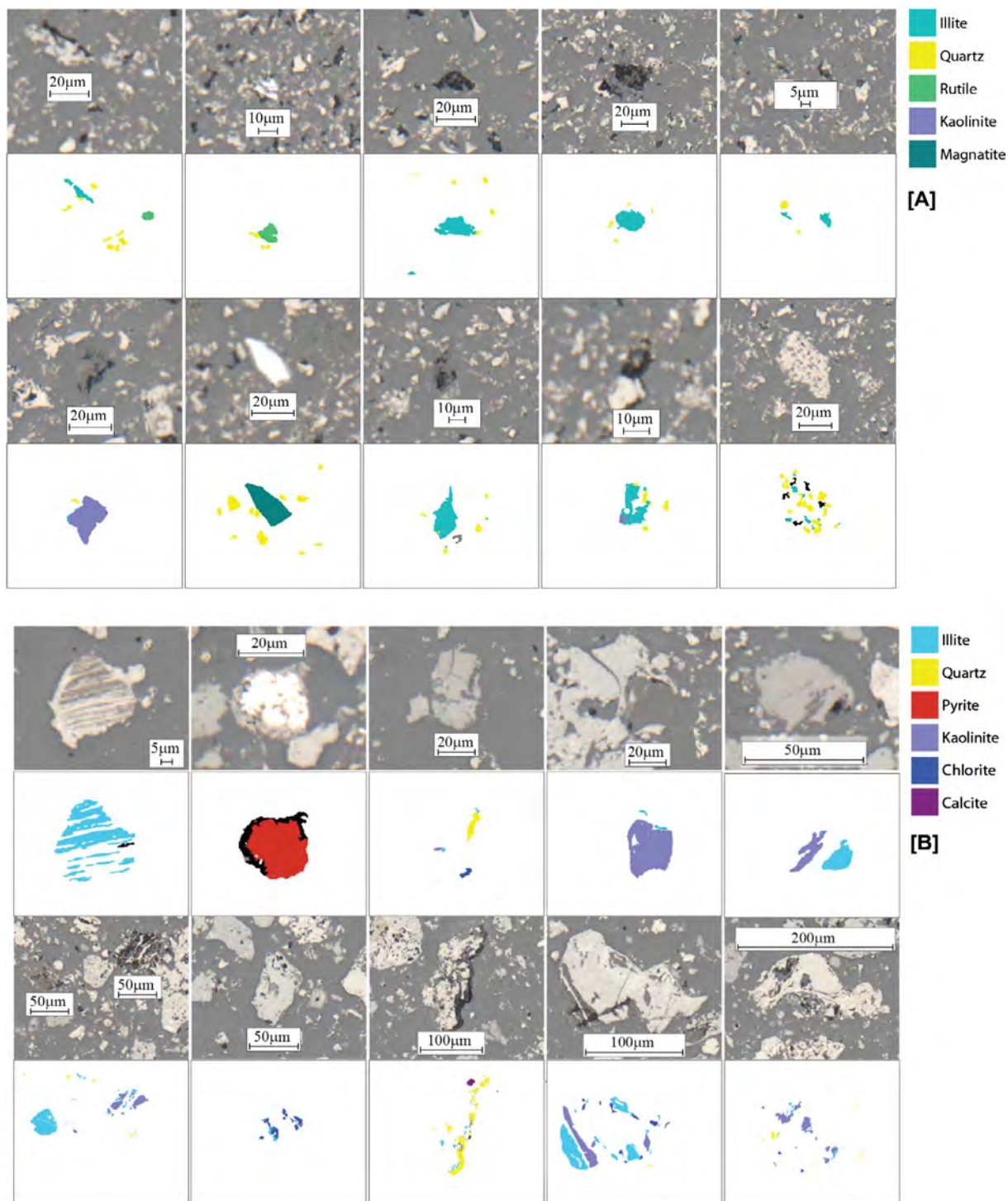
Fig. 5. Physical mineral distribution of within char particles shown with optical and MLA analysis technique [A] CT-700 [B] CC-700.

reported results, the inhibiting influence of quartz was investigated from 10 wt% SiO_2 up to 50 wt% of the total solid electrode and this is therefore outside the previously reported on range. At a lower loading and elevated temperature (600 °C compared to 500 °C), quartz does not appear to inhibit electrochemical performance substantially. Potentially, at this higher temperature quartz dissolution is increased [21] and its impact at the electrode surface mitigated, although it is likely that some interfacial blocking of the carbon at the triple phase boundary is still occurring.

3.4.2. Effect of kaolinite interfacial contact area on electrochemical activation

In order to confirm the importance of mineral distributions within the solid carbon anode, the activity of graphite has been assessed using kaolinite distributed in the electrode in two different arrangements. In the first, kaolinite was sieved to a particle size below 32 μm and intimately mixed with graphite powder using a mortar and pestle. The resulting mixture was pressed into an electrode pellet and tested for electrochemical activity as outlined in Section 2 (referred to as 'distributed' kaolinite electrode). In the second arrangement, pure kaolin was compressed into a pellet and cut into a solid square. This square of
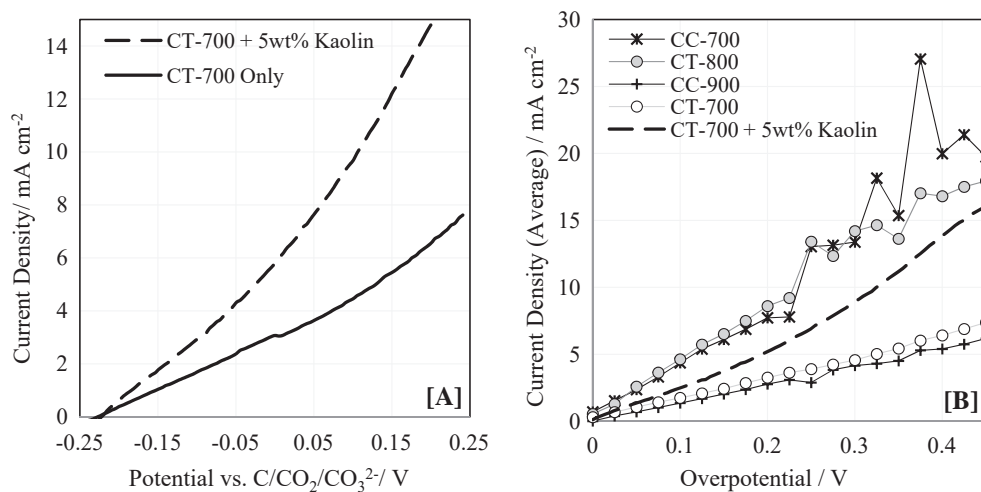
Fig. 6. [A] Kaolinite catalyst effect on CT-700 char versus reference [B] Electrochemical performance of coal chars (average current for three linear voltammetry scans) normalised versus OCP for comparison (see Ref [13] for further details).
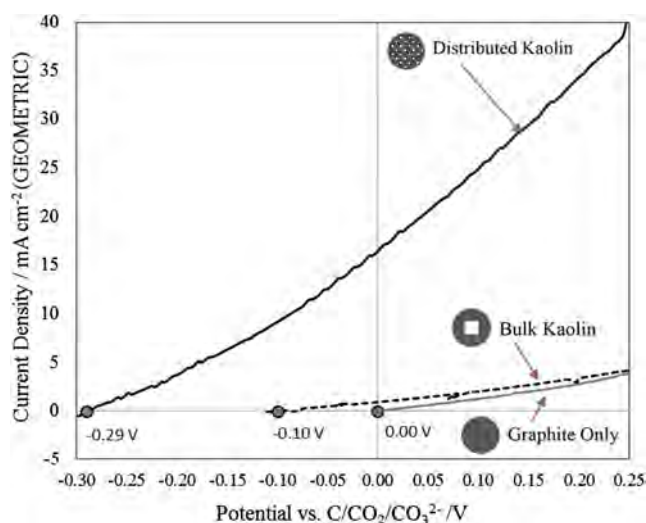
Fig. 7. Electrochemical response for graphite with and without addition of kaolinite of different particle size (5 mV/s, ternary carbonate eutectic, 600 °C).

kaolinite was then placed below pure graphite powder and compressed, resulting in an electrode where the solid kaolinite square was surrounded by graphite powder (referred to as 'bulk' kaolinite electrode). Both electrodes were subsequently tested for electrochemical activity at 600 °C in a ternary carbonate eutectic using standard electrochemical test procedures outlined in Section 2. Results for pure graphite, distributed kaolin and bulk kaolin are shown in Fig. 7 where they have been normalised for total geometric surface area, which was the same for each electrode.

It can be seen that the distributed kaolinite electrode shows an extremely high level of activation and shifted onset potential compared to both the pure graphite and the bulk kaolinite electrode. Indeed, compared to active coals investigated previously, the average current density measured over a 5 min interval while holding at 0.5 V vs C/CO$_2$/CO$_3^{2-}$ is more than four times as high for the distributed kaolinite electrode (72.6 mA cm^{-2}) as that seen for a 25 wt% CC-700 electrode (16.8 mA cm^{-2}). Meso and micro porous surface area and a high O/C ratio [10], as well as bulk lattice disorder and conductivity [11] have previously been said to be key to activity of carbon in the DCFC, however it can be seen in Fig. 7 that the involvement of mineral matter also has a dramatic effect on the electrochemical performance. Even graphite, which generally displays lower electrochemical activity compared to more functionalised high surface area carbons, can display high performance as observed in Fig. 7. The bulk graphite electrode

shows comparatively limited performance when normalised for geometric area, the main difference compared to pure graphite being the onset potential (0.1 V compared to 0.0 V for graphite). Potentially this could result from small differences in immersion time in the melt, which was not controlled in these experiment and which has previously been observed to impact on open circuit measurements in molten carbonate systems [22].

The surface area of carbon available for oxidation is slightly less (kaolinite chunk of 0.19 cm^2 used in a 1.33 cm^2 electrode), which might be expected to decrease the current density, however a similar result is achieved and current density observed at 0.5 V is almost identical (14.0 mA cm^{-2} for graphite, 13.8 mA cm^{-2} for bulk kaolinite electrode). It is likely therefore that increased electrochemical activity at the interface of graphite and kaolin leads to some limited improvement in performance for the bulk electrode, which counteracts expected decrease from reduction of the available carbon area.

It has previously been proposed that kaolinite may act as a catalyst through different mechanisms including enhanced wetting of the carbonate at the electrode surface, or through mediation of oxide transfer to reactive sites [5]. There is a third possibility which has not previously been discussed and is specific to solid anodes incorporating kaolinite. This mechanism involves the selective dissolution of kaolinite in the molten carbonate electrolyte, leading to enhanced carbon surface area. All three catalytic mechanisms are shown graphically in Fig. 8. Kaolinite solubility in a ternary carbonate eutectic was discussed as a possibility by Glenn et al. to explain shifts in melt behaviour of alkali-metal carbonates when the mineral was intimately mixed with the salt [23]. The transformation of minerals in the presence of carbonate salts was also discussed by Bruno et al. who showed that kaolin and illite are both converted to potassium aluminosilicates such as kaliophilite and kalsilite (KAlSiO$_4$) when heated to 973 K in the presence of coal and K$_2$CO$_3$ [24].

If the kaolinite present were to dissolve, the enhanced performance of the distributed electrode can be understood through the resulting dramatic increase in surface area compared to the bulk or pure graphite electrode. Dissolution of the smaller kaolinite particle present in this case would also be more likely due to their increased surface area in the distributed electrode. However, dissolution of kaolinite in molten carbonates was observed by Glenn et al. [23] to take place over several melt/freeze cycles of the carbonate media, which is not carried out in this case. Dissolution might therefore be expected to be relatively low for the electrodes investigated here. Additionally, dissolution is not likely explain the change in open circuit potential observed for the electrode which becomes more negative when kaolinite is distributed in small chunks (Fig. 7).

Chen et al. showed that the OCP can be observed to vary depending

[A] Increase in SA through kaolinite dissolution
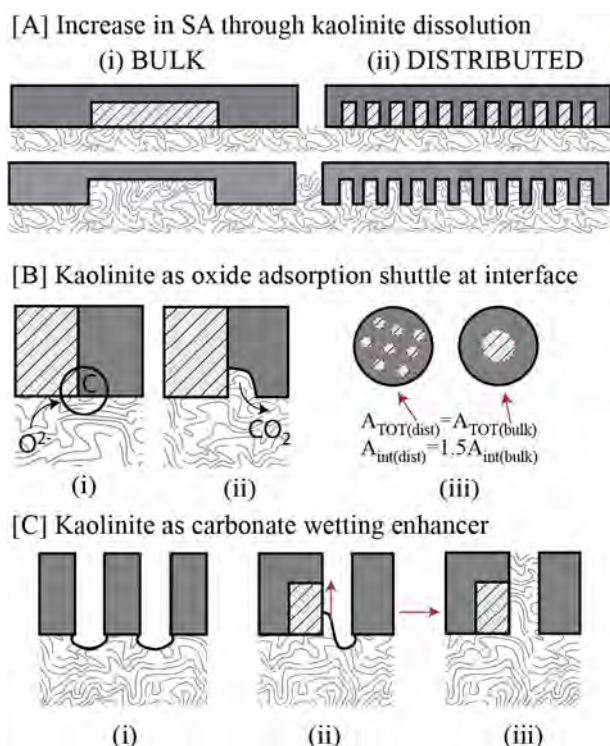
Fig. 8. Role of kaolinite as a catalyst [A] through surface area increase [B] through oxide shuttle mechanism [C] through pore saturation (improved wetting).

on the immersion length and immersion time of a solid carbon electrode [22]. This was said to be a result of a change in the wetting of the carbon surface with molten carbonate on a micropore level, and the specific adsorption of both carbon monoxide and oxide species at the interface, disrupting interfacial activity considering oxide as an electrochemical reactant, and therefore open circuit potential. Carbon monoxide was proposed by the authors to form by reverse Bouduard gasification of the carbon species. These experiments were conducted under a carbon dioxide gas atmosphere, and carbon dioxide is also produced from the electrochemical oxidation of carbon. The OCP measured was seen by Chen et al. to become more negative (versus a different reference system) when wetting was increased either as a function of immersion time or immersion level in the molten carbonate melt [22]. The negative shift in OCP observed for the distributed kaolinite electrode (-0.29 V compared to 0.00 V for pure graphite) could therefore be due to a change in the gasification conditions at the electrode surface and subsequent formation of CO. The interaction of carbon, alkali metal carbonates and minerals including kaolin has have previously been shown to have a clear impact on gasification outcomes [25,26].

Fig. 8[B] outlines a final proposed enhancement mechanism involving the role of kaolinite as oxide adsorption sites. The more polar surface of the mineral matter could act to adsorb carbonate or oxide species preferentially over the non-polar carbon surface. This would mean the interfacial area between the kaolinite and carbon would be extremely active and would explain why smaller, distributed particles give better results compared to a single large chunk of kaolinite. In the example given in Fig. 8[B] (iii), kaolinite has the same geometric area (A_{TOT}) for each electrode shown, however in the distributed case the interfacial area (A_{int}) is 1.5 times that of the bulk case. Since very small particles were used compared to a single large chunk in Fig. 7, this difference would be expected to be much larger.

4. Discussion

Analysis of mineral distribution and type in coal chars is a useful tool for assessing characteristics of the carbon fuel. The technique enables assessment of the mineral content without high temperature treatment of the fuel prior to assessment. It also allows accurate identification of minerals and their particle sizes compared to the particle size of the coal char. Qualitative assessment of the distribution of mineral components with carbonaceous particles can also be carried out. Matched with electrochemical analysis of these chars, this is a powerful technique which can help to understand differences in electrochemical oxidation performance. Although electrochemical investigations have been carried out here with a solid electrode, it is also expected that even in slurry-type system the impact of mineral distribution could be significant in enhancing the triple phase boundary of the electrochemical reaction through allowing greater contact of oxidant (through molten carbonate medium) and fuel.

Optical analysis of chars has shown that initial particle sizing of the raw coal is not a sufficient description in the case of coking coals as these coal chars tend to be composed of particles which have fused, forming larger char particles. This immediately introduces a point of difference between the chars and suggests they are not directly comparable despite similar pyrolysis temperatures.

Clear differences between coal types in terms of mineral distribution including composition, size and contact with char can be observed. CC chars investigated show substantially lower quartz content than the thermal coal chars (CT) with the majority of the mineral composition being kaolinite. Both overall char and individual mineral particle sizes were seen to be larger for the CC than CT chars and the minerals were more intimately mixed with the char particles for CC chars. CT chars showed a prevalence of physically separated mineral matter in individual particles, while CC chars were more likely to have mineral matter combined into a larger particle.

Between pyrolysis temperatures for the same chars, very little variation can be observed. No clear difference quantitatively or qualitatively can be seen for mineral matter present in CT-700 and CT-800. Since there is a difference in electrochemical activation, the reason does not appear to be related to the mineral content, as previously proposed. Between CC-700 and CC-900, however, changes in the mineral content can be observed. Differences include an increase in the quartz content and decrease in kaolinite content when the pyrolysis temperature is increased from 700 °C to 900 °C. Small changes in kaolinite content may contribute to difference in electrochemical performance of these chars since addition of only 5 wt% kaolin to the otherwise inactive CT-700 demonstrated enhanced performance at the same polarisation.

Activation observed in CT coals with change in pyrolysis temperature could be related to electrical resistance since the resistivity of CT-800 is substantially lower than CT-700, while other observed properties, including BET SA and mineral distribution as discussed here, did not change to the same extent. Change in electrical resistivity is a result of change in carbon structure at 800 °C. Structural change impacts on the degree of carbon crystallinity and crystallite size, which has been shown to impact on electrochemical performance of carbon in particulate form [2].

It is suggested here that CC coals appear to have improved electrochemical performance when they still have lower conductivity. It is also discussed here that this could be due to the enhancement effect of clays present, and, more importantly, close contact of mineral content throughout larger char particles observed in the case of CC chars. As demonstrated through use of graphite electrodes with kaolinite having different interfacial contact area, size and contact of the mineral to the carbon fuel is crucial to activation of the electrode. Deactivation of CC chars between 700 and 900 °C is likely a result of both the decreased functionalisation of the material (O/C, H/C ratios) as well as changes in clay composition. This high temperature region is well known to evolve light gases as well as undergoing an exothermic contraction [27,28] during pyrolysis. This graphitisation process results in a more ordered carbon structure which likely causes a decrease in reactivity. Coking coals undergoing a thermoplastic transition (below 500 °C) allow the

fusion of disparate particles to take place, in particular, allowing the softening vitrinite components to fuse together with non-softening inertinites and mineral matter. This is likely to create a different interfacial contact between these components compared to the thermal coal, which would retain the interfaces based on the raw coal (essentially as deposited). This may be one reason why thermal coals have been observed to exhibit lower levels of exothermic behaviour during this high temperature contraction [29].

Recent work on coal macerals have shown that vitrinite concentrates from Australian coking coals typically contain far lower levels of mineral matter than inertinite concentrates [30]. This trend has been observed in several studies [31,32] and has allowed the separation and concentration of these maceral components through density separation. This suggests that the vitrinite and inertinite components of coal may offer different electro-chemical behaviour based on their intrinsic differences in mineral distribution. Furthermore, it offers the potential to optimise such behaviour through traditional coal separation techniques. This previous maceral research has also shown that these maceral concentrates produce significant differences in thermal behaviour, notably greater levels of thermo-swelling and subsequent contraction at high temperatures for vitrinite concentrates. This presents a fundamental avenue for future electro-chemical research; in part by using the vitrinite component as a means of controlling porosity (through thermoplasticity). However of particular interest is the potential higher value use for the inertinite component as it is typically favoured as being of lower value and often discarded as reject in a coal preparation plant.

5. Conclusion

It is shown here that coal char mineral type and distribution vary considerably between parent coal types. Coking coal chars analysed had larger mineral particles than the thermal coal and are more intimately mixed with mineral component of the char. These chars also have a high kaolinite content, determined through MLA analysis, which has previously shown catalytic effects on carbon electro-oxidation and is shown here to have a catalytic impact on the electrochemical performance depending on the distribution in the solid carbon anode. Coking coal chars trialled therefore were suggested to have their electrochemical performance partially linked to the chemical composition of the mineral content. Thermal coals investigated have a high quartz content as well as small mineral particle sizes, which have minimal interaction with the organic component of the coal char. Quartz has been shown previously to be inhibiting to electrochemical oxidation of carbon fuels and, although a clear inhibition is not observed for the thermal coal investigated here despite relatively high loading of quartz, activation of the char does not occur at the same pyrolysis temperature as the coking coal. It is discussed here that the lack of clay catalysts in this material could limit its comparative electrochemical performance when treated at the same pyrolysis conditions as chars which contain these species. Instead, physical properties, such as resistivity of the thermal coal char, are more likely to determine its final activation. The mineral content of raw coal applied to the direct carbon fuel cell is clearly of key importance in terms of electrochemical performance of coal chars and its contact with the carbon fuel will also affect this heavily.

Acknowledgements

References

[1] CCS Retrofit: Analysis of the Globally Installed Coal-Fired Power Plant Fleet. In:

Agency IE, ed.: International Energy Agency; 2012.

[2] Giddey S, Badwal SPS, Kulkarni A, Munnings C. A comprehensive review of direct carbon fuel cell technology. Prog Energy Combust Sci 2012;38(3):360–99.

[3] Gür TM. Critical Review of Carbon Conversion in "Carbon Fuel Cells". Chem Rev 2013;113(8):6179–206.

[4] Jiao Y, Tian W, Chen H, Shi H, Yang B, Li C, et al. In situ catalyzed Boudouard reaction of coal char for solid oxide-based carbon fuel cells with improved performance. Appl Energy 2015;141:200–8.

[5] Tulloch J, Allen J, Wibberley L, Donne S. Influence of selected coal contaminants on graphitic carbon electro-oxidation for application to the direct carbon fuel cell. J Power Sources 2014;260:140–9.

[6] Li X, Zhu ZH, De Marco R, Bradley J, Dicks A. Evaluation of raw coals as fuels for direct carbon fuel cells. J Power Sources 2010;195(13):4051–8.

[7] Eom S, Ahn S, Kang K, Choi G. Correlations between electrochemical resistances and surface properties of acid-treated fuel in coal fuel cells. Energy 2017;140(Part 1):885–92.

[8] Rady AC, Giddey S, Badwal SPS, Ladewig BP, Bhattacharya S. Review of Fuels for Direct Carbon Fuel Cells. Energy Fuels 2012;26(3):1471–88.

[9] Li X, Zhu ZH, De Marco R, Bradley J, Dicks A. Modification of coal as a fuel for the direct carbon fuel cell. J Phys Chem A 2010;114(11):3855–62.

[10] Cao DX, Wang GL, Wang CQ, Wang J, Lu TH. Enhancement of electrooxidation activity of activated carbon for direct carbon fuel cell. Int J Hydrogen Energy 2010;35(4):1778–82.

[11] Cherepy NJ, Krueger R, Fiet KJ, Jankowski AF, Cooper JF. Direct conversion of carbon fuels in a molten carbonate fuel cell. J Electrochem Soc 2005;152(1). A80-A7.

[12] Li X, Zhu Z, Chen J, De Marco R, Dicks A, Bradley J, et al. Surface modification of carbon fuels for direct carbon fuel cells. J Power Sources 2009;186(1):1–9.

[13] Allen JA, Glenn M, Donne SW. The effect of coal type and pyrolysis temperature on the electrochemical activity of coal at a solid carbon anode in molten carbonate media. J Power Sources 2015;279:384–93.

[14] Hackett GA, Zondlo JW, Svensson R. Evaluation of carbon materials for use in a direct carbon fuel cell. J Power Sources 2007;168(1):111–8.

[15] Li C, Shi Y, Cai N. Performance improvement of direct carbon fuel cell by introducing catalytic gasification process. J Power Sources 2010;195(15):4660–6.

[16] O'Brien G, Firth B, Adair B. The application of the coal grain analysis method to coal liberation studies. Int J Coal Prep Util 2011;31(2):96–111.

[17] Hapugoda P, O'Brien G, Krahenbuhl G, Warren K. A new method for obtaining detailed chemical and mineral information on individual coal particles as prepared for power generation and coke making. In: 31st Annual Meeting of the Society for Organic Petrology. Sydney, Australia; 2014.

[18] Benfell KE, Liu G-S, Roberts DG, Harris DJ, Lucas JA, Bailey JG, et al. Modeling char combustion: the influence of parent coal petrography and pyrolysis pressure on the structure and intrinsic reactivity of its char. Proc Combust Inst 2000;28(2):2233–41.

[19] Steibel M, Warren K, O'Brien G, Roberts D, Harris D, Spliethoff H. Investigation of the maceral composition of coals with different ranks and of the char morphology during high temperature and high pressure entrained flow gasification. Australia: ICCS&T/ACSE. Melbourne; 2015.

[20] Cheng H, Liu Q, Yang J, Frost RL. Thermogravimetric analysis of selected coalbearing strata kaolinite. Thermochim Acta 2010;507–508:84–90.

[21] Glenn M. Development and Optimization of the Direct Carbon Fuel Cell. Chemistry. PhD (Chemistry). University of Newcastle; 2017.

[22] Chen CC, Maruyama T, Hsieh PH, Selman JR. Wetting behavior of carbon in molten carbonate. J Electrochem Soc 2012;159(10):D597–604.

[23] Glenn MJ, Allen JA, Donne SW. Thermal investigation of a doped alkali-metal carbonate ternary eutectic for direct carbon fuel cell applications. Energy Fuels 2015;29(8):5423–33.

[24] Bruno G, Buroni M, Carvani L, Piero GD, Passoni G. Water-insoluble compounds formed by reaction between potassium and mineral matter in catalytic coal gasification. Fuel 1988;67(1):67–72.

[25] Formella K, Leonhardt P, Sulimma A, van Heek KH, Jüntgen H. Interaction of mineral matter in coal with potassium during gasification. Fuel 1986;65(10):1470–2.

[26] Kühn L, Plogmann H. Reaction of catalysts with mineral matter during coal gasification. Fuel 1983;62(2):205–8.

[27] Strezov V, Lucas JA, Strezov L. Experimental and modelling of the thermal regions of activity during pyrolysis of bituminous coals. J Anal Appl Pyrol 2004;71(1):375–92.

[28] Stanger R, Xie W, Wall T, Lucas J, Mahoney M. Dynamic behaviour of coal macerals during pyrolysis - associations between physical, thermal and chemical changes. Proc Combust Inst 2013;34(2):2393–400.

[29] Strezov V, Lucas JA, Strezov L. Quantifying the heats of coal devolatilization. Metall Mater Trans 2000;31B(5):1125.

[30] Xie W, Stanger R, Lucas J, Mahoney M, Elliott L, Yu J, et al. Thermo-swelling properties of particle size cuts of coal maceral concentrates. Energy Fuels 2015;29(8):4893–901.

[31] Tran QA, Stanger R, Xie W, Lucas J, Yu J, Stockenhuber M, et al. Maceral separation from coal by the reflux classifier. Fuel Process Technol 2016;143:43–50.

[32] Xie W, Stanger R, Lucas J, Wall T, Mahoney M. Coal macerals separation by reflux classification and thermo-swelling analysis based on the computer aided thermal analysis. Fuel 2013;103:1023–31.

Thermal and Electrochemical Impact of Kaolin on a Direct Carbon Fuel Cell

Simin Moradmand[1], Jessica A. Allen[1], Scott W. Donne[2] *

[1]Chemical Engineering and [2]Chemistry, University of Newcastle, University Drive Callaghan NSW

2289, Australia

Abstract

This paper investigates the impact of kaolin, a dominant coal mineral, on the thermal and electrochemical behaviour of the molten ternary carbonate eutectic ($(Li,Na,K)_2CO_3$) in the direct carbon fuel cell (DCFC) as a means to simulate long-term operation with a continuous coal feed. Thermogravimetric and differential thermal analysis, coupled with kinetic modelling using the Friedman method, shows a substantial decrease in activation energy for eutectic melting with the addition of kaolin. Electro-oxidation of carbon (graphite) is also enhanced with kaolin in the electrolyte, increasing from 17.68 mA/cm^2 at 0 wt.% kaolin to the highest value of 162 mA/cm^2 with 15 wt.% kaolin added. It is shown that the improvement is due to increasing oxide concentration resulting from kaolin dissolution in the electrolyte.

* Corresponding Author (Scott W. Donne)

P: +61 2 4921 5477; F: +61 2 4921 5472; E: scott.donne@newcastle.edu.au

1.   INTRODUCTION

Coal has been used for decades as the main fuel source in conventional power plants, producing electricity with a maximum achievable efficiency of 30-40% [1-5]. This operation also releases CO_2, NO_X, SO_X and particulates into the atmosphere as by-products, which is of course a major environmental issue [4]. Improving on this inefficient process through new technologies is needed to enable energy production from coal in a much more environmentally conscious fashion. The share of coal in electricity production is still very high in comparison with other energy sources (its share is predicted to be more than 30% in 2040), despite growing concerns over global warming [6] and so its poor efficiency must be addressed. Although various coal technologies, including gasification and supercritical applications [4], have been investigated to increase fuel conversion efficiency and reduce environmental impact, the absence of a substantially higher efficiency technology remains elusive. The electrochemical conversion of carbon into electrical energy offers higher theoretical efficiencies than chemical processes, as well as fewer environmental problems. Direct carbon fuel cells (DCFCs) generate electrical energy using a completely different approach to coal-fired plants. They can achieve almost double the efficiency of current power plants with 50% fewer greenhouse gas emissions and CO_2 to be sequestered [7].

DCFC technology has attracted great interest in recent times due to its advantageous high efficiency and low emissions. However, it is in the early stages of practical development and needs further effort to enable its widespread use as the next generation carbon-fuelled power plant. The DCFC is a high temperature fuel cell system that enables electrochemical oxidation of carbon to produce electrical energy, with CO_2 gas as the product. The overall reaction of carbon in DCFC is the same as that used in a coal-fired power station; i.e.,

$$C(s) + O_2\,(g) \rightarrow CO_2(g) \qquad\qquad \text{Overall reaction} \qquad \ldots(1)$$

This overall reaction can be broken down into individual cathodic and anodic half-reactions; i.e.,

$$O_2 + 4e^- \rightarrow 2O^{2-} \qquad\qquad \text{Cathode reaction} \qquad \ldots(2)$$

$$C + 2O^{2-} \rightarrow CO_2 + 4e^- \qquad\qquad \text{Anode reaction} \qquad \ldots(3)$$
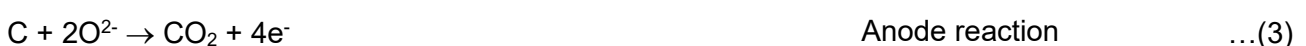
A molten mixture of Li_2CO_3, Na_2CO_3, and K_2CO_3 is used commonly as the electrolyte in the DCFC anode compartment due to its excellent ionic conductivity and chemical stability during high temperature operation [9]. In this role it functions essentially as an oxide ion carrier [9]. Among the

52   various combinations of these salts, including $(Li/Na)_2CO_3$, $(Li/K)_2CO_3$, $(Na/K)_2CO_3$ and

53    $(Li/K/Na)_2CO_3$, the binary eutectic $(Li/K)_2CO_3$ and ternary eutectic $(Li/K/Na)_2CO_3$ have exhibited the

54   best outcomes in terms of carbon electro-oxidation [9]. Jiang et al. showed that in presence of binary

55    $(Li/K)_2CO_3$ eutectic electrolyte the power output was higher than when a solid oxide electrolyte was

56   used due to lower polarization resistance in the system [8]. Although the binary $(Li/K)_2CO_3$ eutectic

57   outperformed the ternary $(Li/Na/K)_2CO_3$ electrolyte in this work, the ternary eutectic mixture

58   displayed lower melting temperature which will affect energy consumption and operability of the

59   system [9, 10]. Suspension of the carbon fuel within the carbonate electrolyte (slurry type DCFC

60   which refers to mixture of solid carbon with molten carbonate electrolyte, investigated in [7])

61   enhances the active reaction sites and triple phase boundary, consequently improving the

62   performance in comparison with other DCFC modes of operation [11]. The authors explained that

63   the reason for enhancement was due to the active reaction zone from two-dimensional increased to

64   three-dimensional zone in slurry mode [7,11].

65   When coal particles are suspended in the carbonate electrolyte in the DCFC, carbon will be

66   consumed via an electrochemical reaction (Eqn (3)). Non-carbonaceous components of the coal,

67   such as mineral matter, will remain in the electrolyte so it is of considerable importance to understand

68   what impact, if any, their presence has on carbon electro-oxidation and hence DCFC performance.

69   Specifically, during continuous operation, the presence of mineral matter can build-up in the DCFC

70   molten carbonate electrolyte and affect the performance of the cell. Although there are some studies

71   in molten carbonate-based fuel cell in batch systems to address some of those impacts [12-14], the

72   increasing concentration of mineral matter in electrolyte has not been studied yet.

73   A limited number of studies have been carried out to investigate the impact of different coal

74   minerals (ash) on DCFC performance. Weaver et al. [12] reported that 10 wt.% of ash added to the

75   ternary carbonate eutectic did not affect system performance, which in this case utilized graphite as

76   the source of carbon. They showed that there was no difference between the measured open circuit

77   potential (OCP) of the cell with and without ash, and the only problem observed was ash build-up at

78   the base of the cell. They did not study the impact of individual coal minerals, nor the performance

79   change when the concentration of minerals increased in the molten carbonate electrolyte. Another

80   study [13] showed that adding different minerals (at the 8 wt.% level) into the coal-carbonate slurry

did not affect the anodic reaction significantly (Eqn (3)), especially at high overpotentials. The authors proposed that minerals like MgO, CaO and Fe_2O_3 played a catalytic role increasing DCFC performance, while Al_2O_3 and SiO_2 acted as inhibitors for carbon electro-oxidation. Liu et al. [14] examined the impact of different sulfur compounds on carbon electro-oxidation in the DCFC. They showed that some sulfur compounds improved cell performance at high temperature via enhancement of the Boudouard reaction, while inorganic compounds of sulfur had no impact on graphite electro-oxidation. Apart from its electrochemical influence, the presence of sulphur has also been observed to poison the anode in cases where nickel was used at high temperature, reducing the system lifetime [5, 15].

Although some studies have investigated the impact of coal impurities on DCFC performance, most considered only a single concentration of the mineral mixed with the coal rather than a range of concentrations [12-14]. The high concentration of mineral in the electrolyte is an important matter for long-term operation of the DCFC, as well as the electrolyte recycling/recovery. There is a lack of information about the influence of the increasing mineral matter concentration in the electrolyte, related thermal and electrochemical influences of those mineral matter, and their maximum allowable concentration in the DCFC. Previous work [16] investigated the influence of different concentrations of coal mineral matter on graphite electro-oxidation kinetics when included as a solid additive to the carbon electrode. Results demonstrated that the inclusion of kaolin and alumina catalyzed the oxidation of graphite, while silica decreased electrochemical performance, possibly as the result of passivation of carbon reactive sites. In another study [17], different coal minerals (5 wt.% concentration) were introduced into the ternary alkali metal carbonate electrolyte to observe the changes in electrolyte melting. Mineral inclusion lowered the electrolyte melting temperature, with specific minerals such as kaolin and calcium carbonate, resulted in lowering the relative enthalpy required for melting.

In this work kaolin has been examined as an additive mineral matter of coal to the ternary alkali metal carbonate eutectic at various concentrations (5-20 wt.% (dry basis)). The impact of this inclusion has been investigated in two different ways relevant to DCFC application. First, the thermal behaviour of the electrolyte has been examined using differential thermal analysis (DTA) and thermogravimetric analysis (TGA) to explore electrolyte melting as a function of additive level.

110 Furthermore, the crystal structure of the fused electrolyte was also investigated using X-ray

111 diffraction (XRD) to explore the formation of new phases. Second, the electro-oxidation of graphite

112 was measured in electrolytes containing various kaolin concentrations using a half-cell configuration

113 that eliminates mass transfer limitations, allowing a focus on kinetic performance [37]. Furthermore,

114 a concentration cell has been designed and used to examine oxide activity in kaolin-doped

115 electrolyte and its electrochemical impact on graphite oxidation.

116

117

118 **2. EXPERIMENTAL**

119 **2.1. Thermal Analysis: Sample Preparation and Procedure**

120   The pure ternary alkali metal carbonate eutectic was prepared by mixing the single carbonate

121 salts (dried in an oven at 110°C for at least 24 hours) Li_2CO_3, Na_2CO_3 and K_2CO_3 (>99% purity;

122 Sigma Aldrich and Chem-Supply, Australia) with the mass ratio 32.0:33.5:34.5, respectively. This

123 powdered mixture was ball-milled (Fritsch Pulverisette 6) for at least 1 h as the initial homogenization

124 step. Dried kaolin (Chem-Supply, Australia; 99% purity) was then added to separate samples of the

125 milled ternary carbonate eutectic at levels of 5, 10, 15 and 20 wt.%, followed by mortar and pestle

126 grinding for 15 min. All thermal analysis (thermogravimetric analysis (TGA) and differential thermal

127 analysis (DTA)) was carried out using a Netzsch STA 2500 Regulus,Japan instrument with α-Al_2O_3

128 (Aesar; 99.99% purity) as the reference material. 10-15 mg of each sample was used for TGA and

129 DTA studies. Analysis were performed under a CO_2 atmosphere (40 mL.min^{-1}) to prevent carbonate

130 decomposition [18] using the following thermal cycling procedure to ensure a reproducible and

131 consistent response:

132   (a) Moisture removal step – the sample was heated at 5°C.min^{-1} from ambient temperature to

133 150°C, where it was held for 1 hour;

134   (b) Homogenization step – three heating and cooling cycles (5°C.min^{-1}) were applied over the

135 temperature range 300°-600°C to homogenize the sample; and,

136   (c) Data collection – samples were then heated and cooled over the range 300°-600°C using

137 rates of 2, 5, 10, 15 and 20°C.min^{-1}.

138

2.2. Electrolyte and Electrode Preparation for Electrochemical Experimentation

2.2.1. Electrolyte Preparation

The desired electrolyte was prepared using the same procedure as described in Section 2.1. Approximately 400 g of this mixture was then placed in 10 cm diameter, 6 cm deep circular alumina crucible (the electrochemical cell) and thermally homogenized at 600°C for 1 h under a flowing CO_2 atmosphere (40 mL.min^{-1}).

2.2.2. Electrode Fabrication

Graphite pellets were fabricated by pressing graphite powder (0.8 g; Timrex SFG44) in a 13 mm diameter die press (ICL; USA) under 31 MPa for 5 min to make the working electrode (~5 mm thick). A silver wire current collector was then cemented to the back of the graphite pellet with conductive silver paste (Fuel Cell Materials, USA). This electrode pellet was then cemented into the end of a 15 mm inner diameter alumina tube (~5 cm long) with non-conductive Resbond 989 adhesive (Ceramic Oxide Fabricators, Australia) and cured in an oven at 100°C for 24 h. Graphite reference and counter electrodes (10 mm diameter, 5 cm long; >99.99% purity; Alfa Aesar) were prepared using a similar approach to previous work [16].

2.3. Electrochemical Cell Assembly and Testing

2.3.1. Electrochemical Performance

The electrochemical cell was based on a 10 cm diameter, 6 cm deep cylindrical alumina crucible covered by a fitted alumina lid with access ports through the lid for electrodes and gas inlets and outlets. Approximately 400 g of the previously homogenized and fused electrolyte in the alumina crucible was used with all three electrodes (working, counter and reference) in their access ports in the alumina lid. The crucible was heated up to 600°C in a furnace at a rate of 5°C.min^{-1} under a flowing CO_2 atmosphere (40 mL.min^{-1}; Figure 1(a)). After 1 h equilibration at 600°C, the open circuit potential (OCP) of the working electrode was recorded before subjecting the working electrode to a 5 mV.s^{-1} anodic linear sweep potential to evaluate performance. All experiments were conducted using a Solartron 1286 Electrochemical Interface controlled by CorrWare software.

2.3.2. Concentration Cell Assembly

The purpose of this cell was to measure the potential difference between similar electrodes in different electrolytes separated by a solid-state oxide ion conductor. The basis of this cell was the covered alumina crucible described in the previous section. A 15 mm outer diameter, 2 mm wall thickness, 8 mol% yttria-stabilized zirconia (YSZ) closed-end tube (Highborn Co., China) was used in this study to contain the unmodified ternary carbonate electrolyte (reference electrolyte), while the same ceramic crucible as used in the previous section contained the alkali metal carbonate eutectic modified with kaolin (test electrolyte). A pair of identical 3 mm diameter graphite rods (purity >99.99%; Alfa Aesar) were used as the sensing electrodes in this setup. Before use graphite rods were heat treated at 600°C under a CO_2 atmosphere (40 mL.min^{-1}) in a tube furnace for 2 h to remove any surface residue and ensure good physical stability for high-temperature testing. All experiments were carried out under 40 mL.min^{-1} CO_2 atmosphere and in this case only the open circuit potential of the cell was measured. This setup is shown in Figure 1(b).

2.4. X-Ray Diffraction Analysis

To examine the nature of the phases present in the alkali metal carbonate eutectic doped with kaolin, room temperature X-ray diffraction (XRD) was carried out. A Philips X'Pert diffractometer was used with Cu Kα radiation (1.5418 Å) at a scanning rate of 2°.min^{-1} over the 2θ range 10-90°. Samples examined included the milled and fused alkali metal carbonate eutectic, as-received and fused kaolin, and the fused eutectic after being modified with kaolin.

3. RESULTS AND DISCUSSION

3.1. Thermal Analysis

3.1.1. Thermogravimetric Analysis (TGA)

TGA was used to observe any sample mass changes during heating and cooling cycles to examine system stability, as well as the possibility of chemical reactions. Analysis was conducted

195   on both the pure starting materials (the ternary alkali metal carbonate eutectic and the as-received

196   kaolin), as well as various mixtures of the kaolin in the carbonate eutectic.

197   When kaolin was heated to 600°C under a CO_2 atmosphere, a mass loss of 12.5% was

198   observed (Figure 2(a)). The main mass loss process for kaolin occurred over the temperature range

199   420°-520°C, and was attributed to the removal of water from kaolin to form metakaolin [19]; i.e.,

   $$Al_2[Si_2O_5](OH)_4 \rightarrow Al_2O_3.2SiO_2 + 2H_2O \qquad \qquad …(4)$$

200   Any discrepancy between the reported mass loss of kaolin (11.2-14.5%) [19-21] and the theoretical

201   amount of 13.95% (based on the loss of water and formation of metakaolin (Eqn 4)) can be explained

202   by the influence of material properties. It was reported that the degree of kaolin disorder [22], heating

203   rate of the thermal process [23] or impurities present in kaolin [24] were the main reasons for

204   observed discrepancy. It was also found here that reheating of the sample after the initial heating-

205   cooling cycle did not show any further mass loss. This suggests that all thermal changes of kaolin

206   within this temperature range are irreversible processes, in agreement with previous work [25].

207   Thermal analysis of the pure ternary carbonate eutectic (Figure 2(a)) shows that after surface

208   moisture removal up to 150°C, very limited mass loss occurs over the remainder of the temperature

209   range., it recommends that any mass loss might be   due to carbonate decomposition [26], which is

210   known to be minimal under CO_2 atmospheres; i.e.,

   $$M_2CO_3(s) \leftrightarrow M_2O(s) + CO_2(g) \qquad \qquad …(5)$$

211   where M = Li, Na or K. Table 1 shows a summary of mass loss data from mixtures of the alkali metal

212   carbonate eutectic with kaolin after the first heating cycle, over the full heating and cooling program,

213   and also the calculated mass loss based on Eqn (4).

214   It was expected that the highest concentration of kaolin should have the highest mass loss

215   (Figure 2(b)) since it contains the highest level of water that can be released during metakaolin

216   formation (Eqn (4)). To determine whether the total mass loss was consistent with the water loss

217   expected from the kaolin (Eqn (4)), the mass loss from each sample was also calculated (Table 1).

218   These calculations showed that initial and final mass loss of all of the samples are higher than

219   calculated amounts, suggesting that other reactions beyond water loss from kaolin are occurring

220   (Figure 2(b)). The majority of this mass loss occurs in the first cycle, likely due to the interaction of

221 water with carbonate at elevated temperatures. Additional mass loss observed during cycling may

222 be attributable to the dissolution of kaolin in the eutectic melt forming new species which may react

223 to further release CO_2 or H_2O [27]. To confirm that the highest mass loss occurred during the first

224 fusing, pre-fused 15 wt.% kaolin was subjected to the same heating/cooling protocol as an untreated

225 sample, and the results are compared with an unfused sample in Figures 2(c) and (d). The results

226 presented the constant mass throughout repeated heating and cooling cycles for the pre-fused

227 mixture. It demonstrates the mixture is stable under operating temperatures with very little initial

228 mass loss which confirms the most of mass loss occurred during the first heat-up cycle.

229

230 ### 3.1.2. Differential Thermal Analysis (DTA)

231 The normalized DTA response during extended heating and cooling cycles of various mixtures

232 was analyzed to explore melting process which includes the impact of kaolin on carbonate melt

233 kinetics. The Friedman method was employed to model the kinetics of melting, in which case the

234 DTA response with various heating rates was required.

235 Initially, the thermal behaviour of the pure ternary carbonate eutectic was studied to establish

236 a baseline for comparison. The DTA response from melting the pure ternary carbonate eutectic at

237 different heating rates is shown in Figure 3(a), revealing that melting occurs in the temperature range

238 370°-410°C, as previously observed [17]. The single peak of the DTA response shows that the

239 sample is a well-homogenized mixture and the broad shape of the curve represents kinetic limitations

240 with melting. In this study, the onset temperature of the DTA curve is considered as the melting point

241 and this consideration is applied to all samples to ensure consistency.

242 The same heating program was applied to the ternary carbonate eutectic doped with kaolin, in

243 which case the DTA response was modified both in terms of melting point and area bounded by the

244 curve, as shown in Figure 3(b). The melting point can be seen to be lowered from 385°C for the pure

245 eutectic to ~380°C for a 5 wt.% kaolin-modified mixture. The main reason for this decrease in melting

246 temperature is believed to be the dissolution of kaolin into the molten carbonate eutectic, which has

247 been shown to act as an excellent solvent, able to dissolve metal oxides and compounds of alkali

248 and alkaline earth metals [28]. A decrease in melting point was also observed by Glenn et al. [17]

249 with 5 wt% kaolin doped carbonate which was discussed due to disruption of liquid-phase resulting

250 in a lower chemical potential. There is little information in the literature regarding the interaction of

251 kaolin with alkali metal carbonate salts at high levels and high temperatures, including any

252 information on the possibility of forming new phases. Heller et al. [29] showed that the interaction

253 between kaolin and carbonate salts (Na_2CO_3 and K_2CO_3) at temperatures below $600°C$ in air formed

254 a modified metakaolin, in which cations of alkali metal salts were incorporated directly into the

255 alumina-silicate structure of kaolin without any change in Al/Si ratio. The reaction commenced with

256 dehydroxylation of kaolin, which acted as the solvent at temperatures even lower than the alkali

257 metal carbonate melting point via the following proposed reaction:

$$2SiO_2.Al_2O_3.2H_2O + M_2CO_3 \rightarrow 2SiO_2.Al_2O_3.M_2O + H_2CO_3 + H_2O \qquad \qquad …(6)$$
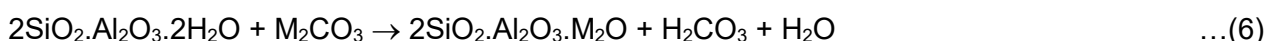
258 where M denotes Na or K. They also showed that reaction between carbonate salts and kaolin was

259 much faster than with pre-heated metakaolin due to presence of water in the kaolin structure, which

260 appeared to act as a catalyst for the reaction in Eqn (6). However, in the current study, the mixture

261 of ternary carbonate salts melts at a much lower temperature than single salts, and the presence of

262 water is therefore apparently not essential for commencing this reaction.

263   It was observed that by increasing the proportion of kaolin in the mixture (10-15 wt.%), the

264 melting point increased by ~$12°C$ (Figure 3(b)) compared to the pure eutectic probably due to

265 disruption of melting behaviour of carbonate in presence of higher amount of kaolin suspended in

266 system. The melting point did not increase any further with the addition of 20 wt.% kaolin as result

267 of meeting the saturation limit of kaolin in the carbonate melt. Moreover, other qualitative changes

268 did appear in the DTA results, including changes in the DTA response with the development of a

269 second peak after 10 wt.% kaolin, as well as changes in the DTA peak area. The introduction of the

270 second peak is likely a result of suspended kaolin, not dissolved because of saturation.

271   The activation energy of the melting process represents the amount of energy required for the

272 electrolyte to undergo a solid to liquid phase change, and it can be an important factor in determining

273 the energy consumption of a DCFC system and the level of thermal disruption of the melt. In this

274 regard, the pure alkali metal carbonate eutectic, as well as kaolin, were evaluated in terms of the

275 activation energy for melting. Among different approaches for determining the activation energy, the

276 Friedman method was selected for this study because it does not consider any kinetic order or

277 thermal model in its formula [17]; i.e.,

$$\beta \frac{d\alpha}{dT} = Af(\alpha)\exp\left(-\frac{E_A}{RT}\right) \qquad \qquad \dots(7)$$

278 where β is the heating rate (K.min^{-1}), α is the extent of conversion for the thermal process, T is the

279 temperature (K), A is the pre-exponential factor (min^{-1}), $f(\alpha)$ is a function describing the nature of the

280 thermal process under study, E_A is the activation energy of the process (J.mol^{-1}), and R the gas

281 constant (8.3143 J.K^{-1}.mol^{-1}). To begin analysis, the extent of conversion (α) is calculated from the

282 DTA response and normalized per mg of sample (μV.mg^{-1}), as shown in Figure 3(c). The activation

283 energy can then be determined from Eqn (7) by plotting $\ln(\beta d\alpha/dT)$ versus 1/T, in which case the

284 slope is $-E_A/R$. Examples of the calculated activation energy, as a function of extent of conversion,

285 are shown in Figure 3(d), in this case pure eutectic and the 10 wt.% kaolin modified samples have

286 been selected as the example. Addition of up to 10 wt.% kaolin to the electrolyte decreased the

287 activation energy of melting process substantially, the implication being that less energy is required

288 to liquefy the electrolyte in comparison with pure eutectic. Changes in the activation energy for

289 melting has been observed previously with addition of other types of coal mineral matter in a ternary

290 carbonate electrolyte (up to 5 wt.% mineral loading) [17]. , It was suggested that dissolution of the

291 additive into the electrolyte occurred in this temperature range [17].

292

293 **3.2. Structural Studies**

294   XRD analysis was used to explore crystalline structures in the alkali metal carbonate eutectic,

295 as well as kaolin modified samples after being homogenized at 600°C. It is worth noting that all

296 samples were cooled to room temperature under a CO_2 atmosphere, and that the solid sample will

297 not necessarily reflect the species present in the molten phase. Some products would be expected

298 to be soluble in molten carbonates and by decreasing the temperature they will precipitate out of the

299 mixture. However, the formation of new solid phase after fusion is a clear indication of the chemical

300 interaction between the kaolin and carbonate salt.

301   Kaolin has been shown to undergo solid state reactions with alkali metal carbonates, in which

302 case the alkali metal cation can exchange for protons in the kaolin structure, leaving the basic

303 alumina-silicate framework unchanged [30]. However, the diffusion rate of each cation into the kaolin

304 framework is dependent on its ionic radius and operational temperature. Heller et al. showed that

the reaction of kaolin and K_2CO_3 produced synthetic kaliophilite ($KSiAlO_4$) if there is an excess of carbonate salt at 500°-590°C [31]. Phase transition of K_2CO_3 happened at about 400°C in this case and was converted to an active phase which could react effectively with different oxides including SiO_2 and Al_2O_3 within the kaolin structure, suggesting kaolin did react directly with K_2CO_3 [31]. However, Na_2CO_3 undergoes a phase transition at a much higher temperature, and did not show the same high reactivity with kaolin as K_2CO_3 resulting in a limited Na^+-exchanged material, the structure of which was consistent with carnegieite ($NaAlSiO_4$) [31]. The reaction between Li_2CO_3 and kaolin was similar to Na_2CO_3 with the formation of β- ucryptite ($LiAlSiO_4$) [32]. In this study, a mixture of all three alkali carbonates exists instead of a single salt which melts at a temperature lower than 400°C, and as such the reaction between carbonate and kaolin could occur at both the solid-solid and solid-liquid interface during heating.

XRD patterns of each starting material and the products of the reaction between kaolin and the ternary alkali carbonate eutectic are shown in Figure 4. The patterns for kaolin and kaolin heat-treated under a CO_2 atmosphere at 600°C (fused kaolin) are shown in Figure 4(a), indicating that kaolin has undergone a transition to amorphous metakaolin in this temperature range [25, 33], as suggested previously in the thermal studies (Figure 2(a)). Mechanical mixing (milling) of the alkali metal carbonates has caused the formation of new compounds (Figure 4(a)), which are a combination of the individual carbonates, such as $LiKCO_3$ and $NaKCO_3$. The presence of these new phases is also evident, although somewhat altered, after thermal treatment at 600°C (Figure 4(a)).

With the addition of kaolin to the ternary alkali metal carbonate eutectic, the XRD patterns change noticeably, with evidence of new peaks, changes in intensity of some already peaks, as well as the removal of others (Figure 4(b)). This comparison allows us to see clearly that the dissolution of kaolin or the reaction of kaolin with the molten carbonate eutectic does occur under the operating conditions used here. Evidence for species such as $NaAlSiO_4$, $KAlSiO_4$, $LiAlSiO_4$ and SiO_2 can be seen in Figure 4(b). Increasing the kaolin content in the electrolyte changed the XRD patterns only slightly.

3.3. Electrochemical Analysis

3.3.1. Electrochemical Performance

334　　　　The half-cell used here to assess electrochemical performance focuses specifically on the

335　　intrinsic anodic behaviour. Graphite is used as the working electrode due to its high electrical

336　　conductivity at high temperature [16]. However, graphite has lower wettability towards the molten

337　　carbonate electrolyte than other types of carbon such as coal [34, 35], which have higher disorder

338　　and more active surface sites. Additionally, the more uniform graphite is expected to have slower

339　　oxidation kinetics compared to coal-based sources, resulting in poorer performance [36]; however,

340　　it is a better material for obtaining more fundamental and comparative kinetic data [37] as required

341　　here because of its uniformity, unlike coal. The electrochemical half-cell shown in Figure 1(a) was

342　　set up to evaluate the impact of kaolin on graphite electro-oxidation when it was mixed with

343　　electrolyte. Electrochemical measurements include the open circuit potential (OCP), to determine

344　　stability, and linear sweep voltammetry (LSV) to evaluate performance.

345　　　　The OCP of the system under study was measured after 1 h of stabilization at 600°C, with

346　　OCP data collected over 5 min shown in Figure 6(a). To ensure reproducibility, each test was

347　　repeated in triplicate. Slight deviations were observed so the average value is reported along with

348　　the standard deviation. The potential difference between the graphite working (pellet) and reference

349　　(rod) electrodes is -0.24±0.05 V vs $C/CO_2/CO_3^{2-}$. Since both electrodes are made of graphite, the

350　　OCP value is expected to be zero. One possible reason for this difference is the impact of

351　　atmospheric CO_2 gas environment around the reference electrode, which does not exist around the

352　　working electrode (surrounded by just molten electrolyte and no gaseous CO_2). This result indicates

353　　the gas environment around the electrode affects its OCP, and this influence has also been reported

354　　by different research groups [38, 39]. Jiang et al. found that higher OCP under N_2 compared with

355　　CO_2, which was attributed to changes in overall gas equilibria [8].

356　　　　Carbon can be electro-oxidized in a molten carbonate electrolyte via [36, 40]:

$$C + 2CO_3^{2-} \rightarrow 3CO_2 + 4e^- \qquad\qquad\qquad …(8)$$

$$C + CO_3^{2-} \rightarrow CO_2 + CO + 2e^- \qquad\qquad\qquad …(9)$$

357　　The carbonate ions themselves can also be produced and consumed according to an equilibrium

358　　which exists in the melt; i.e.,

$$CO_2 + O^{2-} \leftrightarrow CO_3^{2-} \qquad\qquad\qquad …(10)$$

359   If complete oxidation of carbon occurred (Eqn (8)) at the working electrode surface (this assumption

360   is employed for simplifying the calculation), the OCP of the cell (E_{Cell}) according to the Nernst

361   equation can be described by:

$$E_{Cell} = E_W - E_R = \frac{3RT}{4F} \ln\left(\frac{P_{CO_2,W}}{P_{CO_2,R}}\right)$$

where   …(11)

$$E_W = E^\circ + \frac{RT}{4F} \ln\left(\frac{P^3_{CO_2,W}}{a_C \cdot a^2_{CO_3{}^{2-}}}\right) \text{ and } E_R = E^\circ + \frac{RT}{4F} \ln\left(\frac{P^3_{CO_2,R}}{a_C \cdot a^2_{CO_3{}^{2-}}}\right)$$

362   where R is the universal gas constant (8.3143 J/K/mol), T is the temperature (K), F is Faraday's

363   constant (96486.7 C/mol), P is the partial pressure of CO_2 (Pa), E° is the standard reduction potential

364   for Eqn (8) (the value is the same for both electrodes), a_C is the activity of carbon (which is unity for

365   solid graphite) and $a_{CO_3{}^{2-}}$ is the activity of carbonate ion in the electrolyte. Carbonate activity is the

366   same for both reference and working electrode since both electrolytes are based on the molten alkali

367   carbonate eutectic. From Eqn (11) and the measured OCP ($E_{Cell} = -0.24 \pm 0.05$ V vs $C/CO_2/CO_3{}^{2-}$)

368   it can be concluded that the partial pressure of CO_2 gas in carbonate electrolyte near the working

369   electrode at 600°C is 1.3×10³ Pa ($P_{CO_2,R} = 101.325 \times 10^3$ Pa, since the experiment is performed

370   under atmospheric pressure and electrode is exposed to the CO_2 atmosphere).

371   Introducing kaolin into the pure electrolyte and increasing its mass ratio from 5 to 20% (Figure

372   5(a)), the OCP value did not change noticeably from zero, and small variations in OCP are within an

373   expected standard deviation of error. The reason for this phenomenon could be due to a change in

374   electrolyte viscosity after dissolution of kaolin [28]. Changing electrolyte viscosity could cause the

375   impact of CO_2 gas atmosphere to become negligible between the working and reference electrodes,

376   so both electrodes behave similarly (OCP values about zero). The direct observation of electrolyte

377   at 600°C after experiments shows that its viscosity appears to increase with the addition of kaolin

378   and its flowability decreases. This behaviour was also reported by Shen et al. [28] who showed that

379   addition of 10 wt.% kaolin to a ternary alkali metal carbonate eutectic increased the viscosity of the

380   electrolyte.

381   To evaluate graphite electro-oxidation in the presence of kaolin, linear sweep voltammetry

382   (LSV) of the half-cell was also carried out in the different electrolytes using a 5 mV/s scan rate from

383   the OCP to +0.5 V vs $C/CO_2/CO_3^{2-}$. It should be noted that all current responses in Figure 5(b) are

384   averaged from three separate repeat experiments and all data are normalized according to the

385   geometric surface area of the working electrode (1.13 cm^2). It can be seen that the current density

386   of the system increased after adding kaolin from 18 mA/cm^2 to 162 mA/cm^2 at the limit of the LSV

387   sweep (0.5 V vs $C/CO_2/CO_3^{2-}$) for the pure electrolyte and 15 wt.% kaolin, respectively. This indicates

388   about an order of magnitude increase in performance with the added kaolin. The catalytic response

389   to kaolin has been observed previously by Allen et al. [41]; however, in this literature case it was

390   attributed to surface effects (including modification of surface polarity and enhancing the surface

391   area) as the kaolin was integrated into a solid electrode . In the present study, kaolin is present only

392   in the liquid phase and therefore the mechanism is likely to be different. The catalytic behaviour of

393   kaolin for carbon electro-oxidation might be as a consequence of the dissolution of kaolin in the

394   electrolyte, which releases more reactive oxide into the molten electrolyte. It can accelerate the

395   chance of carbon to be oxidised according to Eqn (3).

396   To observe the impact of overpotential on graphite electro-oxidation, the performance of the

397   cell at low and high potential regions is displayed in Figure 5(c). At lower applied potentials (0.2 V),

398   the difference between various electrolytes is not great; however, at 0.5 V the difference between

399   experiments is significant. The reason might be due to the changing nature of the rate determining

400   step with changing potential as explained in previous work that rate determining step was dependant

401   on the potential region of oxidation and carbon type   [42].

402   To investigate performance of the system further and find the optimum concentration of kaolin

403   in electrolyte, the concentration was increased further up to 25 wt.%. As shown in Figures 5(b) and

404   (c), the addition of such high kaolin levels inhibits the performance and lowers the current density of

405   the system to 20 mA/cm^2 for 20 wt.% (at 0.5 V), and lower still for 25 wt.%. It can also be seen that

406   the shape of the voltametric data with 20 wt.% kaolin is different from others. This may be due to

407   saturation of electrolyte with kaolin at 20 wt.% and the subsequent increase in its viscosity [28] which

408   potentially could inhibit CO_2 release from the reaction sites. Another possible hypothesis is that the

409   new phases after reaction between kaolin and carbonate are not in the molten state (particulate

410   species, as shown through double peaks in the DTA responses) which may increase the resistance

411   of the electrolyte [13].

412   All the above experiments were performed with kaolin mixed with ternary carbonate and results

413   have shown that kaolin acted as a catalyst for graphite electro-oxidation. In order to compare these

414   results with metakaolin in terms of graphite oxidation, 15 wt.% metakaolin mixed with ternary

415   carbonate and subjected to the same heat treatments as kaolin was carried out and its performance

416   is presented in Figure 5(d). Metakaolin addition is shown to have the same improved performance

417   as 15 wt.% kaolin with a slightly higher current density value. This difference may be due to faster

418   reaction/dissolution rate of metakaolin with the ternary carbonate. The lower reaction rate of kaolin

419   with ternary carbonate may reflect its shorter exposure time to carbonate at high temperature in

420   comparison with metakaolin. Since metakaolin was first fused at 600°C and then mixed with ternary

421   carbonate and finally fused prior to performing experiments.

422

3.3.2. Impact of Temperature

424   To observe the impact of temperature on carbon electro-oxidation, half-cell experiments were

425   carried out with the pure eutectic and with 15 wt.% kaolin at different temperatures. Note that each

426   experiment was run with fresh electrodes and electrolytes, heated up from room temperature to the

427   designated temperature and the presented results are the average of two separate repeated

428   experiments. Figures 6(a) and (b) show that by increasing the reaction temperature from 400°C

429   (about the melting temperature of electrolyte) to 600°C the performance of the cell is enhanced as

430   expected due to the increasing kinetics of carbon electro-oxidation. Figure 6(b) clearly shows that

431   the changes observed in performance for 15 wt.% kaolin were significant. As the kaolin doped

432   electrolyte has a slightly higher melting temperature (seen in DTA results in Section 3.2) than the

433   pure electrolyte, it is reasonable to observe lower performance at 400°C. It is due to being closer to

434   its melting temperature (possible incomplete dissolution) and higher resistance to oxide ion transfer.

435   However, when the electrolyte is well above its melting temperature (600°C) the impact of kaolin is

436   remarkable compared with lower temperature and undergoes a step change in performance. At

437   500°C the pure electrolyte still revealed better performance than the kaolin doped electrolyte (Figure

438   6(c)), possibly due to lower dissolution rate of kaolin in carbonate electrolyte in comparison with

439   higher temperature (Figure 6(d)). The slope of the I-V curve improved with increasing operational

440   temperature for both pure electrolyte and kaolin-modified electrolyte, showing that the kinetics of

441   carbon electro-oxidation were enhanced at higher temperatures, as expected [11, 43]. However, the

442   changes in the I-V curves are more noticeable in the presence of kaolin at a higher temperature

443   (600°C), compared with lower temperature. If increased oxide activity enhances the performance,

444   the results in Figure 6 can be understood that at high temperatures dissolution of kaolin has

445   increased the activity of oxide ions through a faster mechanistic pathway.

446

447   ### 3.3.3. Concentration Cell

448   To investigate how kaolin affects the oxide activity in the half-cell, a purpose-built concentration

449   cell was developed (Figure 1(b)). The YSZ composite is employed in this study due to its high ionic

450   (oxide) conductivity at elevated temperature in both reducing and oxidizing environments and also

451   its good thermal and chemical stability under the corrosive carbonate environment [44]. The pure

452   eutectic electrolyte was kept inside of the YSZ tube in all tests and referred to as the reference

453   electrolyte. Kaolin-modified electrolyte outside of the YSZ tube was varied and is referred to as the

454   working electrolyte. It is worth noting that the two electrolytes were connected ionically with the YSZ

455   membrane and all data were collected after 1 h resting at 600°C while reaching a stable response

456   (Figure 7(a)).

457   Figure 7(b) shows that OCP value increased almost linearly with increasing mass ratio of kaolin

458   in the electrolyte. To explain these changes the relevant electrochemical reaction in the presence of

459   kaolin is given by Eqn (3), where oxide ions can oxidize the carbon in addition to carbonate ions from

460   the electrolyte. Analysis of the potential difference using the Nernst equation shows that the

461   experimental variables that can contribute to the potential difference are the partial pressure of CO_2,

462   the activity of solid carbon (a_C) and oxide ion activity ($a_{O^{2-}}$); i.e.,

$$E = E^\circ + \frac{RT}{4F} \ln\left(\frac{P_{CO_2}}{a_C \cdot a_{O^{2-}}^2} \right) \qquad \qquad \dots(12)$$

463   Because the partial pressure of CO_2 and activity of solid carbon are kept constant in this arrangement

464   (Figure 1(b)), as opposed to the previous calculation in Section 3.3.1, consequently the OCP (ΔE) of

465   the cell can be calculated by:

$$\Delta E = \frac{RT}{2F} \ln \left(\frac{a_{O^{2-},W}}{a_{O^{2-},R}} \right)$$
        …(13)

466   It can be concluded that oxide ion activity indeed increased with the addition of kaolin and, therefore

467   resulted in the positive potential difference between electrodes. This assumption must be attributed

468   to the dissolution of kaolin in carbonate melt and subsequent modification of kaolin (reacting with

469   carbonate to form new ionic species), as suggested by XRD results (Section 3.2). Figure 8 shows a

470   schematic of possible reactions occurring on the surface of graphite before and after the addition of

471   kaolin. As can be seen in Figure 8(a) with pure electrolyte, carbonate ions are the probable oxidant

472   required to contact the carbon surface and produce electrons and CO_2 (Eqn (8)). Some oxide is likely

473   also present, however the CO_2 gas atmosphere used in experiments pushed the equilibrium of Eqn

474   (10) to favour the preference of carbonate ions. The excess of oxide ions present at the surface of

475   the electrode after addition of kaolin (Figure 8(b)). It potentially lowered CO_2 dissolution in the melt

476   whichsuggest that both carbonate and oxide ions are present and result in enhanced electrochemical

477   performance.

478   Another possible pathway for enhanced performance could be through reduced CO_2 activity in

479   the electrolyte. Oxide from the dissolution of kaolin could combine with available CO_2 dissolved in

480   the electrolyte and reduce the CO_2 activity in the electrolyte. It would also be expected to result in an

481   increase in the OCP value as shown in Nernst equation Eqn (8) [45].

482   Increasing oxide content in carbonate electrolyte due to the dissolution of kaolin at 600ºC is

483   suggested here to be the main reason for the improvement of performance in the electrochemical

484   cell. Graphite electro-oxidation in the absence of kaolin in electrolyte showed a limited activity in

485   current density response but it was improved after addition of kaolin from 10 wt% and reached to the

486   highest value at 15 wt%. Even though kaolin is the mineral matter in coal and might be expected to

487   have an inhibitory effect on carbon oxidation [13], this study showed that the presence of 15 wt% of

488   kaolin not only enhanced the current density of the cell, but also the degree of its improvement is

489   about one order of magnitude (current density of undoped electrolyte and 15 wt% kaolin is 18

490 mA/cm^2 and 162 mA/cm^2 ,respectively). It was also presented that addition of kaolin more than 15

491 wt% in ternary carbonate electrolyte, for instance, 20 wt%, can cause an inhibitory effect on the

492 performance of electrochemical cell. It is due to saturation of the electrolyte with kaolin which can

493 increase the ionic resistivity of the system. The dissolution mechanism of kaolin in the electrolyte as

494 explained in this study is similar to metal oxide dissolution in carbonate melt which was studied by

495 different research groups [46] in terms of increasing oxide content in the electrolyte and enhancing

496 the electrochemical cell. It was previously reported that the addition of 10 wt% ash to ternary

497 carbonate melt did not have any effect on the current density of the cell [47], however the maximum

498 allowable level of ash in system without disruption in power output has not previously been reported.

499

500

501 **4. CONCLUSIONS**

502 The kaolin content of coal showed a substantial impact on the performance of the direct carbon

503 fuel cell in terms of thermal and electrochemical performance. The increasing weight ratio of kaolin

504 in the electrolyte changed the thermal behaviour of the electrolyte, as well as carbon electro-

505 oxidation performance in an electrochemical cell, expected to extend to a full DCFC system. The

506 role of kaolin in the melting behaviour of eutectic ternary carbonate electrolyte was investigated by

507 TGA and DTA and demonstrated that adding kaolin to the electrolyte reduced the melting

508 temperature of the mixture, as well as the activation energy of melting process due to dissolution of

509 kaolin in molten carbonate. Addition of kaolin up to 10 wt.% lowered the melting point of the

510 electrolyte, while addition of additional kaolin past this loading was observed to result in an increased

511 melting temperature, and an expectation of carbonate saturation with kaolin was implied past this

512 point. The electrochemical impact of kaolin doping in the ternary alkali metal carbonate eutectic at

513 600°C under a CO$_2$ atmosphere indicated that kaolin behaved as a catalyst, providing an enhanced

514 mechanistic pathway for graphite electro-oxidation. 15 w.t% kaolin in the eutectic showed the best

515 electrochemical performance, with an almost order of magnitude increase compared to the pure

516 electrolyte due to release of oxide ions in electrolyte as a result of dissolution. Higher levels of kaolin

517 inhibited carbon electro-oxidation showing that 15 wt.% is the optimum level of kaolin in a real

system. Increasing oxide ion concentration in the electrolyte is suggested to be the main reason for the electrochemical enhancement of the cell.

6. REFERENCES

1.   Giddey, S., et al., A comprehensive review of direct carbon fuel cell technology. Progress in Energy and Combustion Science, 2012. 38(3): p. 360-399.

2.   G r, T.M., Critical review of carbon conversion in "carbon fuel cells". Chemical reviews, 2013. 113(8): p. 6179-6206.

3.   Deleebeeck, L. and K.K. Hansen, Hybrid direct carbon fuel cells and their reaction mechanisms—a review. Journal of Solid State Electrochemistry, 2014. 18(4): p. 861-882.

4.   Cao, T., et al., Recent advances in high-temperature carbon–air fuel cells. Energy & Environmental Science, 2017. 10(2): p. 460-490.

5.   Cooper, J.F., Direct conversion of coal derived carbon in fuel cells, in Recent trends in fuel cell science and technology. 2007, Springer. p. 248-266.

6.   Gür, T.M., Review of electrical energy storage technologies, materials and systems: challenges and prospects for large-scale grid storage. Energy & Environmental Science, 2018. 11(10): p. 2696-2767.

7.   Allen, J.A., M. Glenn, and S.W. Donne, Analysis of theoretical efficiency in a model 10 kW direct carbon fuel cell using a coal based carbonate slurry. Electrochimica Acta, 2020. 329: p. 135131.

544   8.   Jiang, C. and J.T. Irvine, Catalysis and oxidation of carbon in a hybrid direct carbon fuel cell.

545   Journal of Power Sources, 2011. 196(17): p. 7318-7322.

546   9.   Allen, J., et al., Molten carbonate composition effects on carbon electro-oxidation at a solid

547   anode interface. Journal of The Electrochemical Society, 2015. 162(1): p. F76-F83.

548   10.   Jiang, C., et al., Application of ternary carbonate in hybrid direct coal fuel cells. Ecs

549   Transactions, 2014. 59(1): p. 281-288.

550   11.   Jain, S.L., et al., Electrochemical performance of a hybrid direct carbon fuel cell powered by

551   pyrolysed MDF. Energy & Environmental Science, 2009. 2(6): p. 687-693.

552   12.   Weaver, R. and L. Nanis. Electrochemical oxidation of carbon in a molten carbonate coal-air

553   fuel-cell. in JOURNAL OF THE ELECTROCHEMICAL SOCIETY. 1980. ELECTROCHEMICAL

554   SOC INC 10 SOUTH MAIN STREET, PENNINGTON, NJ 08534.

555   13.   Li, X., et al., Evaluation of raw coals as fuels for direct carbon fuel cells. Journal of Power

556   Sources, 2010. 195(13): p. 4051-4058.

557   14.   Liu, J., et al., Effect of sulfur and its compounds on the performance of graphite

558   electrooxidation in molten carbonate. Journal of Power Sources, 2015. 274: p. 71-76.

559   15.   Gong, M., et al., Sulfur-tolerant anode materials for solid oxide fuel cell application. Journal of

560   Power Sources, 2007. 168(2): p. 289-298.

561   16.   Tulloch, J., et al., Influence of selected coal contaminants on graphitic carbon electro-

562   oxidation for application to the direct carbon fuel cell. Journal of Power Sources, 2014. 260: p. 140-

563   149.

564   17.   Glenn, M.J., J.A. Allen, and S.W. Donne, Thermal Investigation of a Doped Alkali-Metal

565   Carbonate Ternary Eutectic for Direct Carbon Fuel Cell Applications. Energy & Fuels, 2015. 29(8):

566   p. 5423-5433.

567   18.   An, X., et al., Determination and evaluation of the thermophysical properties of an alkali

568   carbonate eutectic molten salt. Faraday discussions, 2016. 190: p. 327-338.

569   19.   Hindar, J., et al., Investigation of Some Kaolines by Simultaneous DTA/TG and

570   Thermosonimetry, in Thermal Analysis. 1980, Springer. p. 313-318.

571   20.   Van Olphen, H. and J.-J. Fripiat, Data handbook for clay materials and other non-metallic

572   minerals: providing those involved in clay research and industrial application with sets of

573   authoritative data describing the physical and chemical properties and mineralogical composition of

574   the available reference materials. 1979: Pergamon.

575   21.   Ptáček, P., et al., The influence of structure order on the kinetics of dehydroxylation of

576   kaolinite. Journal of the European Ceramic Society, 2013. 33(13-14): p. 2793-2799.

577   22.   Heide, K. and M. Földvari, High temperature mass spectrometric gas-release studies of

578   kaolinite Al2 [Si2O5 (OH) 4] decomposition. Thermochimica Acta, 2006. 446(1-2): p. 106-112.

579   23.   Castelein, O., et al., The influence of heating rate on the thermal behaviour and mullite

580   formation from a kaolin raw material. Ceramics International, 2001. 27(5): p. 517-522.

581   24.   MacKenzie, K., EFFECTS OF IMPURITIES ON FORMATION OF MULLITE FROM

582   KAOLINITE MINERALS. 2. EFFECT OF EXCHANGEABLE ANIONS. TRANSACTIONS OF THE

583   BRITISH CERAMIC SOCIETY, 1969. 68(3): p. 101-+.

584   25.   Insley, H. and R.H. Ewell, Thermal behavior of the kaolin minerals. J. Res. Natl. Bur. Stand,

585   1935. 14(5): p. 615-27.

586   26.   White, S. and U. Twardoch, The solubility and electrochemistry of alkali metal oxides in the

587   molten eutectic mixture of lithium carbonate-sodium carbonate-potassium carbonate. Journal of

588   applied electrochemistry, 1989. 19(6): p. 901-910.

589   27.   Yan, K., et al., Decomposition and phase transformation mechanism of kaolinite calcined

590   with sodium carbonate. Applied Clay Science, 2017. 147: p. 90-96.

591   28.   Shen, J., et al., Interactions between molten salts and ash components during Zhundong

592   coal gasification in eutectic carbonates. Fuel, 2017. 207: p. 365-372.

593   29.   Heller-Kallai, L., Reactions of salts with kaolinite at elevated temperatures. I. Clay Minerals,

594   1978. 13(2): p. 221-235.

595   30.   Kubo, Y., G. Yamaguchi, and K. Kasahara, Inverted phase relation in the formation of

596   nepheline and carnegieite from the system kaolinite—sodium carbonate. American Mineralogist:

597   Journal of Earth and Planetary Materials, 1966. 51(3-4_Part_1): p. 516-521.

598   31.   Heller-Kallai, L. and I. Lapides, Thermal reactions of kaolinite with potassium carbonate.

599   Journal of thermal analysis and calorimetry, 2003. 71(3): p. 689-698.

600   32.   Kubo, Y. and T. Yamada. Mechanism of solid state reactions between Kaolin and alkali

601   (Lithium, Sodium and Potassium) carbonates. in Proceedings of International Clay Conference.

602   1969.

603   33.   Cheng, H., et al., The thermal behavior of kaolinite intercalation complexes-A review.

604   Thermochimica Acta, 2012. 545: p. 1-13.

605   34.   Chen, M., et al., Carbon anode in direct carbon fuel cell. International journal of hydrogen

606   energy, 2010. 35(7): p. 2732-2736.

607   35.   Cooper, J.F. and R. Selman, Electrochemical oxidation of carbon for electric power

608   generation: a review. Ecs Transactions, 2009. 19(14): p. 15-25.

609   36.   Cherepy, N.J., et al., Direct conversion of carbon fuels in a molten carbonate fuel cell.

610   Journal of the Electrochemical Society, 2005. 152(1): p. A80-A87.

611   37.   Allen, J.A., et al., Kinetic Analysis of the Anodic Carbon Oxidation Mechanism in a Molten

612   Carbonate Medium. Electrochimica Acta, 2014. 129(0): p. 389-395.

613   38.   Jiang, C., et al., Demonstration of high power, direct conversion of waste-derived carbon in a

614   hybrid direct carbon fuel cell. Energy & Environmental Science, 2012. 5(5): p. 6973-6980.

615   39.   Rady, A.C., et al., Catalytic gasification of carbon in a direct carbon fuel cell. Fuel, 2016. 180:

616   p. 270-277.

617   40.   Gür, T.M., Mechanistic Modes for Solid Carbon Conversion in High Temperature Fuel Cells.

618   Journal of The Electrochemical Society, 2010. 157(5): p. B751-B759.

619   41.   Allen, J.A., et al., An investigation of mineral distribution in coking and thermal coal chars as
620   fuels for the direct carbon fuel cell. Fuel, 2018. 217: p. 11-20.

621   42.   Allen, J.A., et al., Kinetic analysis of the anodic carbon oxidation mechanism in a molten
622   carbonate medium. Electrochimica Acta, 2014. 129: p. 389-395.

623   43.   Xu, X., et al., A comparative study of different carbon fuels in an electrolyte-supported hybrid
624   direct carbon fuel cell. Applied energy, 2013. 108: p. 402-409.

625   44.   Jiang, C., et al., Challenges in developing direct carbon fuel cells. Chemical Society
626   Reviews, 2017. 46(10): p. 2889-2912.

627   45.   Nabae, Y., K.D. Pointon, and J.T. Irvine, Electrochemical oxidation of solid carbon in hybrid
628   DCFC with solid oxide and molten carbonate binary electrolyte. Energy & Environmental Science,
629   2008. 1(1): p. 148-155.

630   46.   Wang, C.Q., et al., Significant improvement of electrooxidation performance of carbon in
631   molten carbonates by the introduction of transition metal oxides. Journal of Power Sources, 2013.
632   233: p. 244-251.

633   47.   Vutetakis, D., D. Skidmore, and H. Byker, Electrochemical Oxidation of Molten Carbonate-
634   Coal Slurries. Journal of the electrochemical society, 1987. 134(12): p. 3027-3035.

635

636

637

638

639

Thermal behaviour of silica in contact with an alkali-metal carbonate mixture used in direct carbon fuel cell applications

Simin Moradmand[1], Scott Donne[2], Jessica Allen[1]*

[1] Discipline of Chemical Engineering, University of Newcastle, University Drive Callaghan NSW 2308

[2] Discipline of Chemistry, University of Newcastle, University Drive Callaghan NSW 2308

ABSTRACT

The potential impact of coal mineral matter on the thermal behavior of an alkali-metal carbonate ternary eutectic, commonly employed in direct carbon fuel cells (DCFC), has been considered here. Silica (or quartz), as one of the dominant mineral compounds in coal, has been used in this study to investigate its impact on the thermal behaviour of eutectic ternary alkali carbonate electrolyte, $(Li/Na/K)_2CO_3$, when doped up to 20 wt% with silica. Results from thermal analysis have revealed that silica can increase the melting point of the electrolyte up to 17°C, depending on the silica mass ratio. Thermogravimetric studies showed a significant mass loss after addition of silica to the ternary carbonate, corresponding to a chemical reaction between silica and carbonate salts which was evidenced by the formation of new silicate phases and the evolution of CO_2 gas. Formation of new phases has been shown with characteristic tests including XRD, SEM/EDS and FTIR. Results suggest that all three alkali-metal

carbonates reacted with silica simultaneously, forming a number of corresponding silicate species. It can be concluded that silica-rich ash with a concentration beyond 15 wt% in the electrolyte will lead to irreversible changes in composition and character of the electrolyte in DCFC applications, and must be considered when designing a continuously operating system.

Keywords:

Alkali-metal carbonate; Silica; Coal mineral matter; Molten salt thermochemistry; direct carbon fuel cell

* Corresponding Author: Dr Jessica Allen, e: j.allen@newcastle.edu.au ph: +612 40 339359

1. Introduction

A high-temperature direct carbon fuel cell (DCFC) can generate electricity from different sources of carbon fuels at elevated temperature in the presence of a liquid or solid electrolyte to achieve high electrical efficiency with low CO_2 emissions [1]. Among several variations of DCFC arrangement, the hybrid direct carbon fuel cell (H-DCFC) combines both molten and solid electrolytes to increase electrochemical conversion of carbon by extending triple-phase boundaries and reducing cell resistance [2]. Alkali metal carbonates have been commonly used as the molten electrolyte in H-DCFC due to their high chemical stability and low decomposition loss under CO_2 atmosphere, as well as a good ionic conductivity at high operating temperature [2-3]. However, some fundamental and design challenges must be addressed before scale-up of this efficient system including fabrication of stable materials against the corrosive carbonate electrolyte at high temperature, improving the electrochemical performance of the cell and fuel pre-processing which can affect the long term stability of the system [2-3].

Among different sources of fuels for the DCFC, coal has been shown to have a high power output when it was tested in different arrangements [4-7]. The fuel type and its properties such as surface area, particle size, structure and surface functional groups have been known as important factors in the determination of cell performance [8]. The impact of coal mineral matter on the performance of a fuel cell containing molten carbonate electrolyte has not been investigated widely with only a limited number of studies [9-11]. Moreover, it is very important to understand the changes in electrolyte properties which may occur if coal mineral matter interacts with electrolyte in a slurry type of DCFC.

Alkali carbonates including Li_2CO_3, Na_2CO_3, K_2CO_3 are commonly used as an electrolyte with eutectic binary or ternary composition in various DCFC set-ups. The reason for using eutectic binary or ternary composition is its lower melting temperature compared with a single salt [12] which results in a more flexible operating temperature range. After the addition of coal in the electrolyte, the mineral matter of coal can change the properties of electrolyte from the initial state, especially if the concentration of mineral matter increased during the long-term application of DCFC. These impacts can be important in different aspects such as changing the ionic conductivity of the electrolyte, the viscosity or thermal conductivity of electrolyte depending on the type of mineral matter and its concentration in the mixture [13-16].

The influence of coal mineral matter on the thermal properties of the electrolyte is another important factor since impurities may dissolve in the electrolyte and alter the chemical composition of the molten electrolyte. For instance, the inclusion of 1 wt% silica nanoparticles in eutectic Li_2CO_3 - K_2CO_3 mixture increased the specific heat capacity by 25% compared to pure binary molten salt, regardless of the size of silica particles [17]. It was explained that the surface area of new compounds increased due to formation of the needle-like structured nanomaterial after addition of silica to molten salts at 560ºC, consequently enhancing specific

heating capacity. Shen et al. showed that coal minerals including kaolin, silica, $CaSO_4$ and $CaCO_3$ reacted with a carbonate electrolyte and Si/Al compounds in coal minerals increased the viscosity of the ternary electrolyte and decreased the thermal conductivity [13]. Other mineral compounds were not found to have a significant influence, however, they did not vary concentration of the specific mineral impurity used in their study [13]. Glenn et al. showed that coal mineral contaminations affected thermal behaviour of carbonate electrolyte in terms of the melting temperature and activation energy required for melting if those minerals are mixed with carbonate mixture at 5 wt% level [14].

Silica has been used in glass-ceramic industries as well to determine the properties of the crystalline phase after reaction with single alkali salts, mostly in a binary system composed of Li_2O-SiO_2 [18] [19]. However, in glass-ceramic industries, the information about the possible new phases limited to the mainly solid-state reaction between single salts and silica and the research regarding the molten phase reaction between binary or ternary alkali carbonate with silica is rare. Addition of silica to single alkali salts has been also studied in CO_2 capture areas to investigate the capacity of different silicate compounds in absorbing CO_2 gas in different situations [20-22]. Even though there has been some progress in the above-mentioned area, the impact of silica in molten electrolyte properties in a fuel cell system has not been studied with the purpose to correlate the performance the fuel cell with electrolyte properties in presence of different mass ratio of mineral matter. There is almost no additional work available to show the changes of melting behaviour of electrolyte if the mass ratio of impurities increases in the mixture or what will be an optimum level of coal mineral matter without thermal disruption of molten carbonate electrolyte. Most of the studies regarding the impact of coal mineral matters on DCFC were about the electrochemical impact of ash on the cell without consideration of the possible impact on the electrolyte [10-11].

Herein, silica (quartz) has been selected as the most dominant mineral matter of coal [23], to study its impact on the thermal properties of electrolyte. The eutectic ternary mixture of Li_2CO_3, Na_2CO_3, and K_2CO_3 has been considered as the mass percentage of silica is added to the electrolyte from 5-30 wt%. The thermal behaviour is investigated by differential thermal analysis (DTA) and thermogravimetric analysis (TGA) to find comprehensive information about the changing melting behaviour of electrolyte in the presence of silica. Furthermore, the characteristic properties of new products formed after reaction between silica and ternary eutectic electrolyte have been tested with XRD, FTIR, and SEM-EDS methods.

2. Experimental

2.1. Carbonate sample preparation

A eutectic ternary alkali carbonate has been prepared with a composition of Li_2CO_3, Na_2CO_3 and K_2CO_3 (Sigma Aldrich and Chem Supply, >99% purity) in 32.0%:33.5%:34.5% weight ratio, respectively. All chemicals were dried in an oven at 110ºC for at least 24 hours before mixing to remove any surface moisture. For making a homogeneous ternary mixture, a ball mill (Fritsch Pulverisette 6) was used to mix all single salts for one hour using a stainless steel bowl and balls. Oven-dried silica (Sigma Aldrich, 99%> purity, 5-10 μm particle size) has been added to milled ternary alkali salt mixture in the mass ratio of 5 to 30 wt% and again a ball milling procedure has been carried out for silica and ternary carbonate mixtures (this mixture referred as the milled mixture for later). These samples have been used for thermal analysis tests.

Milled 5, 10, 15, 20 wt% silica samples have been fused in a muffle furnace at 600ºC with a heating rate of 3ºC min^{-1} from room temperature under 40 mL.min^{-1} CO_2 (Food grade, BOC) atmosphere. All samples have been fused at 600ºC for 2hr to ensure a good homogeneous mixture. All fused samples were grounded to fine particles with mortar and pestle after cooling

down to room temperature under CO_2 atmosphere. These powders were used for characteristic tests.

2.2. Thermal analysis experiment procedure

Thermal behaviour of different samples has been investigated with thermogravimetric analysis (TGA) and differential thermal analysis (DTA) by a Netzsch STA 2500 Regulus instrument. 10-15 mg of each milled sample placed in alumina crucible with α-Al_2O_3 (Alfa Aesar; 99.99% purity) used as the reference material. Thermal protocol as following has been applied for all samples under 40 mL.min^{-1} CO_2 atmosphere:

1) From room temperature to 150°C with 5°C.min^{-1} heating rate and holding the samples at 150°C for 1 hr to ensure all surface moisture removed.

2) Three heating and cooling cycles from 300°C to 600°C with 5°Cmin^{-1} heating rate to achieve a good homogenized mixture.

2.3. Characterisation tests

Different characterisation tests were carried out to investigate the changes happening in the electrolyte before and after heat-treatment in the absence and presence of silica. X-ray diffraction (XRD) performed with a Philips X'Pert diffractometer with Cu Kα radiation (1.5418 Å) with the step size of 0.007^o over the 2θ range of 10°-90° at a voltage of 40 kV and a current of 30 mA. Samples including parent materials (eutectic ternary alkali carbonate and silica) and fused doped silica with different mass ratio have been prepared for XRD test. Data analysis was performed with the X'Pert HighScore software.

Fourier transform infrared spectroscopy (FT-IR) was carried out by PerkinElmer UATR Two spectrophotometer instrument over the range of 400-4000 cm^{-1} wavenumber using four scans with a resolution of 2 cm^{-1}.

SEM images were taken with a Zeiss Sigma VP FE-SEM with SSD EDS detector with 15 kV voltage. All sample powders were coated with Pt to prevent charging after even distribution on the carbon tape. Energy Dispersive X-ray Spectroscopy (EDS) analysis was used to detect the element concentration on the determined points.

3. Results and discussions

3.1. Thermal analysis

3.1.1. TGA of ternary carbonate eutectic

Thermal behaviour of a eutectic ternary alkali carbonate has been studied with TGA in the presence and absence of silica to monitor the mass changes during the designated temperature programme. The results indicated there were two steps in terms of mass changes during the heating program including a large initial mass loss followed by a very stable trend shown in Fig 1-a. The first step mass loss appeared with a significant drop for all silica doped samples, which was occurred within an initial heat-up cycle up to 600ºC, Fig 1-b, after the dehydration stage (all samples have been dried at 150°C for one hour before collecting data). Further heating and cooling cycles did not change sample weight any further, showing very stable response on TGA results.
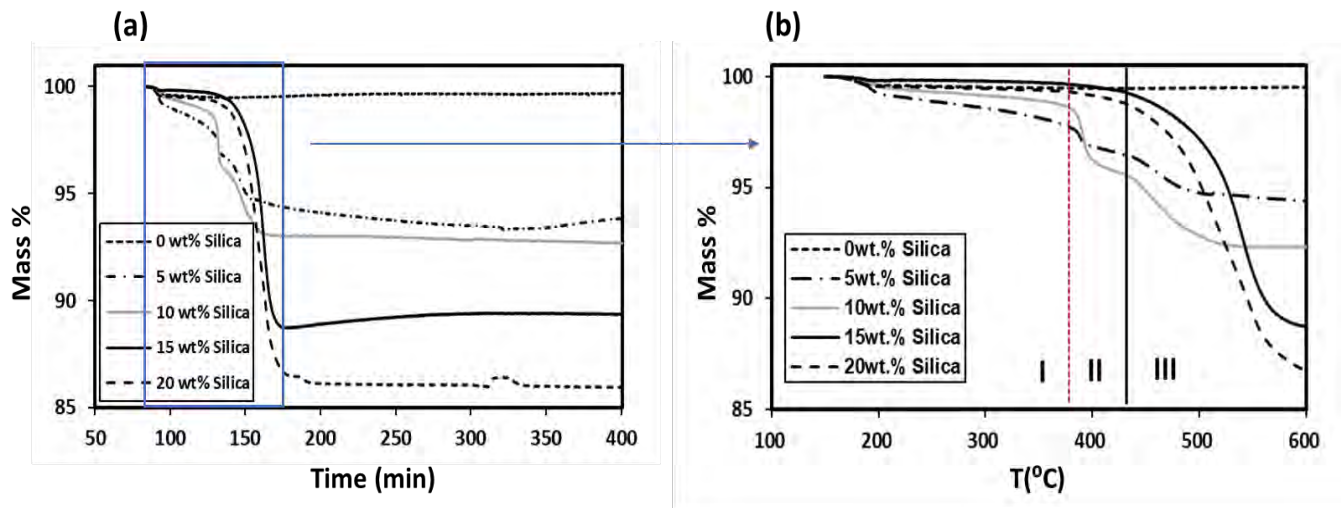
Fig 1. TGA response of eutectic ternary alkali carbonate doped with different mass ratio of silica, indicated in legend, under CO_2 atmosphere with 5⁰C/min heating rate for a) whole heating cycles process and b) for the first heat-up cycle only (red line and black line indicate the melting point of eutectic ternary alkali carbonate and the starting point of massive mass loss of 15 and 20 wt% silica, respectively).

The pure electrolyte showed very good stability with a mass reduction of ~1 wt% under operational conditions (600°C and 100% CO_2 atmosphere). Addition of silica into eutectic ternary alkali carbonate decreased the mass of samples systematically, suggesting more silica in the electrolyte results in more mass loss in the mixture. Moreover, the shape of TGA curves was different at lower silica doping ratio (<15 wt%) compared with higher silica doped (≥15wt%). As shown in Fig 1-b there were three regions of mass loss at a lower concentration of silica (region I, II, III), while at a higher concentration just one step mass loss was detected (region II, III).

These different responses were potentially due to different interaction pathways between silica and molten carbonate particles and their dependence on the mass ratio of carbonate to silica. The first step mass loss at the lower level of silica doped samples started from solid-state

contact between reactants (region I, before eutectic melting point) followed by a large loss at the melting point of carbonate, indicated by a red line in Fig 1-b (region II), and finally a mass drop after further heating of the samples (region III) up to 600ºC. However, for highly doped samples (15 and 20 wt%) there was a significant single mass loss where commenced beyond the normal melting point of the ternary eutectic (region III) and showing a bigger overall mass loss compared to the lower level of silica doped ones. A significant weight drop happened for lower silica doped samples after melting of ternary carbonate salts, region II, corresponding to the decomposition of carbonate salts accelerated after the formation of the liquid phase of salt due to silica presence. If the mass change of pure ternary carbonate is compared with silica doped carbonate after melting point, it is clearly shown that pure ternary carbonate was very stable under operational condition while silicate formation from Eqn (1) is likely to occur and accelerate the decomposition of ternary carbonate (where M is Li, Na, K) [24]:

$$M_2CO_3 + SiO_2 \rightarrow M_2SiO_3 + CO_2 \tag{1}$$

The late mass drop of higher silica doped samples (15 and 20 wt% silica) may be due to different reasons including a higher melting temperature of the mixture caused by the potential disruption of the eutectic properties, pushing the phase change to start at far beyond the point of lower silica doped samples (5 and 10 wt% silica). Alternatively, the comparatively lower content of carbonate salts in the highly doped samples could make the interaction between salts and silica take place at a much higher temperature. Regardless of doping level, when the temperature is increased all samples experienced their largest overall mass loss (region III) as shown in Table 1.

Table 1. Mass loss of different samples (initial mass loss indicates dried base mass loss of different samples from 150ºC-600ºC and subsequent mass loss indicates mass loss after initial mass loss up to end of 3rd thermal cycle. Each thermal cycle contains heat and cooling cycles from 300ºC-600ºC under CO_2 atmosphere)

Silica in Mixture [wt%]	Mass loss in region I [wt%]	Mass loss in region II [wt%]	Mass loss in region III [wt%]	Initial mass loss [wt%]	Subsequent mass loss [wt%]
0	0.52	0.01	0.01	0.51	0.50
5	2.10	1.34	2.15	5.14	1.61
10	1.31	3.04	3.31	7.66	0.93
15	0.76	0.42	10.36	11.24	0.15
20	0.69	0.73	11.69	13.28	0.72

It can be concluded that after melting of the salt, all silica can react with ternary carbonate salt and irreversibly decompose a higher amount of carbonate salts. Decomposition of some ternary carbonate salt can be aligned with the formation of new silicate phases and evolve more CO_2 as Eqn (1).

The interaction of single carbonate salts (Li_2CO_3, Na_2CO_3 and K_2CO_3) with silica has been investigated with different researchers showing different mechanisms controlling the reaction pathway. Kim et al. reported that the final products of interaction between silica and single alkali carbonate (specifically Li_2CO_3) were strongly dependant on the mixing mole ratio of

alkali carbonate to silica [25-26]. Their finding was focused on single salt interaction under inert gas atmosphere showing that if the mole ratio of Li_2CO_3/SiO_2 was more than one, two reactions were occurring in the system with the intermediate compound of Li_2SiO_3 (Eqn (2)) and the final product of Li_4SiO_4 (Eqn (3)) [26] and if mole ratio was lower than one, the reaction between silica and lithium carbonate stopped in Eqn (2) [27] and did not proceed to Eqn (3).

$$Li_2CO_3 + SiO_2 \rightarrow Li_2SiO_3 + CO_2 \qquad \Delta G = -88.472 \; kJ \quad at \; 750^0C \qquad (2)$$

$$Li_2CO_3 + Li_2SiO_3 \leftrightarrow Li_4SiO_4 + CO_2 \qquad\qquad\qquad\qquad (3)$$

Decomposition of Na_2CO_3 and K_2CO_3 was also reported with the addition of silica suggesting the reactions between salts and silica continued until one of the reactants has been consumed totally [25], via Eqn (4 and 5).

$$Na_2CO_3 + SiO_2 \rightarrow Na_2SiO_3 + CO_2 \qquad \Delta G = -46.478 \; kJ \quad at \; 750^0C \qquad (4)$$

$$K_2CO_3 + SiO_2 \rightarrow K_2SiO_3 + CO_2 \qquad \Delta G = -39.428 \; kJ \quad at \; 750^0C \qquad (5)$$

The interaction between binary $(Li/Na)_2CO_3$ with fly ash as the source of silica was examined by Sanna et al. indicated that products of the reaction were a wide variety of crystalline silicate phases, dependant on the molar ratio of each reactant [28].

In the current work, a ternary mixture of alkali carbonate salts was used to react with silica under CO_2 atmosphere, so a different reaction pathway is expected compared with single salt or binary mixture under different gas atmosphere. If we assume each carbonate salt individually reacts with silica, without the interference of other salts according to Eqn (2), (4) and (5) for Li_2CO_3, Na_2CO_3, and K_2CO_3 respectively (the general equation is shown in Eqn (1)), the calculated mass loss for the reaction of single salts (via CO_2 generation) can be compared with observed value as shown in Fig 2-a.
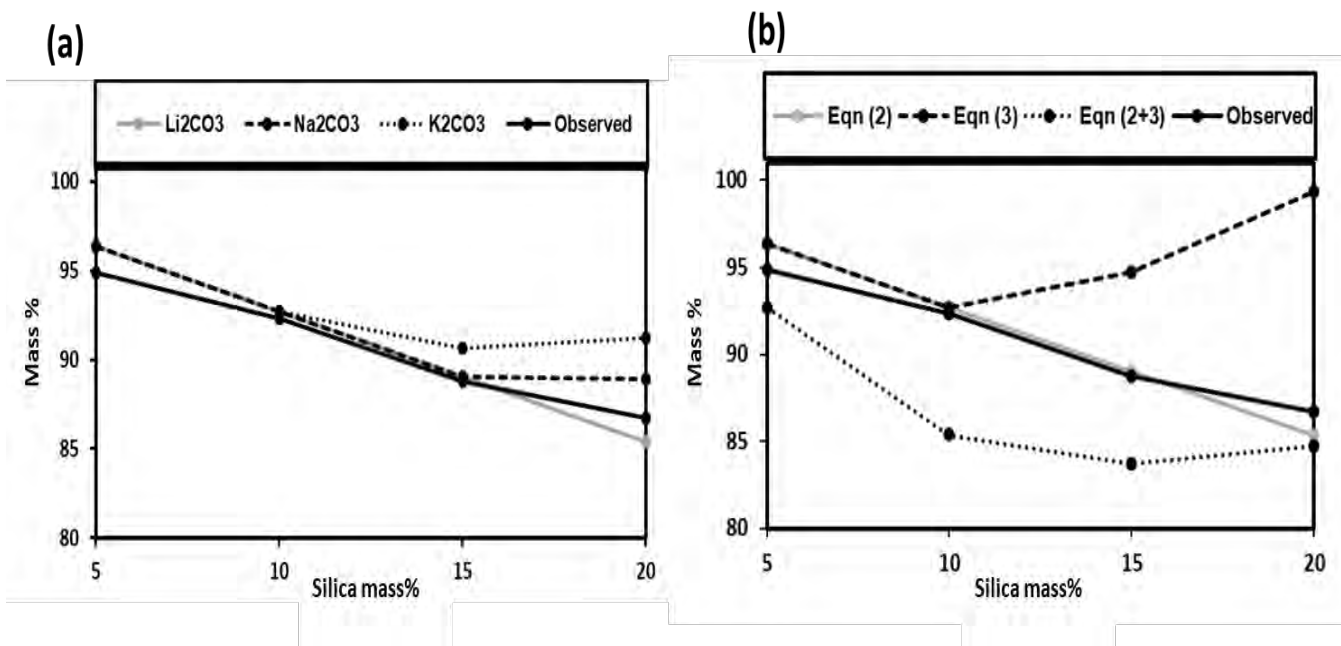
Fig 2. Calculated mass loss of a) individual carbonate salt according to Eqn (1), b) according to Eqn (2 and 3) compared with an observed mass loss from first heating-up cycle at 600°C (i.e. initial mass loss in Table 1) under CO_2 atmosphere.

Mass loss comparison indicated that at the lowest doped level of silica in the ternary carbonate, 5 wt%, observed mass loss was more than the calculated value for each carbonate salt via Eqn 1 (Fig 2-a). This suggests that the solid-phase mass loss, which started from the first contact between ternary salt and silica, was greater than mass loss expcted for one single salt. From a thermodynamic point of view, the Gibbs free energy of formation of Li_2SiO_3 is lower than other carbonate salts according to Eqn (2-5), so the reaction between Li_2CO_3 and silica is thermodynamically more favourable than other salts. If it this the case, due to the presence of the excess amount of Li_2CO_3 at lower silica level in the mixture, Table 2, additional mass loss can be expected to proceed via the formation of Li_4SiO_4, Eqn (3), causing more CO_2 evolution and mass loss. If the mass loss was attributed to mass loss from lithium compounds only and formation of Li_4SiO_4 (Eqn 3) occurred immediately after the formation of Li_2SiO_3 (Eqn 2), the expected mass loss from this is much larger than observed as shown in Fig 2-b, which considers

12

Eqn (2+3). Thus, the results suggest that the simultaneous reaction of Eqn (2) and Eqn (3) may not happen to its full extent in ternary carbonate mixture and all three salts might be involved in the mass loss at lower silica concentration mixture. This is in disagreement with findings of Kim et al. [26] related to the dependence of the type of product to mole ratio of silica to carbonate.

Table 2. *Mole concentration of individual salts with different silica loadings*

Silica [wt%]	Silica [mol %]	Li_2CO_3 [mol%]	Na_2CO_3 [mol%]	K_2CO_3 [mol%]
5	8	41	29	22
10	16	37	27	20
15	23	34	24	19
20	30	31	22	17

At the higher silica level, 10 and 15 wt%, the calculated mass loss for a single salt and the observed ternary mixture showed very similar values, Fig 2-a. However, at 20 wt% silica mixture, the observed mass loss showed a smaller value than the calculated one. It can be understood that at 20 wt% silica, according to the stoichiometry of Eqn (2,4 and 5) and Table 2, the limiting reactants are Na_2CO_3 and K_2CO_3, while there is enough Li_2CO_3 in the mixture. The lack of excess or a sufficient amount of all individual salts in the mixture might be a reason for the change in the mass loss shape for the highest loading. It might have been assumed only lithium carbonate is reacting with silica since the observed mass loss most closely follows this single salt trend, however the observed mass loss reflected the fact that all three salts are likely to be reacting simultaneously with silica.

3.1.2. TGA response in different gas environments

The stability of different samples under continuous heating and cooling cycles as outlined in 2.1 was also investigated under different gas atmospheres for different silica concentrations and the results are shown in Fig 3.
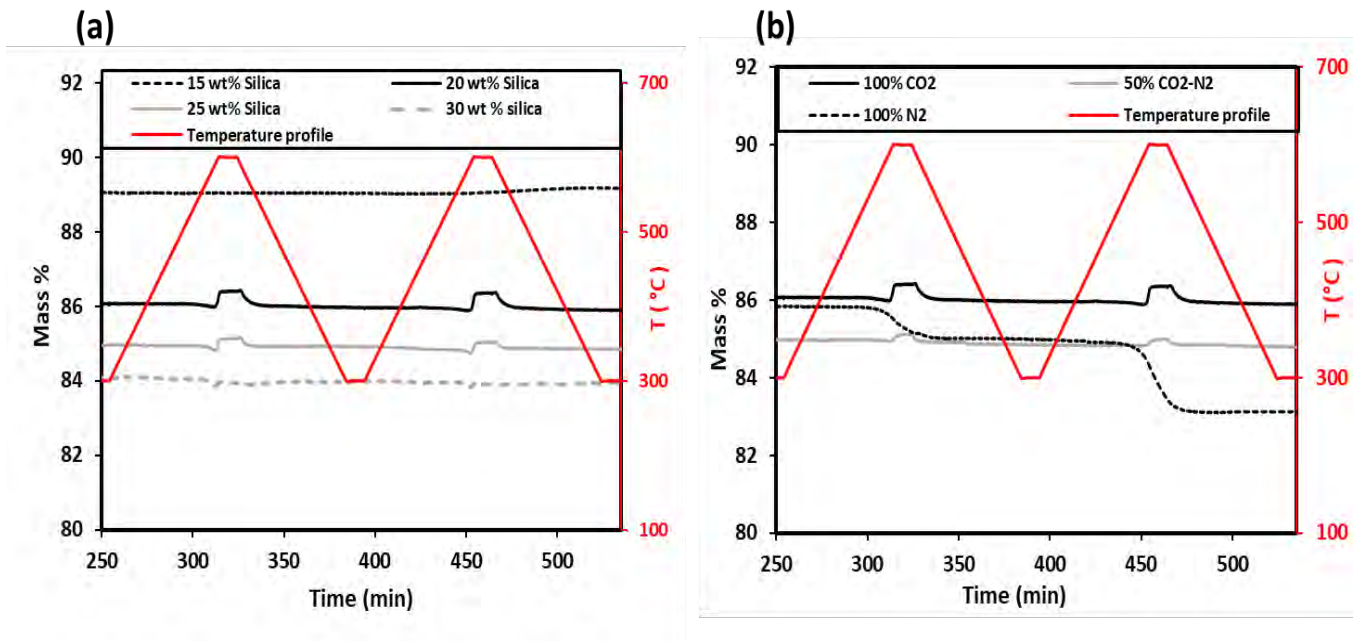

Fig 3. TGA response with 5⁰C heating rate after an initial heating cycle of a) different silica concentration samples under CO_2 atmosphere and b) 20 wt% silica under a different gas atmosphere as indicated in the figure legend.

A reversible mass gain observed for samples with 20 and 25 wt% silica after the first heat-up cycle when the temperature held hold at 600⁰C under 100% CO_2. This phenomenon was is highly dependent on silica content in the mixture and gas atmosphere as depicted in Fig 3. A mass gain of 0.38 wt% and 0.25 wt% for 20 and 25 wt% silica respectively have been observed when the temperature reached to 600⁰C and they did not show any mass change as long as the samples were kept at 600⁰C and this behaviour constantly occurred during further thermal

cycling. The mass gain of the sample under 100% CO_2 might be due to equilibrium with CO_2 as Eqn (6) (where M is Li, K or Na) :

$$M_2SiO_3 + CO_2 \leftrightarrow SiO_2 + M_2CO_3 \tag{6}$$

It is therefore worth investigating the presence of new phases acting as CO_2 gas absorbent in the mixture. It was reported that K_2SiO_3 and Na_2SiO_3, new phases formed after reaction of molten salts and silica as Eqn (4) and (5), can act as a promoter on CO_2 capture and they showed a very good capacity to absorb CO_2 at high temperature [20, 29-31] which might be responsible for observed mass gain in TGA response of this study under CO_2 atmosphere.

At a lower or higher concentration of silica (15 wt% or 30 wt%), Fig 3-a, no mass gain observed during continuous heating and cooling cycles and there was a constant mass during multiple heating and cooling cycles. This could be due to the absence of an efficient contact between gas adsorbent particles and CO_2 gas to allow CO_2 to adsorb on the surface of sorbents. At lower concentration of silica, it can be explained that CO_2 adsorbent particles surrounded by a considerable amount of molten phase of electrolyte which makes transport of CO_2 gas difficult through a liquid phase to reach to the adsorbent surface [20]. While at the higher level of silica, 30 wt% silica, access to CO_2 absorbent particles can be prohibited by non-adsorbent particles exist in the mixture such as solid Li_2SiO_3 as the possible product after reaction between Li_2CO_3 and silica, Eqn (2).

To confirm gas atmosphere effect on the observed mass change, CO_2 gas atmosphere was switched to N_2 and TGA results showed in Fig 3-b. Decreasing CO_2 concentration above the sample can be an informative way to explore mass changes if the mass gain was due to reactivity with CO_2 gas. Firstly, CO_2 concentration decreased to half (50 vol% CO_2- 50 vol%N_2) at 20 wt% silica (the highest value of observed mass gain among different silica samples) and all other experimental conditions kept unchanged. The result showed a smaller

mass gain in TGA response, Fig 3-b than 100% CO_2 prooving the impact of CO_2 gas concentration on observed mass gain. To confirm this hypothesis precisely, the entire gas atmosphere above 20 wt% silica sample changed to 100 vol% N_2. As expected, no mass gain exhibited in TGA response under 100 vol% N_2 confirming that CO_2 reactivity with the sample was the main reason for observed mass gain which directly depended on the concentration of CO_2 gas above the sample. Not only mass gain has not been noticed at 100% N_2, but also there was a large mass loss detected in this situation which might be due to two reasons. The reaction between alkali carbonates and silica proceed further in the absence of CO_2 to decompose carbonate more via forming silicate species as Eqn (1) or the unreacted carbonate in doped samples can be also decomposed in absence of CO_2, i.e. $M_2CO_3 = M_2O + CO_2$. Decomposition of a ternary carbonate sample under non-CO_2 atmosphere was reported after its melting temperature and its decomposition was accelerated depending on the type of gas atmosphere [32].

3.1.3. DTA of silica doped samples

The response of differential thermal analysis (DTA) of different silica doped samples was investigated to determine the thermal behaviour of the electrolyte especially melting point when the mass ratio of silica increased in the electrolyte. DTA graph of the first heat-up cycle (150ºC to 600ºC) depicted in Fig 4-a showing that all samples regardless of silica content represented an endothermic peak correspondent to melting process of eutectic ternary alkali carbonate. The onset temperature of the DTA curve was considered as the melting point and applied to all samples to ensure consistency. The melting point of the mixture increased slightly with increasing of silica mass ratio at first heat-up cycle showing that all samples behaved similarly regardless of silica content in the mixture. However, the area bounded by DTA curve decreased systematically with increasing silica level in the mixture which might be due to lower

level of molten state of ternary alkali carbonate according to stoichiometric of reaction, Eqn (1) and Table 2.
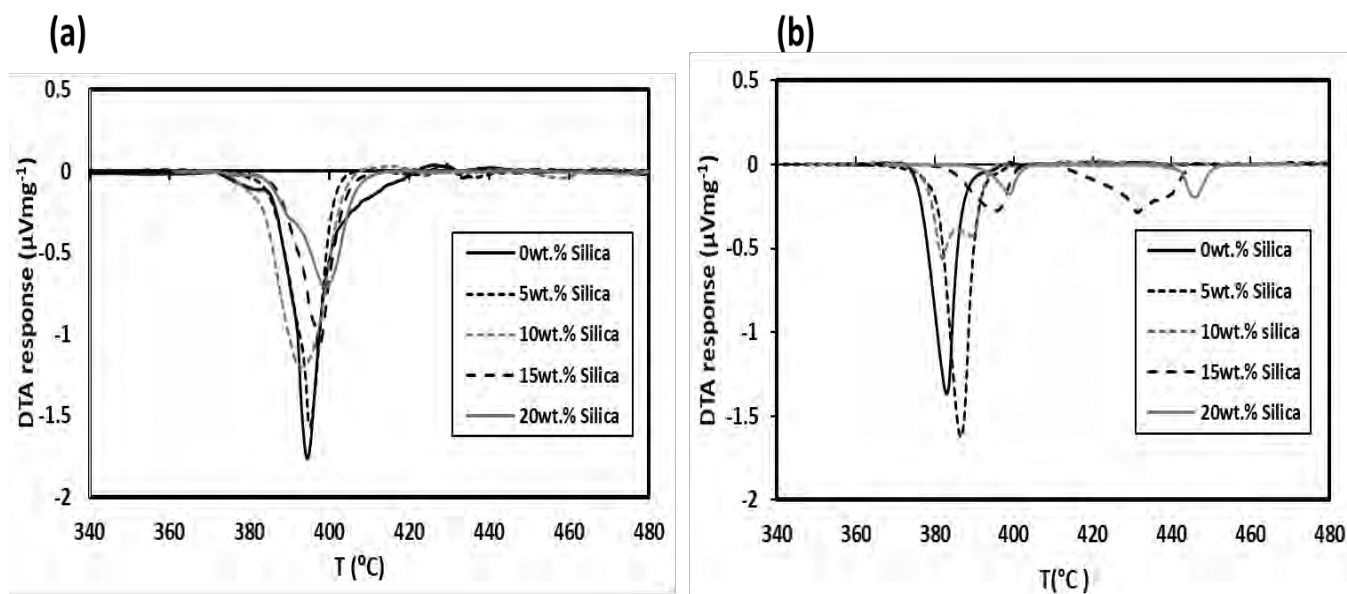

Fig 4. DTA response of different samples with 5°C/ min heating rate under CO_2 atmosphere a) first heat-up cycle and b) after homogenisation cycles

After homogenisation steps, composed of three heating and cooling cycles, DTA response of samples was different in comparison with the first heat-up step as can been seen in Fig 4-b. The reproducible melting temperature and similar DTA curves were observed after three heating and cooling cycles demonstrating the slow kinetics of the melting process of carbonate and silica dissolution in molten carbonate as well. The addition of silica to ternary carbonate changed its melting behaviour in different ways compared with the first heat-up cycle including modification of melting point, the area under DTA curve and introduction of the second peak for higher concentrations of silica. All samples doped with silica increased the apparent melting point of ternary alkali carbonate eutectic. The sample with 5 wt% silica showed 4°C higher melting point than the pure electrolyte, which might be due to the interaction between silica and electrolyte, generating solid compounds suspended in the molten state of electrolyte

and disrupting the eutectic melting behaviour [14]. The extent of this disruption increased with increasing silica in the mixture, causing a second peak in the DTA curve at 10 wt%. The addition of more silica to carbonate from 5 wt% to 10 wt% did not change the melting point of the mixture to a higher value, however, the area under curve decreased remarkably as mentioned before.

At 15 and 20 wt% silica, a noticeable increase of melting point was observed about 10°C and 17°C higher than the pure electrolyte respectively, as well as splitting the second peak from the first peak. Both melting of ternary carbonate salt and formation of silicate are endothermic process [25-26] which may happen simultaneously in the same region showing one endothermic peak at DTA response in the first heat-up cycle. Because TGA response showed one mass drop just in the first heat-up cycle, it can be explained that the first endothermic peak corresponded to the melting of carbonate salts which was in excess for the reaction between salts and silica. The appearance of the second endothermic peak from the second heat-up cycle (which did not exist in the first heat-up cycle) might be due to dissolution of the new phase that was formed from first heat-up in the molten electrolyte as the temperature rises. Another hypothesis regarding the second endothermic peak might correspond to the glass transition temperature (T_g) which appeared from 10 wt% silica and increased with silica level in the mixture. It has been reported that the incorporation of K_2O in Li_2O: SiO_2 system can change T_g depending on mole ratio of Si_2O: Li_2O and Si_2O: K_2O from 480°C to 505°C [19] and also the similar finding with K_2O: Nb_2O_5: SiO_2 glass system was found by Pernice et al. [33]. Increasing T_g with increasing SiO_2: K_2O mole ratio is in agreement with observations of this study if the second peak considered as the T_g, although there is a difference between T_g value in this study from previous ones due to presence of different components in the mixture and also different gas atmosphere [19].

The temperature of the second peak increased from its first emergence at 10 wt% from 384ºC to 443ºC at 20 wt% likely indicating a higher concentration of silicate species in the mixture needed a higher temperature to dissolve in the molten state of carbonate. Note that the second peak was not observed at 5 wt% silica due to the lower content of silicate species in molten carbonate which resulted in the dissolution and melting phenomenon cannot be differentiated from DTA response to show a second peak separately. These results clearly showed that the silica to carbonate ratio played a crucial role in the thermal behaviour of ternary alkali carbonate eutectic through strong influence on the extent of melting temperature disruption.

3.2. Characteristic analysis of carbonate and doped samples

3.2.1. FT-IR analysis

Silica has been shown a very reactive species in contact with eutectic ternary alkali carbonate, modifying the electrolyte behaviour in different ways as discussed in section 3.1. The degree of this alteration needs to be investigated comprehensively in respect of silica concentration. Fig 5 illustrated the FT-IR spectroscopic analysis of parent materials (eutectic ternary alkali carbonate and silica), milled 10 wt% silica (unfused/no heat treatment), and different loadings of fused silica- carbonate mixtures under CO_2 atmosphere.
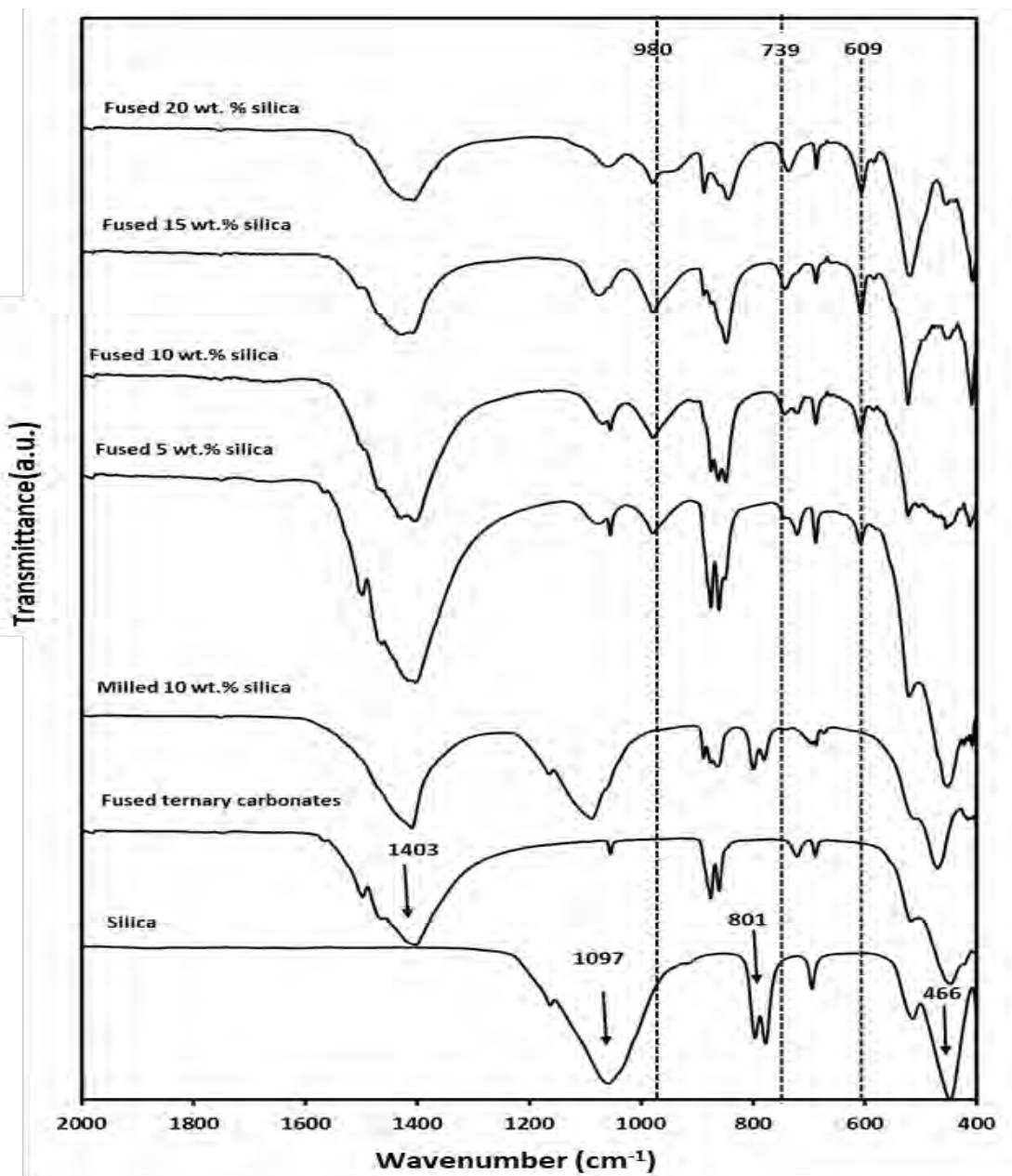
Fig 5. FT-IR spectra of different samples at different heat treatment states (fusing carried out at 600°C under CO_2 atmosphere for 2hours)

Fused ternary alkali carbonate showed a very strong peak at 1403 cm^{-1} corresponding to C=O bands which is consistent for all mixtures from milled 10 wt% SiO_2 to fused 20 wt% SiO_2 samples [28]. Table 3 shows a full summary of bands relevant to the discussion.

Table 3. Observed major FT-IR peaks of different samples and their corresponding vibration

Observed Wavenumber (cm $^{-1}$)	Assign Structure
1403	C=O symmetric stretching vibration
1097	Si-O-Si asymmetric stretching vibration
980	Si-O stretching vibration
801	Si-O-Si symmetric stretching vibration
739	Si-O symmetric stretching vibration
609	O-Si-O symmetric bending vibration
466	Si-O-Si bending vibration

The intensity of the C=O carbonate band decreased at a higher level of doped silica, as expected due to the existence of the lower level of unreacted carbonate in the mixture. Silica, as another parent material, presented the intense peaks at regions of 466 cm^{-1}, 801 cm^{-1} and 1097 cm^{-1} attributed to Si-O-Si bending vibration, Si-O-Si symmetric stretching vibration, and Si-O-Si asymmetric stretching vibration bond, respectively [34]. Heat treatment of samples doped with silica generated new peaks in FT-IR spectra indicating the formation of new phases during fusing. Note that 10 wt% milled silica represented all bands assigned to both parents without creating new peaks. For instance, it depicted very strong peaks in both areas of carbonate dominant (1403 cm^{-1}) and silica dominant (1097 cm^{-1}, and 801 cm^{-1}). However, after heat treatment of silica doped samples, as explained in thermal studies, silicate was expected to be the main new compound after reaction between ternary carbonate and silica which FT-IR spectra also confirmed with the appearance of new peaks. The new bands at 609 cm^{-1}, 739 cm^{-1}, and 980 cm^{-1} assigned to O-Si-O symmetric bending vibration, Si-O symmetric stretching

vibration, and Si-O stretching vibration, respectively [35-37] which did not exist in parent spectra. New peaks were generated from the lowest concentration of heat-treated samples, without the formation of new peaks at higher concentration of silica doped mixture, indicating further addition of silica into ternary alkali carbonate has not made new compounds up to 20 wt% silica. However, the intensity of some peaks, for example at 739 cm^{-1}, increased at a higher level of silica doped sample (fused 20 wt% silica in comparison with 5 wt% silica), likely due to a higher concentration and a greater crystallinity of new silicate compounds. The most important finding from FTIR tests was that all bonds assigned to pure silica disappeared after heat-treatment of silica doped samples, suggesting that silica was fully converted to silicate compounds, while carbonate peaks remained after heat-treatment meaning that carbonate compounds were not the limiting factor in reaction. Due to constraints of FT-IR instruments, the stretching vibration of Li-O band is not detectable under 400 cm^{-1} wavenumber which is known for Li_2SiO_3 compound [38-39]. To determine the type of silicate formed after the reaction, it is necessary to use another characteristic method.

3.2.2. XRD Analysis

Samples with different concentration of doped silica have been examined with XRD to indicate the type of silicate compounds which was not detectable in the FT-IR study. As it can be seen in Fig 6, new peaks appeared on XRD spectra after addition of silica to ternary carbonate at 600ºC under CO_2 atmosphere, corresponding to different silicate phases.
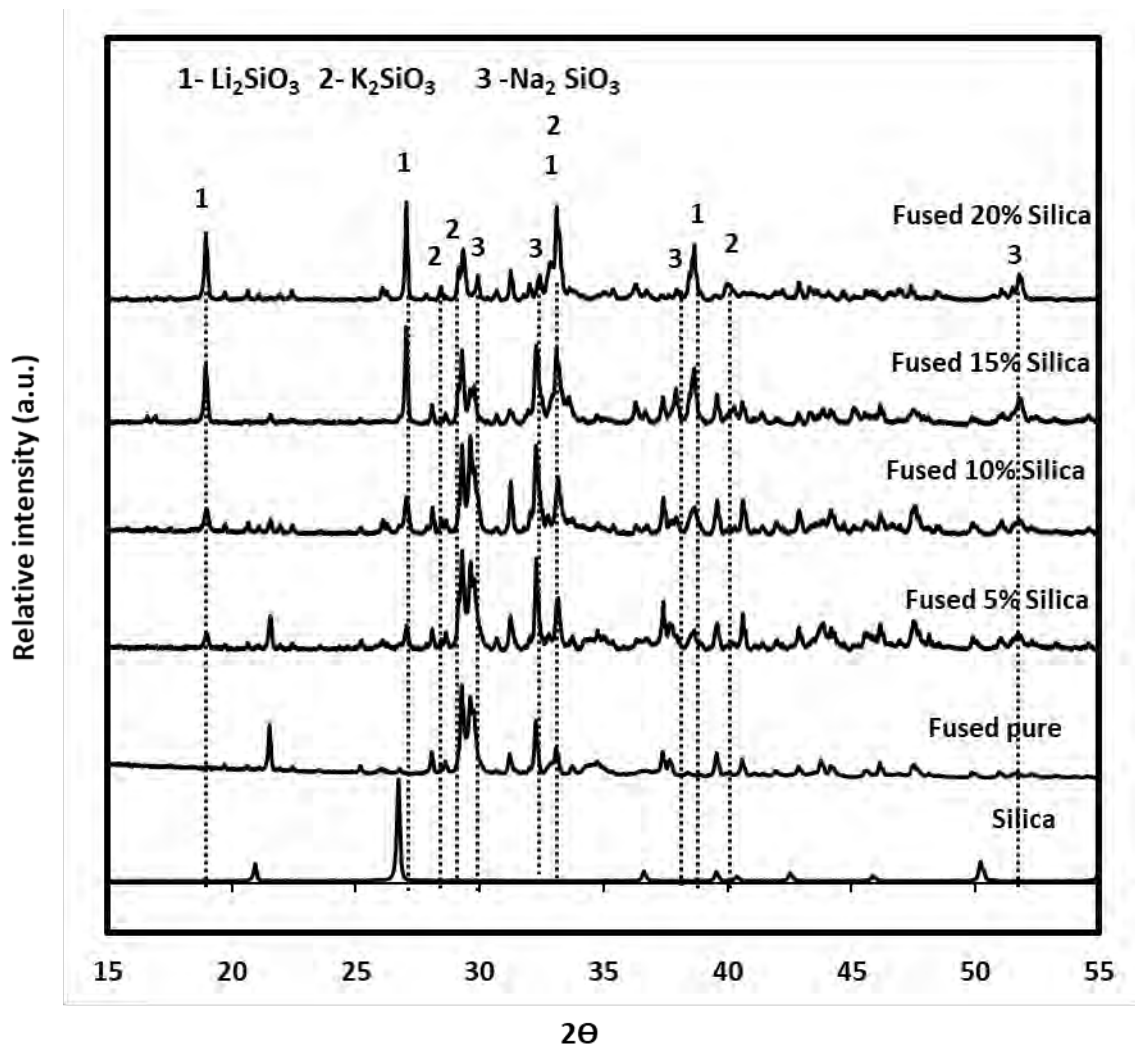
Fig 6. XRD pattern of different silica concentration in the electrolyte fused at 600°C under CO_2 atmosphere and cooled down to room temperature otherwise indicated.

The peaks of Li_2SiO_3 have been detected from the lowest to the highest concentration of silica doped samples (fused 5 wt%-20 wt% silica) at 19-27-33-38 ° Θ where the intensity of those peaks was weaker at 5 wt% silica compared with 20 wt% silica due to its lower concentration in the mixture, as expected [40]. If the concentration of silica increased in the mixture, very clear peaks of Li_2SiO_3 stand out particularly in XRD patterns of 20 wt% of silica indicating higher crystallinity or higher concentration of Li_2SiO_3 compared to other silicate species existing in the mixture.

TGA results showed the presence of some CO_2 sorbents in 20 wt% silica doped carbonate caused mass gain at 600ºC under 100% CO_2 atmosphere, Eqn (6). To find the peaks corresponding to only CO_2 absorbents such as Na_2SiO_3 and K_2SiO_3, differentiating the peaks corresponding to those sorbents from parents' peaks can be challenging due to presence of four different compounds in parents' materials as shown in XRD. Although Li_2SiO_3 showed very sharp peaks in XRD pattern of fused silica doped samples, it was shown a very low reactivity to absorb CO_2 at high temperature compared with other silicate species such as K_2SiO_3 and Na_2SiO_3 [28-29, 41]. The comparison of XRD patterns between 15 wt% and 20 wt% silica clearly showed that the CO_2 absorbents' peak intensity is significant at 20 wt% silica indicating the presence of CO_2 absorbents in the mixture which is in agreement with TGA results (Fig 3-a). For instance, the peaks corresponding to K_2SiO_3 and Na_2SiO_3 at 28.5-29..2-30-32.4-40 Θ^o only appeared in 20 wt% silica and they did not appear at a lower concentration [42]. This might be due to a lower crystallinity of those compounds in the mixture which were surrounded by high crystalline Li_2SiO_3 or a considerable amount of unreacted carbonate electrolyte.

3.2.3.   Morphology of the Electrolyte

The morphology of different samples was studied under SEM to investigate the changes on the surface microstructure of electrolyte after addition of silica and heat treatment. As can be seen in Fig 7-a, silica has a micro-size crystalline structure while the fused ternary alkali carbonate eutectic Fig 7-b presented a rough homogeneous cluster with non-porous morphology.
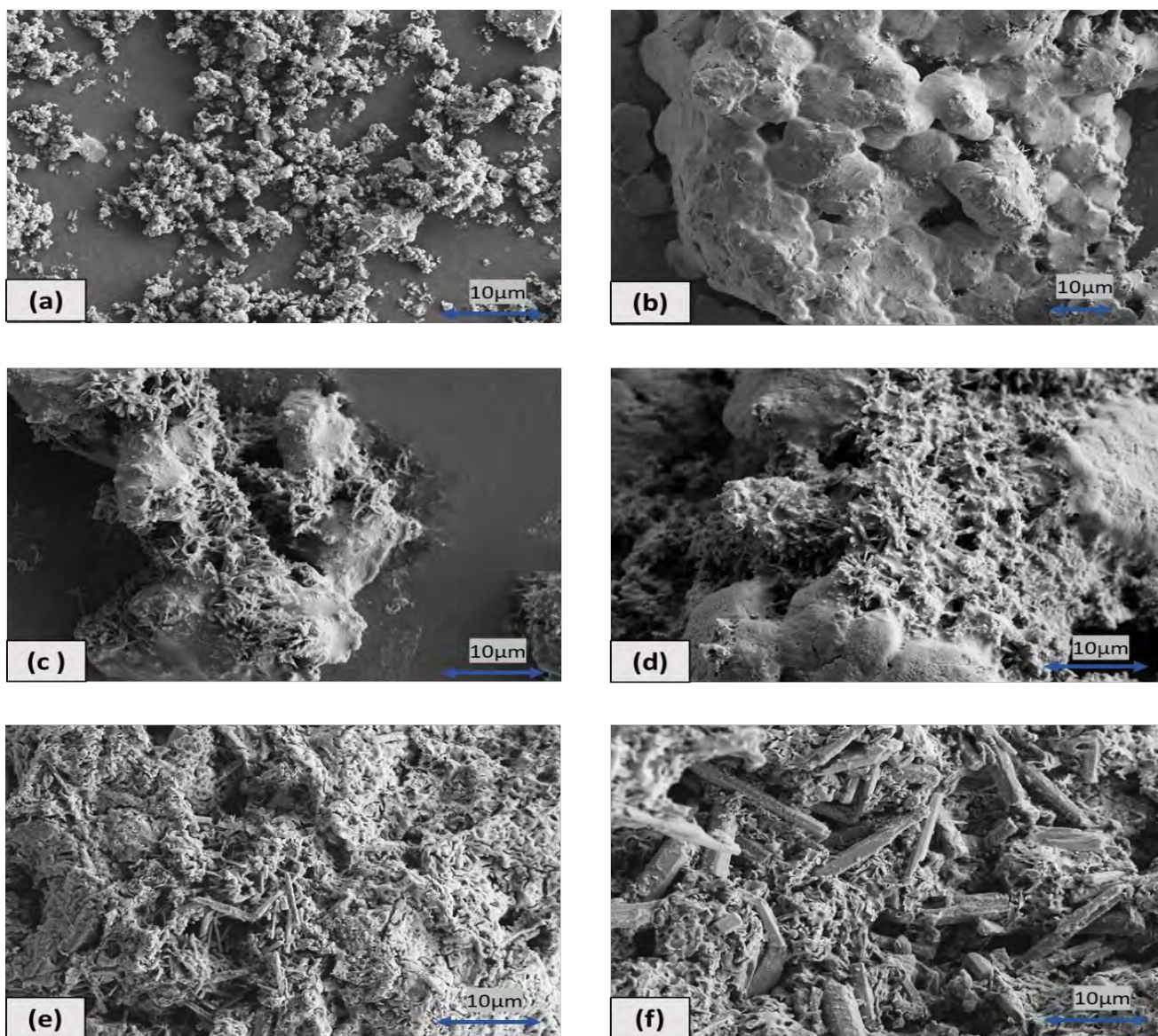
Fig 7. SEM of different samples a) silica, b) fused ternary alkali carbonate eutectic, c) fused 5 wt.% silica, d) fused 10 wt.% silica, e) fused 15 wt.% silica, and f) fused 20 wt.% silica

5 wt% and 10 wt% silica introduced a new phase of small lath-like crystals (a narrow, thin and splinter-like shape) which might indicate the formation of silicate compounds since this structure was not observed in any of the starting materials [19]. At lower silica content (Fig 7-c), there was still a rough layer of ternary carbonate at the outer surface of lath-like crystals indicating both phases, parents and new phases, exist simultaneously. At higher silica content, 15 and 20 wt%, the diameter and length of lath-like crystals increased and turned to very thick

solid compounds mixed with a porous texture. As silica ratio increased in the mixture to 20 wt%, the lath-like crystals phase reached its highest concentration in comparison with other samples Fig 7-d. The homogenised cluster structure of the ternary carbonate phase, which existed at 5 and 10 wt% silica, and to some extent at 15wt%, was not observed at higher silica content. It can be explained from DTA response and FT-IR patterns that the amount of ternary carbonate phase decreased in the mixture at 15 and 20 wt% silica (through a drastically reduced area under the DTA curve) which SEM images confirm since the morphology of carbonate also changed due to the reaction between silica and carbonate. To determine the elemental differences between lath-like crystals and the rest of the mixture, EDS analysis of fused 20 wt% silica carried out and results depicted in Fig 8.
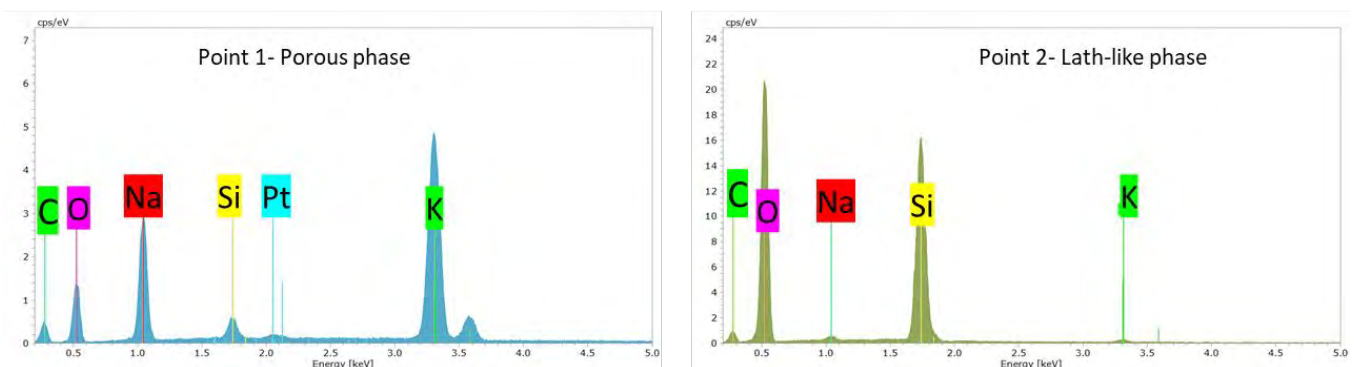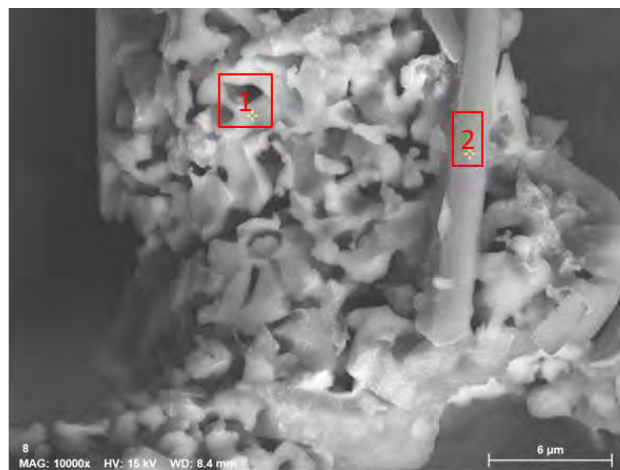

Fig 8. EDS analysis of fused 20 wt.% silica at 600C under CO2 atmosphere (Pt peak was due to coating)

EDS revealed that lath-like crystals were rich in silicon and oxygen and very poor in potassium and sodium, while the porous phase showed more than 20 times higher concentration of potassium and sodium than the lath-like crystals. As lithium is not detectable in EDS analysis due to its lightweight and silica was entirely used after reaction with carbonate (confirmed by both XRD and FT-IR results), lath-like species are concluded to be lithium silicate. The porous phase, outlined in Point 1 in Fig 8, contained the cracked and burst like shape on its surface indicating CO_2 gas evolving may occur in this phase which made those holes left behind during the cooling down process. EDS results suggested a high concentration of silicon, sodium, and potassium in the porous phase pointing to the presence of K_2SiO_3 and Na_2SiO_3 phase which acted as the CO_2 sorbents explained in previous sections.

4. Conclusion

Silica, representing a dominant a mineral component of coal, showed a very significant impact on the thermal behaviour of eutectic ternary alkali carbonate $(Li/Na/K)_2CO_3$ electrolyte. It was suggested that silica-rich ash concentration beyond 15 wt% within the DCFC led to irreversible changes in composition. The eutectic carbonate electrolyte at 600ºC under CO_2 atmosphere formed silicate phases and the degree of reaction depended on the mass ratio of silica in the electrolyte. DTA results indicated that the melting temperature of electrolyte increased in presence of silica where addition of 20 wt% silica in electrolyte raised the melting temperature 17ºC above the undoped electrolyte. It was shown that silica was consumed completely in the reaction with carbonate electrolyte and decreased the molten state of electrolyte with the formation of silicate species. It was also suggested that all three alkali carbonate species reacted with silica simultaneously to form corresponding silicate compounds, however, some of them such as Li_2SiO_3 showed more crystallinity compared with others.

References

1.   Allen, J.; Glenn, M.; Donne, S., Analysis of Theoretical Efficiency in a Model 10 Kw Direct Carbon Fuel Cell Using a Coal Based Carbonate Slurry. *Electrochimica Acta* **2020**, *329*, 135131.

2.   Jiang, C.; Ma, J.; Corre, G.; Jain, S. L.; Irvine, J. T., Challenges in Developing Direct Carbon Fuel Cells. *Chemical Society Reviews* **2017**, *46*, 2889-2912.

3.   Giddey, S.; Badwal, S.; Kulkarni, A.; Munnings, C., A Comprehensive Review of Direct Carbon Fuel Cell Technology. *Progress in Energy and Combustion Science* **2012**, *38*, 360-399.

4.   Li, X.; Zhu, Z.; De Marco, R.; Bradley, J.; Dicks, A., Modification of Coal as a Fuel for the Direct Carbon Fuel Cell. *The Journal of Physical Chemistry A* **2009**, *114*, 3855-3862.

5.   Kouchachvili, L.; Ikura, M., Performance of Direct Carbon Fuel Cell. *International Journal of Hydrogen Energy* **2011**, *36*, 10263-10268.

6.   Eom, S.; Cho, J.; Ahn, S.; Sung, Y.; Choi, G.; Kim, D., Comparison of the Electrochemical Reaction Parameter of Graphite and Sub-Bituminous Coal in a Direct Carbon Fuel Cell. *Energy & Fuels* **2016**, *30*, 3502-3508.

7.   Ahn, S. Y.; Eom, S. Y.; Rhie, Y. H.; Sung, Y. M.; Moon, C. E.; Choi, G. M.; Kim, D. J., Application of Refuse Fuels in a Direct Carbon Fuel Cell System. *Energy* **2013**, *51*, 447-456.

8.   Chien, A. C.; Arenillas, A.; Jiang, C.; Irvine, J. T., Performance of Direct Carbon Fuel Cells Operated on Coal and Effect of Operation Mode. *Journal of The Electrochemical Society* **2014**, *161*, F588-F593.

9.   Li, X.; Zhu, Z.; De Marco, R.; Bradley, J.; Dicks, A., Evaluation of Raw Coals as Fuels for Direct Carbon Fuel Cells. *Journal of Power Sources* **2010**, *195*, 4051-4058.

10.   Vutetakis, D.; Skidmore, D.; Byker, H., Electrochemical Oxidation of Molten Carbonate-Coal Slurries. *Journal of the electrochemical society* **1987**, *134*, 3027-3035.

11.   Tulloch, J.; Allen, J.; Wibberley, L.; Donne, S., Influence of Selected Coal Contaminants on Graphitic Carbon Electro-Oxidation for Application to the Direct Carbon Fuel Cell. *Journal of Power Sources* **2014**, *260*, 140-149.

12.   JANZ, G. J.; LORENZ, M. R., Solid-Liquid Phase Equilibria for Mixtures of Lithium, Sodium, and Potassium Carbonates. *Journal of chemical and Engineering data* **1961**, *6*, 321-323.

13.   Shen, J.; Hu, H.; Xu, M.; Liu, H.; Xu, K.; Zhang, X.; Yao, H.; Naruse, I., Interactions between Molten Salts and Ash Components During Zhundong Coal Gasification in Eutectic Carbonates. *Fuel* **2017**, *207*, 365-372.

14.   Glenn, M. J.; Allen, J. A.; Donne, S. W., Thermal Investigation of a Doped Alkali-Metal Carbonate Ternary Eutectic for Direct Carbon Fuel Cell Applications. *Energy & Fuels* **2015**, *29*, 5423-5433.

15.   Raistrick, I.; Ho, C.; Huggins, R. A., Ionic Conductivity of Some Lithium Silicates and Aluminosilicates. *Journal of the Electrochemical Society* **1976**, *123*, 1469.

16.   Kong, L.; Bai, J.; Li, W.; Wen, X.; Li, X.; Bai, Z.; Guo, Z.; Li, H., The Internal and External Factor on Coal Ash Slag Viscosity at High Temperatures, Part 1: Effect of Cooling Rate on Slag Viscosity, Measured Continuously. *Fuel* **2015**, *158*, 968-975.

17.   Tiznobaik, H.; Shin, D., Enhanced Specific Heat Capacity of High-Temperature Molten Salt-Based Nanofluids. *International Journal of Heat and Mass Transfer* **2013**, *57*, 542-548.

18.   Höland, W.; Apel, E.; van't Hoen, C.; Rheinberger, V., Studies of Crystal Phase Formations in High-Strength Lithium Disilicate Glass–Ceramics. *Journal of Non-Crystalline Solids* **2006**, *352*, 4041-4050.

19.   Fernandes, H. R.; Tulyaganov, D. U.; Goel, A.; Ferreira, J. M., Effect of K2o on Structure–Property Relationships and Phase Transformations in Li2o–Sio2 Glasses. *Journal of the European Ceramic Society* **2012**, *32*, 291-298.

20.   Liu, J.; Wang, Z.; Wang, Z.; Song, J.; Li, G.; Xu, Q.; You, J.; Cheng, H.; Lu, X., Alkali Carbonates Promote Co 2 Capture by Sodium Orthosilicate. *Physical Chemistry Chemical Physics* **2019**, *21*, 13135-13143.

21.   Seggiani, M.; Puccini, M.; Vitolo, S., Alkali Promoted Lithium Orthosilicate for Co2 Capture at High Temperature and Low Concentration. *International Journal of Greenhouse Gas Control* **2013**, *17*, 25-31.

22.   Yang, Y.; Liu, W.; Hu, Y.; Sun, J.; Tong, X.; Li, Q.; Zhou, Z., Novel Low Cost Li4sio4-Based Sorbent with Naturally Occurring Wollastonite as Si-Source for Cyclic Co2 Capture. *Chemical Engineering Journal* **2019**, *374*, 328-337.

23.   Allen, J. A.; Glenn, M.; Hapugoda, P.; Stanger, R.; O'Brien, G.; Donne, S. W., An Investigation of Mineral Distribution in Coking and Thermal Coal Chars as Fuels for the Direct Carbon Fuel Cell. *Fuel* **2018**, *217*, 11-20.

24.   Habboush, D.; Kerridge, D.; Tariq, S., Molten Lithium Carbonate—Sodium Carbonate—Potassium Carbonate Eutectic: The Reaction of Ten Main Group Acidic Oxides and Oxyanions. *Thermochimica Acta* **1978**, *25*, 357-366.

25.   Kim, J.-W.; Lee, Y.-D.; Lee, H.-G., Decomposition of Na2co3 by Interaction with Sio2 in Mold Flux of Steel Continuous Casting. *ISIJ international* **2001**, *41*, 116-123.

26.   Kim, J.-W.; Lee, Y.-D.; Lee, H.-G., Decomposition of Li2co3 by Interaction with Sio2 in Mold Flux of Steel Continuous Casting. *ISIJ international* **2004**, *44*, 334-341.

27.   Devyatkin, S.; Pisanenko, A.; Shapoval, V., Chemical and Electrochemical Behavior of Carbonate Melts Containing Silicon Oxide. *Russian journal of applied chemistry* **2002**, *75*, 562-564.

28.   Sanna, A.; Ramli, I.; Maroto-Valer, M. M., Development of Sodium/Lithium/Fly Ash Sorbents for High Temperature Post-Combustion Co2 Capture. *Applied Energy* **2015**, *156*, 197-206.

29.   Kalinkin, A.; Kalinkina, E.; Zalkind, O.; Makarova, T., Mechanochemical Interaction of Alkali Metal Metasilicates with Carbon Dioxide: 1. Absorption of Co 2 and Phase Formation. *Colloid journal* **2008**, *70*, 33-41.

30.   Hu, Y.; Liu, W.; Yang, Y.; Qu, M.; Li, H., Co2 Capture by Li4sio4 Sorbents and Their Applications: Current Developments and New Trends. *Chemical Engineering Journal* **2019**, *359*, 604-625.

31.   Kim, H.; Jang, H. D.; Choi, M., Facile Synthesis of Macroporous Li4sio4 with Remarkably Enhanced Co2 Adsorption Kinetics. *Chemical Engineering Journal* **2015**, *280*, 132-137.

32.   Olivares, R. I.; Chen, C.; Wright, S., The Thermal Stability of Molten Lithium–Sodium–Potassium Carbonate and the Influence of Additives on the Melting Point. *Journal of solar energy engineering* **2012**, *134*.

33.   Pernice, P.; Aronne, A.; Sigaev, V. N.; Sarkisov, P. D.; Molev, V. I.; Stefanovich, S. Y., Crystallization Behavior of Potassium Niobium Silicate Glasses. *Journal of the American Ceramic Society* **1999**, *82*, 3447-3452.

34.   Chen, X.; Jiang, J.; Yan, F.; Tian, S.; Li, K., A Novel Low Temperature Vapor Phase Hydrolysis Method for the Production of Nano-Structured Silica Materials Using Silicon Tetrachloride. *RSC Advances* **2014**, *4*, 8703-8710.

35. Devarajan, V.; Shurvell, H., Vibrational Spectra and Normal Coordinate Analysis of Crystallinelithium Metasilicate. *Canadian Journal of Chemistry* **1977**, *55*, 2559-2563.

36. Nakagawa, A.; Kuwata, N.; Matsuda, Y.; Kawamura, J., Thin Film Lithium Battery Using Stable Solid Electrolyte Li4sio4 Fabricated by Pld. *ECS Transactions* **2010**, *25*, 155-161.

37. Nakagawa, A.; Kuwata, N.; Matsuda, Y.; Kawamura, J., Characterization of Stable Solid Electrolyte Lithium Silicate for Thin Film Lithium Battery. *Journal of the Physical Society of Japan* **2010**, *79*, 98-101.

38. Nocuń, M.; Handke, M., Identification of Li–O Absorption Bands Based on Lithium Isotope Substitutions. *Journal of Molecular Structure* **2001**, *596*, 145-149.

39. Carella, E.; Hernandez, M., High Lithium Content Silicates: A Comparative Study between Four Routes of Synthesis. *Ceramics International* **2014**, *40*, 9499-9508.

40. Cruz, D.; Bulbulian, S.; Lima, E.; Pfeiffer, H., Kinetic Analysis of the Thermal Stability of Lithium Silicates (Li4sio4 and Li2sio3). *Journal of Solid State Chemistry* **2006**, *179*, 909-916.

41. Pfeiffer, H., Advances on Alkaline Ceramics as Possible Co2 Captors. In *Advances in Co2 Conversion and Utilization*, ACS Publications: 2010; pp 233-253.

42. Sanna, A.; Maroto-Valer, M. M., Co2 Capture at High Temperature Using Fly Ash-Derived Sodium Silicates. *Industrial & Engineering Chemistry Research* **2016**, *55*, 4080-4088.